CORA Cork Open Research Archive
Cartlann Taighde Oscailte Chorcaí

Title	Modelling and control of a floating oscillating water column
Authors	Kelly, James F.
Publication date	2016
Original Citation	Kelly, J. F. 2016. Modelling and control of a floating oscillating water column. PhD Thesis, University College Cork.
Type of publication	Doctoral thesis
Rights	© 2016, James Francis Kelly. - http://creativecommons.org/licenses/by-nc-nd/3.0/
Download date	2026-09-13 12:01:49
Item downloaded from	https://hdl.handle.net/10468/3471

UCC
University College Cork, Ireland
Coláiste na hOllscoile Corcaigh

Modelling and Control of a Floating Oscillating Water Column

James Francis Kelly

A thesis submitted to the National University of Ireland, Cork

For the degree of Doctor of Philosophy

September 2016

Supervised by Dr. William Wright

Head of Department: Professor Nabeel A. Riza

Department of Electrical and Electronic Engineering

University College Cork

Ireland

Table of Contents

Declaration vi

Abstract vii

Acknowledgements viii

Associated Publications ix

List of Figures x

List of Tables xiv

Nomenclature xv

1. Introduction 1

1.1. Renewable Energy 1

1.2. Wave Energy Converters 2

1.2.1. Oscillating Body Systems 2

1.2.2. Overtopping Devices 7

1.2.3. Oscillating Water Column 8

1.3. Self-Rectifying Turbines 11

1.3.1. Wells Turbine 11

1.3.2. Impulse Turbine 12

1.4. WEC Modelling 14

1.4.1. Sea Wave Modelling 15

1.4.2. Hydrodynamic Modelling 15

1.4.3. Thermodynamic Modelling 16

1.4.4. Turbine Modelling 16

1.4.5. Numerical Modelling 17

1.5. Thesis Plan 17

1.5.1. Chapter2: Numerical Model Development 18

1.5.2. Chapter 3: Verification of the Model with Experimental Data 19

1.5.3. Chapter 4: Design and CFD Modelling of an Impulse Turbine 20

1.5.4. Chapter 5: Control Theory and Energy Storage System Testing 21
1.5.5. Chapter 6: Conclusions and Future Work 21
2. Numerical Modelling for a BBDB OWC 22
2.1. Oscillating Water Column Modelling 22
2.1.1. Hydrodynamic Model 23
2.1.2. Thermodynamic Model 29
2.1.3. Impulse Turbine Model 31
2.1.4. Controller and Generator Model 34
2.1.5. Full Numerical Model 38
2.2. CORES Project Synopsis 42
2.3. Impulse Turbine Design Parameters 43
2.3.1. Turbine Hub and Blade Height 43
2.3.2. Turbine Blade Geometry 45
2.3.3. Turbine Guide Vane Geometry 47
2.4. Conclusion 51
3. Numerical Model Verification 53
3.1. Turbine and Torque-Speed Controller Model 54
3.1.1. Determination of Indirect Experimental Variables 55
3.1.2. Modelled and Experimental Results and Comparison 57
3.2. Thermodynamic Model 64
3.2.1. Determination of Indirect Experimental Variables 64
3.2.2. Model Results and Comparison 65
3.3. Hydrodynamic Model 76
3.4. Investigation of Experimental Data Anomalies 78
3.4.1. Hypothesis: Mechanical Brake Failure 80
3.4.2. Hypothesis: Movable Guide Vane Failure 82
3.5. Conclusion 85

4. Full Scale Impulse Turbine 87
4.1. Site Specific Design Parameters 87
4.1.1. BBDB Design and Performance 88
4.1.2. Turbine Matching 90
4.2. Building the Turbine in SolidWorks 95
4.2.1. Turbine Hub 96
4.2.2. Guide Vane Hubs 97
4.3. Computational Fluid Dynamics Preparation 98
4.3.1. Methodology for Characterisation of the Turbine Model 99
4.3.2. Initial Settings 100
4.4. Computational Fluid Dynamics Modelling 109
4.4.1. 300 mm Turbine CFD Modelling 110
4.4.2. 2.5 m Turbine CFD Modelling 116
4.5. Mathematical Performance Characteristics for Model 122
4.5.1. Power Coefficient 124
4.5.2. Pressure Coefficient 125
4.5.3. Damping Coefficient 126
4.6. Conclusions 128
5. Control Strategy and Short-term Energy Storage Testing 130
5.1. Power Quality of Wave Energy Converters 132
5.2. Energy Storage 133
5.3. Turbine Inertia Selection and Design 134
5.4. Simulated Sea States and Internal Water Surface Motion 136
5.5. Device Control Strategies 139
5.5.1. Low-Inertia Turbine Controller 140
5.5.2. High-Inertia Turbine Controllers 144
5.6. Simulation Results 150

5.6.1. Low-Inertia Turbine 151
5.6.2. High-Inertia Turbine 155
5.6.3. Discussion 164
5.7. Conclusions 169
6. Conclusions and Future Work 170
6.1. Chapter Two 170
6.2. Chapter Three 171
6.3. Chapter Four 173
6.4. Chapter Five 174
6.5. Future Work 175
Appendix A: MATLAB code for generating random sea state arrays based on the Bretschneider Spectrum 178
Appendix B: MATLAB Function 'IWS_Amplitude' 180
Appendix C: BBDB OWC SIMULINK Model 181
Bibliography 184

DECLARATION

I, James Francis Kelly, hereby declare that the thesis submitted is my own work and has not been submitted for another degree either at University College Cork or elsewhere.

Work carried out by others has been duly acknowledged in the thesis.

Signed: _____

Date: _____

ABSTRACT

A novel numerical model of a Bent Backwards Duct Buoy (BBDB) Oscillating Water Column (OWC) Wave Energy Converter (WEC) was created based on existing isolated numerical models of the different energy conversion systems utilised by an OWC to harvest the kinetic energy of sea waves and generate electrical energy. The novel aspect of this numerical model is that it incorporates the interdependencies of the different power conversion systems rather than modelling each system individually. This was achieved by accounting for the dynamic aerodynamic damping caused by the changing turbine rotational velocity by recalculating the turbine damping for each simulation sample and applying it via a feedback loop. The accuracy of the model was validated using experimental data collected during the Components for Ocean Renewable Energy Systems (CORES) EU FP-7 project, which culminated in the deployment of a 1:4 scale BBDB OWC at the Sustainable Energy Authority of Ireland (SEAI) test site in Galway Bay, Ireland. The model was found to accurately recreate the experimental data with errors ranging from approximately 2%-10%, depending on the process analysed. During the verification process, it was discovered that the model could also be applied as a valuable tool when troubleshooting device performance. Following the validation process, the 1:4 scale model was recreated at full scale. A new turbine was developed for the full scale model, investigated using Computational Fluid Dynamics (CFD) software, and added to the full-scale numerical model. Finally, the energy storage capacity of the impulse turbine was investigated by modelling the turbine with both high and low inertia and applying three turbine control theories to the turbine using the full scale model. Of the three control theories, a single Maximum Power Point Tracking (MPPT) algorithm was applied to the low-inertia turbine, while both a fixed and dynamic control algorithm was applied to the high-inertia turbine. The low-inertia turbine with MPPT control had the most efficient pneumatic-to-electrical power conversion rate, but the quality of the electrical output power was very poor. For the high-inertial turbine, the conversion efficiency suffered, but the power quality improved significantly. The fixed controller performed considerably better than the dynamic controller. These results suggest that the high-inertia turbine could be used as a flywheel energy storage device that could help minimize output power variation despite the low operating speed of the impulse turbine. This research identified the importance of applying dynamic turbine damping to a BBDB OWC numerical model, revealed additional value of the model as a device troubleshooting tool, and found that an impulse turbine could be applied as an energy storage system on an OWC.

ACKNOWLEDGEMENTS

There are many people who have supported and helped me while I was on this great endeavour that was my time as a PhD student. I would like to thank a few whom without I would not have been able to complete this monumental task.

To my supervisor Bill Wright, who agreed to take me on as his own PhD student when my original supervisor moved on from academics to the private sector. He helped structure my work and my thesis so that it might properly come together to become the completed project documented in this book and was instrumental in helping me sculpt my technical writing style. He was key to keeping me on track when I needed someone to steady the ship, whether the issues were technical, writing, or personal. And he made sure that I stuck to the task at the end and got my thesis in under the line before the April 1st 2016 deadline.

To Ray Alcorn, who has informally served as a mentor to me throughout my time as an employee at the Hydraulics and Maritime Research Centre as well as my time as a PhD student. He has helped me from the original decision to take on the challenge of becoming a PhD student, through tough decisions as to the direction of my work, and the professional decisions I have made during and since I completed my thesis. I would not be where I am today without his support.

To Dara O'Sullivan and Tony Lewis, who were my original co-supervisors. They helped me to draft my original concept for the work I undertook, and they remained ready to help me after they left their duties at UCC. Without them, this project never gets started.

I wish to acknowledge and show my appreciation to the Irish Research Council for Science Engineering and Technology (IRCSET) for funding this research under the Enterprise Initiative, and to the Marine Institute for funding my PhD.

I would like to thank the staff of the Department of Electrical and Electronic Engineering in University College Cork. A special word of appreciation goes to the administrative staff Geraldine Mangan, Ralf O'Flaherty, Niamh O'Sullivan, Mary Costello, and Rita Sarteschi. I'd also like to thank Dr. Gordon Lightbody for serving as my internal examiner. Also for allowing me access to the facilities of the department, I'd like to thank Professor Nabeel A. Riza and Professor Michael Creed.

To everyone at the MaREI centre, formally the Hydraulics and Maritime Research Centre (HMRC), particularly Darren, Tom, Niall, Sarah, and Judy, I thank you for all your help through the first few years of my PhD when I was based at the HMRC and for continuing to help support me after I moved to the Electrical Engineering Building.

To my parents James and Lucy, my brother Bill, and all of my massive family back in the states. Thank you all for your unwavering support, patience and encouragement. It's taken a long time, but I am officially 'Dr. Jim Bob'.

To everyone in the first floor PhD room in the electrical engineering building, Megan, Brian, Allison, Oksana, Rehan, Haiyang, and Wentao for making the office a good place to be and making getting my work done both easier and harder.

ASSOCIATED PUBLICATIONS

- J. Kelly, D. O'Sullivan, R. Alcorn, A.W. Lewis, "Challenges and Lessons Learned in the Deployment of an Off Shore Oscillating Water Column", *Proceedings from the EVER 2012 Conference, Monte Carlo, Monaco,* 2012.

- J. Kelly, W. Wright, D. O'Sullivan and A. Lewis, "Potential supervisory Real Time Integrated Monitoring and Control System (RTIMCS) solutions for wave energy converters," in *European Wave and Tidal Energy Conference,* Aalborg, Denmark, 2013.

- J. Kelly, D. O'Sullivan, W. Wright, Alcorn, R. and A. Lewis, "Challenges and lessons learned in the deployment of an offshore oscillating water column," *COMPEL: The International Journal for Computation and Mathematics in Electrical and Electronic Engineering,* vol. 33, no. 5, pp. 1678-1704, 26 August 2014.

- J. Kelly, W. Wright, W. Sheng, K. O'Sullivan, "Implementation and verification of a wave-to-wire model of an oscillating water column with impulse turbine," *IEEE Transactions on Sustainable Energy,* vol. 7, no. 2, pp. 546-553, April 2016.

LIST OF FIGURES

Fig. 1.1: Wavebob two-body heaving WEC 3
Fig. 1.2: Prototype of the Wavestar multi-body heaving WEC 4
Fig. 1.3: Archimedes Wave Swing submerged heaving WEC 5
Fig. 1.4: Pelamis pitching WEC 6
Fig. 1.5: Oyster near-shore bottom-hinged WEC 6
Fig. 1.6: Wave Dragon overtopping WEC 7
Fig. 1.7: Pico Island OWC 9
Fig. 1.8: The CORES BBDB OWC during deployment in Galway Bay 10
Fig. 1.9: Spar buoy OWC 11
Fig. 1.10: Wells turbine blades with NACA0021 profile 12
Fig. 1.11: Impulse turbine rotor blades and guide vanes 13
Fig. 2.1: Bent Backwards Duct Buoy OWC schematic. 24
Fig. 2.2: CORES buoy RAO of the internal water surface. 25
Fig. 2.3: Examples of Bretschneider spectral densities 26
Fig. 2.4: Curve Fitting used to determine the control law coefficients 36
Fig. 2.5: Plot of the R2 values for the curve fits 38
Fig. 2.6: Model flow chart. 39
Fig. 2.7: An impulse turbine rotor 44
Fig. 2.8: Plan view of the turbine blade geometry 46
Fig. 2.9: Plan view of the guide vane geometry 48
Fig. 2.10: The blade and guide vane profile in plan view 49
Fig. 2.11: Turbine hub blade sweep angles 50
Fig. 3.1: P ressure sensor used to calculated flow through the Bernoulli method. 56
Fig. 3.2: Modelled and experimental data for the turbine rotational speed and braking torque demand for the data set where H_s=1.22 m and T_z =3.96 s. 59
Fig. 3.3: Modelled and experimental data for the turbine rotational speed and braking torque demand for the data set where H_s=1.09 m and T_z =3.57s. 60
Fig. 3.4: Modelled, experimental and the modelled wrong control law coefficients data for the turbine rotational speed and braking torque demand for the data set where H_s=1.09 m and T_z =3.57s. 61
Fig. 3.5: Modelled and experimental data for mechanical power output and electrical power output for the data set where H_s=1.22 m and T_z =3.96 s. 62

Fig. 3.6: Modelled and experimental data for mechanical power output and electrical power output for the data set where H_s=1.09 m and T_z =3.57s. 62
Fig. 3.7: Histogram of the electrical power output from the experimental and model data sets 63
Fig. 3.8: Experimental, dynamically damped model, and statically damped model data for the plenum chamber pressure for the data set where H_s=1.09 m and T_z =3.57 s. .. 69
Fig. 3.9: Experimental, dynamically damped model, and statically damped model data for flow across the turbine for the data set where H_s=1.09 m and T_z =3.57 s. 70
Fig. 3.10: Histogram of the experimental, dynamically damped model, and statically damped model data for chamber pressure for the data sets where H_s=1.09 m and T_z =3.57 s. 71
Fig. 3.11: Turbine model, thermodynamic model, and experimental data for the turbine rotational speed and braking torque demand for the data set where H_s=1.22 m and T_z =3.96 s. 73
Fig. 3.12: Turbine model, thermodynamic model, and experimental data for the mechanical power output and electrical power output for the data set where H_s=1.22 m and T_z =3.96 s. 74
Fig. 3.13: Turbine model, thermodynamic model, and experimental data for the turbine rotational speed and braking torque demand for the data set where H_s=1.09 m and T_z =3.57 s. 74
Fig. 3.14: Turbine model, thermodynamic model, and experimental data for the mechanical power output and electrical power output for the data set where H_s=1.09 m and T_z =3.57 s. 75
Fig. 3.15: Wave spectra for the Galway Bay test site 78
Fig. 3.16: Modelled and experimental rotational velocity based on the experimentally measured flow across the turbine. 79
Fig. 3.17: Example of experimental data not matching model predictions.. 80
Fig. 3.18: Brake housing and generator stator temperatures and turbine rotational velocity during brake failure of the CORES OWC deployment 82
Fig. 3.19: Guide vane position relative to the plenum chamber pressure and the effect the guide vane position has on the rotational velocity of the turbine. 83
Fig. 3.20: Example of the edits performed on the compromised data sets 84
Fig. 4.1: BBDB design measurements 89
Fig. 4.2: RAO for the IWS of the OWC designed for the M1 site. 90

Fig. 4.3: Energy contribution scatter plot from the M1 buoy for 2005. 93
Fig. 4.4: 2.5 m diameter impulse turbine hub and blades 96
Fig. 4.5: Upstream and downstream guide vanes for the 2.5 m turbine 98
Fig. 4.6: Full turbine within duct as created for CFD simulations. 99
Fig. 4.7: Surface goal selection for turbine torque calculation. 103
Fig. 4.8: Point goal selection for calculating air flow velocity 104
Fig. 4.9: Fluid mesh generated by Flow Simulation 105
Fig. 4.10: Partial mesh generated by Flow Simulation 106
Fig. 4.11: CFD Turbine characteristics vs. mesh resolution 109
Fig. 4.12: Experimental and CFD results for 300 mm turbine for C_t vs ϕ 113
Fig. 4.13: Experimental and CFD results for 300 mm turbine for C_a vs ϕ 114
Fig. 4.14: Experimental vs. CFD MSE vs ϕ for 300 mm turbine. 116
Fig. 4.15: Experimental and CFD results for 2.5 m turbine for C_t vs ϕ 119
Fig. 4.16: Experimental and CFD results for 2.5 m turbine for C_a vs ϕ. 120
Fig. 4.17: Experimental vs. CFD MSE vs ϕ for 2.5 m turbine 122
Fig. 4.18: Power coefficient vs. flow coefficient for 2.5 m turbine 124
Fig. 4.19: Power coefficient curve fitting 125
Fig. 4.20: Pressure vs. flow coefficient for 2.5 m turbine 126
Fig. 4.21: Pressure coefficient curve fitting 126
Fig. 4.22: Damping coefficient vs. flow coefficient for 2.5 m turbine 127
Fig. 4.23: Damping coefficient curve fitting. 128
Fig. 5.1: The low-inertia and high-inertia impulse turbines 135
Fig. 5.2: RAO vs. wave frequency for the BBDB OWC 137
Fig. 5.3: Turbine efficiency vs. flow coefficient for the 2.5 m impulse turbine. 141
Fig. 5.4: Mechanical power output of the impulse turbine at different rotational speeds for pneumatic power from 50 kW to 1,000 kW in 50 kW steps 143
Fig. 5.5: MPPT estimated electrical braking torque based on turbine speed 144
Fig. 5.6: CL1 estimated electrical braking torque based on turbine speed. 147
Fig. 5.7: CL2 torque-speed curves 150
Fig. 5.8: Low-inertia turbine pneumatic and electrical power output for sea B07 152
Fig. 5.9: Low-inertia turbine rotational velocity for sea B07. 153
Fig. 5.10: Low-inertia turbine pneumatic and electrical power output for sea B01. .154
Fig. 5.11: Low-inertia turbine rotational velocity for sea B01 154

Fig. 5.12: High-inertia turbine pneumatic and electrical power output based on CL1 for sea B07 157
Fig. 5.13: High-inertia turbine rotational velocity based on CL1 for sea B07 158
Fig. 5.14: High-inertia turbine pneumatic and electrical power output based on CL1 for sea B01 159
Fig. 5.15: High-inertia turbine rotational velocity based on CL1 for sea B01. 159
Fig. 5.16: High-inertia turbine pneumatic and electrical power output based on CL1 for sea B07. 162
Fig. 5.17: High-inertia turbine rotational velocity based on CL2 for sea B07. 162
Fig. 5.18: High-inertia turbine pneumatic and electrical power output based on CL1 for sea B01 163
Fig. 5.19: High-inertia turbine rotational velocity based on CL2 for sea B01. 164
Fig. 5.20: Average available pneumatic energy per sea state 166
Fig. 5.21: Average electrical power output per sea state. 166
Fig. 5.22: Coefficient of Variation for each controller 168

LIST OF TABLES

Table 2.1: Determination of control law coefficients. 37
Table 2.2: Impulse turbine rotor design ratios 47
Table 2.3: Impulse turbine guide vane design ratios.. 50
Table 3.1: Experimental and modelled power and speed 58
Table 3.2: Experimental and modelled pressure and flow with dynamic damping. 67
Table 3.3: Experimental and modelled pressure and flow with static damping. 68
Table 3.4: Experimental and modelled power and speed with dynamic damping 72
Table 3.5: Experimental and modelled power and speed with static damping 72
Table 4.1: 2.5 m impulse turbine hub dimensions 96
Table 4.2: 2.5 m impulse turbine guide vane dimensions 97
Table 4.3: CFD hardware and software specifications 100
Table 4.4: Initial settings for CFD software 101
Table 4.5: CFD resolution settings tested 108
Table 4.6: CFD results at a rotational velocity of 24 rads·s^{-1} 108
Table 4.7: The values of ϕ, C_a, C_t, and η for the 300 mm turbine 111
Table 4.8: CFD results for the 2.5 m impulse turbine at maximum efficiency 117
Table 4.9: The values of ϕ, C_a, C_t, and η for the 2.5 m turbine 118
Table 5.1: Sea state conditions for the west coast of Ireland. 138
Table 5.2: Bretschneider sea state conditions tested in Chapter 5 138
Table 5.3: Optimum operating rotational velocity of the turbine at the tested sea states and the mean torque value required to maintain the steady speed. 146
Table 5.4: Input variables for the sea state dependant torque-speed algorithm 149
Table 5.5: Results from low-inertia turbine simulations with MPPT control 152
Table 5.6: Results from high-inertia turbine simulations with CL1 156
Table 5.7: Results from high-inertia turbine simulations with CL2. 161
Table 5.8: Coefficients of variation for the three control strategies. 168

NOMENCLATURE

AWS	Archimedes Wave Swing
BBDB	Bent Backwards Duct Buoy
BEM	Boundary Element Method
CAD	Computer-aided Design
CFD	Computational Fluid Dynamics
CL1	Control Law 1
CL2	Control Law 2
CORES	Components for Ocean Renewable Energy Systems
ESS	Energy Storage System
EWS	External Water Surface
FP7	Seventh Framework Programme
HMRC	Hydraulic and Maritime Research Centre
IP	Intellectual Property
ISSC	International Ship and Structures Congress
IWS	Internal Water Surface
MPPT	Maximum Power Point Tracking
OPC	Open Platform Communication
OWC	Oscillating Water Column
PLC	Programmable Logic Controller
PTO	Power Take-Off
RAO	Response Amplitude Operator
RMS	Root Mean Square
SCADA	Supervisory Control And Data Acquisition
SEAI	Sustainable Energy Authority of Ireland
TRL	Technology Readiness Levels
WP1	Work Package 1
WP4	Work Package 4
a	Turbine blade suction side elliptical semi-major axis (m)
a_{CL}	Proportional constant for Control Law 2
A_p	Plenum chamber water surface area (m^2)
A_t	Turbine sweep area (m^2)
A_w	Amplitude of ocean wave (m)

b	Turbine blade height (m)
b_{CL}	Exponential constant for Control Law 2
B	Coefficient of friction
c_v	Coefficient of variation
C	Proportional constant for Control Law 2
C_a	Turbine input power coefficient
$C_g(f)$	Group velocity of waves (m s^{-1})
C_t	Turbine torque coefficient
D	Turbine diameter (m)
e	Turbine blade suction side elliptical semi-minor axis (m)
f_m	Modal frequency (Hz)
g	Acceleration due to gravity (m^2 s^{-1})
G	Gap between turbine rotor blades and guide vanes (m)
h_d	Buoy draft height (m)
h_i	Internal water surface height (m)
h_p	Buoy plenum chamber height (m)
H_s	Significant wave height (m)
J	Turbine inertia (kg m^2)
k	Damping coefficient
l_d	Buoy duct length(m)
l_g	Guide vane chord length (m)
l_p	Buoy plenum chamber length(m)
l_r	Turbine rotor blade chord length (m)
l_s	Length of straight section of guide vane (m)
m	Mass of air (kg)
N	Turbine speed (rpm)
p	Air pressure (Pa)
p_c	Plenum chamber air gauge pressure (Pa)
p_d	Duct air pressure (Pa)
p_o	Atmospheric air pressure (Pa)
P_e	Electrical power (Watts)
P_m	Mechanical power (Watts)
P_p	Pneumatic power (Watts)
P_w	Available wave power (Watts)

Q_C	Air flow calculated from CORES data ($m^3\ s^{-1}$)
Q_d	Air flow at chosen design point ($m^3\ s^{-1}$)
Q_p	Air flow across the turbine ($m^3\ s^{-1}$)
Q_w	Air flow based on change in volume in the plenum chamber ($m^3\ s^{-1}$)
r_h	Turbine hub radius (m)
r_r	Turbine rotor blade cup side radius (m)
r_R	Turbine mid-span radius (m)
r_t	Turbine tip radius (m)
R_a	Radius of the curved section of the guide vanes (m)
$S(f)$	Bretschneider spectral density
S_g	Guide vane pitch (m)
S_r	Turbine rotor blade pitch (m)
t	Time (s)
t_{sim}	Simulation time (100 ms)
T_{02}	Average wave period (s)
T_p	Peak wave period (s)
T_z	Zero crossing wave period (s)
U_R	Linear velocity of turbine blade at mid-span ($m\ s^{-1}$)
v_a	Air velocity at turbine mid-span ($m\ s^{-1}$)
v_d	Air velocity in turbine duct ($m\ s^{-1}$)
V	Volume of plenum chamber (m^3
w	Buoy bow plate width (m)
y_{CL}	Proportional constant for Control Law 2
z	Number of turbine blades
z_{CL}	Exponential constant for Control Law 2
γ	Specific heat ration of air ($kJ\ kg^{-1}\ K^{-1}$)
Δp	Pressure drop across the turbine (Pa)
Δp_f	Pressure loss due to friction (Pa)
η	Turbine efficiency
H	Turbine efficiency
κ	Turbine damping ($Pa\ s\ m^{-3}$)
μ	Mean output power (Watts)
ξ	Turbine hub-to-tip ratio
ρ_a	Density of air ($kg\ m^{-3}$)

ρ_c	Density of air inside the plenum chamber (kg m^{-3})
ρ_o	Density of air at atmospheric pressure (kg m^{-3})
ρ_w	Density of sea water (kg m^{-3})
σ	Output power standard deviation
σ_b	Blade solidity ratio
τ_f	Frictional torque (Nm)
τ_o	Torque (Nm)
τ_m	Mechanical torque (Nm)
τ_{ref}	Reference electrical torque (Nm)
Y	Pressure coefficient
ϕ	Flow coefficient
Φ	Flow coefficient
Φ_w	Volumetric flow coefficient
Ψ	Power coefficient
ω	Turbine rotational velocity (rads s^{-1})

1. INTRODUCTION

1.1. RENEWABLE ENERGY

There have been two major factors driving the advancements in the renewable energy generation sector over the last few decades: anthropic climate change related to carbon dioxide (CO_2) emissions and concerns of global energy security [1].

Mitigating global temperature rise caused by climate change, largely fuelled by human activities, is considered one of the greatest challenges of the 21st century. The link between CO_2 emissions and climate change has long been accepted among the scientific community and led to in-depth studies over a vast range of subjects from agricultural pest control [2] to nature water watersheds [3] to children's health [4] that are expected to be significantly affected by rising global temperatures. The growing list of concerns related to climate change have increased urgency and led to more stringent views taken on allowable regional CO_2 emissions targets including eventually reaching new global emissions of zero [5]. There are several steps that must be taken to achieve net global CO_2 emissions of zero, and one of the more prominent steps being taken worldwide is the replacement of traditional fossil fuel electrical generation with electrical generation from renewable energy sources.

While fossil fuel energy sources are traded on the world market and can be transported globally, renewable energy is typically generated by local sources, making renewable energy sources affectively immune from strategic and geopolitical interests and conflicts. Many of the large energy consuming and producing nations like Russia, China, USA, and OPEC countries have aligned their energy policies with the national foreign and security policies. Following the 2005-2006 natural gas conflict between Russia and Ukraine, which affected natural gas supplies to EU member states, the EU began to follow suit with their energy security policy [1]. Renewable energy sources can help to both diversify energy portfolios and limit dependencies on foreign countries for energy supply, which acts to strengthen energy security of supply [6].

In 2007, the European Union (EU) set targets to reduce CO_2 emissions, reduce overall energy consumption, and increase the consumption of energy from renewable energy sources [7]. The large-scale use of renewable energy has the ability to significantly mitigate the negative environmental and socioeconomic impacts caused by the use of fossil fuels, but the application of such energy sources requires large scale

improvements on energy conversion and distribution systems [8]. While the focus of renewable energy generation from this directive was wind and solar energy, the development of other sources of renewable energy is also being encouraged. One area of renewable energy generation that has not reach commercial maturity but is nearing commercialization is ocean energy generation, which commonly refers to wave, tidal, and thermal energy sources [9]. The theoretical global potential for ocean energy has been estimated to be between 20,000-92,000 TWh/year, with the available wave energy estimated to be between 1000-10,000 GWh/year [10]. Wave energy is a widely available energy resource with good correlation between resource and demand [11]. An effective method for converting the energy available in ocean waves could be a significant positive development for world energy generation, but there are many challenges that must yet be overcome before wave energy conversion can become a commercially solution to electrical energy production.

1.2. WAVE ENERGY CONVERTERS

There is a wide variety of Wave Energy Converter (WEC) technologies, with over one thousand prototypes developed to date [11]. Over the years, WECs have been classified by numerous methods including location, size, and working principle [12]. For this thesis, the WECs were classified by their working principle, which was divided into three distinct types: oscillating bodies, overtopping devices, and Oscillating Water Columns (OWCs) [13]. Oscillating bodies are typically offshore devices and were further categorized by their oscillating motion, while overtopping devices and OWCs were further categorized as either near-shore fixed and offshore floating [14]. The examples given here represent devices that have reached the large-scale prototype stage or developed significantly enough to have been considered for large-scale prototyping, and it is not meant to be a comprehensive list.

1.2.1. OSCILLATING BODY SYSTEMS

Most offshore devices are either floating or fully submerged oscillating bodies. Oscillating bodies typically rely on the more powerful waves available in water depths of 40 m or more, which is classified as deep water [13]. These systems use the motions of the water to induce motion in the Power-Take Off (PTO) of the device, and the induced motion that is dictated by the device design is used for classification. The oscillating body systems can be classified into heaving, pitching, and hinged systems.

1.2.1.1. HEAVING SYSTEMS

Heaving systems are devices that use vertical motion and include single-body heaving buoys, two-body heaving systems, multi-body heaving systems, and fully submerged heaving systems. Single-body heaving systems are the simplest heaving devices. They react against a fixed frame of reference, usually a bottom fixed structure, and they are considered point absorbers, as their horizontal dimensions are significantly smaller than the wavelength of the sea in which they operate [13]. An example of a single-body heaving buoy was recently developed at Oregon State University and consists of a deep-draught spar and an annular saucer-shaped buoy that was used to drive a linear electrical generator [15].

In two-body heaving systems, a second moving body replaces the fixed reference frame used in single-body systems. This acts to mitigate problems that may be caused by very deep water or substantial tidal oscillations. The PTO of a two-body heaving system depends on converting energy from the relative motion between the two separately oscillating bodies, and this interaction has been analysed in detail in [16]. The Wavebob device, illustrated in Fig. 1.1, is an example of a two-body heaving device that relies on a high-pressure hydraulic oil system to convert the two-body heaving motion into electricity, and it has been tested at quarter scale at the SEAI test site in Galway Bay, Ireland [17].

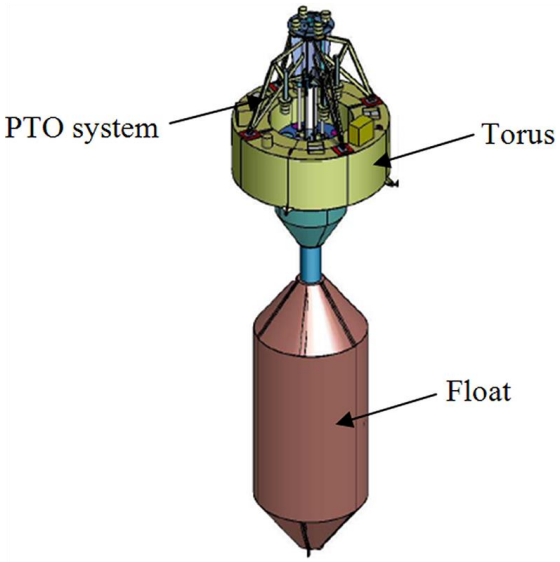

Fig. 1.1: Wavebob two-body heaving WEC [18].

Surface-based heaving systems can also be made of multi-body systems, which are often large collections of single-body devices attached to a common frame. The Wavestar, which consists of 20 hemispherical floats attached to a single platform, is an example of this. The central platform is the PTO of the system, using the motion of the 20 floats to pump hydraulic oil onto the platform and converting the high-pressure hydraulic oil into potential energy that is used to drive generators and produce steady power which can be sent to the grid [19]. A similar Brazilian hyperbaric converter uses a similar design to the Wavestar, but it uses hydraulic pressure to accelerate water into a water jet, which then excites a Pelton turbine and generator system [20]. Fig. 1.2 is a photo of a Wavestar prototype deployed near Hanstholm, Denmark [21].

Fig. 1.2: Prototype of the Wavestar multi-body heaving WEC [21].

The most well-known example of a fully submerged heaving device is the Archimedes Wave Swing (AWS), which consists of an oscillating floater and a bottom-fixed base. The floater is pushed down by the excess pressure created when the wave crest is directly above it and moves up as the water pressure decreases when a wave trough is directly above the device. A 2 MW AWS prototype using a linear electrical generator was tested off the northern coast of Portugal in 2004 [22]. Fig. 1.3 illustrates and AWS and how the waves affect its movement.

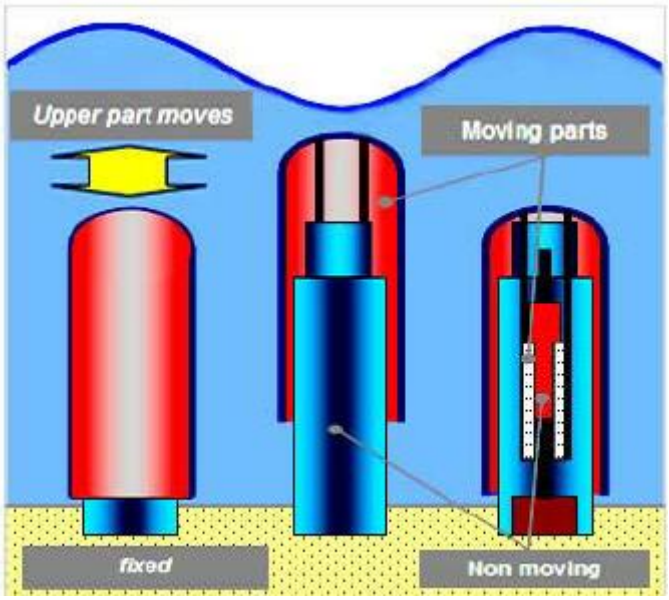

Fig. 1.3: Archimedes Wave Swing submerged heaving WEC [23].

1.2.1.2. PITCHING DEVICES

The energy conversion of pitching devices is based on the rotational motion caused when the device pitches as waves propagate past the device. Salter's Duck is one of the most recognisable examples of a pitching WEC. Salter's Duck was a cam-like floating device that oscillated with the changing wave pitch and initially used a hydraulic-electric PTO system. Despite extensive research and development efforts, there was never an iteration of Salter's Duck that was deployed at full-scale [13].

Another well-known pitching device is the UK-developed Pelamis. The Pelamis was made up of a set of semi-submerged cylinders linked by hinged joints, which move relative to each other across two degrees of freedom. The relative movement of the cylinders pumps hydraulic fluid into high-pressure accumulators which are used for short-term energy storage. Hydraulic motors are driven using the pressure built up in the accumulators, and the motors are used to drive electrical generators [24]. Fig. 1.4 illustrates how the Pelamis device was orientated against the waves and the two degrees of freedom between the individual cylinders.

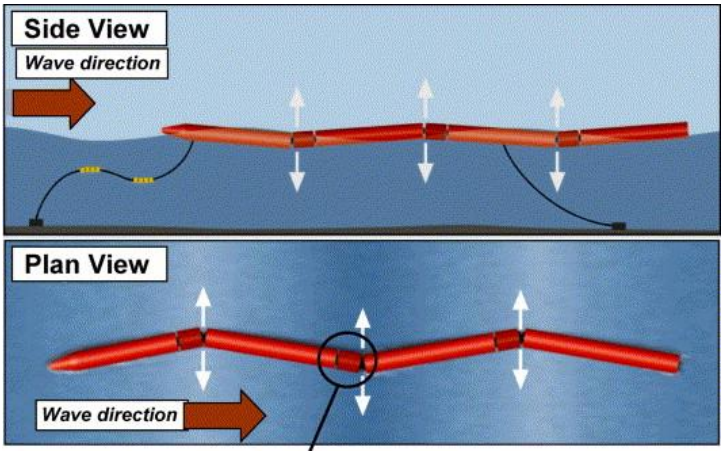

Fig. 1.4: Pelamis pitching WEC showing the two degrees of freedom between each cylinder [24].

1.2.1.3. BOTTOM-HINGED SYSTEMS

Bottom-hinged systems are typically oscillating-body devices based on the concept of an inverted pendulum hinged at the sea bed. Examples of bottom hinged systems include the WaveRoller and the Oyster, and both devices are designed for near-shore deployment. The WaveRoller is a fully submerged bottom-hinged system with a plate anchored to the sea floor. The movement of bottom waves moves the plate, and the kinetic energy produced is collected using a hydraulic pump, which can be used to power a hydraulic motor-generator system [25]. The Oyster is a surface-piercing flap-type device sometimes referred to as an Oscillating Wave Surge Converter. The Oyster PTO is similar to the WaveRoller, but the Oyster uses pistons to pump high-pressure water that drives an onshore hydro-electric turbine [26]. Fig. 1.5 is an illustration of the Oyster WEC.

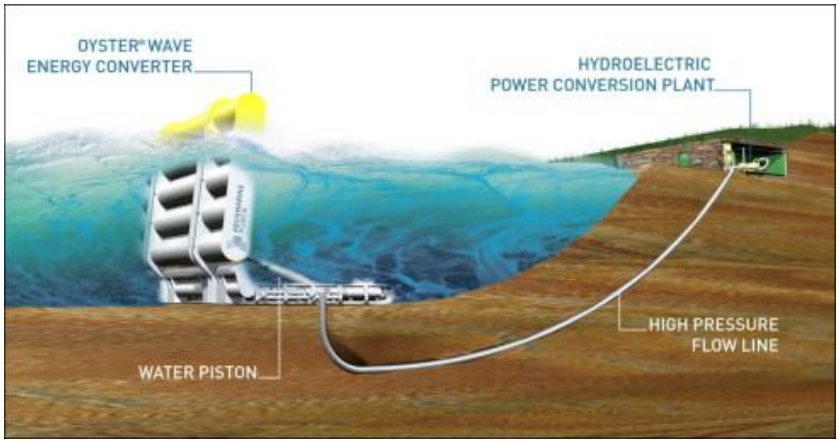

Fig. 1.5: Oyster near-shore bottom-hinged WEC [26].

1.2.2. OVERTOPPING DEVICES

Overtopping devices are partially submerged WECs that capture water from wave crests in small reservoirs and use low-head hydro-turbines to generate electricity [27]. This is achieved because the reservoir is set a higher level than the average free-surface of the surrounding sea. The kinetic energy of the waves is converted to potential energy when incoming waves are led up a ramp and collected in the reservoir. The potential energy is extracted when the water returns to the sea via the low-head turbines [14]. Both shoreline-fixed and floating offshore varieties of overtopping devices have been developed and tested in open water.

An example of a shoreline-fixed overtopping device is TepChan which was developed in Norway in the 1980s. A 350 kW prototype was installed at Toftestallen, Norway in 1985 [28], and it includes a collector, converter, water reservoir, and low-head hydro-turbine. The collector is horn-shaped and used to concentrate the incoming waves as they enter the converter. This acts to amplify the wave height to maximize the water that spills over the converter and into the reservoir [13].

The Wave Dragon, which is a floating offshore overtopping device, operates in same manner. The Wave Dragon consists of a slack moored floating structure with two wave reflectors that focus the incoming waves towards a double curved ramp. The wave crests are directed into a reservoir with a set of low-head hydro-turbines. A 1:4.5 scale prototype of the Wave Dragon, with a rated power of 140 kW was deployed at Nissum Bredning, Denmark in 2003 [29]. Fig. 1.6 illustrates the Wave Dragon, showing both a plan view and the cross-sectional view of the device.

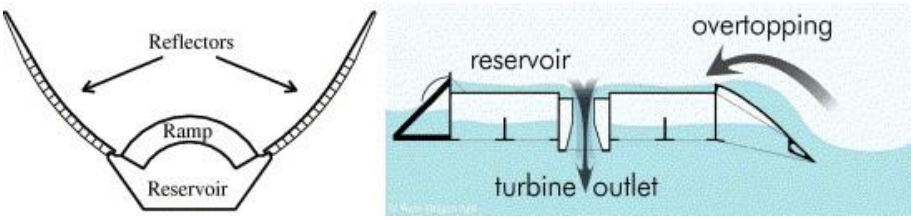

Fig. 1.6: Wave Dragon overtopping WEC plan and cross-sectional views [29].

1.2.3. OSCILLATING WATER COLUMN

The Oscillating Water Column (OWC) operates based on a partially submerged chamber with an Internal Water Surface (IWS) that rises and falls in response to ocean waves. The IWS acts as a piston that forces air across a turbine, and the turbine operates as the device PTO, driving a generator to produce electricity. The OWC is one the oldest documented WECs, with a patent being issued for the whistling buoy in the 1880's [30]. The first OWC to use an air turbine to produce electricity was developed in Japan in the 1940's and used to power navigational buoys [13]. During the 1980's and 1990's, support for wave energy technologies saw increasing support, and as a result, OWC device research and design saw significant growth [14]. A variety of sizes and types of OWC has been built and rigorously tested over the last few decades. OWCs can be separated into two basic categories: shoreline-fixed and offshore-floating.

1.2.3.1. SHORELINE-FIXED OWC

The shoreline-fixed OWCs typically stand on the sea bottom or are fixed to a rocky cliff and are steel reinforced concrete structures. Shoreline devices are easier to install and maintain because of easier access to the device. They also do not require underwater cable runs or deep water mooring systems, which can quickly increase the initial cost of deployment. However, the energy available to shoreline-fixed OWCs is less that than available to offshore-floating devices, particularly those deployed in deep water. Isolated shore-line fixed OWCs include the 500 kW LIMPET OWC on Islay, UK [31] and the 400 kW European Wave Energy Pilot Plant on Pico, Azores, Portugal [32]. Fig. 1.7 is a photo of the Pico Island OWC during high seas taken in autumn of 2013.

More recently, OWC plants have been developed into breakwaters, which include added advantages like shared constructional costs and easier access for operation and maintenance [13]. The Mutriku which consists of 16 small turbine pairs is an example of a breakwater OWC plant [33].

Fig. 1.7: Pico Island OWC as a wave breaks over top of it.

1.2.3.2. OFFSHORE-FLOATING OWC

Offshore-floating OWCs are typically slack-moored to the sea bed and deployed in deep water well beyond the surf-zone. Like the shoreline-fixed OWC, they depend on oscillating air flow to drive turbines, but unlike the fixed OWCs, the floating OWCs derive power from both the changing water pressure caused by propagating waves and their own motion relative to the sea surface. The first electricity producing OWCs were Japanese navigation buoys, which were naturally offshore-floating OWCs. The buoys generated only enough power to remain self-sufficient; the power range was typically 50-700 W. During the late 1970's, the Kaimei barge was developed in Japan and included eight separate OWC chambers with a range of PTO turbines tested during deployment [30]. The Kaimei barge proved inefficient in converting wave motion to pneumatic energy, but its failure led to the development of other more efficient device concepts, with the Bent Backward Duct Buoy (BBDB) becoming one of the most successful designs that resulted from the work [34].

The BBDB is a buoyancy caisson-type module with a distinctive L-shape design. The submerged opening was originally designed to face the incoming waves, however it was found following testing that the BBDB OWC performed much better when the device was turned backward and the submerged opening faced away from the prevailing wave direction. The BBDB OWC has been tested in Galway Bay at 1:4 scale with both a Wells turbine [35] and an impulse turbine with movable guide vanes [36].

The length of the submerged section of the BBDB determines the resonant frequency of the device, and the average wave period of the chosen deployment site is taken into account during device design to maximize conversion efficiency. Fig. 1.8 shows the BBDB OWC that was deployed in Galway Bay in 2011 as part of the CORES project.

Fig. 1.8: The CORES BBDB OWC during deployment in Galway Bay in 2011 [36].

The spar buoy is another, simpler type of floating OWC that consists of a long submerged vertical tail that is open at either end [37]. It has an axisymmetric design that makes it insensitive to wave direction and depends mostly on heaving motion to drive the IWS. Similar to the BBDB, the depth of the tube of the spar buoy determines the resonant frequency of the device and is dictated by the average wave period found at the selected deployment site. The spar buoy design was the basic concept used for most wave-powered navigation buoys [34]. Fig. 1.9 shows the basic design of a spar buoy OWC.

Other offshore-floating OWCs that have been tested more recently include the Mighty Whale [38], which was deployed in Japan in 1998 and tested for several years, and the sloped buoy, which is made up of three sloped immersed tail tubes designed to oscillate at an intermediate angle between the heave and surge directions [34]. While these designs have their own unique features, most OWCs, both fixed and floating, depend on a reciprocating air flow to drive a turbine-generator set.

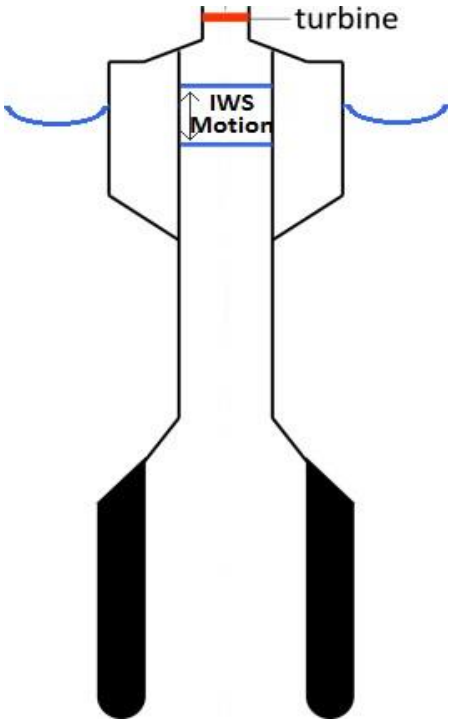

Fig. 1.9: Spar buoy OWC [37].

1.3. SELF-RECTIFYING TURBINES

Typical air and steam turbines used in electrical generation are unidirectional, so the oscillatory nature of the air flow produced by OWCs presents a unique challenge. Due to the oscillating nature of the air flow used for turbine excitation, unidirectional turbines, which rotate in the same direction regardless of flow orientation, have been developed for use in OWCs [39]. Energy conversion could be achieved by using a system of non-return valves along with a conventional turbine, however, the complexity that such a system would add to an OWC device has helped to drive the creation of self-rectifying turbines that provide unidirectional rotation and torque regardless of air flow direction. The most common unidirectional turbines applied in OWCs are the Wells turbine [40] and the impulse turbine [41], although in more recent years radial turbines have seen more development in OWC applications [42]. Other self-rectifying turbines that have been investigated for use in OWCs include radial turbines [42], the cross flow turbine, and the Savonius turbine [43].

1.3.1. WELLS TURBINE

The Wells turbine has been the most common mechanical PTO used in OWC platforms. The rotor of the turbine consists of symmetrical aerofoil blades positioned

around a central hub, and the chord planes are normal to the axis of rotation. The Wells turbine relies on classical aerofoil theory for the generation of a lifting force normal to the air flow direction. The aerofoil blades of the Wells turbine have seen various aerodynamic profiles, like the CA9, NACA0020, and NACA0021, as research drives turbine innovation. Due to the symmetrical design of the aerofoil and the way the blades are positioned around the axis of rotation, the turbine rotor will always rotate in the same direction regardless of air flow direction [44]. Fig. 1.10 shows a plan view of Wells turbine blades with a NACA0021 profile.

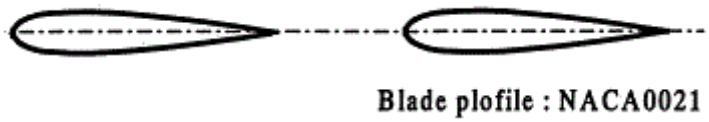

Fig. 1.10: Wells turbine blades with NACA0021 profile [45].

The Wells turbine has been widely studied, modelled, built, and tested in recent years. It was the primary turbine in both the LIMPET OWC on Islay [46] and in the Pico Island OWC [47]. More recently, the Mutriku wave power plant in Spain was fitted with 16 Wells turbine pairs, with each pair driving 18.5 kW generators [33]. Although the ability to create torque in the same direction regardless of air flow makes the Wells turbine a good fit for an OWC, the turbine is not without its deficiencies. The most significant shortcoming of the Wells turbine is the aerodynamic stall it encounters at high flows. Stall causes a large drop in efficiency and also generates a significant amount of noise [44]. Many modifications to the Wells turbine have been investigated since its initial inception, including developing a biplane turbine [48], using contra-rotating turbines [49], guide vanes [50], and self-pitch controlled rotor blades [51]. While various alterations have helped to boost performance, the aerodynamic stall of the Wells turbine remains a major concern and has led to the development of alternative self-rectifying turbines for use in OWCs.

1.3.2. IMPULSE TURBINE

Another self-rectifying turbine that has received considerable attention for application in OWCs is the impulse turbine. Unlike the Wells turbine, the impulse turbine is not susceptible to aerodynamic stall. It delivers useful efficiency over a wide range of flows, has good starting characteristics, and operates at much lower speeds

than the Wells turbine [41]. The impulse turbine consists of an impulse-type rotor and upstream and downstream guide vanes which mirror each other [52]. The blades are symmetrical cup-like blades with an elliptical shape on the suction side and a circular shape on the pressure side [53]. The guide vanes redirect the flow across the rotor blades, and the rotor blade geometry helps to increase the pressure differential. Fig. 1.11 is a plan view of the rotor blades and guide vanes of an impulse turbine with fixed guide vanes.

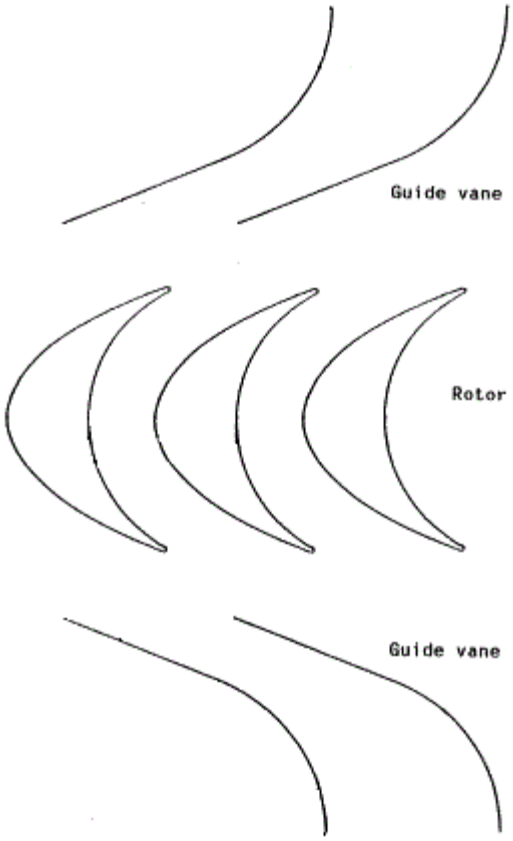

Fig. 1.11: Impulse turbine rotor blades and guide vanes [41].

The impulse turbine is composed of significantly more rotor blades than a Wells turbine and also requires guide vanes for operation, where a Wells turbine does not. The rotor blades are fixed, but both fixed and moving guide vanes have been investigated. The moving guide vanes can be either passive or active, but while moving guide vanes increase efficiency, they add increased complexity to the design and introduce extra points of failure to the turbine [52]. The peak efficiency of the Wells turbine is higher than that of an impulse turbine with fixed guide vanes. However, the

impulse turbine with both fixed and movable guide vanes can potentially have a higher overall efficiency because it does not suffer from aerodynamic stall and has a higher efficiency at high flow rates. The aerodynamic stall of a Wells turbine produces very loud noise which may harm marine wildlife environments, which is a phenomenon that is not present in the operation of an impulse turbine. These differences between an impulse and Wells turbine make the impulse turbine worthy of further investigations for OWC PTO applications. Impulse turbines have not been the subject of as much testing during live deployment as the Wells turbine, but an impulse turbine with active moving guide vanes was recently tested in a 1:4 scale BBDB during the final states of the CORES project [54].

1.4. WEC MODELLING

The increase in investment of human and financial resources in wave energy conversion has been driving the need for thorough, accurate system modelling. Ocean energy development in Europe and the United States has adopted Technology Readiness Levels (TRL) to categorize device development [55]. While prototyping and open water deployment remain the most comprehensive methods for evaluating device performance, the exorbitant capital and material costs associated with open water deployment testing minimizes the number of opportunities for large scale experimentation. The early stages of TRL include small scale tank testing and open water testing is reserved for the later stages, and throughout the TRL process development is supported by numerical models.

Most devices require multiple numerical models that represent various system interactions that occur during operation. The number and type of models depends on where the device is to be deployed, the type of device being modelled, and the nature of the device PTO. For this thesis, four separate and isolated models were brought together to create a unified numerical model of a BBDB OWC. The models utilized were irregular sea wave modelling base on theoretical spectra, hydrodynamic modelling to determine device interaction with sea waves and how that effected the IWS, thermodynamic modelling of the interaction between the air in the plenum chamber of the OWC and the IWS motion, and the interaction between the air flow calculated by thermodynamics and the turbine which acts at the mechanical PTO of the OWC.

1.4.1. SEA WAVE MODELLING

The area of deployment dictates the type of sea conditions that the device will encounter, and the waves are typically modelled based on theoretical standard spectra including Bretschneider, Pierson-Moskowitz, and JONSWAP [56]. The spectrum observed is dependent on the dominant wave conditions of the selected location of deployment [57]. The Bretschneider spectrum predictions have been found to agree well to more energetic conditions where swell waves dominate [58]. Such wave spectra function as good average approximations for sea conditions over a long period of time, but the approximation breaks down under short time conditions particularly those under 24 hours [59]. While a model-generated wave spectrum cannot accurately model a single sea state wave for wave, the approximations can be used reliably to model expected ocean wave conditions for device testing, both physically in wave tanks and numerically in mathematical models.

1.4.2. HYDRODYNAMIC MODELLING

Hydrodynamic modelling of WECs relies on the standard radiation-diffraction theory, which utilizes linearized potential flow theory that is solved in the frequency domain to model the hydrodynamic response of WECs in regular and irregular seas [60]. The standard radiation-diffraction theory is performed using Boundary Element Method (BEM) based numerical formulae [61]. Well-known frequency domain-based commercial modelling software, including WAMIT and ANSYS Aqwa, is commonly employed when performing BEM-based hydrodynamic modelling [62]. This type of hydrodynamic modelling has been used for simulations of hydraulic PTO-based WECs including Pelamis [24], Wavebob [63], and Wave Star [64], and it has also been used for modelling both floating and fixed OWCs [31] [65]. The first-order standard radiation-diffraction theory linear model performs well when modelling hydrodynamic responses in lower energy seas, when device response is known to be linear in nature; however, during large-amplitude motion, device response becomes more non-linear in nature and modelling the hydrodynamic response becomes more complex [66]. To maintain accurate hydrodynamic modelling of device response, the system modelling should remain below the non-linear threshold when using frequency domain-based solutions.

1.4.3. THERMODYNAMIC MODELLING

In comparison to the hydrodynamic modelling of OWCs, the thermodynamics of the air within the plenum chamber of an OWC and the effects of air compressibility have been studied by relatively few researchers [67]. In a time-domain approach for shoreline-fixed OWCs, the flow field has been divided into interior and external problems [68]. There are significant differences between the air inhalation and exhalation processes [69]. In exhalation, the air that passes through the turbine is pressurised above atmospheric conditions and has a higher density than the air passing through the turbine during inhalation. The condition of the air within the plenum chamber can be considered as a uniform body during the exhalation process because it does not go through any mixing as no new air is introduced to the system during this process. During the inhalation process, the air within the plenum chamber is de-pressurised, and its density and temperature are lower than the atmosphere. When air at atmospheric pressure and temperature is inhaled, a complex mixing process occurs between the air within the chamber and the newly introduced air that has passed through the turbine. For simplification, the air mixing process can normally be assumed instantaneous [70]. In this case, the air is considered an isentropic gas within an open thermodynamic system [67]. The mass and energy exchanges happen only through the open boundaries; in an OWC those boundaries are the IWS and the turbine. While air compressibility has been shown increase power capture of OWCs, it typically will reduce overall power capture of a device [71]. The effects of air compressibility in the chamber can be accounted for by applying the known characteristics of the turbine. An ordinary differential equation has been derived for the chamber pressure and the chamber volume, and by solving the differential equation, the effects of the air compressibility can be obtained and accounted for during the numerical modelling process [72].

1.4.4. TURBINE MODELLING

The numerical modelling of the air turbines typically used as the mechanical PTO for OWCs is based on characteristic curves. The characteristic curves centre around the non-dimensional flow coefficient, which is determined from turbine diameter, turbine rotational velocity, and turbine mass flow rate [73]. The non-dimensional flow coefficient can be used to determine non-dimensional coefficients for pressure, torque, input power, and output power. The pressure and torque coefficients have second-order

polynomial relationships with the rotational velocity of the turbine, and the input power and output power coefficients have third-order polynomial relationships with the turbine rotational velocity. From these coefficients and their related characteristic curves, key turbine characteristics including pressure drop across the turbine, generated mechanical torque, mechanical power output, and the pneumatic-to-mechanical power conversion efficiency can be determined with numerical modelling. Wells turbines and the impulse turbines can be modelled by applying the same non-dimensional coefficients, which makes the different turbines interchangeable within a more complete OWC numerical model. This allows for various turbines to be tested in a single system through modelling, and the turbine that best fits a given device and deployment site can be chosen prior to the physical deployment.

1.4.5. NUMERICAL MODELLING

Numerical models are tools that can be used to calculate power output from a WEC under specified wave conditions. They can be used to assess and optimize WEC performance and provide knowledge of the device behaviour in various operating conditions [74]. Models are important mechanisms for exploring different dynamic effects that occur among interrelated systems, which can help to create better understanding of WECs and can in turn further device development [75]. In recent years, the focus on developing models of WECs has led to models including hydraulic PTOs [19] [75], hyperbaric PTOs [20], and WEC arrays [61] [76]. To date, there are no known published works on the development of numerical models of BBDB OWC WECs created by combining the four models described in this section.

1.5. THESIS PLAN

The goal of the work presented in this thesis was to build a numerical model of a BBDB OWC, verify the accuracy of the model against experimental data, and use the verified model to test the effectiveness of several control theories.

The numerical model was created by combining the models of the various energy conversion stages of the BBDB OWC. A 1:4 scale BBDB OWC model was built to match the 1:4 scale device deployed in Galway Bay during the CORES project in 2011 [54, 77, 78], and the experimentally collected CORES data was used to validate the numerical model. Typically, prototype device deployment results are closely guarded Intellectual Property (IP) owned by the developer and rarely disseminated to the public.

However, CORES was a publicly funded project, and the results of the project were available in the public domain. While the version of the model verified using experimental data was 1:4 scale, the goal of the thesis was to test a full scale device. Scaling the model from 1:4 to 1:1 scale could be performed without compromising the accuracy of the model, but the design of the impulse turbine with active-moving guide vanes used in the initial 1:4 scale model contained IP belonging to one of the CORES partners. Due to the lack of availability of the 1:4 scale turbine design, a new 1:1 scale impulse turbine with fixed guide vanes was designed based on publicly available information from multiple sources. This new impulse turbine was evaluated using Computational Fluid Dynamics (CFD) software. To confirm the accuracy of the CFD model, the results of the simulations were verified against published experimental data on similar turbines. The verified CFD simulation results were used to create a numerical model of the turbine that was added to the 1:1 scale BBDB OWC model in place of the 1:4 impulse turbine used in the verification stage. The full numerical model, complete with the newly designed turbine, was used to assess various control laws and assess a high-inertia impulse turbine as a short-term Energy Storage System (ESS). The availability of the experimental results and the well-publicized and widely available numerical models of the BBDB OWC led to the development of this thesis.

1.5.1. CHAPTER2: NUMERICAL MODEL DEVELOPMENT

Chapter 2 presents the numerical model of the BBDB OWC developed for this thesis. The model was constructed from four isolated models of the different systems that are combined in an OWC to generate electrical energy from the kinetic energy of propagating sea waves. The numerical models combined to form the completed model include irregular sea waves based on the Bretschneider spectrum, the hydrodynamic response of the OWC to the sea waves as they propagate past the device, the thermodynamic behaviour of the internal air chamber to changes in volume induced by the hydrodynamic response, and the mechanical performance of the air turbine as air flows are forced across it by the ever changing thermodynamic system. The four numerical models, which have been presented in isolation in OWC related applications, are presented individually in Chapter 2. However, the hydrodynamic, thermodynamic, and mechanical systems are interdependent and do not operate in isolation, and the integration of these systems for the completed model is described. Modelling the interdependencies was the greatest challenge in creating the model presented here.

The completed model was validated using experimental data collected during the BBDB OWC deployment stage of the CORES project. A synopsis of the CORES project is presented, and the reason for developing a new impulse turbine with fixed guide vanes to be implemented in the full scale model is specified. The impulse turbine is divided into the various physical dimensions required for turbine design. The relationship between the different dimensions of the rotor blades, guide vanes, and hub diameter are found, so that the 1:1 turbine used for the full scale model can be designed and built for CFD simulations.

1.5.2. CHAPTER 3: VERIFICATION OF THE MODEL WITH EXPERIMENTAL DATA

Chapter 3 presents the process carried out to verify the accuracy of the numerical model using the data collected from the CORES project. The process was carried out in three stages; first the turbine model was investigated, followed by the combined thermodynamic and turbine models, and finally the hydrodynamic model was added to test the full model. The process was divided into these three stages to allow for a more thorough investigation of each model.

The turbine model verification process was performed by eliminating the thermodynamic and hydrodynamic processes from the model, leaving only the turbine and controller-generator model. The air flow data collected directly from the CORES project was used as the input to the turbine model in lieu of output from the thermodynamic model. The control algorithm was extrapolated from the experimental data and integrated into the controller model. Simulations were then performed for each of the eight available data sets. The resulting turbine speed and electrical power outputs generated by the model simulation were compared to the experimental data collected. Both the average and instantaneous results are presented and discussed.

For the second stage of the verification process, the movement of the IWS calculated from the CORES experimental data was used as the input to the thermodynamic model rather than the output of the hydrodynamic model. The thermodynamic model was combined with the turbine and controller-generator model, and the feedback from the turbine was included when calculating the pressures and flows generated by the thermodynamic model. As with the first stage of the verification process, the turbine speed and electrical power output of the model and experimental data were compared and discussed. In addition to this, the pressures and flows generated by the model were

compared to the pressures and flows measured experimentally. As was done in the first stage, both average and instantaneous results are presented and discussed.

For the final stage of the verification process, the Bretschneider generated wave spectral array was combined with the hydrodynamic model to create IWS motion, and that IWS motion was used as the input the to the thermodynamic model to create the complete numerical model. The summary statistics used to generate the spectral array were taken from the wave rider buoy deployed in Galway Bay near the deployment site of the CORES OWC. The summary statistics taken from the wave rider buoy were matched chronologically with the eight experimental data sets taken from the CORES project. As the IWS movement was synthetically generated, only the average values from the simulations and experimental data could be compared.

1.5.3. CHAPTER 4: DESIGN AND CFD MODELLING OF AN IMPULSE TURBINE

In Chapter 4, the full size, 1:1 scale, impulse turbine used in the final model was designed and modelled in SolidWorks. The SolidWorks model geometry was analysed using the SolidWorks CFD software package Flow Simulation, and the data generated from the CFD simulations were used to numerically characterize the turbine so that it could be used as an alternative to the CORES turbine in the complete model. To fully assess the validity of the Flow Simulation software package, a 300 mm turbine was also simulated in SolidWorks, and the model results were compared to experimental results published by other authors on physical tests performed on an identical 300 mm turbine.

The design process for the full size turbine is described, and the final dimensions chosen for the full-size turbine are given. The technique for constructing the model turbine and guide vane hubs after selecting the turbine size is explained, and the final turbine system is presented. The completed system includes the turbine hub, the upstream and downstream guide vanes, the air duct in which the turbine resides, and the end caps on either end of the air duct, which were required to perform the CFD simulations.

The settings applied to Flow Simulation are documented in this section and identical settings were applied for both turbine sizes. The results for the CFD simulations, which were performed over a range of input pressures and turbine rotational velocities, are presented. The results of the simulations carried out for both turbine sizes are compared against the published experimental data, and the implications of the results are

discussed. Finally, the resulting CFD data gathered on the full size turbine is used to create the numerical models necessary to implement the turbine in the full model.

1.5.4. CHAPTER 5: CONTROL THEORY AND ENERGY STORAGE SYSTEM TESTING

In Chapter 5, the full model presented in Chapter 2 and verified in Chapter 3 is combined with the impulse turbine model described in Chapter 4, and the new system is used to investigate the effectiveness of three different control algorithms. One algorithm is created for and applied to a turbine with low inertia, and two algorithms were created for and applied to a turbine with high inertia. The low-inertia turbine controller is based on the Maximum Power Point Tracking (MPPT) algorithm, and the high-inertia controllers include a fixed control algorithm which is applied to all sea state conditions and a variable control algorithm that is adjusted to optimize turbine performance depending on sea state conditions. The high-inertia turbine is also tested to investigate if an impulse turbine can be used as a flywheel for short-term energy storage. The Wells turbine has been found to effectively serve as a flywheel due to the high rotational velocity at which it operates. The impulse turbine operates at much lower rotational velocities and may not be as suitable as an energy storage system, so one aim of Chapter 5 was to investigate this further.

To test the control theories and energy storage capacity of the impulse turbine, the model was simulated in ten different sea states. The summary statistics of each of the ten sea states are disclosed, as is the rationale for selecting them. The sea states were generated in MATLAB using the Bretschneider spectrum as described in Chapter 2. The generated sea states were designed to be 30 minutes in duration, and five 30-minute sea wave arrays were generated for each of the ten sea states investigated. The three controller-turbine combinations were simulated using all fifty of the sea wave arrays, and the results from those simulations are presented in this chapter. The pneumatic-to-electrical power conversion efficiency and the electrical power output quality from the simulations for each of the three combinations are compared and discussed.

1.5.5. CHAPTER 6: CONCLUSIONS AND FUTURE WORK

Chapter 6 presents the conclusions drawn from the work described in this thesis. It also illustrates projects that could be performed in the future using the work and results originating in this thesis as a starting point.

2. NUMERICAL MODELLING FOR A BBDB OWC

This chapter presents the various numerical models that were used to create a numerical model of a Bent Backward Duct Buoy (BBDB) Oscillating Water Column (OWC). Furthermore, the CORES FP-7 project, which provided the data that was used to validate the model, is discussed in this chapter. The CORES project OWC was a 1:4 scale device, and the model used during validation was also 1:4 scale to match the CORES OWC. Following model validation, the scale was increased from 1:4 to 1:1, and the model was used to test control theory and the energy storage of an impulse turbine. For IP related reasons, the turbine used in the CORES project and in the model validation could not be implemented in a full scale model, so it was replaced with an impulse turbine with fixed guide vanes. The geometric parameters of the impulse turbine with fixed guide vanes that were used to design the full scale turbine are detailed in the final section of this chapter.

2.1. OSCILLATING WATER COLUMN MODELLING

Numerical modelling of WECs is an essential part of the research and development necessary to progress a device from initial concept to commercially viable energy converter. It is used to predict device performance and provides an in-depth view of the wave structure interaction. Numerical modelling can also be used to develop projected yields from a large scale model, and it is a tool that is applied to help optimize both the physical device and device control to maximize power output at a relatively lower cost [79]. In producing projection yields, models can be used in economic terms to help garner capital and political support to assist development at larger scales. Wave-to-wire models offer a complete look at a device from ocean wave behaviour to electrical power output.

For this thesis, a mathematical model of a BBDB OWC was created to incorporate interaction between various subsystems of the device in open ocean waters, allowing for testing and development of physical dimensions of the buoy, various turbine designs, and turbine control strategies. The model was built using existing models of ocean waves and the various energy conversion systems inherent to an OWC. The ocean wave models were used as the input to the OWC model. The systems of the OWC modelled are the device hydrodynamic response to the passing waves, the thermodynamic behaviour of the plenum chamber of the OWC, which converts the

hydrokinetic energy to pneumatic energy, the pneumatic turbine, which converts the pneumatic energy to mechanical energy, and the controller and generator system, which converts the mechanical energy to the electrical energy. The isolated system models cannot account for the interaction between the turbine, the thermodynamic system and the hydrodynamic system. The model presented here worked to incorporate those interactions to create a more complete and accurate numerical model of an OWC.

2.1.1. HYDRODYNAMIC MODEL

Modelling the conversion of wave motion to electrical energy by an OWC requires finding the motion of the Internal Water Surface (IWS) in response to the changing elevation of the ocean surface. The IWS acts like a piston and forces air across a turbine, which operates as the mechanical PTO of the system. For a BBDB OWC, the dimensions of the IWS are dependent on the dimension of the full buoy, which is designed to match the expected sea conditions of the chosen deployment site. When building a numerical model of an OWC, the first step is to choose a deployment site and design the BBDB. The designed BBDB can then be used to model the motion of the IWS in a given wave climate. Recent publications, including [65, 80] have explored how the hydrodynamics of the BBDB OWC can be reliably modelled.

A BBDB OWC is modelled in this chapter and is shown schematically in Fig. 2.1. The modelling of the IWS inside the BBDB is calculated using a Boundary Element Method (BEM) solver to find the pressure distribution implicitly, as presented in [60, 81]. The implicit calculations solved with the BEM using reciprocity relations to find the IWS parameters from the oscillating structure were introduced in [82]. The implicit calculations were performed on the BBDB model using linearized frequency domain numerical modelling, carried out by the industry standard commercial code WAMIT v6.4 [83]. The hydrodynamic terms related to the IWS movement, including air-pressure fluctuations, can all be obtained from potential flow code without explicitly solving for the radiation potential of the internal water surface using WAMIT v6.4. Hence, the resulting air flow calculated from the IWS includes both the excitation and radiation flows. The excitation flow is caused by movement of the IWS with a fixed body for reference, and the radiation flow is caused by the unit-oscillation velocity of the body with the air chamber vented to the atmosphere. The verification of this process is given in detail in [65].

Frequency domain modelling was employed to determine the motion Response Amplitude Operators (RAO) of the BBDB. The Response Amplitude Operator is the relationship between wave surface elevation amplitude at a reference location and the vessel response amplitude, and the phase lag between the two. The RAO analysis of the BBDB was restricted to head seas, where the wave propagation direction is perpendicular to the front of the device, as performance of the OWC in head seas is assumed to be more efficient. The assumption is made because during deployment, the BBDB is slack moored, and the device design causes it to weathervane into the propagating waves. During modelling, the surge, heave, pitch and IWS RAO's were determined for the BBDB and presented in [84].

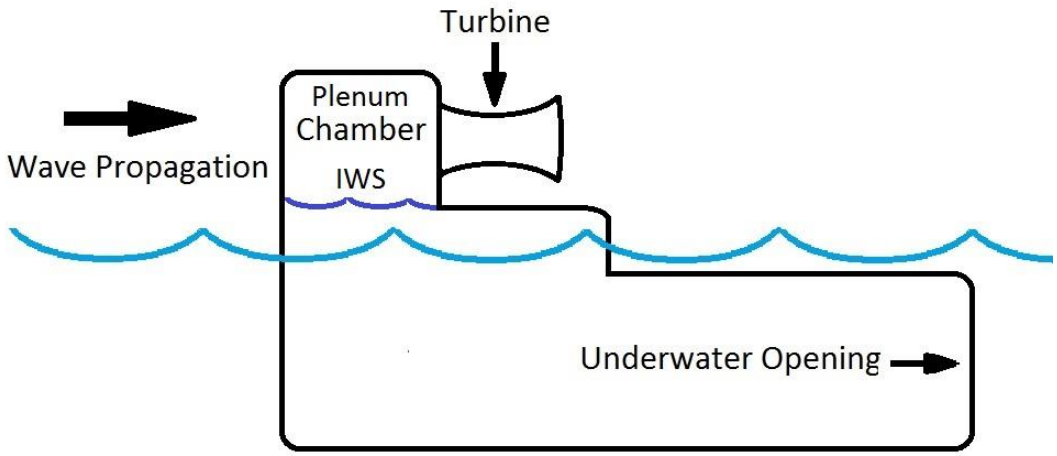

Fig. 2.1: Schematic diagram of a typical Bent Backwards Duct Buoy OWC.

The resonance periods of the IWS RAO plots produced by the WAMIT simulations are illustrated in Fig. 2.2. To obtain an RAO through WAMIT, the geometry of the OWC was modelled in WAMIT. The influences of the turbine and moorings are supplied through external mass, stiffness, and damping values that are linked to WAMIT, and the WAMIT simulations take place in the frequency domain [85]. For the simulations performed on the BBDB OWC investigated in this thesis, The maximum RAO of the device, which is plotted in Fig. 2.2, matches the most common period at the SEAI test site in Galway Bay where the CORES buoy was deployed [58]. This was designed intentionally to extract the maximum energy from the resource [59].

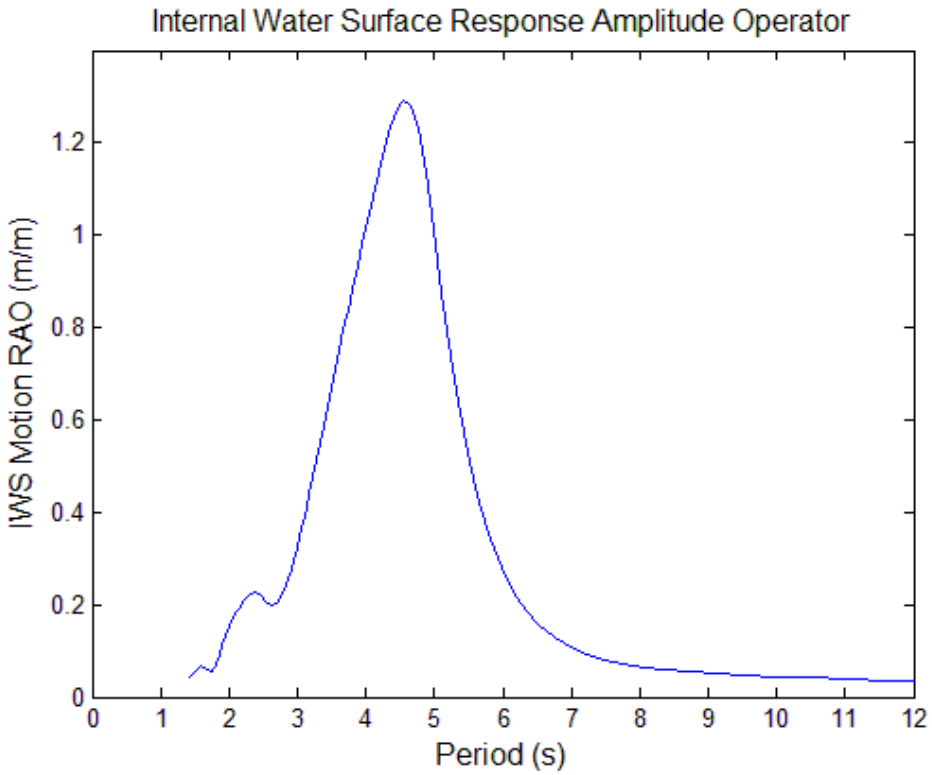

Fig. 2.2: Internal Water Surface Response Amplitude Operator of CORES buoy.

In order to validate these predictions made by WAMIT and the empirical damping applied from various sources, a basic tank 1/50 scale testing campaign was undertaken using the device configuration for the BBDB [84]. The model testing was performed and verified in the wave flume at the National Ocean Test Facility (formerly the Hydraulic and Maritime Research Centre), University College Cork, Ireland, and the details and results of the tests are given in detail in [84]. The plot in Fig. 2.2 is the frequency response results produced by the WAMIT simulations on the BBDB OWC. Fig. 2.2 represents the hydrodynamic interaction between frequencies present within a wave series are amplified or attenuated within the plenum chamber Internal Water Surface (IWS). The plot is used to determine the changing elevation of the IWS in response to the passing ocean waves. Due to the non-linear responses of hydrodynamic systems in higher energy sea states, the RAO response is limited to simulating seas with a significant wave height, H_s, of 4 m and below [66].

The verified IWS RAO response was then used in conjunction with a randomized sea state based on the Bretschneider spectrum to model the IWS movement in the BBDB in various sea conditions. The Bretschneider spectrum [86] is one of several parametric functions commonly used to approximate spectral densities for engineering and design

purposes, and it is derived from statistical analysis of large databases. Similar parametric functions include the Pierson-Moskowitz spectrum [87] and the JONSWAP spectrum [88]. While each parametric function can be used to simulate real sea waves, the Bretschneider spectrum was chosen because of its flexibility, general accuracy, ease of use, and it most accurately models the sea conditions present in the Irish North Atlantic [59]. Currently unimodal forms of parametric functions are the best available means for simulating ocean waves. However, they do have their limitations and may not allow for an accurate depiction of complex sea-states [89].

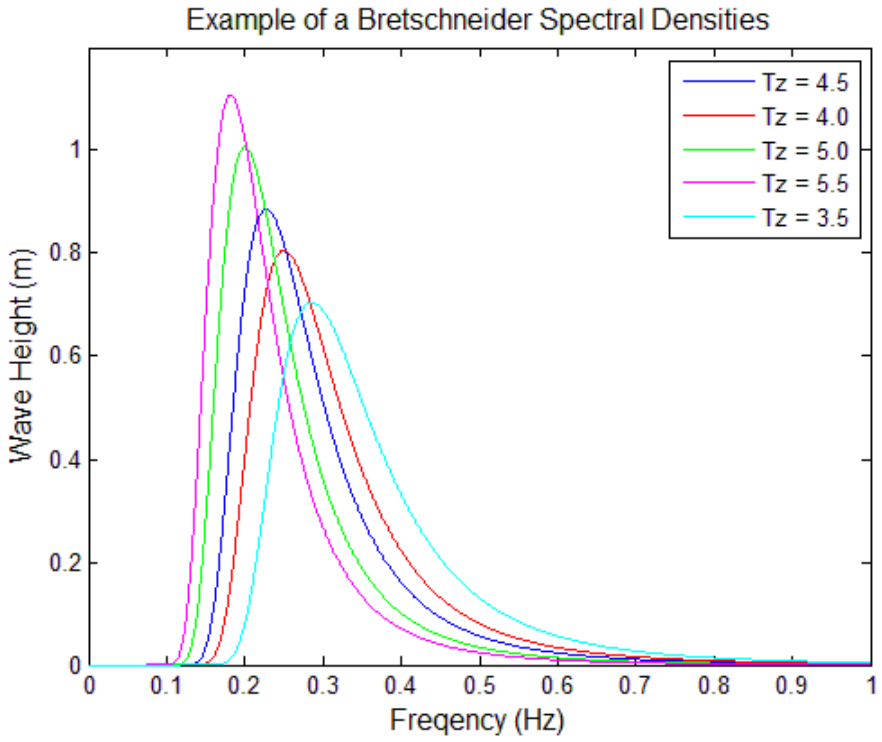

Fig. 2.3: Example of Bretschneider spectral densities with a H_s of 1.5 m and a various T_p values.

A Bretschneider wave spectrum is also known as an International Ship and Structures Congress (ISSC) or modified Pierson-Moskowitz spectrum [86], and it has a constant relationship between periods, where the average period, T_{02}, and the peak period, T_p, has a constant ratio of T_p/T_{02} = 1.406 [59]. That relationship leads to only needing two input parameters to create a Bretschneider spectrum, the total variance, m_0, which is represented by the significant wave height, H_s, and the peak period. Equation (2.1) represents the Bretschneider spectrum [90]

$$S(f) = \frac{5}{16} H_s^2 * {f_m^4}/{f^5} * e^{-1.25\left({f_m}/{f}\right)^4}, \quad (2.1)$$

where f_m is the modal frequency, which is the inverse of the peak period T_p. Fig. 2.3 below is an example of a the Bretschneider spectral density as present in (2.1). For the spectral densities shown in Fig. 2.3, the significant wave height, H_s, for each of the five spectra is 1.5 m and the peak period, T_z, varies from 3.5 s to 5.5 s, so that the spectral densities matches ocean wave conditions that could be present at the SEAI Galway Bay test site.

To generate a full irregular sea state of a given duration, an array representing the amplitudes of sinusoidal components of irregular ocean waves was created using (2.1). The array consisted of twice the simulation time given in 100 ms portions such that

$$\mathrm{d}f = \frac{1}{2t_{sim}}, \quad (2.2)$$

where df is the length of the frequency step and t_{sim} is the length of the simulation in seconds multiplied by which due to the sampling rate of 10 Hz. The step time was chosen based on Shannon's sampling theorem. The frequency range of the array was $0 \leq f \leq 1$ Hz in steps of df. For all simulations presented in this chapter, the duration of the created sea state was 30 minutes, or 1800 seconds, and therefore df was 1.1 mHz. The 30-minute duration was chosen because summary statics for sea states are based on 30-minute data intervals, and therefore a 30-minute sample was long enough to represent a sea state. The amplitude of the component was represented by

$$A_w(f) = \sqrt{2\, S(f)\, df}, \quad (2.3)$$

where A_w is the amplitude of the waves and df is the minimum sampling frequency in Hz, which is the inverse of the simulation time, $0.5T^{-1}$, as dictated by Shannon's Sampling Theorem [91].

The array of wave amplitudes was used to create a series of sinusoidal waves, one for each of the 36,000 frequencies, which repeats for 18,000 samples, and each sinusoidal wave was given a random phase shift, resulting in:

$$EWS(t) = \sum_{n=0}^{n-1} A_w(n\,df)\ \sin(2\pi n\,dt + \theta_n), \quad (2.4)$$

where *EWS* is the external water surface and θ_n is the uniform random phase shift $-\pi<n\leq\pi$. The 36,000 waves are then added together to create a single irregular wave pattern that serves to represent the behaviour of the ocean water surface with the selected Bretschneider spectrum.

To find motion of the Internal Water Surface of the BBDB chamber in the generated sea, each of the 36,000 single sinusoidal waveforms are combined with the RAO produced by the WAMIT model. The RAO is multiplied to the initial amplitude determined by (2.3) for every sinusoidal waveform before the waveforms are added together. The sum of the waveforms results in the motion of the Internal Water Surface such that

$$IWS(t) = \sum_{n=0}^{n-1} RAO(n\,df)A_w(n\,df)\ \sin(2\pi n\,dt + \theta_n), \quad (2.5)$$

where *IWS* is the internal water surface and *RAO* is the response amplitude operator of the frequency as determined by the WAMIT model.

A MATLAB program was written that created a random Bretschneider sea state, *S(f),* based on values for the significant wave height and significant period of the desired conditions. The MATLAB code is presented in Appendixes A and B. To create the sea conditions used in the models, a Bretschneider spectral density array of a selected time was created using (2.1). The desired conditions and the duration of the modelled sea state can be adjusted as desired. The modal frequency chosen is based on the peak period of the sea state, T_p, which is found by multiplying the zero crossing period, T_z, for the desired sea state by the standard Bretschneider ratio of 1.4 [58].

The Bretschneider sea state was created in MATLAB using the values for the significant wave height and significant period of the desired conditions, and the desired duration of the sea state. The movement of the sea water surface was then combined with the IWS RAO to create an array that represented the movement of the IWS in the given sea state. To generate the ocean waves, a multitude of sinusoidal waveforms in the time domain were created based on the Bretschneider spectral density. Each sinusoidal wave had a different frequency and a random phase shift; the waveforms

were superimposed upon each other to produce a single array that represented the height of the water level at the device. To find the water level within the chamber based on the generated waves, the amplitude of each sinusoidal component of the array was multiplied by the RAO value that corresponded to the sinusoidal wave period as shown in Fig. 2.2. The results from the RAO multiplier were superimposed upon each other to produce an array that represented the water level of the IWS. The changes in the water level were used to calculate the volumetric changes within the plenum chamber, and those volumetric changes were used in the thermodynamic model.

2.1.2. THERMODYNAMIC MODEL

The thermodynamics of the air in an OWC chamber have not been as thoroughly researched as the hydrodynamics [46]. The compressibility of a large volume of air in OWC operation was presented in [92, 71], and it has been used in time-domain modelling in [68]. The air flow across the turbine is driven by the change in volume of the air chamber, which is dictated by the movement of the IWS. Equation (2.6) is the differential equation used to represent the change of mass within the air chamber, while (2.7) is the flow rate calculated from the movement of the IWS [67].

$$\frac{dm}{dt} = \rho_c \frac{dV}{dt} + V \frac{d\rho_c}{dt}, \tag{2.6}$$

$$Q_w = -\frac{dV}{dt}, \tag{2.7}$$

where m is the mass of air in the chamber in kg, ρ_c is the density of air inside the chamber in $kg \cdot m^{-3}$, V is the volume of air inside the chamber in m^3, and Q_w is rate of air flow in $m^3 \cdot s^{-1}$ based on change in volume of the plenum chamber caused by the motion of the IWS. The change of volume was calculated from the WAMIT RAO results, as described earlier, and it is based on the static radiation admittance value in units of $m^3 \cdot s^{-1} \cdot Pa^{-1}$, which is the inverse of aerodynamic damping [82].

Due to the compressibility of air and the need to account for the changing density of the air flow across the turbine, separate thermodynamic equations were used: one for inhalation when the chamber pressure is lower than atmospheric pressure, and one for exhalation when the chamber pressure is higher than or equal to atmospheric pressure, as shown in (2.8):

$$\begin{cases} Q_p = -\frac{1}{\rho_c}\frac{dm}{dt}, p \geq 0, \\ Q_p = -\frac{1}{\rho_0}\frac{dm}{dt}, p < 0, \end{cases} \tag{2.8}$$

where p is the gauge pressure of the OWC chamber in Pa, ρ_o is the density of air at atmospheric conditions in kg·m^{-3}, and Q_p is the rate of volumetric air flow across the turbine in m^3·s^{-1}.

In exhalation, the air within the chamber is essentially a single entity that remains uniform in terms of its thermodynamic behaviour. However, during inhalation, the residual air inside the chamber goes through a complex mixing process with the air induced from the atmosphere. To simplify the mathematical model of this process, the mixing can be considered to be instantaneous and thus the air within the chamber is assumed homogenous and isentropic, allowing for adiabatic expansion to be applied to calculate the final volume and pressure during both inhalation and exhalation [70, 72]. With this assumption, the air can be expressed by the uniformity parameters, including pressure, density, and temperature. The complete dynamic system can then be approached as an open thermodynamic system.

In an open isentropic system, the state equation can be written as

$$\frac{p_0+p}{\rho_c^{\gamma}} = \frac{p_0}{\rho_0^{\gamma}}, \tag{2.9}$$

where p_0 is air pressure at atmospheric conditions in Pa and γ is the specific heat ratio of air and $\gamma = 1.4$ at STP.

Equation (2.6) can be rewritten and linearized while solving for density, ρ_c, as shown in [67, 72]. Further work in [67] shows that for pressures up to 15 kPa the error between the linearized equation (2.10) and the non-linearized equation is less than 0.2%. The small error allows substituting the linear equation in place of the non-linear equation. The linear equation can be more easily differentiated and is shown in (2.11),

$$\rho_c = \rho_0\left(1 + \frac{p}{\gamma p_0}\right), \tag{2.10}$$

$$\frac{d\rho_c}{dt} = \frac{\rho_0}{\gamma p_0}\frac{dp}{dt}. \tag{2.11}$$

Combining (2.6), (2.7), and (2.11) with (2.8) results in (2.12) which can be used to find the pressure, density, and the volumetric air flow rate across the turbine and can be written as:

$$\begin{cases} Q_p = Q_w - \frac{V}{\gamma p_0 + p}\frac{dp}{dt}, p \geq 0, \\ Q_p = \left(1 + \frac{p}{\gamma p_0}\right) Q_w - \frac{V}{\gamma p_0}\frac{dp}{dt}, p < 0. \end{cases} \tag{2.12}$$

The impulse turbine, which is used in this model, operates as a nonlinear PTO. The pressure drop across the turbine can be approximated using a second-order polynomial of the flow rate, as shown in (2.13) [72],

$$\begin{cases} p = kQ_p^2, \ p \geq 0, \\ p = -kQ_p^2, \ p < 0, \end{cases} \tag{2.13}$$

where k is the damping coefficient of the turbine in Pa $m^{-6}s^{-2}$ and is related to the radiation admittance of the turbine. Combining (2.12) and (2.13) yields

$$\begin{cases} \frac{dV}{dt} + \frac{V}{\gamma p_0 + p}\frac{dp}{dt} + \sqrt{p/k} = 0, \ p \geq 0, \\ \left(1 + \frac{p}{\gamma p_0}\right)\frac{dV}{dt} + \frac{V}{\gamma p_0}\frac{dp}{dt} - \sqrt{-p/k} = 0, p < 0. \end{cases} \tag{2.14}$$

Equation (2.14) represents the relationship between the chamber pressure and the air volume for a nonlinear PTO. If pressure, p, or volume, V, is known, the other can be found using this equation.

2.1.3. IMPULSE TURBINE MODEL

The self-rectifying impulse turbine has become more widely considered for the OWC due to its non-stall feature and better efficiency than a standard Wells turbine at high flow coefficients. Studies have been carried out to characterise the turbine through laboratory testing and Computational Fluid Dynamics simulation. Equations (2.15)-(2.18) published in [41, 43, 53, 93, 94] can be used at any scale to characterise the turbine and can be used in turbine design.

$$\phi = \frac{v_a}{U_R}, \tag{2.15}$$

$$C_t = \tau_o/\{\rho_a(v_a^2 + U_R^2)bl_r z r_R/2\}, \tag{2.16}$$

$$C_a = \Delta pQ/\{\rho_a(v_a^2 + U_R^2)bl_r z v_a/2\}, \tag{2.17}$$

$$\eta = \frac{(T\omega)}{(\Delta pQ)} = C_t/(C_a\phi). \tag{2.18}$$

Here, ϕ is the flow coefficient, v_a is the velocity of air at the turbine in m s^{-1}, U_R is the blade linear velocity at the mid-span of the turbine blade in m s^{-1}, C_t is the torque coefficient, τ_o is the torque in Nm, b is the blade height in m, l_r is the blade chord length in m, z is the number of blades, r_R is the turbine mean radius in m, C_a is the input power coefficient, η is the efficiency of the turbine, and ω is the rotational velocity of the turbine in rads·s^{-1}. These non-dimensional equations are used to determine the turbine characteristics in terms of expected performance under steady flow conditions. The denominators of (2.16) and (2.17) characterize the total work and power available if the turbine was 100% efficient. The terms b, l_r, and z represent the available surface area of the turbine blades, while the terms ρ_a and $v_a^2+U_R^2$ represent the energy available in the air flow. The difference between the two denominators are the values r_R in (2.16) and v_a in (2.17), so (2.16) signifies the energy available in Joules, while (2.16) signifies the power available in Watts. To find the values of the torque and input power coefficients, C_t and C_a, at given flows and rotational speeds of the turbine, the torque exerted on the turbine rotor, τ_o, and pressure drop across the turbine, Δp, must be determined experimentally and then the coefficients can be calculated from the resulting data. These calculations are complex and are indirectly related to the flow coefficient. It has been shown that impulse turbine performance can also be characterized using parameters that are direct functions the flow coefficient [52].

The turbine performance depends on the rotational speed of the turbine, the volumetric flow rate, the density of the air, and the diameter of the turbine. With these values, the most important performance characteristics, mechanical power, pressure drop across the turbine, and pneumatic to mechanical power conversion efficiency can be found using the following simplified non-dimensional functions of the flow coefficient [94]. Equation (2.19) represents the flow coefficient, Φ, that can be used in

parabolic equations that represent the performance characteristics based on fewer variables when compared to (2.15) through (2.18).

$$\Phi = Q_p/(\omega D^3), \tag{2.19}$$

where ω is the rotational velocity of the turbine in rads·s^{-1} and D is the diameter of the turbine in m.

Substitution was used to show the relationship between ϕ and Φ. The two values are linked by a constant multiplier that is related to the hub-to-tip ratio, ξ. As the two variables are linked by a constant, the characteristics that they are used to determined can be used interchangeable in the designs and evaluations of a turbine. Equations (2.20) and (2.21) show the substitution used to represent the mid-blade radius, r_R, and the turbine area, A_t, in terms of the turbine diameter, D, and the hub-to-tip ratio ξ.

$$r_R = \frac{r_t + r_h}{2} = \frac{r_t(1+\xi)}{2} = \frac{D}{2}\frac{(1+\xi)}{2} = \frac{D(1+\xi)}{4}, \tag{2.20}$$

$$A_t = \pi(r_t^2 - \xi r_h^2) = \pi r_t^2(1-\xi^2) = \pi\frac{D^2}{4}(1+\xi)(1-\xi), \tag{2.21}$$

where r_t is the turbine radius in m, and r_h is the hub radius in m.

Using substitution from (2.20) and (2.21), U_R, v_a, and ϕ can be defined in terms of Q_p, ω, D, and ξ in (2.22)-(2.24), which shows that (2.15) and (2.19) are interchangeable.

$$U_R = \omega r_R = \frac{\omega D(1+\xi)}{4}, \tag{2.22}$$

$$v_a = \frac{Q_p}{A} = \frac{4Q_p}{\pi D^2(1+\xi)(1-\xi)}, \tag{2.23}$$

$$\phi = \frac{v_a}{U_R} = \frac{Q_p}{\omega D^3}\left\{\frac{16}{\pi(1+\xi)^2(1-\xi)}\right\} = \Phi\left\{\frac{16}{\pi(1+\xi)^2(1-\xi)}\right\}. \tag{2.24}$$

With the relationship between ϕ and Φ known, the parabolic equations from [52] which are polynomials of Φ that represent mechanical power, pressure drop across the turbine, and pneumatic to mechanical power conversion efficiency of the turbine and are also found experimentally and are represented by:

$$\Psi = \frac{P_m}{(\rho\omega^3 D^5)} = f(\Phi) = \Psi_3\Phi^3 + \Psi_2\Phi^2 + \Psi_1\Phi + \Psi_0, \quad (2.25)$$

$$\Upsilon = \frac{\Delta p}{(\rho\omega^2 D^2)} = g(\Phi) = \Upsilon_2\Phi^2 + \Upsilon_1\Phi + \Upsilon_0, \quad (2.26)$$

$$H = \frac{P_m}{\Delta p Q_p} = \frac{\Psi}{\Upsilon\Phi} = h(\Phi) = \frac{\Psi_3\Phi^3+\Psi_2\Phi^2+\Psi_1\Phi+\Psi_0}{\Upsilon_2\Phi^3+\Upsilon_1\Phi^2+\Upsilon_0\Phi}, \quad (2.27)$$

where ρ is the density of air in kg·m^{-3}, Δp is the pressure drop across the turbine in Pa, P_m is the mechanical power in W, Ψ is the power coefficient, Υ pressure coefficient, and H is the efficiency of the turbine.

For modelling purposes, (2.25) is the most important part of the mathematical model of the turbine as it is used to calculate the mechanical power input of the turbine and is rewritten as (2.28):

$$P_m = (\rho\omega^3 D^5)(\Psi_3\Phi^3 + \Psi_2\Phi^2 + \Psi_1\Phi + \Psi_0), \quad (2.28)$$

where Ψ_n are the experimentally determined power coefficients. The values of Ψ_n for the CORES turbine were found experimentally and published in [95] and were used in the SIMULINK model so that,

$$P_m = (\rho\omega^3 D^5)(0.3634\Phi^3 + 3.438\Phi^2 - 0.155\Phi - 0.0003). \quad (2.29)$$

The mechanical power output of the turbine is used along with the turbine rotational velocity to find the mechanical torque, τ_m, exerted on the turbine in Nm,

$$\tau_m = \frac{P_m}{\omega}. \quad (2.30)$$

The mechanical torque is then combined with mechanical losses and the electrical braking torque of the generator later in the model to calculate the change in speed of the turbine.

2.1.4. CONTROLLER AND GENERATOR MODEL

The generator applied to the OWC presented in this thesis is assumed to be a permanent magnet machine, and the mathematical model was designed to mimic the

performance of an OWC over a macro time period that is measured in seconds, minutes, and hours. Due to this macro approach using a permanent machine generator, it is not necessary to use software like Simscape Power Systems [96] to create a complex power electronic model of a generator. In place of a complex generator model, the electrical power output was modelled assuming an ideal converter and the electrical power was calculated based on the applied braking torque and the rotational velocity of the turbine:

$$P_e = \omega\tau_{em}, \omega < 82, \tau_{em} < 143\ Nm, \tag{2.31}$$

where P_e is the electrical power generated by the OWC in W, τ_{em} is the electrical braking torque applied to the generator in Nm, and ω is the speed of the turbine in rads·s^{-1}. The electrical braking torque is limited by the power rating and speed rating of the electrical motor, which in the case of the CORES generator was 11 kW and 82 rads·s^{-1}. The braking torque limit is applied in the model by applying a ceiling limiter to the reference torque, and the rotational speed limit is applied to the braking torque as a multiplier that limits the applied braking torque when the system overspeeds. This method has shown to be satisfactory when power extraction from sea waves is being simulated [97].

The generator controller most commonly applied during deployment is used in the model presented in this chapter, as there was significantly more data available from that controller than the other control laws combined. The control law resolves the amount of electrical braking torque applied to the generator based on the rotational speed of the turbine. The braking torque is calculated using the 3rd-order polynomial equation:

$$\tau_{ref} = \tau_3 n^3 + \tau_2 n^2 + \tau_1 n + \tau_0, \tag{2.32}$$

where n is the speed of the turbine in rpm and τ_x are the control law coefficients. As the turbine speed increases, the power captured by the turbine increases and vice versa. The coefficients for the control law were calculated through simulations over sea states appropriate to the deployment location using a MATLAB SIMULINK model with pneumatic data collected through tank testing and turbine characteristics from laboratory testing [95].

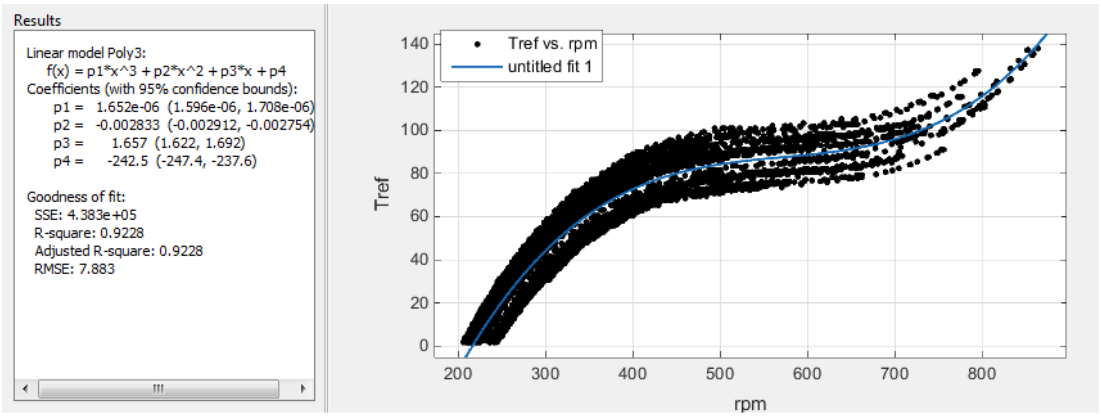

Fig. 2.4: Application of the MATLAB Curve Fitting App [98] to determine the control law coefficients for a single data set from the CORES output.

Fig. 2.4 is an example of how the controller coefficients were determined for a single data set using the curve fitting app in MATLAB [98]. The data points on the y-axis are the applied braking torque collected from the available experimental data sets. The model simulations that were used for device verification were directly based on experimental data collected from 8 different operational periods with different sea conditions, which totals approximately 3 hours of experimental data. The different operational periods occurred over a variety of sea states, and the coefficients used in the controller for each sea state were unique. The data collected were taken in conditions which were uncontrolled and subject to any manner of unknown influences and the accuracy of the results would be less precise than they would have been in a controlled laboratory environment. For each production data set, the control law coefficients were adjusted for experimental purposes, and the values of the coefficients of the control law were not published in the documentation or data files available from the CORES deployment. During the work carried out in this chapter, the coefficients used for each of the 8 data sets were determined based on experimentally collected data. The coefficients, τ_3, τ_2, τ_1, and τ_0, of the 3rd-order polynomial controller, (2.32), used in the model were found by plotting the real torque reference against the rotational velocity from each of the 8 data sets and using a curve fit to match the data.

If the coefficients of the control laws used in the model were not adjusted to match those found experimentally, the modelled data were found to be inaccurate. The inaccuracy of the results of the model found when using improper control law coefficients showed the effect the controller model had on the output of the model and helped to further confirm the accuracy of the model.

Along with the changing control law coefficients, the controller model also included an input delay of speed feedback of the turbine of 4 samples. The delay was introduced to match the time delay of 0.4 s found in the data transmission to the PLC of the ABB frequency converter measurement that was used as the input to the experimental controller [95].

Table 2.1 shows the R^2 values of the curve fits used to determine the control law coefficients, and the total time duration of each of the 8 samples analysed. In general, the longer the duration of the data sample, the less accurate the controller coefficients found using the curve fitting method. To better illustrate the drop in accuracy of the model as the duration of the sample data increases, Fig. 2.5 shows the R^2 values plotted against sample duration time.

Sea State		Controller Curve Fit	Duration of
H_s(m)	T_z(s)	R^2 Value	Sample (min)
1.26	3.53	0.9947	9
1.09	3.57	0.9995	10
1.09	3.57	0.9947	11
1.44	3.80	0.985	12
1.28	3.65	0.9228	17
1.64	4.45	0.6545	31
1.68	4.43	0.7967	35
1.22	3.96	0.6668	43

Table 2.1: R^2 values for the curve fits used to determine the control law coefficients and the duration of data collected for each sample.

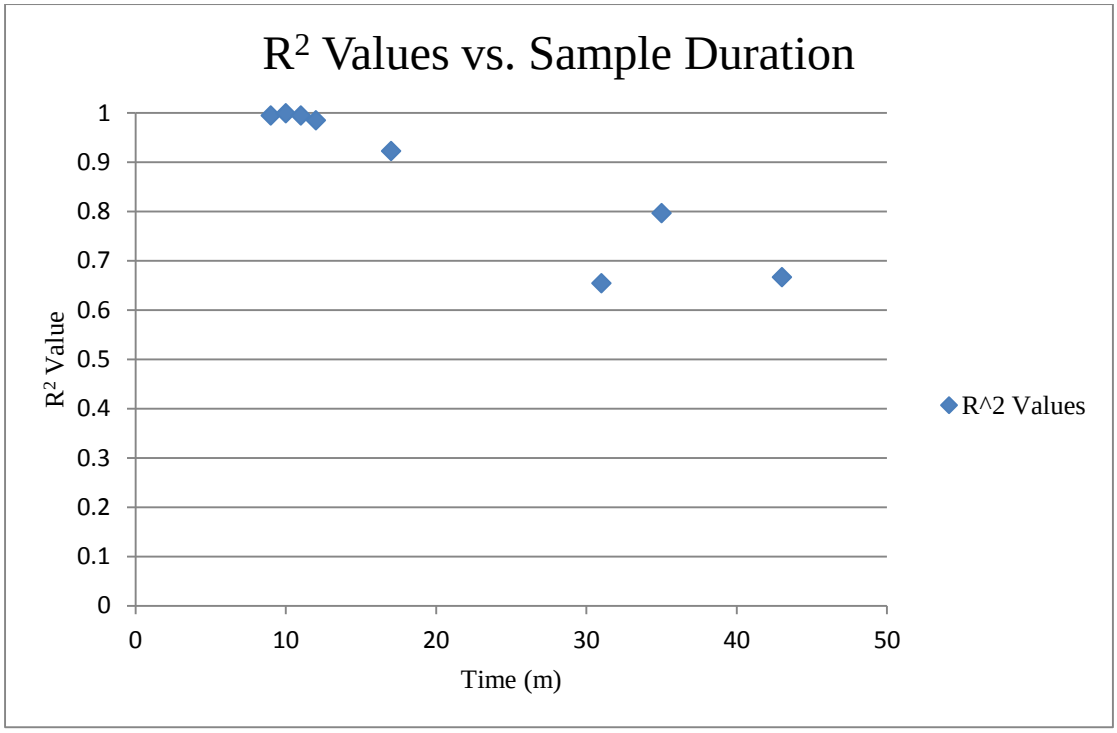

Fig. 2.5: Plot of the R^2 values for the curve fits used to determine the control law coefficients and the duration of data collected for each sample to illustrate the change in accuracy as the sample duration increases.

2.1.5. FULL NUMERICAL MODEL

By combining the techniques described previously, a complete model of an OWC in the time domain was created in SIMULINK, which can be seen in Appendix C. This model, with the adjusted controller coefficients, has shown good correlation with the real observations from the CORES deployment in 2011. This single model was constructed by finding the interdependent variables between the four independent modelling steps and linking them to create the most complete model possible. The primary co-dependent variable for the full system is the radiation admittance or aerodynamic damping of the system produced by the turbine. It affects the pressure within the air chamber and the volumetric flow across the turbine, and the variation of the air pressure in the chamber affects the movement of the IWS. The flow chart in Fig. 2.6 illustrates how the full model works.

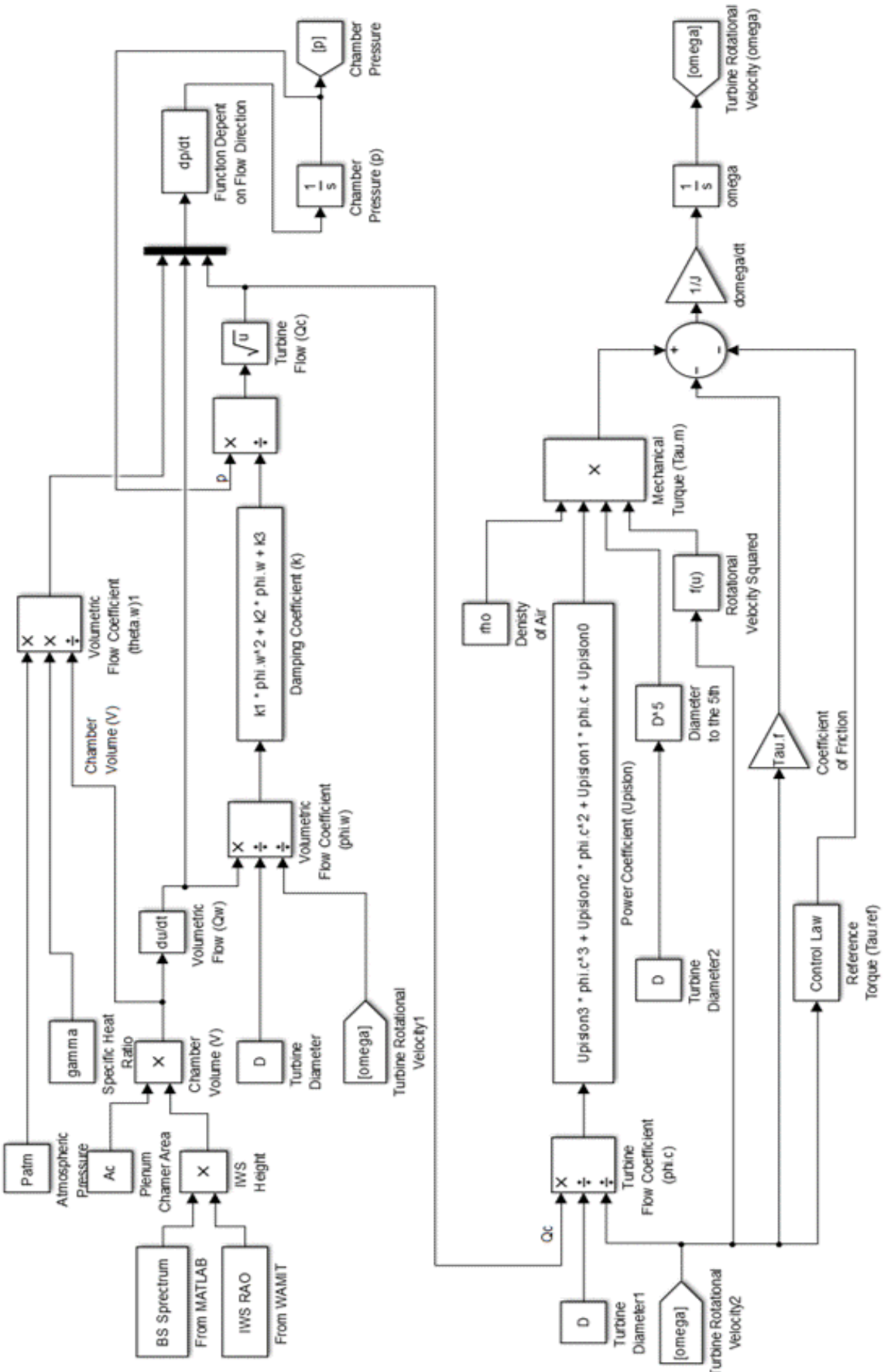

Fig. 2.6: Model flow chart.

The WAMIT model could not be directly coupled to the SIMULINK model in the method used to create the numerical model investigated in this thesis. the changes in the radiation admittance caused by the turbine damping could not be directly applied to the movement of the IWS. To address this inconsistency, the volumetric flow produced by the IWS motion was used along with the rotational speed of the turbine to find the flow coefficient based on Q_w, which was then used to approximate the damping coefficient of the turbine. The damping coefficient of the turbine, k, was calculated from the second order polynomial function of the flow coefficient that was determined experimentally using:

$$k = k(\Phi) = k_2\Phi^2 + k_1\Phi + k_0. \tag{2.33}$$

The calculated value of k was then used in (2.13) to determine the change in pressure, $\frac{dp_c}{dt}$, over the sample time. With the new pressure value, p_c, calculated, the damping coefficient was used to determine the value of Q_p, which was then used with equations (2.23)-(2.25) to approximate the behaviour of the impulse turbine. The mechanical torque, τ_m, applied to the turbine by the calculated flow, Φ_c, was combined with the electrical braking torque, τ_{ref}, applied by the generator to determine the changing rotational speed of the turbine. The estimated speed of the turbine was then used to adjust the electrical torque demand as dictated by the controller. The electrical braking torque was combined with the rotational speed of the turbine to determine the electrical power output, P_e, of the system. By calculating Q_p based on the turbine damping and applying that flow to the turbine model rather than using the flow calculated directly from the hydrodynamic system, the model acts to mitigate the limitations inherent to the indirectly coupled hydrodynamic system. This step makes the calculation and application of the damping coefficient of the turbine, k, crucial to the modelling process, as it, along with the new calculation of Q_p, are relied upon to correct the imperfections found when applying the IWS movement from the hydrodynamic model. It is accepted that this is not the best solution for incorporating the turbine damping into an OWC model, and the changing turbine damping should be integrated into the hydrodynamic model. However, there is currently no software solution available to perform this task and creating such a solution is beyond the scope of this thesis.

Due to the disconnect between the hydrodynamic model and the rest of the system, the motion of the IWS was calculated first for the full duration of the simulation. The hydrodynamic array, which represents the level of the IWS every 100 ms, was then used as the input for the change in volume in the thermodynamic model. The 100 ms sampling rate can be applied here as thermodynamic changes occur at a much slower rate. The thermodynamics are dependent on the turbine model, and the turbine model is dependent on the controller output. At the beginning of a simulation, the turbine speed must be given as an initial condition because the calculations carried out for the thermodynamic model, the turbine model, and the controller model are dependent on the rotational speed of the turbine. Flow data was combined with the rotational velocity of the turbine and was used to calculate the mechanical power of the turbine using (2.34) The mechanical power of the turbine and the rotational velocity were used to find mechanical torque. The mechanical torque, τ_m, combined with frictional losses, τ_f, turbine inertia, J, and electrical braking torque, τ_{ref}, applied by the controller, was used to infer the change in the rotational velocity of the turbine.

$$\frac{d\omega}{dt} = \frac{\tau_m - \tau_{ref} - \tau_f}{J} \tag{2.34}$$

where τ_{ref} is the electrical braking torque from the generator in Nm, τ_f is the braking torque due to friction in Nm, and J is the inertia of the turbine kg m^2. The result of (2.34) was then integrated and used as the updated speed of the turbine.

To recreate the output of a BBDB OWC, the model works through the following steps for each sample time of *dt*:

1) *Ocean wave elevation generated using the Bretschneider wave spectrum;*
2) *Height of IWS estimated by applying RAO to wave elevation;*
3) *Volumetric flow across the turbine is estimated based on change in IWS height;*
4) *Damping coefficient calculated from volumetric flow and turbine speed;*
5) *Chamber pressure calculated from turbine damping and volumetric flow;*
6) *Mass flow rate is calculated from pressure, damping, and volumetric flow;*
7) *Flow coefficient, Φ, is determined from mass flow rate and turbine speed;*
8) *Turbine mechanical power is calculated from the flow coefficient;*
9) *Mechanical torque is estimated from turbine speed and mechanical power;*
10) *Applied electrical braking torque is determined from turbine speed;*

11) *Changed in turbine speed estimated from mechanical and electrical torque, friction, and turbine inertia;*
12) *Electrical power calculated from applied electrical torque and turbine speed.*

2.2. CORES PROJECT SYNOPSIS

The Components for Ocean Renewable Energy Systems (CORES) project was an EU funded FP7 collaborative research project completed in 2011 and coordinated by the Hydraulics and Maritime Research Centre (now MaREI) in University College Cork. It included thirteen partners, from both academia and industry, from seven European countries. The project was intended to further develop components and systems required by the wave energy sector including generators, control systems, moorings, instrumentation, telemetry, and grid interface technology [99, 100]. The culmination of the project was a 3-month sea trial of the systems integrated onto a 1:4 scale BBDB hull at the Galway Bay Wave Test Site in Ireland [36].

The ultimate objective of the CORES project was to create a wave-to-wire modelling 'toolbox' that would allow developers to evaluate the effect of changes in device components on the performance and economics of their devices [99, 100]. It consisted of four separate work packages, each of which represents a fully operational system. Work package 1 (WP1) focused on the air turbine system and led to the design of an impulse turbine with active moving guide vanes. Work package 4 (WP4) focused on modelling, system integration, and field trials, and WP4 is where the experimental data used for the model validation presented in Chapter 3 were generated [99].

The CORES OWC was equipped with a suite of sensors for measuring the electrical parameters of the generator, hydraulic and pneumatic parameters in the chamber and duct, environmental parameters, and electrical system parameters. The sensors fed the on-board data acquisition system, where the information captured by the sensors was evaluated by a Supervisory Control and Data Acquisition (SCADA) system and stored on an Open Platform Communication (OPC) client [95]. The data collected were used for a myriad of system analyses during deployment and following decommissioning. The performance of the impulse turbine used for power take-off was among the subsystems closely studied.

An impulse turbine was chosen over a Wells turbine for the CORES project for several reasons. Its lower operational speed makes it less constrained by Mach number effects and centrifugal stresses. This is an important advantage in floating OWC

applications, which expects larger air pressure oscillations when compared to shore-line fixed OWCs [95]. The impulse turbine is not susceptible to aerodynamic stall, which offers a larger operating flow range when compared to a Wells turbine [43]. The impulse turbine used for the project has active moving guide vanes, which were added to minimise the aerodynamic losses caused by excessive incident flow angle at the entry guide vanes on the outlet side of the turbine [95]. The impulse turbine tested during the deployment of the OWC was one small piece of the considerable IP generated through the CORES project [99].

2.3. IMPULSE TURBINE DESIGN PARAMETERS

The initial model is a numerical model of 1:4 scale BBDB OWC deployed for the CORES project, so that the complete numerical model could compared to available experimental data for validation. Once validated, the model was used to investigate turbine control strategies at full scale. As the impulse turbine installed on the OWC for the CORES device contained IP, a full scale impulse turbine with fixed guide vanes was designed using parameters publicly available via several publications to further this thesis.

To design the impulse turbine for this thesis, the parameters from the fixed guide vane turbine presented by Takao and Setoguchi in [39] were deconstructed to find the ratio-based relationships between various dimensions, which would allow for turbines of different sizes to be constructed while maintaining the same basic aerodynamic properties. The ratios were used to create a spreadsheet that would update all the design parameter measurements to match the chosen turbine diameter. The newly created spreadsheet can be used as a parametric turbine design tool, simplifying the design process down to choosing the turbine diameter. A new turbine design developed by applying the newly created design tool was then characterized using Computational Fluid Dynamics (CFD) software, and the results were used to fit the turbine into the full scale BBDB OWC model. This section presents the basic turbine geometry and design parameters collected from the available publications that were applied to the turbine build presented in Chapter 4.

2.3.1. TURBINE HUB AND BLADE HEIGHT

The initial ratio that needs to be found is the hub-to-tip ratio, which represents the fraction of the diameter that is made up by the solid hub portion of the turbine. All the

other ratios used to find the various design parameters of the turbine blades and the turbine guide vanes are based on the hub-to-tip ratio of the turbine. The hub-to-tip ratio, ξ, is defined in (2.35):

$$\xi = {}^{r_h}/_{r_t}, \tag{2.35}$$

where r_h is the hub radius in m, and r_t is turbine tip radius in m.

The hub-to-tip ratio is usually 0.7, which means that the ratio between the blade height, b, and the turbine radius will be 0.3. The mid-span radius, r_R, is used in finding the relationships between the various geometric designs of the turbine.

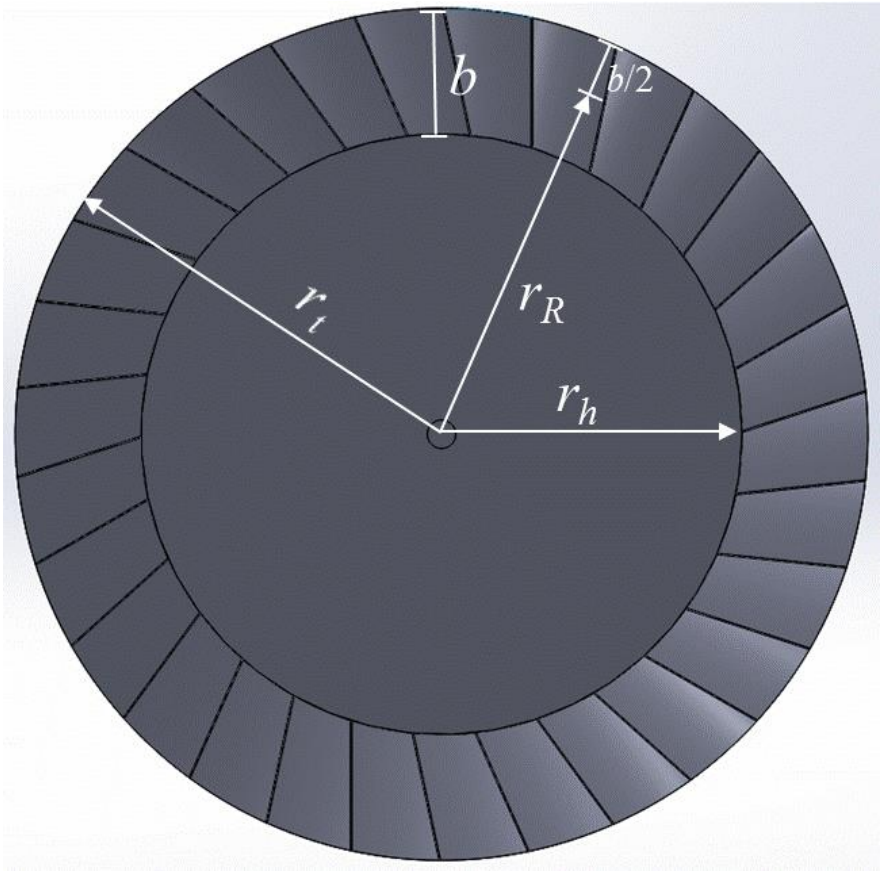

Fig. 2.7: An impulse turbine rotor with the values of the turbine radius, r_t, hub radius, r_h, mid-span radius, r_R, and the blade height, b.

The mid-span radius of the turbine measures from the centre of the turbine to the middle part of the blade and is defined in (2.36).

$$r_R = r_h + {}^{b}/_{2}. \tag{2.36}$$

The ratio of r_R to r_t is 0.85. The ratios were all taken from the 300 mm diameter impulse turbine, designed and tested by Setoguchi, which has been presented in several publications [41, 43, 101, 102, 103]. Fig. 2.7 shows the turbine radius, r_t, the turbine hub radius, r_h, the mid-span radius, r_R, and the blade height, b, of an impulse turbine rotor.

2.3.2. TURBINE BLADE GEOMETRY

After the hub radius and the blade height have been determined, the next step in designing an impulse turbine is the blade geometry. The blade profile is made using an elliptical suction-side leading edge combined with a circular pressure-side trailing edge, which helps to maximise the pressure differential between the two sides of the blade and maximises the lift produced by the blade [102]. The main design parameters for the turbine blade are the blade chord length, l_r, the semi-major and semi-minor axes of the ellipse, a and e respectively, and the pressure side radius r_r. Fig. 2.8 illustrates the turbine blade from a plan view with the four geometrical design parameters.

The impulse turbines which have been tested for use with an OWC have 30 symmetrical blades that are equally spaced about the rotor. The blade pitch, S_r, is based on the spacing of the blades at the mid-span radius. The value of S_r is most easily determined by finding the circumference of the circle based on the mid-span radius and dividing that number by the 30 blades. The blade solidity ratio is defined as the ratio of blade cord length to blade pitch:

$$\sigma_b = {}^{S_r}/_{l_r}, \tag{2.37}$$

where σ_b is the blade solidity ratio. The solidity ratio directly impacts the aerodynamic damping of a turbine.

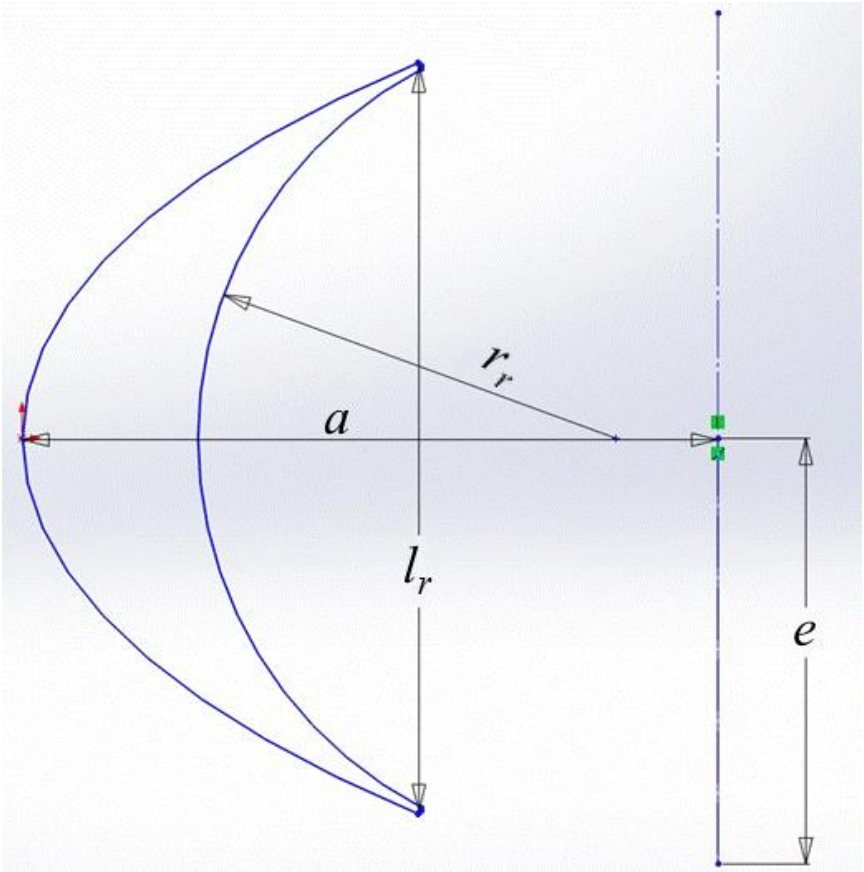

Fig. 2.8: Plan view of the turbine blade geometry with the main design parameters shown.

Research carried out by [104] investigated the effects of solidity ratio on the impulse turbine, but the focal point of the research was the ratio between guide vanes and rotor blades and not rotor solidity. Most published studies rely on a blade pitch based on 30 blades and any significant redesign of the turbine is beyond the scope of work for this thesis.

By comparing the blade pitch and the chord length from the original 300 mm diameter turbine, it was found that the blade solidity ratio was found to be approximately 0.5. The rest of the blade design ratios were based on the ratio between the blade pitch and the chord length. Table 2.2 shows the various values and ratios used when designing an impulse turbine blade.

Parameter	300 mm Design (mm)	Ratio	
Blade Pitch (S_r)	26.7	$2\pi\ r_R/30$	n/a
Blade Cord Length (l_r)	54.0	S_r/l_r	0.50
Pressure Side Cup Radius (r_r)	30.2	r_r/l_r	0.56
Suction side semi-minor axis (e)	41.4	e/r_r	1.37
Suction side semi-major axis (a)	125.8	a/e	3.03

Table 2.2: The dimensions of the 300 mm diameter impulse turbine rotor blade, along with the calculated design ratios based on the original turbine design

.

2.3.3. TURBINE GUIDE VANE GEOMETRY

The impulse turbine requires guide vanes to redirect the airflow in the turbine duct in order to create lift on the blades and torque on the turbine rotor, so the design of the guide vanes is as important to the overall turbine as the design of the rotor blades. The determination of the geometry of the turbine guide vanes was accomplished using similar dimensionless geometric ratios ratios as were used for the rotor blades. The geometry of the guide vanes is less complex than that of the turbine blades. The guide vanes can be broken into two geometric sections, the curved inlet section of the guide vane, which consists of a 60º section of a circle that is used to redirect the air, and a straight section that allows the air flow to settle in the new direction before it enters the rotating turbine [103]. The key measurements of the guide vanes include the chord length, l_r, the curved radius, R_a, and the length of the straight section, l_s. Both plate and airfoil guide vane geometry were tested in [41], and it was found that there was no discernible difference in performance between the two. The plate guide vanes were used repeatedly in experimental and CFD testing of guide vanes [39, 41, 43, 52, 94, 101, 102, 103, 105, 106]. Due to the simpler design and ubiquitous use of the plate guide vane geometry, they were chosen for this thesis. Fig. 2.9 illustrates the guide vane from a plan view with the three geometrical design parameters.

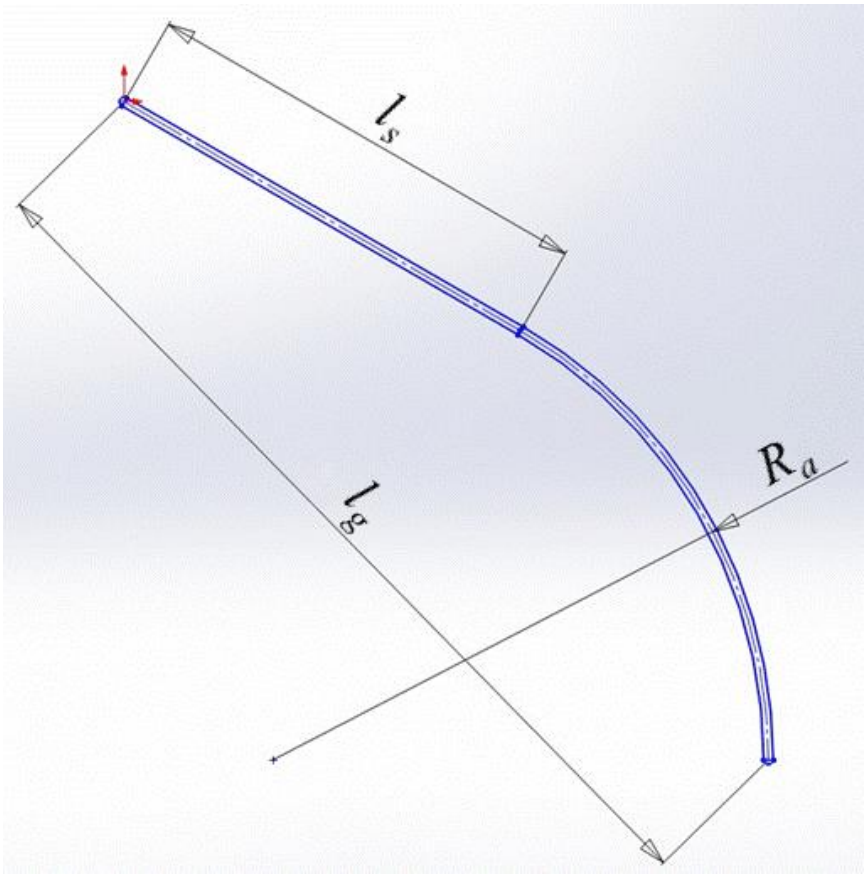

Fig. 2.9: Plan view of the guide vane geometry with the main design parameters shown.

The guide vanes for the impulse turbine design chosen for this project included 26 symmetrical vanes that are equally spaced and are mirrored on both sides of the turbine. Two recent studies have been published investigating the effects of guide vane solidity on the performance of impulse turbines. In [107], a unidirectional impulse turbine was tested in a laboratory under the same conditions that Setoguchi's 300 mm impulse was tested, and it was concluded in that paper that 23 guide vanes was optimal. However, in [104], a bidirectional impulse turbine modelled after the same 300 mm impulse turbine was tested using CFD, and it was concluded following that study that 30 guide vanes was optimal. Due to the contradictory results from the referenced studies and that further investigation into guide vane solidity is beyond the scope of this thesis, the original design of 26 guide vanes, which has been used in most studies of impulse turbines, was used for the turbine presented in this thesis.

The guide vane pitch, S_g, is based on the spacing of the guide vanes at the mid-span radius. Like the value of S_r, the value of S_g is determined by finding the circumference

of the circle based on the mid-span radius and dividing that number by the number of vanes (26).

The other ratios used to determine the design parameters of the guide vanes were found by taking the ratio between the chord length of the turbine blades, l_r, and the guide vanes, l_g, which was approximately 0.771. Fig. 2.10 shows the blade and guide vane profile in plan view along with the blade pitch, S_r, guide vane pitch, S_g, and the gap, G, between the guide vanes and rotor blades. The variable, G, is the length of the gap between the end of the guide vanes and the beginning of the rotating turbine blades. The gap to turbine blade chord length ratio is based on the gap length that leads to the best turbine performance, and the ratio of G/l_r is given as 0.37 in [41]. Table 2.3 shows the various values and ratios used when designing impulse turbine guide vanes.

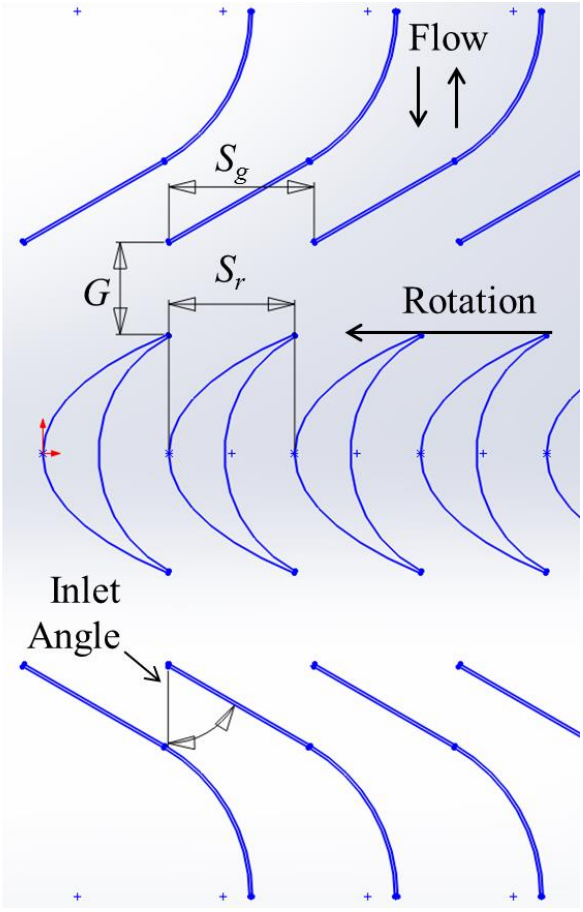

Fig. 2.10: The blade and guide vane profile in plan view along with the blade pitch, S_r, guide vane pitch, S_g, and the gap, G, between the guide vanes and rotor blades.

Parameter	300 mm Design (mm)	Ratio	
Guide Vane Pitch (S_g)	69.2	S_g/S_r	1.15
Chord Length (l_g)	70.0	l_g/l_r	1.30
Gap (G)	20.0	G/l_r	0.37
Straight Part of Guide Vane (l_s)	34.8	l_s/l_g	0.50
Curve Radius (R_a)	37.2	R_a/l_g	0.53

Table 2.3: The dimensions of the 300 mm diameter impulse turbine guide vanes and the calculated design ratios based on the original turbine design.

There are two main design parameters for the turbine blades and guide vanes, which are independent of the size of the turbine. These parameters are both blade angles. The first is the inlet blade angle, which can be seen in Fig. 2.10. Inlet angles for the blade of 50°, 60°, and 70° were tested and found that an inlet angle of 60° was most efficient [39]. The second of these angles is the blade sweep angle, which is the angle between the radial line and the centre line of the turbine blade. Swept blades are used to help limit unwanted compressibility effects that can occur with turbine rotor blades; a similar practice is used for the wings of commercial aircraft [108]. When investigating the effects the sweep angle of the blade had on performance, three different angle, 7.5°, 0° and -7.5°, were tested. The results found that a sweep angle of -7.5° led to the highest efficiency of the three angles [41, 102]. Fig. 2.11 illustrates the various sweep angles originally tested.

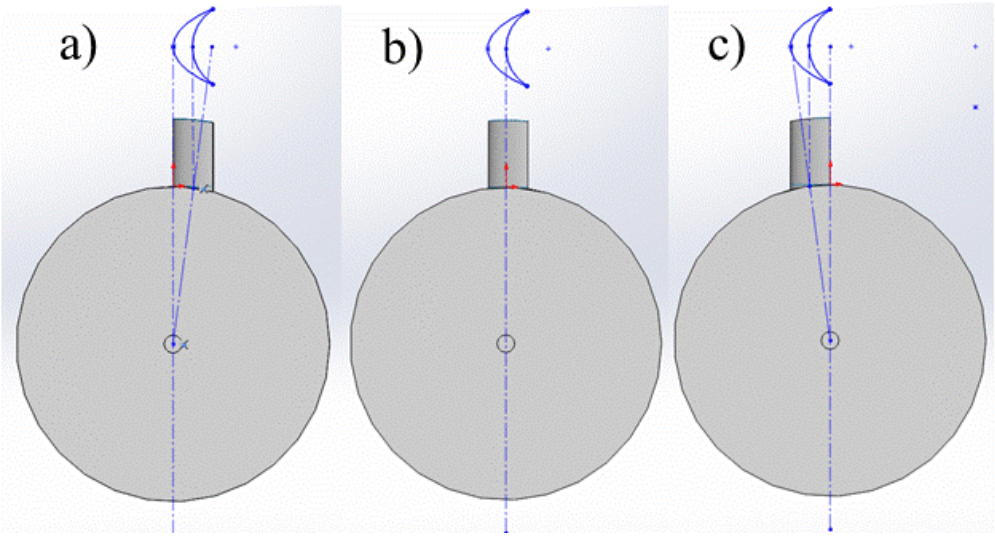

Fig. 2.11: How the blade sweep angles (a) -7.5°, (b) 0°, and (c) 7.5° affect the position of the blade on the turbine hub.

With the ratios necessary for turbine design known, the size and operating rotational velocity of the turbine can now be calculated so that it matches the OWC and corresponding sea conditions of the chosen site. Once the turbine diameter is selected, the various ratios given previously can be used to design and build the impulse turbine model to be used in this thesis.

The turbine model depends on the output of the thermodynamic model, while the thermodynamic model has inputs from both the turbine speed and the change in chamber volume caused by the hydrodynamic action of the buoy. Thus, the full model was verified against the CORES data in reverse order to minimize the complexity during the verification process, i.e. the turbine model was verified first, followed by the thermodynamic model, and finally the hydrodynamic model. This allowed for simpler troubleshooting of the model during development because the accuracy of each stage could be confirmed separately and any inconsistencies in further tests could be attributed to a given area. There were 8 operational periods that spanned between 9 and 43 minutes in duration, totalling approximately 3 hours of experimental data. The four comparison points for experimental versus modelled data were chamber pressure, p, flow, Q_p, electrical power, P_e, and rotational velocity, ω, of the turbine.

2.4. CONCLUSION

Wave-to-wire models can help to drive progress in the field of wave energy conversion at a fraction of the cost of full scale and even 1:4 scale open water deployment. It has been shown in Chapter 2 that the tools necessary for creating a numerical model of a BBDB OWC are available, as are the tools for testing that models validity. Using the tools available, a full model was created such that it can easily be adjusted to account for changes in device deployment site, device dimensions, turbine design or type, and changes to turbine controller. The CORES project, which provided the experimentally collected data used in the verification process for the numerical model, was introduced and the impulse turbine design parameters will be applied in Chapter 4 when creating a turbine to be used in the full scale device model. A parametric design tool for an impulse turbine with fixed guide vanes was also developed.

While they can never fully replace prototype sea trials, numerical models can reduce the need for sea trials, allow for the creation of better prepared prototypes, help in troubleshooting problems in deployed devices, allow for economic studies to be

performed on device production, and be used as a tool to assist in raising capital necessary for large scale deployment by presenting device potential. In Chapter 3, the BBDB OWC numerical model presented in Section 2.1.5 is tested against the experimental data collected during the CORES deployment to assess the accuracy of the model in replicating open water experimental results to find out if the model can be a trusted tool for evaluating the performance of BBDB OWCs.

3. NUMERICAL MODEL VERIFICATION

In Section 2.1 of Chapter 2, the models for the various systems that make up a BBDB OWC were introduced, and it was explained how those individual models were used to create a single complete unified model. In this chapter, the model developed in Chapter 2 will be tested against the experimentally collected data from the CORES project to evaluate the model accuracy. As the model was derived from three separate integrated models, the verification testing was performed in three stages. The verification process was broken up into stages to allow for a more thorough investigation of each model individually and verify the interconnections between the models. It also allowed for easier results presentation and troubleshooting of any problems encountered with model performance during testing.

In the first stage of the verification process, the turbine and controller model was tested using flow input data collected from the CORES project. The electrical power production and associated turbine speed observed experimentally during the interval of time in which the flow data was taken was compared to the electrical power and turbine speed generated by the model. This was carried out to analyse the performance of the turbine and controller model in isolation.

When the first step in the verification process reached a satisfactory conclusion, the next step in the process was carried out. This involved testing the thermodynamic model while using the movement of the Internal Water Surface (IWS) of the BBDB OWC as determined from the CORES project over the same time frames as the flow data taken for the turbine model verification. The outputs of the thermodynamic model included chamber pressure and air flow across the turbine, and the results from the model simulations were compared to the experimental data over the same time frames. The flow data generated from the thermodynamic model was also used an input to the turbine model in place of the experimentally measured flow data that was applied in step one. The behaviour of the turbine model depended on the flow applied to it, and the behaviour of the thermodynamic model depended on the rotational velocity of the turbine. This interaction was an important part of the numerical model and the affect the damping had on the model accuracy is discussed in detail. The modelled electrical output power and rotational velocity were inspected in the same way as they were in the first step of the model verification process. The deviations in flow and pressure from

the thermodynamic model versus the experimental data were found to affect the turbine model results, which confirmed the need for testing the models in isolation.

For the final step of the model verification, wave arrays with summary statistics matching those observed during CORES device production time were created using the Bretschneider spectrum, and the wave arrays were used with the RAO of the hydrodynamic model to determine the IWS motion, which was used along with the thermodynamic model and turbine and controller model to test the full model. The averaged results from the full model tests were compared to averaged results from the CORES experimental results taken during matching sea conditions.

During the verification process, anomalies in the experimental data were found to occasionally appear when comparing the electrical power output and turbine speed data to the modelled data. The anomalies were investigated further, and it was discovered that the model could also be used as a tool for troubleshooting device performance issues. This was an unintended outcome, but it showed that the model could be valuable post-deployment as well as pre-deployment. The nature of the anomalies and the process in diagnosing their origin are discussed in the final section of this chapter.

3.1. TURBINE AND TORQUE-SPEED CONTROLLER MODEL

The turbine and controller models were verified by comparing the output from the model simulations against the output collected from the CORES experimental data. Much of the data from CORES were acquired from direct measurement; however, due to the inability to directly measure every variable, some of the parameters had to be calculated from available experimental measurements, including flow across the turbine, pneumatic power, and mechanical power.

The control law was designed based on optimum power output simulations while concentrating on improving output power quality. The speed in rpm was used as the input and the electrical braking torque to be applied was the output. In the experiments run during the CORES deployment, the coefficients of the torque-speed equation were adjusted based on summary statistics of the sea conditions. The changing values of the coefficients during testing were not documented in any of the available data from the project. As referenced in Section 2.1.4, the coefficients used were determined by plotting the applied reference torque against the rotational speed of the turbine and a 3rd order polynomial curve was fitted to match the data. The resulting equations were used to determine the controller coefficients for each individual data set in the related

simulations tested for this research. For each production data set, the control law coefficients were adjusted, requiring a new curve fit for each simulation. Each new control law equation also had its own minimum speed; any time the rotational velocity of the turbine dropped below that speed, the turbine would be left free spinning with no braking torque applied to the generator.

3.1.1. DETERMINATION OF INDIRECT EXPERIMENTAL VARIABLES

It is extremely difficult in practice to measure air flow across the turbine directly, due to the lack of air flow metering technologies suitable for harsh marine environments with sufficient turndown ratios in rapidly fluctuating flows with high vorticity. Several solutions were investigated for calculating the air flow across the turbine in [95], and it was found that the Bernoulli method was the most accurate and reliable means of calculating flow. The flow across the turbine was calculated from the CORES data using the Bernoulli method as presented in (3.1) and (3.2) [95].

$$v_d = \sqrt{2\left(p_d - p_o \mp \Delta p_f\right)/\rho_o}, \tag{3.1}$$

$$Q_p = v_d A_t, \tag{3.2}$$

where v_d is the air velocity at the pressure sensor in m s^{-1}, p_d is the pressure measured inside the duct in Pa, p_o is atmospheric pressure in Pa, Δp_f is pressure loss due to air friction in Pa, ρ_o is air density at atmospheric pressure in kg m^{-3}, Q_p is flow across the turbine in m^3s^{-1}, and A_t is the swept turbine area in m^2.

Due to the location of the pressure monitor, the loss due to friction is applied before or after the measurement is taken depending on flow direction. In (3.1), the sign given to friction losses depends on the direction of the flow: positive when flows are going into the chamber and negative when the flows are going out of the chamber. Fig. 3.1 shows the location of the pressure sensor used to find the value of p_d, and the accuracy of the sensor was +/- 10 Pa, and with the values of p_d typically ranging from 0 to 500 Pa, the error in the sensor was approximately +/- 2%.

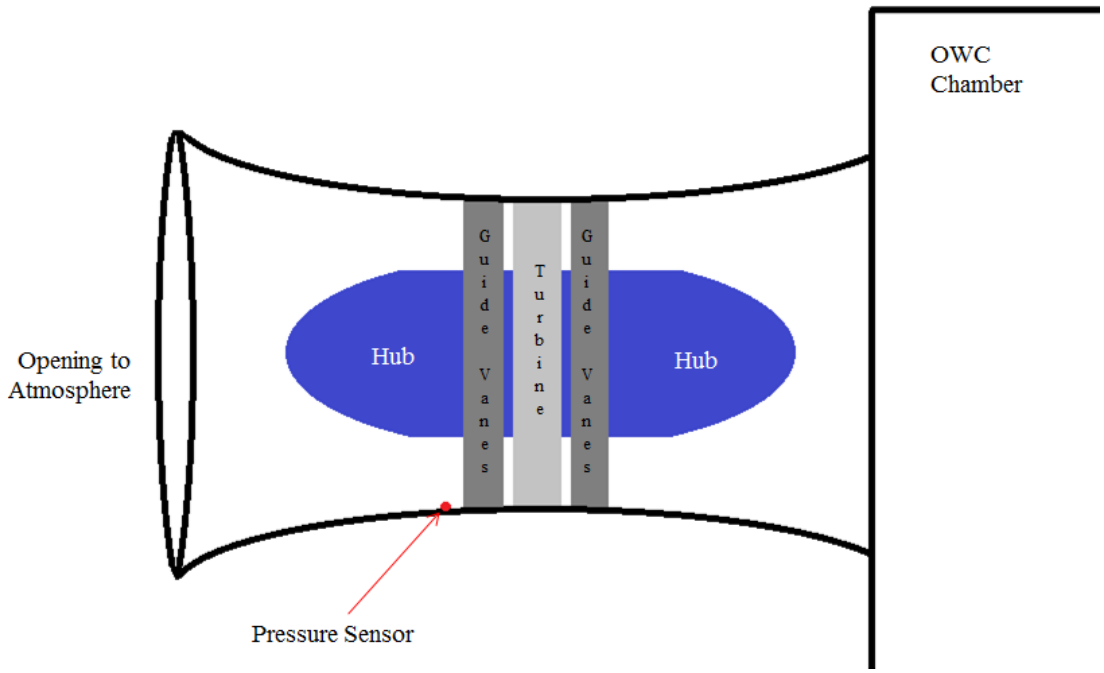

Fig. 3.1: The location of the pressure sensor used to calculated flow across the turbine using the Bernoulli method.

The friction coefficient was not calibrated for the application but the standard value for a duct of the same diameter was used in its place [95]. For the input to the model test in this section, the flow calculated from the CORES data was used in place of the output from the thermodynamic model to isolate the performance of the turbine model and the controller.

The pneumatic power available in the OWC was calculated using the flow across the turbine calculated in (3.2) and the air pressure measured within the plenum chamber,

$$P_p = Q_p p, \tag{3.3}$$

where P_p is pneumatic power in W and p is the gauge pressure measured in the plenum chamber in Pa.

To estimate the mechanical power produced by the turbine, the measured electrical power output was combined with the calculated frictional and inertial losses in (3.4).

$$P_m = P_e + B\omega^2 + J\omega\frac{d\omega}{dt}, \tag{3.4}$$

where P_e is the electrical power as measured by the power electronics that control the generator, B is the coefficient of friction in W s^2, and J is the turbine moment of inertia in kg m^2. For the CORES turbine, the friction coefficient, B, had a value of 0.075 W s^2 and the turbine moment of inertia, J, had a value of 4 kg m^2 [33]. The calculated mechanical power was then combined with the rotational velocity to find the mechanical torque, τ_m, exerted on the generator shaft in Nm. The iron, copper, and inverter efficiency losses were not experimentally determined and published in the papers describing the CORES project and were omitted in (3.4) to maximise continuity between the CORES data and the work performed in this thesis. This omission has most likely caused the mechanical power estimations presented in this chapter to under represent the actual mechanical power applied to the turbine during operation.

The values of pneumatic power, P_p, calculated in (3.3), mechanical power, P_m, calculated in (3.4), mechanical torque, τ_m, along with measured values of electrical power, P_e, applied electrical braking torque, τ_{ref}, and rotational velocity, ω, were used as performance indices for the OWC power take-off system. These values were also generated by the SIMULINK model, and the data in the performance indices were compared to assess the ability of the SIMULINK model to predict the experimental results. For testing the turbine model in isolation, the flow across the turbine measured from the CORES sensors was used in place of flow generated by thermodynamic model. The Q_p values from each of the 8 data sets were used during the verification process. The time frame of the 8 simulations used ran from approximately 10 minutes to nearly 45 minutes. Using Froude Scaling, these simulations could be compared to 20 minutes to 90 minutes at full scale as the CORES BBDB and the conditions in Galway Bay are considered quarter scale [95].

3.1.2. Modelled and Experimental Results and Comparison

The SIMULINK model was executed on a sample-by-sample basis, with a sampling frequency of 10 Hz, which was selected to match the 10 Hz sampling frequency of the Beckhoff Programmable Logic Controller (PLC) used during the CORES project. To start the model simulation, the rotational velocity, ω, of the turbine was given an initial condition to match the experimental data. The initial flow, Q_p, was taken from (3.2) and combined with the rotational velocity of the turbine using (2.17) to find the flow coefficient, Φ, of the first sample evaluated by the model. The flow coefficient was then

combined with the turbine diameter and rotational velocity using (2.26) to find the mechanical power and mechanical torque supplied by the turbine in (2.27).

The electrical braking torque, τ_{ref}, applied to the turbine was calculated based on the rotational speed of the turbine using (2.30). The applied braking torque was combined with the mechanical torque, the frictional torque, and the turbine moment of inertia in (2.32) to calculate the change in rotational velocity of the turbine for the single sample. The turbine velocity was then updated for the next sample and combined with the next air flow sample and the process was repeated for the entire data set being tested.

3.1.2.1. INITIAL MODEL PERFORMANCE

The mean values, averaged over the full duration of each data set, for electrical power and rotational velocity from the experimental and modelled data were compared to evaluate the accuracy of the model. The modelled values were within 3.7% and 0.1% of experimental values, respectively. With error of +/- 2% introduced by the pressure gauge used to estimate flow and the uncertainty added by the means of determining the controller coefficients, the results from the model predicted data are within expected deviation when compared to the experimental results.

Table 3.1 shows the average experimental and modelled electrical power and turbine rotational velocity for the 8 periods of operation used for model validation. In all periods of operation, the modelled data agreed well with the experimental data from the CORES testing. The power output of the model was slightly higher than the experimental results in 7 out of the 8 sea states.

Sea State		Average Electrical Power (W)			Average Rotational Velocity (rpm)		
H_s(m)	T_z(s)	Model	Actual	Error	Model	Actual	Error
1.26	3.53	2969.2	3051.1	-2.6%	607.7	603.5	0.7%
1.09	3.57	2212.1	2141.0	3.3%	555.6	537.8	3.3%
1.09	3.57	2153.2	2047.8	5.1%	503.7	494.8	1.8%
1.44	3.80	2368.7	2316.8	2.24%	391.9	396.3	-1.1%
1.28	3.65	2476.2	2353.2	5.2%	372.2	386.1	-3.6%
1.64	4.45	2040.2	1957.2	4.2%	310.2	312.3	-0.6%
1.68	4.43	2247.5	2023.4	11.0%	323.3	312.8	3.3%
1.22	3.96	1510.5	1447.6	4.3%	343.5	361.6	-5.0%

Table 3.1: Experimental and modelled electrical power and rotational velocity outputs based on real flow conditions averaged over the sample time.

The coefficients of the control algorithm used over the individual samples affected the operating speeds of the turbine in the various simulations. This demonstrates that

the modelled results are ideal for verifying the effectiveness of the control algorithms. The differences caused by the control algorithms can be seen in both the average rotational velocity of the turbine and the power outputs, where power output increases at the higher rotational velocity.

Fig. 3.2 and Fig. 3.3 show the rotational velocity of the turbine and the braking torque demand determined by (2.29) for two different example data sets. On average, the turbine rotational velocity from the model is slightly less than the experimental results and the braking torque demand is slightly higher for the data set represented in Fig. 3.2. In the data set represented in Fig. 3.3, the speed and torque demand for the model more closely follow the speed and torque demand of the experimental results when compared to Fig. 3.2.

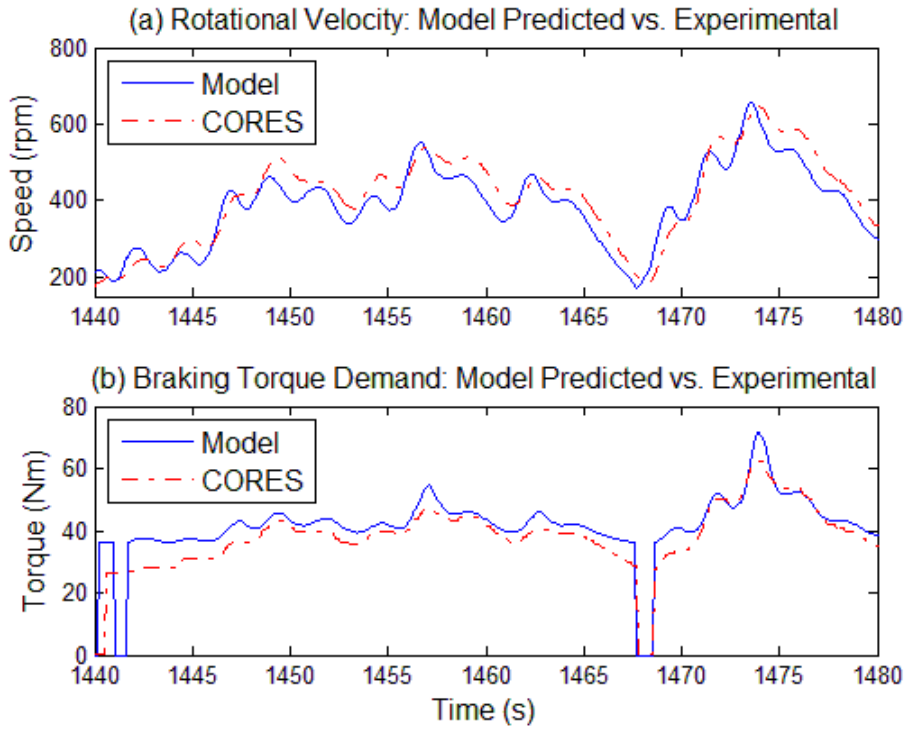

Fig. 3.2: Modelled and experimental data for the turbine rotational speed (a) and braking torque demand (b) for the data set where H_s=1.22 m and T_z =3.96 s.

The difference in accuracy between the two data sets is likely caused by errors in the coefficients used to set the braking torque of the generator. These results are not unexpected because of how the coefficients used in the model were estimated, and the coefficients determined for the controller applied in Fig. 3.3 had a much higher R^2 value

than those determined for the controller applied in Fig. 3.2. Overall, the averaged results for 7 of the 8 simulations were within an acceptable range of approximately 5%.

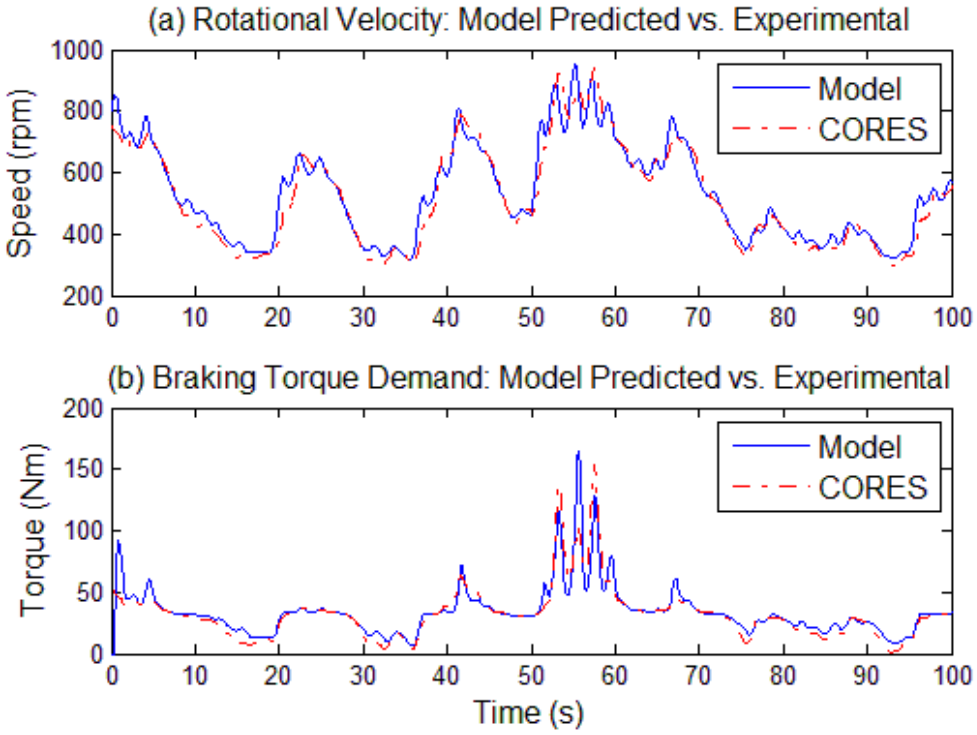

Fig. 3.3: Modelled and experimental data for the turbine rotational speed (a) and braking torque demand (b) for the data set where H_s=1.09 m and T_z =3.57s.

3.1.2.2. INVESTIGATION OF THE EFFECT OF CONTROL LAW COEFFICIENTS

To further illustrate the importance of applying the correct control law to the model, Fig. 3.4 shows a plot of the same data from Fig. 3.3 but includes the modelled results when the control law coefficients used in the simulation Fig. 3.2 are applied in place of the correct coefficients. It is clear from this plot that the control law coefficients affect the performance of the model, thus indicating that the torque controller and the inferred speed of the turbine calculated by the model are reliable.

The results found when applying the incorrect control law coefficients vary, depending on the values of the coefficients and the input data set they are applied to, but in each case, the controller coefficients determined from the correct experimental data sets led to the model data most closely matching the experimental outputs. In the instance presented in Fig. 3.4, the incorrect coefficients generated a higher braking torque during turbine operation than was generated in the experimental data. When

compared to the results presented in Fig. 3.3, the importance of applying the correct coefficients is revealed. The significances of the results of these tests are twofold, the accuracy of the method for determining the coefficients applied to the controller for each sea state is further confirmed, and more importantly, the results when applying different control algorithms to the model are applicable when assessing performance.

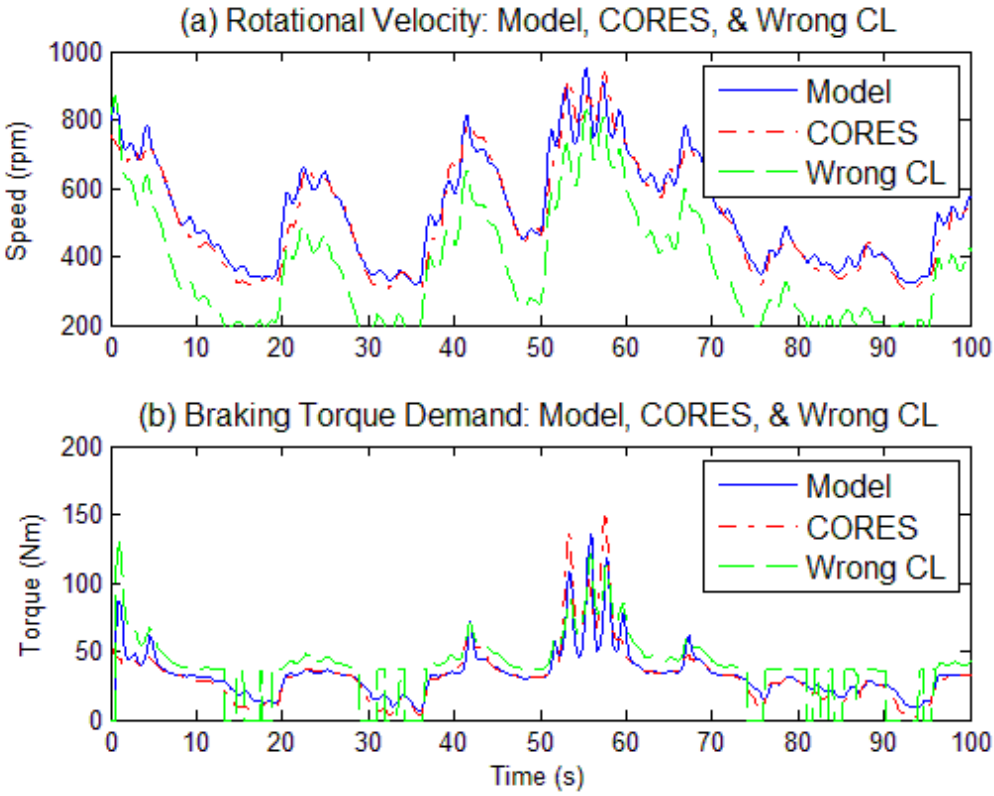

Fig. 3.4: Modelled, experimental and the modelled wrong control law coefficients data for the turbine rotational speed (a) and braking torque demand (b) for the data set where H_s=1.09 m and T_z =3.57s.

3.1.2.3. STATISTICAL ANALYSIS OF MODEL GENERATED DATA

The final step in the assessment of the performance of the turbine model was accomplished using a box plot statistical tool available in MATLAB to further compare the experimental and modelled results. Below, Fig. 3.5 and Fig. 3.6 present the mechanical and electrical power outputs of the model and experimental data from the same samples and over the same time period as the data in Fig. 3.2 and Fig. 3.3. The plots also show good agreement between model predicted and experimental results. These figures are good representations of the results found during all eight time series simulations when compared to the experimental results.

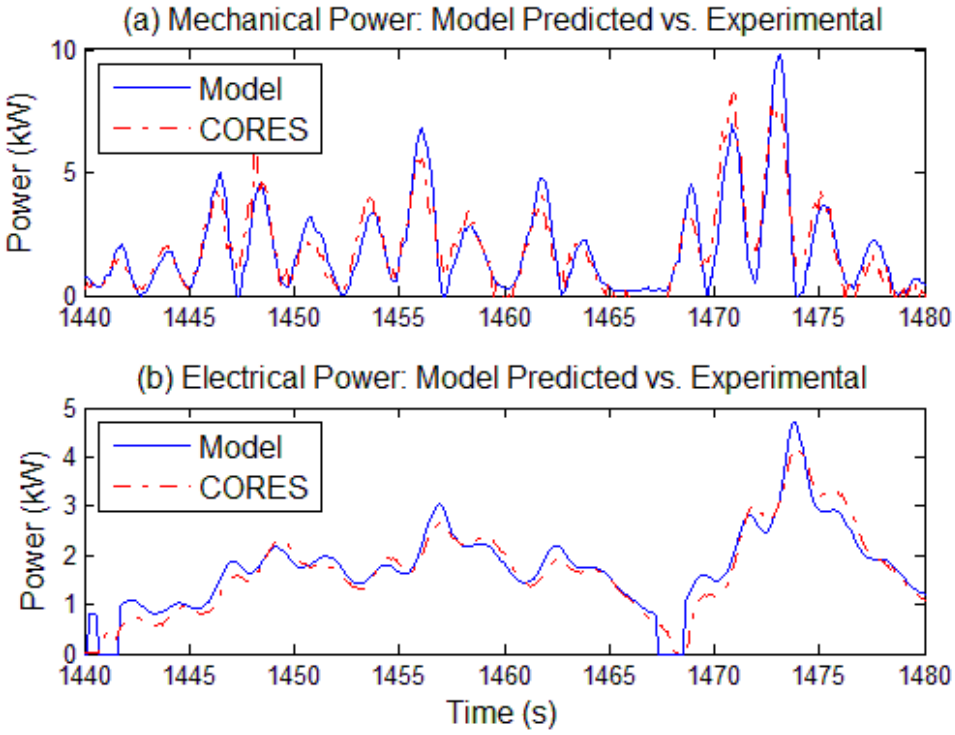

Fig. 3.5: Modelled and experimental data for mechanical power output (a) and electrical power output (b) for the data set where H_s=1.22 m and T_z =3.96 s.

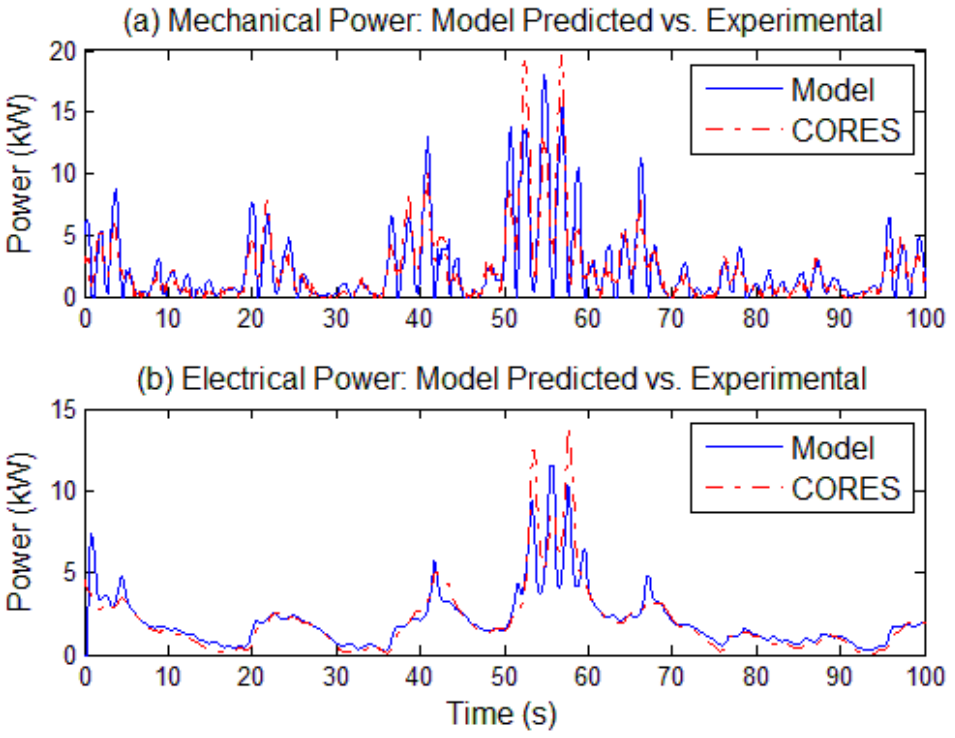

Fig. 3.6: Modelled and experimental data for mechanical power output (a) and electrical power output (b) for the data set where H_s=1.09 m and T_z =3.57s.

As can be seen in Fig. 3.5 and Fig. 3.6, there are times when the experimental data and modelled data do not match perfectly. The most obvious deviations occur at peaks in electrical output power. Typically, the experimental results were greater than the model generated data over a small number of samples. These incidences had an effect on the overall averages investigated in this thesis, made applying Mean Squared Error analysis impractical and affected the averaged values displayed in Table 3.1. **Error! Reference source not found.** is a histogram of the experimental and modelled electrical power output from the data presented in Fig. 3.5.

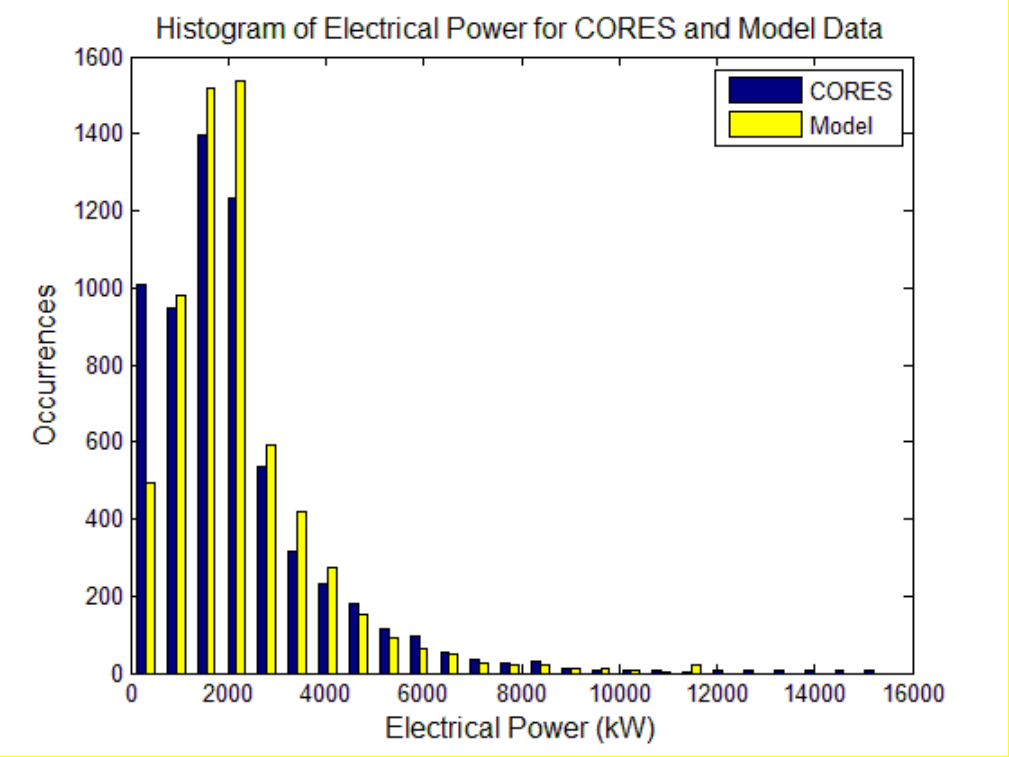

Fig. 3.7: Histogram of the electrical power output from the experimental and model data sets

The histogram shows a higher quantity and larger values of the outliers and near zero results from the experimental data, while the model data has a higher number of results near the centre of the curve. Both histograms have similar shapes, while the greater number of high power results in the CORES data helps to explain why the average electrical power output of the time series is higher for the CORES data when compared to the model data. These results are common for the 8 data sets tested in this chapter,

showing that the turbine model with flow input data from CORES marginally overestimates the performance of the system.

The results presented have shown that the numerical models used to represent the turbine, the electrical controller, and to infer the changing speed of the turbine are accurate, reliable models when used in place of the experimental data available for comparison, and that they can be used to model the mechanical and electrical PTO of an OWC system. With the turbine and controller accuracy tested and verified against the available experimental data, the thermodynamic model was then tested against the same experimental data sets to extend the validation of the model further.

3.2. THERMODYNAMIC MODEL

With the turbine model validated, the accuracy of the thermodynamic model in estimating the pressure in the plenum chamber and the flow across the turbine could be validated using the CORES data in a similar manner. Any changes in the results could be traced back to the thermodynamic model as the turbine model was shown to closely follow the experimental results. The thermodynamic model validation relies on (2.26) and (2.32) to infer the mechanical torque and rotational speed of the turbine, while the pressure in the plenum chamber was inferred using (2.11). The data from the same 8 periods of operation were used in the validation process. The flow generated from the thermodynamic model was used as input to the turbine model, and the resulting rotational speed and electrical output power were again compared to the experimental results. This allowed the accuracy of the combined model to be more closely investigated, as changes in the input flow resulting from using the thermodynamic model output rather than the experimental data may affect the performance of the turbine model.

3.2.1. DETERMINATION OF INDIRECT EXPERIMENTAL VARIABLES

To perform the calculations necessary to find the flow across the turbine, the change in volume of the plenum chamber of the OWC was calculated from the experimental data, which was based on the changing elevation of the IWS. The IWS motion from the CORES project was calculated from the flow used in the turbine model verification, the known surface area of the IWS, and the gauge pressure in the inner chamber of the OWC. The gauge pressure inside the chamber allowed the determination of the flow

direction and therefore the direction of the IWS movement. This was accomplished using:

$$h_I(i) = T\left[{Q_C}/{A_p} * sign(p)\right] + h_I(i-1), \qquad (3.5)$$

where h_I is the height of the IWS in m, Q_C is the flow calculated from the original CORES data in $m^3\ s^{-1}$, A_p is the area of the plenum chamber of the OWC in m^2, and *sign(p)* is the numerical sign of the gauge pressure in the plenum chamber and determines the direction of movement of the IWS.

To test the thermodynamic model, the created arrays representing the movement of the IWS were introduced to the model in place of the output from the hydrodynamic simulation. The change in volume was calculated directly from the IWS motion. While this calculation appears redundant as the movement of the IWS was originally calculated from the volumetric flow rate, the input to the SIMULINK model is IWS movement, so the model was tested in this way.

3.2.2. Model Results and Comparison

As performed in Section 3.1.2, the SIMULINK model was executed on a sample-by-sample basis, with a sampling frequency of 10 Hz. For the thermodynamic model testing, the volumetric flow rate, Q_w, across the turbine was determined from the IWS motion and was used in (2.17) to determine the volumetric flow coefficient, Φ_w. The volumetric flow coefficient was used to determine the damping coefficient, k, with (2.30). The determination of the damping coefficient and the use of the constantly updated damping coefficient is a key part linking the various models together, and the ability of this calculation to accurately model the effects of the turbine on the thermodynamic system was the focus of the verification process.

3.2.2.1. Dynamic Turbine Damping Model

With the damping coefficient known, equation (2.12) was used to calculate the gauge pressure in the plenum chamber based on chamber volume. The gauge pressure calculation relied on the previous pressure calculation, the change in volume in the plenum chamber, and the damping coefficient. Finally, the updated plenum chamber pressure was used with the damping coefficient to calculate the flow across the turbine,

Q_p, which was the flow used to find the mechanical torque input to the turbine. The mathematical steps are presented below in the sequence order in which they are performed in the SIMULINK model:

$$Q_w = A_p \frac{dh_I}{dt}, \tag{3.6}$$

$$\Phi_w = Q_w/(\omega D^3), \tag{3.7}$$

$$k = k_2\Phi_w^2 + k_1\Phi_w + k_0, \tag{3.8}$$

$$\begin{cases} \frac{dV}{dt} + \frac{V}{\gamma p_0 + p_c}\frac{dp}{dt} + \sqrt{p/k} = 0, \ p \geq 0, \\ \left(1 + \frac{p_c}{\gamma p_0}\right)\frac{dV}{dt} + \frac{V}{\gamma p_0}\frac{dp}{dt} - \sqrt{-p/k} = 0, p < 0, \end{cases} \tag{3.9}$$

$$Q_p = \sqrt{p_c/k}, \tag{3.10}$$

$$\Phi_c = Q_c/(\omega D^3), \tag{3.11}$$

$$P_m = \Psi(\rho\omega^3 D^5) = f(\Phi)(\rho\omega^3 D^5), \tag{3.12}$$

$$\tau_m = \frac{P_m}{\omega}. \tag{3.13}$$

To determine the validity of the thermodynamic model, the plenum chamber pressure, p_c, calculated in (3.9) and the flow across the turbine, Q_p, calculated in (3.10) along with the electrical power output and rotational velocity of the turbine were compared with the experimentally measured data in the same way that the data were compared in the previous section. The values of pressure and flow form irregular waves that oscillate around zero, so the average value of each of these data arrays would be approximately zero. The Root Mean Square (RMS), which is the arithmetic mean of the squares of the data set, was used for statistical analysis of the model and experimental data. The RMS allowed for determining the non-zero average value of the pressure and flow data. The Root Mean Square Error (RMSE) was applied measure the differences between the model predicted results and the results that were experimentally observed during the CORES deployment.

The sensor used to collect the experimental pressure measurements had a precision of +/- 40 Pa, which, for RMS values of around 2000 Pa, corresponds to an error of approximately 4%. The errors between the modelled and experimental pressure results ranged from 2.1% to 10.5%, and with the exception of the first data set, which was

taken in the least energetic sea conditions, the experimentally measured pressure was greater than the modelled pressure. The calculated flow data shows better agreement with the measured data with errors between the modelled and experimental results ranging from 0.2% to 5.0%. It was expected that higher pressures and flows would be found in the experimental results, as the damping of the turbine was not taken into consideration when calculating the movement of the IWS. Neglecting the changing aerodynamic damping of the turbine during these calculations could lead to inaccurate estimations of the IWS movement and results in Table 3.2 reinforce this hypothesis. These conditions were not optimal for estimating IWS motion; however, they were the best available option as suggested by [95].

Sea State		Pressure RMS (Pa)			Flow RMS ($m^3 \cdot s^{-1}$)		
H_s(m)	T_z(m)	Model	Actual	Error	Model	Actual	Error
1.22	3.96	1405.2	1375.8	-2.14%	2.710	2.705	-0.20%
1.26	3.53	2090.2	2334.5	10.46%	2.995	3.150	4.91%
1.44	3.80	2029.0	2217.2	8.49%	3.045	3.170	3.94%
1.09	3.57	1730.5	1887.9	8.34%	2.724	2.849	4.38%
1.09	3.57	1703.1	1834.1	7.14%	2.717	2.841	4.34%
1.28	3.65	2047.5	2239.4	8.57%	3.089	3.208	3.70%
1.68	4.43	2001.6	2152.6	7.01%	3.029	3.189	5.03%
1.64	4.45	1902.5	2040.8	6.78%	3.064	3.165	3.18%

Table 3.2: Experimental and modelled RMS values of gauge pressure inside the plenum chamber and flow across the turbine with the model that included the dynamic damping coefficient correction.

3.2.2.2. STATIC TURBINE DAMPING MODEL

To further investigate the effectiveness of the model using the dynamic damping coefficient as a corrective measure, the same model was simulated using a static value for the damping coefficient which represented the typical damping of the turbine at higher flow coefficients and was found through laboratory testing. The static damping coefficient was determined from laboratory experiments performed on the turbine, and it was selected to be same value was applied during the hydrodynamic model used to generate determine the IWS RAO. Table 3.3 below shows the results of the modelling performed with static damping compared with the experimental results.

The results of the SIMULINK model using static damping are less accurate than the results when dynamic damping is included in the model, and with the exception of the

first data set in the table, the results using static damping are much less accurate representations of the experimental data. The first data set is more accurate than the others, and more closely related to the results from the model with dynamic damping because the energy available in that particular sea state, and the flows generated as a result, are much lower than in the other 8 data sets. To illustrate the results, plots of the experimental data along with the output from both models are presented in the next section.

Sea State		Pressure RMS (Pa)			Flow RMS ($m^3 s^{-1}$)		
H_s(m)	T_z(m)	Model	Actual	Error	Model	Actual	Error
1.22	3.96	1283.6	1375.8	6.70%	2.710	2.670	1.30%
1.26	3.53	1543.8	2334.5	33.87%	2.924	3.150	7.17%
1.44	3.80	1589.0	2217.2	28.33%	3.012	3.170	4.98%
1.09	3.57	1295.2	1887.9	31.39%	2.662	2.849	6.55%
1.09	3.57	1289.3	1834.1	29.70%	2.665	2.841	6.18%
1.28	3.65	1636.7	2239.4	26.91%	3.065	3.208	4.45%
1.68	4.43	1626.4	2152.6	24.44%	3.028	3.189	5.03%
1.64	4.45	1623.8	2040.8	20.43%	3.050	3.165	3.63%

Table 3.3: Experimental and modelled RMS values of gauge pressure inside the plenum chamber and flow across the turbine with a static damping coefficient.

3.2.2.3. COMPARISON OF STATIC AND DYNAMIC DAMPING RESULTS

The static and dynamic damping models were compared to determine the effectiveness of modelling plenum chamber pressure. Fig. 3.8 and Fig. 3.9 are plots of the experimental and the dynamic and static damping modelled chamber pressures and flows across the turbine for the same data set and same time period represented in Fig. 3.5 and Fig. 3.6, where H_s=1.09 m and T_z=3.57 s. In Fig. 3.8, the pressure spikes seen in the experimental data were not well represented in the model and this was a significant contributor to the deviations found in the RMS values of the modelled and experimental data. These are likely related to the pneumatic damping of the turbine indicating that at high flows the model turbine was underdamped. While the dynamic damping approach used in the model developed for this thesis underestimated the pressure changes found within the chamber, this approach to modelling the system proved to be a more reliable method than using a static damping coefficient. Fig. 3.9 shows the closer agreement found between the modelled predicted and experimental

flow across the turbine, while there are still small spikes in the flow found at the same peaks where the pressure in the chamber spikes. The flows calculated using dynamic and static damping show little difference, which is also reflected in Table 3.3

.

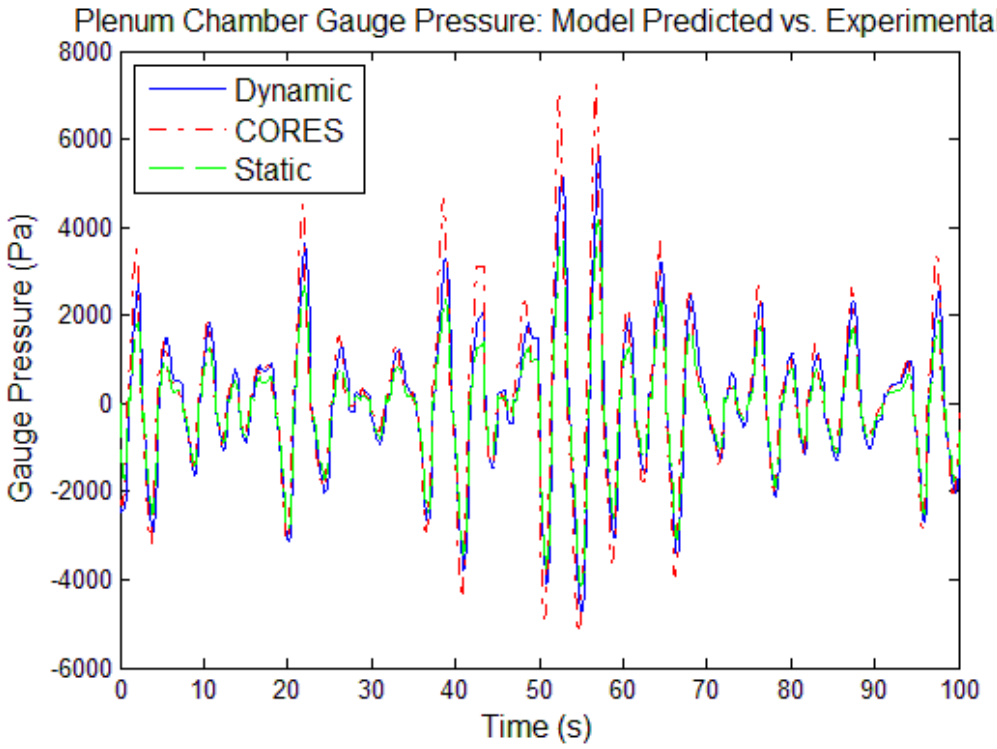

Fig. 3.8: Experimental, dynamically damped model, and statically damped model data for the plenum chamber pressure for the data set where H_s=1.09 m and T_z =3.57 s.

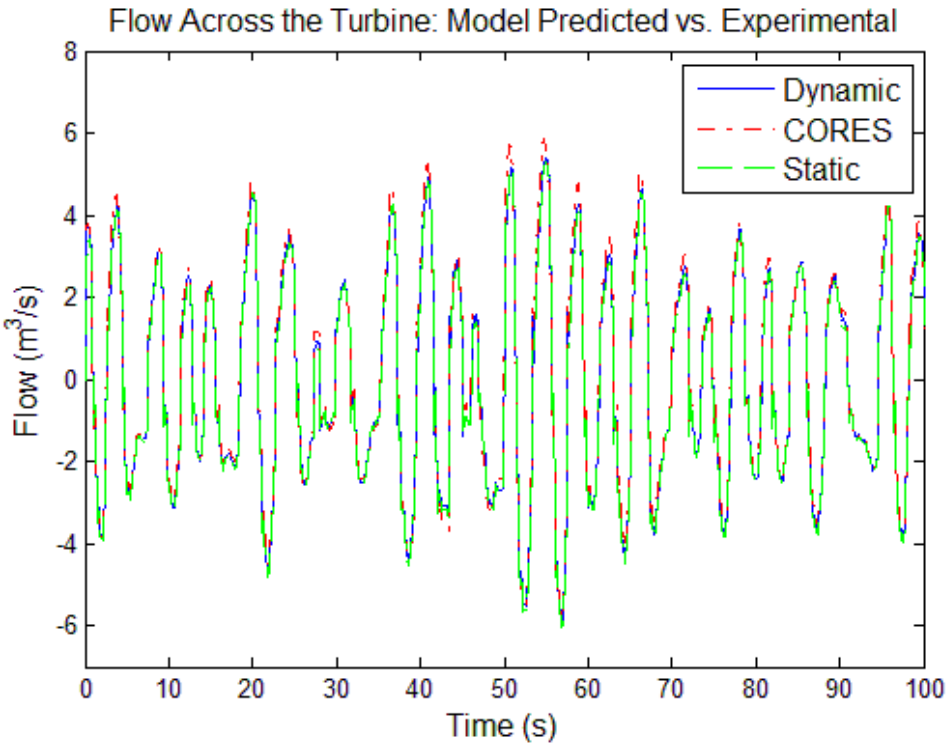

Fig. 3.9: Experimental, dynamically damped model, and statically damped model data for flow across the turbine for the data set where H_s=1.09 m and T_z =3.57 s.

3.2.2.4. STATISTICAL ANALYSIS OF STATIC AND DYNAMIC DAMPING

As the modelled results for chamber pressure had a greater variance, the data sets were presented using histogram plots for additional comparison. Fig. 3.10 is a histogram of the pressure measurement for the experimental, dynamically damped model, and statically damped model. The histograms show that the modelled data with dynamic damping applied much more closely aligned to the experimental data than did the statically damped model. In the statically damped model, the gauge pressure within the plenum chamber rarely reached beyond -2000 Pa or 2000 Pa, while there were over 2500 occurrences where the pressure was near 0 Pa. The histograms help to illustrate how closely the dynamically damped model adhered to the experimental results, as well as the gap between the pressures from the experimental data and the data generated by the statically damped model. The histogram also suggests that the inhalation model does not perform as well in accounting for higher changes in pressure as well as the exhalation model, and presents a challenge that could be investigated in future work.

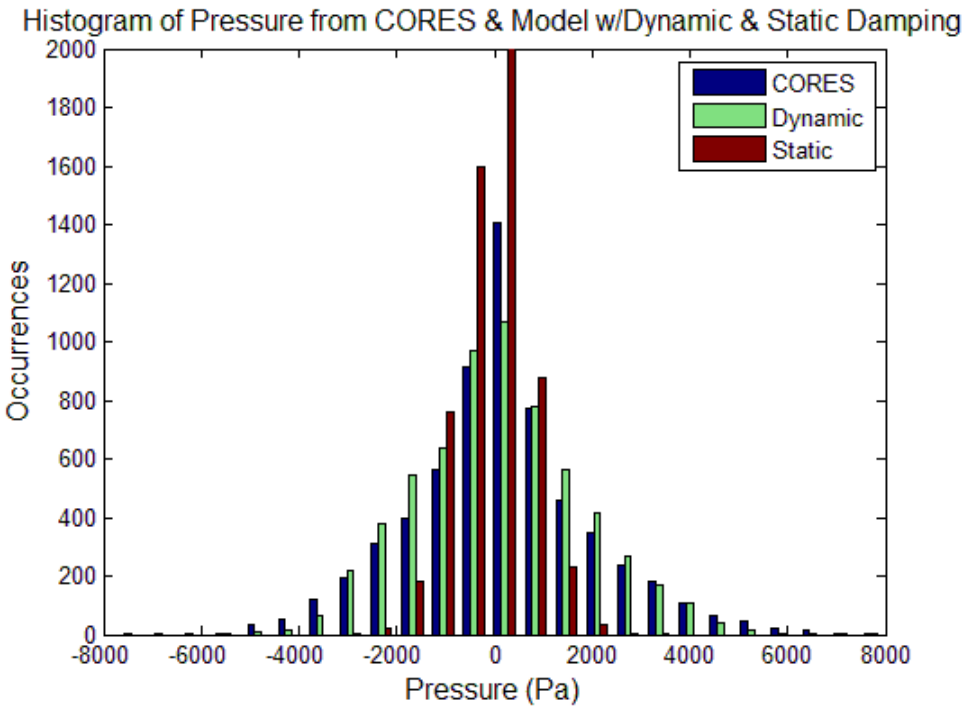

Fig. 3.10: Histogram of the experimental, dynamically damped model, and statically damped model data for chamber pressure for the data sets where H_s=1.09 m and $\underline{T_z}$ =3.57 s.

3.2.2.5. THERMODYNAMIC AND TURBINE MODEL COMBINED PERFORMANCE

Along with the investigation of the pressures and flows determined from the thermodynamic model simulations, the rotational velocity of the turbine and the electrical output of the generator from the thermodynamic model were also compared to the experimental results as was done when validating the turbine and controller model in the previous section. The results are displayed in Table 3.4. The changes in the deviation between model and experimental results when comparing Table 3.4 to Table 3.1 were attributed to applying the calculation of the IWS movement to the thermodynamic model to find the flow across the turbine.

As expected, the average electrical power output of the model was lower than the experimental results for 7 of the 8 data sets, with the data set where the calculated flows were higher than the actual flows. The results generated from the model with applied dynamic damping show electrical power output differences ranging from 6.3% to 16.8%, while the rotational speed ranges from 2.6% to 9.8%. Table 3.5 shows the average results for electrical power and turbine rotational velocity for the model when the static damping for the turbine was applied to the thermodynamic model. The

electrical power output proved to be a less accurate representation of the experimental data than the model that included the dynamic damping, with the differences ranging from 3.3% to 22.3%, while the rotational speed ranges from 5.0% to 11.8%.

Sea State		Electrical Power (W)			Rotational Velocity (rpm)		
H_s(m)	T_z(s)	Model	Actual	Error	Model	Actual	Error
1.22	3.96	1566.2	1447.6	-8.19%	346.7	361.6	4.11%
1.26	3.53	2539.1	3051.1	16.78%	585.4	603.5	3.00%
1.44	3.80	2150.4	2316.8	7.18%	374.0	396.3	5.63%
1.09	3.57	1887.9	2141.0	11.82%	524.0	537.8	2.57%
1.09	3.57	1842.0	2047.8	10.05%	474.4	494.8	4.13%
1.28	3.65	2091.3	2353.2	11.13%	348.2	386.1	9.82%
1.68	4.43	1817.2	1890.6	3.88%	289.0	305.8	5.48%
1.64	4.45	1841.7	1965.6	6.30%	286.3	313.1	8.57%

Table 3.4: Experimental and modelled electrical power and rotational velocity outputs averaged over the sample time from the model that includes the dynamic damping coefficient correction.

Sea State		Average Electrical Power (W)			Average Rotational Velocity (rpm)		
H_s(m)	T_z(s)	Model	Actual	Error	Model	Actual	Error
1.22	3.96	1494.9	1447.6	3.27%	338.7	361.6	6.33%
1.26	3.53	2371.9	3051.1	22.26%	573.2	603.5	5.02%
1.44	3.80	2051.3	2316.8	11.46%	364.6	396.3	7.99%
1.09	3.57	1749.6	2141.0	18.28%	507.6	537.8	5.62%
1.09	3.57	1723.8	2047.8	15.82%	461.9	494.8	6.65%
1.28	3.65	2027.5	2353.2	13.84%	343.8	386.1	10.97%
1.68	4.43	1733.6	1890.6	8.30%	269.7	305.8	11.80%
1.64	4.45	1893.7	1965.6	3.66%	282.7	313.1	9.72%

Table 3.5: Experimental and modelled electrical power and rotational velocity outputs averaged over the sample time of the model that includes the static damping coefficient.

For both the dynamically and statically damped models, the results using the available data produce higher variations than the tests which involve only the turbine model while using CORES flow data. The higher variations between the experimental and modelled data for the combined thermodynamic and turbine model versus the turbine model only validation was an expected result as more uncertainty was introduced into the model by using the calculated IWS values and because the differences found in the pressure and flow calculations were compounded by the deviations caused by the turbine model itself. The dynamically damped model

performed better at predicting the experimental results than the statically damped model, showing that adjusting the damping of the system and the resulting flow based on the changing speed of the turbine was the more effective strategy for modelling the thermodynamic OWC model.

Fig. 3.11 and Fig. 3.12 are sample-to-sample comparisons of experimental data against the turbine-only and turbine-thermodynamic models for the data set where H_s=1.22 m and T_z =3.96 s, and Fig. 3.13 and Fig. 3.14 are the same comparisons for the data set where H_s=1.09 m and T_z =3.57 s. It can be seen in these plots that the modelled data followed the experimental data well. These plots are taken over the same time periods as Fig. 3.2 through Fig. 3.6, and they are presented to illustrate that, while there are differences between all three data plots, the model and experimental outputs have very similar performance throughout.

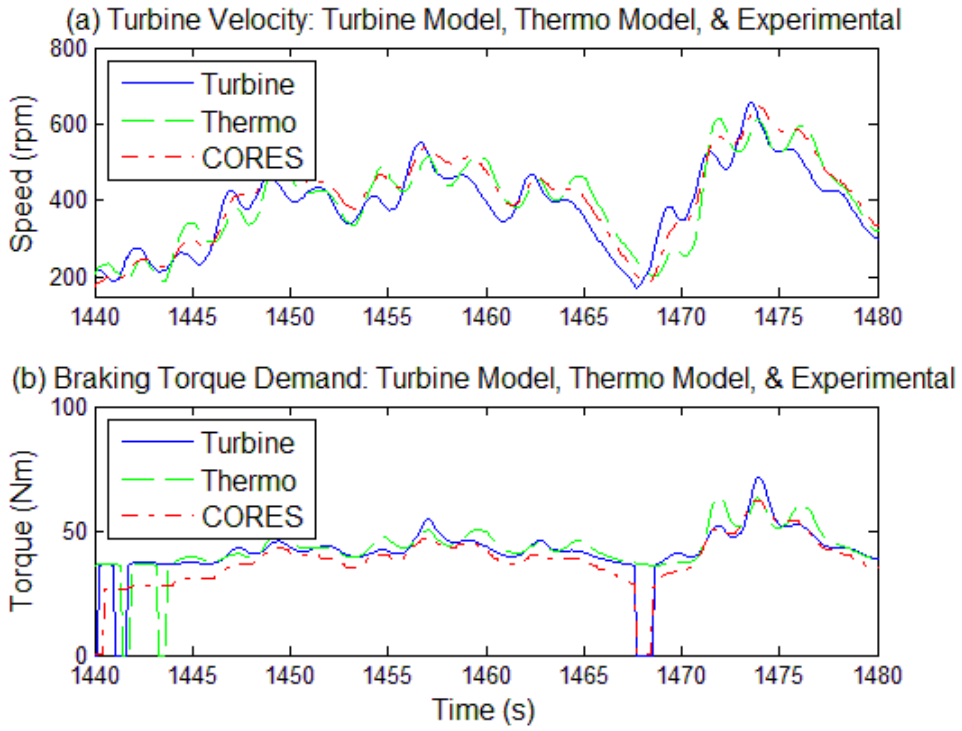

Fig. 3.11: Turbine model, thermodynamic model, and experimental data for the turbine rotational speed (a) and braking torque demand (b) for the data set where H_s=1.22 m and T_z =3.96 s.

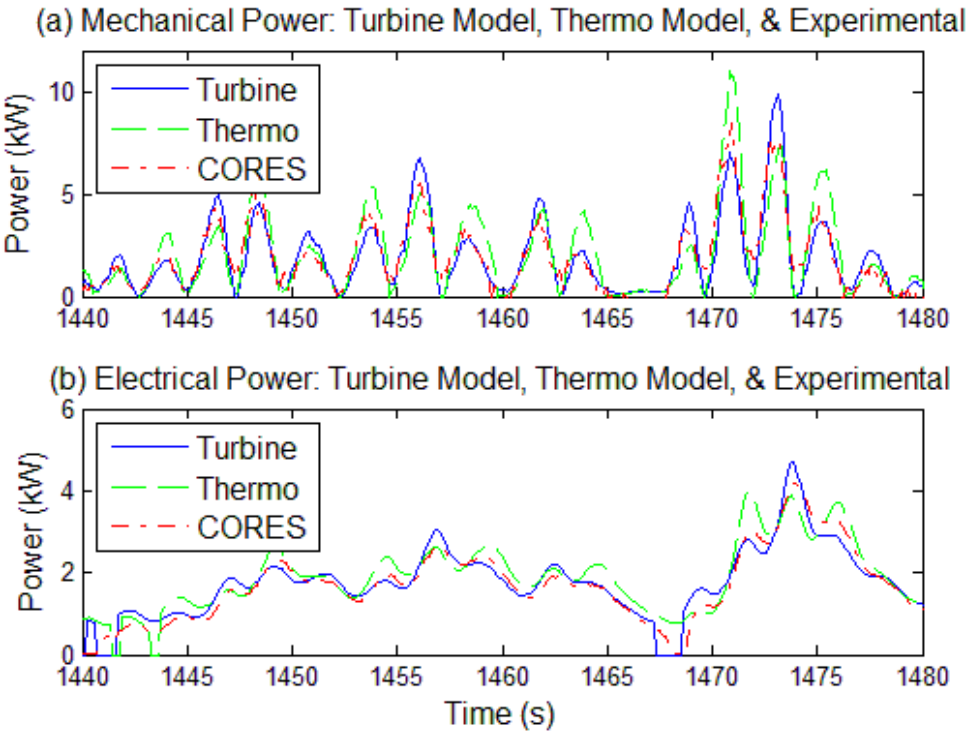

Fig. 3.12: Turbine model, thermodynamic model, and experimental data for the mechanical power output (a) and electrical power output (b) for the data set where H_s=1.22 m and T_z =3.96 s.

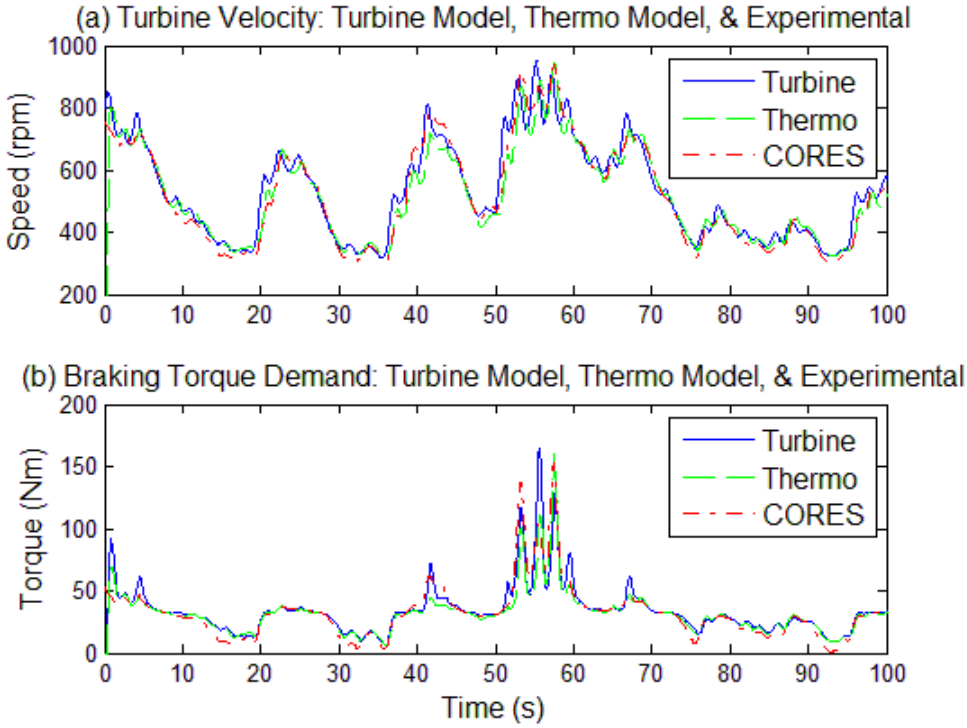

Fig. 3.13: Turbine model, thermodynamic model, and experimental data for the turbine rotational speed (a) and braking torque demand (b) for the data set where H_s=1.09 m and T_z =3.57 s.

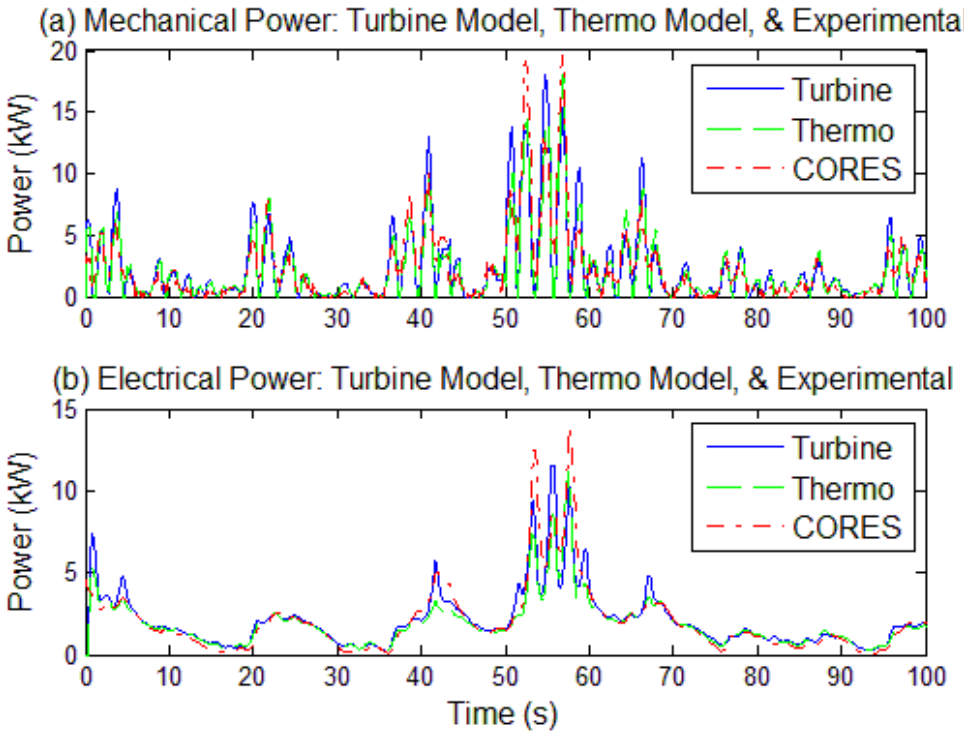

Fig. 3.14: Turbine model, thermodynamic model, and experimental data for the mechanical power output (a) and electrical power output (b) for the data set where H_s=1.09 m and T_z =3.57 s.

Overall, the thermodynamic model performed well when estimating the pressures and flows generated by the movement of the IWS, and the applied dynamic turbine damping had a significant, positive affect on the model accuracy. However, when coupled with the turbine model to estimate electrical power output, the results saw greater discrepancies between modelled and experimental data than were found during testing of the turbine-only model. By combining the thermodynamic and turbine models, the discrepancies between the turbine model and the experimental results were magnified by the inconsistencies introduced when applying the thermodynamic model derived flows in place of the experimentally determined flows. The results of this verification process show the importance of applying a dynamic turbine damping to the system to maximize model accuracy, particularly in chamber pressure estimation. The thermodynamic model performed well in modelling both the pressure in the plenum chamber and the flow across the turbine based on IWS motion, which led to the results of the turbine model being similar to those seen in the previous section, showing that the thermodynamic model can be used to predict device performance, and thus allowing the verification process to move on to attempting to validate the hydrodynamic model.

3.3. HYDRODYNAMIC MODEL

With the turbine and thermodynamic models both validated, the hydrodynamic model could be tested against the CORES data. Some inconsistencies in the model data results were introduced by both the turbine and thermodynamic models, and in this section, any increases in inconsistencies between the experimental and modelled data were to be investigated. However, validating the hydrodynamic model of the OWC by comparing it to the experimental data was more difficult. When verifying the turbine and thermodynamic models, experimental data arrays were available as inputs to the models, allowing for easy and accurate comparisons of model versus experimental data.

For the hydrodynamic model, only the summary statistics of the sea states analysed were available, so wave arrays were created with MATLAB using a Bretschneider spectrum to model the motion of the sea water surface in a predetermined sea state. The hydrodynamic model combined with the Bretschneider spectrum did not perform nearly as well as the turbine and thermodynamic models when compared to the experimental data. The modelled and experimental average mechanical power and electrical power outputs did not match well, and the variances over the different sea state conditions showed little correlation. The most consistent error in the results from the hydrodynamic model was that the average electrical power output from the model was higher than that of the experimental results and was typically between 20%-80% greater than the experimental output.

The source of the high electrical power outputs of the hydrodynamic model was traced to the increased flow rates across the turbine generated by the model, which were significantly higher than those observed experimentally. The flow rates associated with the IWS motion created by the hydrodynamic model reached up to 12 m^3s^{-1}. The maximum flow rates seen in the experimental data were approximately 7 m^3s^{-1}. At pressures over 5,000 Pa, a difference of 1 m^3s^{-1} in flow relates to a 5 kW difference in pneumatic power, so the higher flows in the model substantially affected the modelled power output.

The inconsistencies between the flows calculated in the hydrodynamic model and those recorded by the CORES project are likely to have multiple sources. A study of the spectral data at Arch Point from Section 7 in [59] found that taking the average of the spectra recorded over a month or longer shows good agreement with the Bretschneider spectrum. However, this agreement breaks down as time averaging

scales are reduced to durations of a single day or less. The longest continuous data set from the CORES deployment was less than two hours in duration, making it unlikely that the hydrodynamic model output would match the experimental data.

Additionally, the average spectrum at the Galway Bay test site does not match the common parametric functions used to approximate spectral data because the wave conditions at the site are influenced by both local wind conditions and swell conditions in the North Atlantic [109]. Fig. 3.15 presents individual and averaged spectra measured at the Galway Bay test site for a given sea state measured over a 12 month period, along with the Bretschneider spectrum under the same conditions. The peak frequency occurrence in the Bretschneider spectrum corresponds with a lull in frequency occurrence in the average spectrum, thus making the Bretschneider spectrum a poor representation of the sea conditions under which the CORES buoy operated. To properly evaluate the hydrodynamic model, months of operational data from an open ocean site similar to the SEAI Belmullet test site, where the average spectrum matches the Bretschneider spectrum, or the creation of a spectrum that matches that behaviour of the Galway Bay test site along with significantly more experimental data than was available from the CORES project would be required.

It is potentially possible to create a sea state spectrum, or a combination of spectra, that could be used to generate a wave data series that better represents the conditions observed in Galway Bay. Creating a sea state spectrum that can accurately approximate real conditions is a very difficult endeavour, and it was observed that short-term wave forecasting for the SEAI test site in Galway Bay is much more difficult than short-term wave forecasting in more open seas like those found at the Pico Island, meaning it would most likely be even more difficult to generate a Galway Bay spectrum than to do so for an open ocean site [110]. It is also possible to gather the spectral data from wave rider buoys and generate a wave series with the buoy data. However, creating a new spectrum or generate wave series from the wave rider buoy is beyond the scope of this thesis, but could be considered for future work. Without the ability to validate the hydrodynamic model using the experimental data from CORES, the accuracy of the hydrodynamic data was only supported based on the tank testing performed in [84].

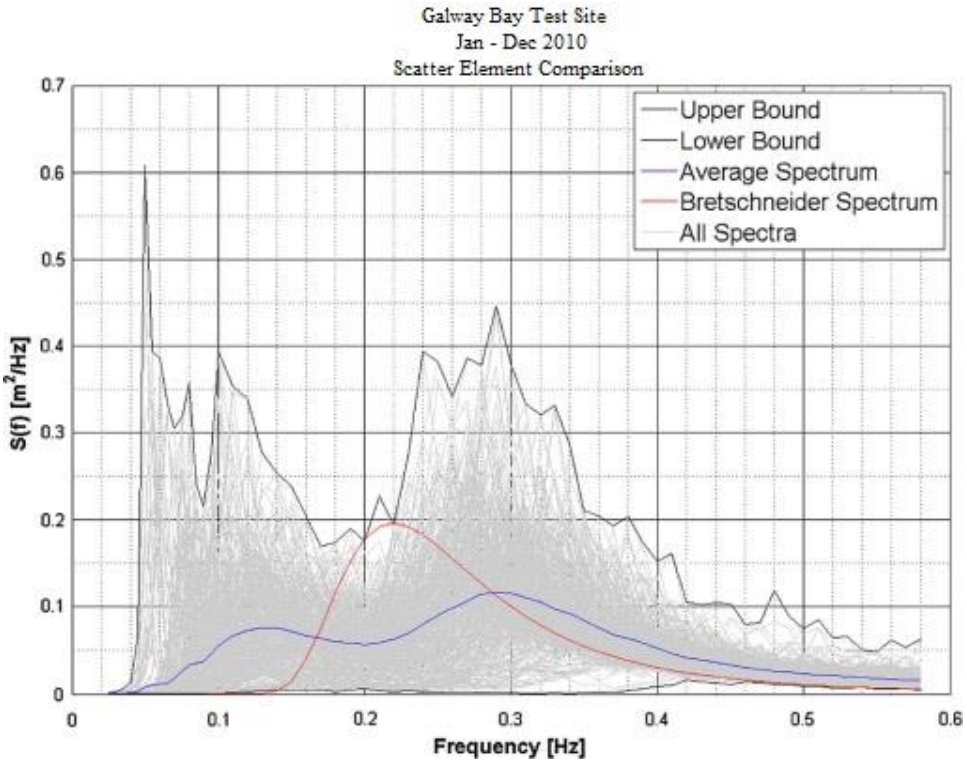

Fig. 3.15: Individual, averaged, and theoretical spectra within the ranges 0.625 m < H_s < 0.75 m and 3.0 s < T_z < 3.5 s for the Galway Bay test site [109].

3.4. INVESTIGATION OF EXPERIMENTAL DATA ANOMALIES

An unanticipated use for the model was discovered during the verification process, when the model data was being compared to the experimental data. As the turbine and control algorithm models were being tested using flow input from the experimental data, there appeared to be data corruption in the experimentally collected data where, in short bursts, it did not match the model predictions which were based on the measured flow. The model generally matched the experimental data well, as discussed in previous sections, and these small sections of seemingly bad data were cause for confusion and concern.

The inconsistencies were initially spotted when comparing the experimentally recorded rotational velocity of the turbine against the model predicted velocity. There were sections found where the model predicted an increase in the rotational velocity, but the experimental data showed that the rotational velocity remained comparatively constant. Fig. 3.16 shows an example of a data set with these inconsistencies.

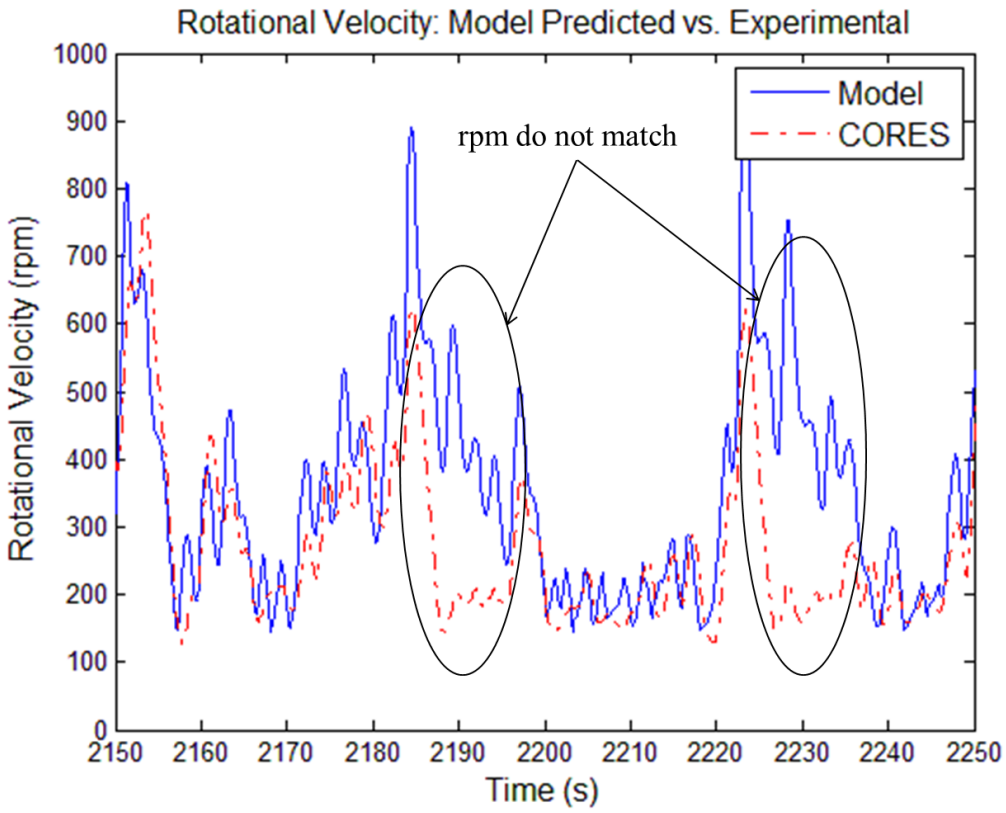

Fig. 3.16: Experimentally measured rotational velocity and model predicted velocity based on measured flow across the turbine.

As can be seen in Fig. 3.16, the rotational velocity recorded during the experiments appears to suddenly drop off and remain at a minimal level for a few seconds before changing to match the model predicted levels again. To first investigate this issue, the recorded flow across the turbine was compared to the recorded rotational velocity, as demonstrated in Fig. 3.17, to determine where the difference might originate.

Fig. 3.17 shows that pneumatic power was available to drive the turbine and increase the rotational velocity of the turbine and the electrical power of the turbine, but that the OWC did not respond as anticipated. Similar discrepancies were noted in several experimental tests, more often occurring in experiments conducted towards the end of the deployment. They had a significant impact on the model-experimental data comparisons, and produced numerical results that made it appear as though the model was a poor substitute for the experimental data. However, data collected from experiments, which did not include these problems, showed that the model performed well when compared to experimental data, and this led to the conclusion that the experimental data, not the modelled data, may be flawed.

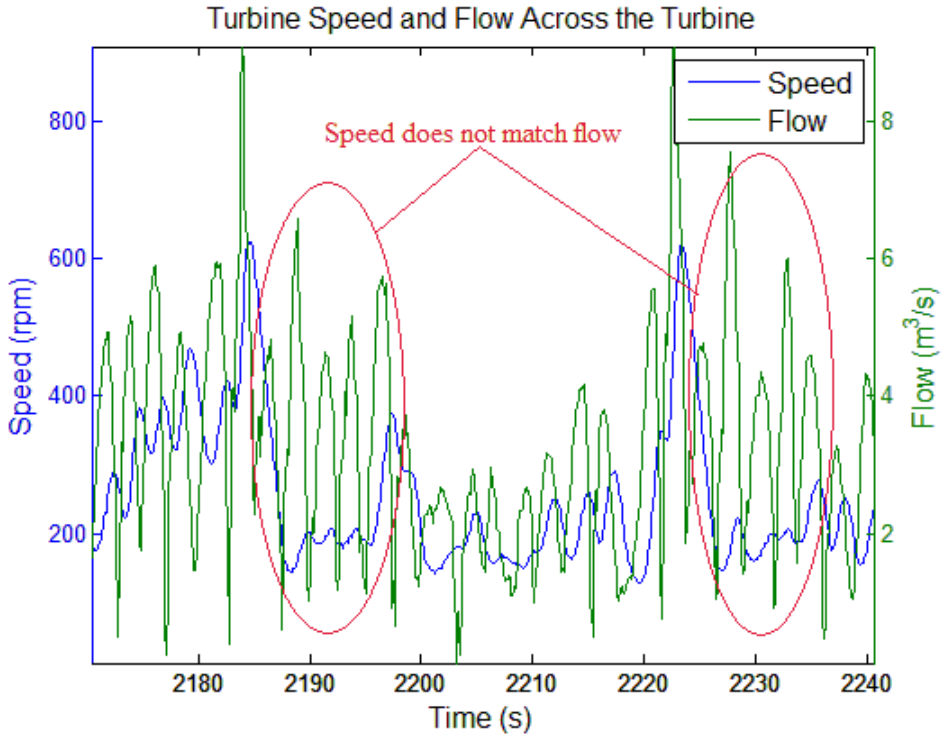

Fig. 3.17: Rotational velocity and flow across the turbine from the same data set as shown in Fig. 3.16. The red circles indicate areas where the turbine velocity did not increase despite the pressure of measured flow high enough to drive the turbine.

3.4.1. HYPOTHESIS: MECHANICAL BRAKE FAILURE

An initial hypothesis for the origin of experimental data corruption presumed that the problem could have been caused by the mechanical brake that was fitted to the turbine and generator to keep the system from overspeeding and to keep the turbine and generator from spinning when the PTO system was not engaged. A mechanical brake was sized and installed on the drive shaft to bring the turbine to a stop when it was spinning. However, an impulse turbine's highest generated torque value is when the turbine is at zero speed, and the brake was undersized for this condition. During periods of high seas when the system was not operating, the brake was engaged, yet the torque generated was able to overpower the mechanical brake and caused irreparable damage to the mechanical brake [36]. Evidence of the initial damage was recorded by a temperature sensor placed inside the nacelle turbine casing near the brake. When the turbine was able to overcome the braking force, it rotated the drive shaft and overheated the brake, distorting it and compromising its functionality. Fig. 3.18 shows the

temperature increase recorded by the resistance temperature detector (RTD) placed near the brake, as well as the speed of the turbine and the temperature readings recorded by the generator RTDs. At the time the data presented in Fig. 3.18 was collected, the mechanical brake was engaged to prevent the turbine from spinning, but due to the energy in the sea at the time, the torque generated by the turbine was enough to overcome the mechanical brake and cause the turbine to spin while the brake was engaged. The energy used to overcome the mechanical brake was transferred into heat energy during the failure, and the generated heat caused the irreparable damage.

The temperature sensors used to record the temperatures presented in Fig. 3.18 were placed near the brake in the nacelle of the generator but not on the brake itself, and the temperature values presented were that of the air around the brake and not its physical temperature. That RTD, along with a second RTD in the generator nacelle placed closer to the stators of the generator, helped to confirm that the heat generated within the turbine was due to the brake and not the generator. Fig. 3.18 also shows the speed of the turbine reaching upwards of 160 rpm when the brake was engaged. During normal operation, the stator temperatures rise much faster and to a much higher level than the temperature near the brake, which further confirms the rise in temperature shown in Fig. 3.18 was caused by the brake overheating. When the CORES OWC was decommissioned, the brake was physically inspected, and it was found that the brake pad had been reduced to dust and the cooling fan had melted off the drive shaft. Approximately 81 hours of possible generation testing was lost because of interference caused by the damaged brake, which behaved as if it was partially engaged at various times during testing [54].

While the indirect evidence appeared to suggest that the damage to the brake could have caused the turbine to unexpectedly slow down, it was difficult to find any direct evidence to support the hypothesis, and the random nature of the breakdowns between modelled and experimental data could not be easily explained away by blaming a melted, malfunctioning friction brake.

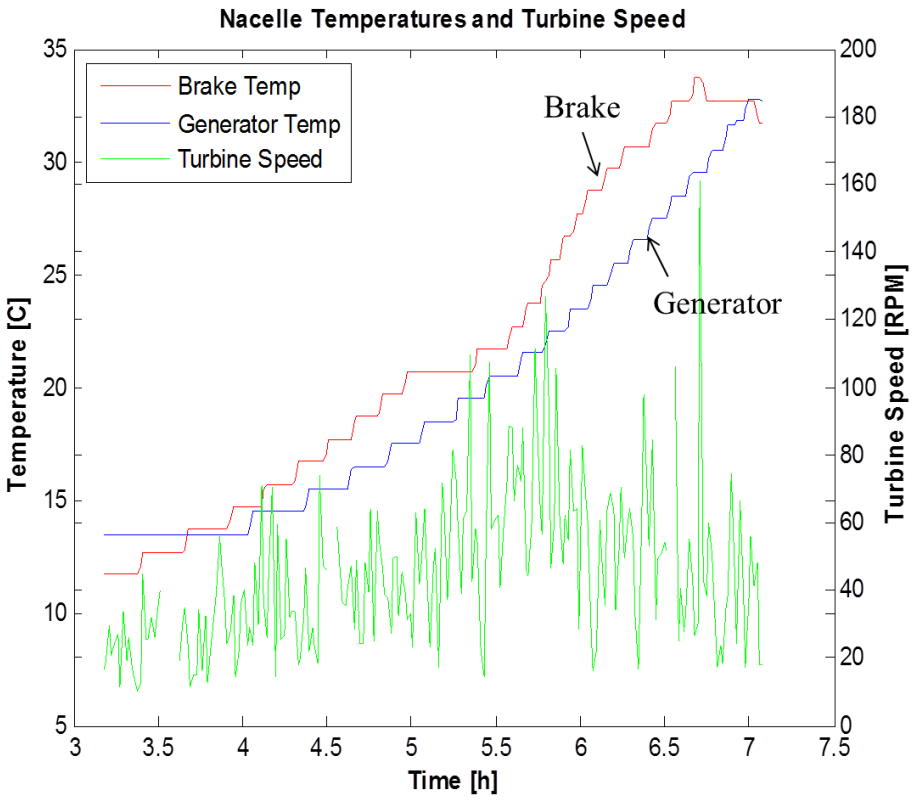

Fig. 3.18: Brake housing and generator stator temperatures and turbine rotational velocity during brake failure of the CORES OWC deployment.

3.4.2. HYPOTHESIS: MOVABLE GUIDE VANE FAILURE

Due to the lack of confidence in the initial hypothesis, a second hypothesis was investigated, where the focus was on the movable guide vanes. The guide vanes were designed to be used in two positions that were based on air flow direction. The flow direction was determined using the gauge pressure measured inside the plenum chamber, which was taken from a single pressure sensor. If the pressure was above zero, the guide vanes would be in one position, and if the pressure was below zero, they would be in the other. Changing the guide vane position took 0.6 s or six samples on average, so the system required an optimized control strategy to dictate where the guide vanes should be. The optimization was carried out using hysteresis bands with two pressure limits. The optimization found that while best average results were found with the limits set at 2 mbar and 2.5 mbar, the actual optimum values were dependent on each individual wave, so the controller was not fully optimized [95].

The positon of the guide vanes was looked at during operation, with the focus on changes in position, and position relative to measured plenum chamber pressure. It was found that when the experimental results were inconsistent with the model predicted results, as shown in Fig. 3.16, that the guide vanes were 180° out of phase with the chamber pressure. As soon as the guide vanes reset themselves and were again in phase with the measured chamber pressure, the turbine would immediately behave as predicted by the model data. Fig. 3.19 presents an example where the guide vanes were out of sync with the chamber pressure. The data are taken from the same sample period that was presented in Fig. 3.16 and Fig. 3.17.

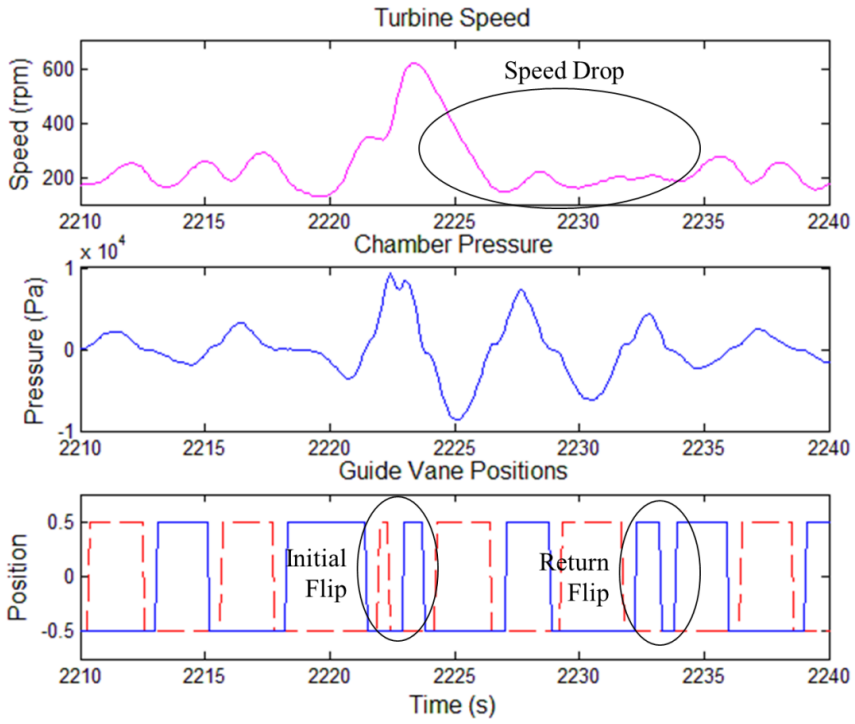

Fig. 3.19: Guide vane position relative to the plenum chamber pressure and the effect the guide vane position has on the rotational velocity of the turbine.

At approximately 2223 seconds into the sample, the guide vanes flip when they should not, which places them 180° out of phase with the pressure inside the chamber. They remain out of phase until approximately 2233 seconds, when the guide vanes reposition themselves back into phase with the chamber pressure. The top plot shows the rotational velocity of the turbine and it can clearly be seen that when the guide vanes are out of phase, the turbine velocity drops to a low value and remains there until the

guide vanes reorient themselves again. Once the guide vanes begin to behave correctly again, the turbine velocity increases as expected.

The condition where the guide vanes were out of phase with the pressure and therefore air flow happened several times over the course of an experimental data set. When the guide vanes were out of phase with the air flow, the polynomial equations used to mathematically model the turbine were no longer accurate representations of turbine performance. This compromised the validation of the model when directly comparing its performance to the experimental data. To mitigate this problem, the sections of data where the guide vanes were found to be out of phase were completely removed from the experimental data sets before the data sets were used within the model. When a section of data is removed, the removed section begins and ends during periods of low power production. The remaining data is combined so that the gap in data that the model encounters appears as seamless as possible. Fig. 3.20 shows a section of data before and after the compromised region of data was removed.

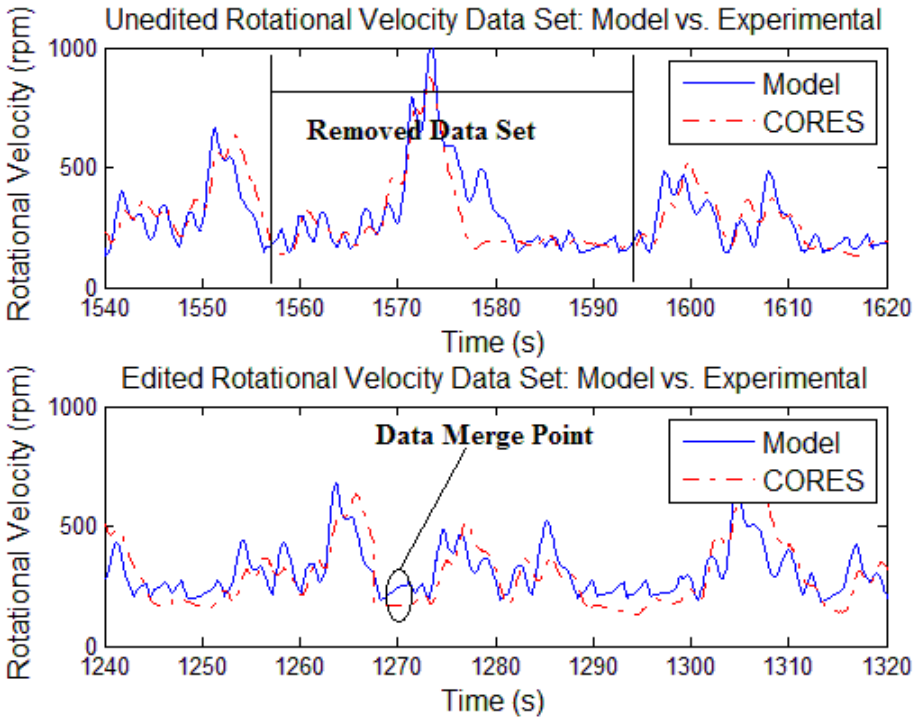

Fig. 3.20: Example of the edits performed on the experimentally collected data to remove the data compromised by the malfunctioning guide vanes.

These edits allowed for the experimental data to be used to verify the mathematical models presented in this the chapter. While ideally the model should be verified with data that did not require editing, data collected from experiments conducted in hostile, uncontrolled environments like the open sea are subject to any number of difficulties like the one presented that cannot be spotted nor corrected for during experiments. Editing the data in this manner causes discontinuity in large dynamic data sets, and it is not generally recommended during data analysis. However, reconducting the experiments was not an option, and in order to further evaluate the model accuracy for average power output and device behaviour over long periods of time, it was deemed that editing the data was the best option available for this particular comparison. The sample-to-sample comparisons were used to strengthen the argument of model accuracy where data editing has weakened it. While this was less than ideal, the problem highlighted the positive application of model-based fault detection by showing a clear example of how the model was used as a diagnostic tool to help troubleshoot a performance related problem of a deployed device.

3.5. CONCLUSION

The combined model was shown to produce accurate representations of the OWC system as a whole. The turbine modelling showed excellent agreement with experimental results of open sea testing, the generator and turbine controllers were accurately and effectively tested, and the thermodynamic modelling of air flow and pressure was accurate. Turbine speed feedback was used to adjust the pneumatic damping of the system. However, the hydrodynamic modelling based on artificially generated Bretschneider wave spectra and WAMIT RAO could not be verified due to the experimental data available.

The model presented in this paper could be used for testing, evaluating, and troubleshooting various components of an OWC. It allowed for the development and testing of control algorithms to help further improve the efficiency of OWCs without the need for full deployment. The model could also be used to predict device behaviour prior to deployment, minimizing the adjustment time required to get a device operating at full potential. Following deployment, the model could serve as a diagnostic tool to help pinpoint device failure points prior to maintenance trips, which would allow for more accurate planning of scheduled and unscheduled repairs. There is still a significant amount of work that needs to be carried out, particularly in understanding the

hydrodynamics of an OWC and the interaction between the non-static turbine damping and hydrodynamic response of a free floating device. Numerical modelling of an OWC can be used in a variety of ways to tests controllers, turbines, and overall system performance, but it cannot be considered a full substitute for open sea deployment and experimentation. However, based on the data available, this model should be a useful addition to device development and maintenance. Having shown promise in all the mentioned areas, the model developed in this chapter will be used to test and develop control strategies for a full scale device with a fixed guide vane impulse turbine that was designed and testing specifically for this thesis and this will be presented in the following chapter.

4. FULL SCALE IMPULSE TURBINE

With the 1:4 scale model validations complete, a full scale numerical model was developed in an effort to test control strategies for the BBDB OWC. The majority of the changes needed to create the full scale model were simply a matter of scaling up the device dimensions to match the selected deployment site. However, the turbine tested in Chapter 3 contained IP and could not be scaled up as the turbine design specifics were not available. Therefore, a new turbine had to be designed to complete the full size model, so the next step in the work performed in this thesis was the development and characterisation of an impulse turbine model that could be used in the 1:1 scale model.

The impulse turbine selected for application in the numerical model was a fixed guide vanes impulse turbine because it minimises complexity and mechanical failure points for the OWC. The impulse turbine was based on the turbine constructed by Setoguchi and published in numerous journals, eg: [41]. In designing the impulse turbine for the BBDB OWC, the only design variables were turbine diameter and operating rotational velocity, which are not independent of each other. The turbine diameter had to be sized to match the BBDB OWC and the selected theoretical deployment site. As the buoy dimensions are dictated by the wave conditions of the deployment site, the deployment site had to be selected, and the OWC dimensions then were scaled to match the expected wave conditions. From there, an average of the expected flows generated by the OWC was approximated, and the turbine diameter was designed around the expected flow.

After the turbine diameter was determined, the dimensions of the turbine blades and guide vanes were resolved by applying the design parameters presented in Section 2.3, and the turbine was drafted using SolidWorks Computer-Aided Design (CAD) software. As a full scale turbine could not be physically produced or tested, Computational Fluid Dynamic (CFD) modelling using SolidWorks Flow Simulation was substituted for laboratory testing to characterise the turbine. The CFD results were compared to the published laboratory testing results of a 300 mm turbine to verify the accuracy of the CFD modelling. The data were generated from CFD simulations and used to create numerical models for the turbine that could be used with the model in Chapter 5 to test turbine performance, energy storage capacity, and control algorithms.

4.1. SITE SPECIFIC DESIGN PARAMETERS

To maximise the efficiency of an OWC, the turbine should be designed to match the optimal damping of the OWC when operating in sea states that produce the most total

power over a 12-month period. Designing the turbine this way can lead to lower power conversion efficiencies in the more energetic sea conditions, but it will allow greater power generation in more common sea conditions and should provide more power over the course of a full year. To begin the design selection process, the deployment site must first be chosen, and a BBDB must be designed to match the selected site.

The deployment site chosen for the turbine and buoy design for this project is the location of the previously deployed M1 data buoy in the Atlantic Ocean off the Galway coast in the west of Ireland (53°7.6'N 11°12'W) [111]. This site was selected because it is very energetic and has ample historical summary statistics data available for the site through the Irish Marine Institute, which include wave periods and significant wave heights. The historical data available can be used to recreate real sea conditions for more realistic model testing. The site has also been assessed for energy availability and device deployment in prior publications, including [84], where a BBDB was designed to match the site conditions. As a BBDB OWC was already configured to best match the expected conditions for the site chosen for the study, the turbine was designed to match the existing buoy and the historical site conditions.

4.1.1. BBDB Design and Performance

Before the turbine can be designed, the BBDB performance must be characterised so that the turbine can be designed to match the OWC. The OWC designed for the M1 site was based on previous tank testing and numerical assessments that were carried out in [112, 113, 114] to help optimise power absorption. The original device tank tested in [113] had a duct length, l_d, of ~1 m, had a peak resonance period of 1.1 s, and the tank testing was carried out in 1:50 scale. Scaled to 1:1 using the Froude scaling method, the duct length of the BBDB was 50 m and the peak resonance period was 8 s, which matches the peak period of the North Atlantic Ocean. Fig. 4.1 illustrates the design dimensions of the BBDB. The ratio of duct length, l_d, and draft height, h_d, for a BBDB with a peak resonance period of 8 s, is $l_d/h_d = 4.3$ [84]. The rest of the BBDB design process depends on several aspect and dimensional ratios. The bow plate, which faces the oncoming waves, should be a square such that the width, w, is equal to the plenum chamber height, h_p, while the ratio between the draft height, h_d, and h_p, and by extension the bow plate width, w, is $h_d/h_p = 0.5$. The ratio between the bow plate width, w, and plenum chamber length, l_p, is $w/l_p = 3$.

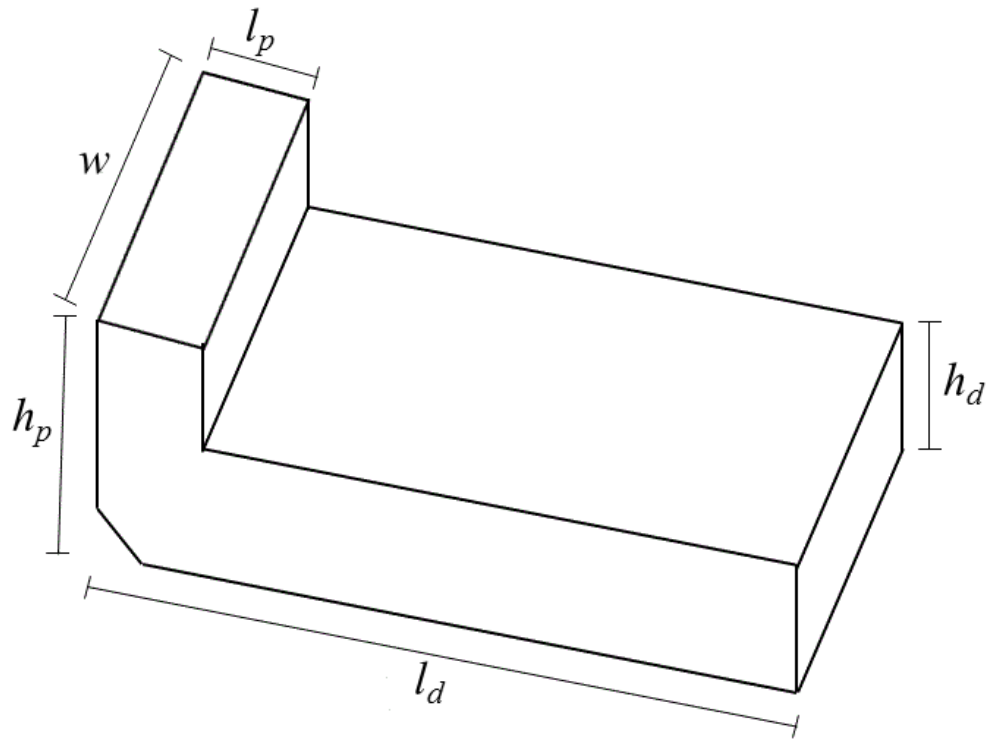

Fig. 4.1: BBDB design measurements: where width is w, draft length is l_d, draft height is h_d, plenum height is h_p and plenum length is l_p.

Using the previous assessments as a base point, the BBDB found to best match the conditions at the M1 buoy site had a draft length, l_d, of 52 m, a bow plate width, w, and height, h_p, of 24 m, a draft height, h_d, of 12 m, and a plenum chamber length, l_p, of 8 m [84]. Allowing for structural support walls within the chamber, the area of the Internal Water Surface (IWS) is estimated to be approximately 147 m^2. This value will be used for calculating flow based on the movement of the IWS, and these flow calculations are instrumental for designing a turbine to properly match the OWC.

After the physical dimensions of the buoy were determined, hydrodynamic numerical modelling was carried out on the BBDB design to determine the RAO of the surge, heave, pitch, and the movement of the IWS of the buoy. The hydrodynamic modelling was performed in [84] using linearised frequency domain numerical modelling using the industry standard commercial code WAMIT. Fig. 4.2 is a plot of the IWS RAO, which can be used to determine the average flows generated by the OWC during operation in known sea conditions.

The RAO for the IWS is a wave amplitude multiplier based on the hydrodynamic behaviour of the BBDB in a singular sinusoidal wave period, and it can be used to find the motion of the IWS from the motion of the waves acting on the device. For example, if the waves acting on the BBDB have a period of 5 s and amplitude of 1 m, the IWS movement will have an amplitude of ~0.2 m, or if the wave period is 10 s and amplitude

of 1 m, the IWS movement will have an amplitude of ~1.2 m. The data plotted in Fig. 4.2 can be used in the hydrodynamic section of the model presented in Chapter 3. It should be noted that the design of the BBDB for the M1 site chosen for this thesis was carried out in the same way as the design for the BBDB deployed at the CORES site, with the only difference between them being their size, which was based on the peak period of the deployment site. This leads to the RAO plots having similar shapes. When compared to Fig. 2.2, which represents the 1:4 BBDB OWC, the RAO in Fig. 4.2 has its peak at a longer period, but the magnitude of the motion response is the same.

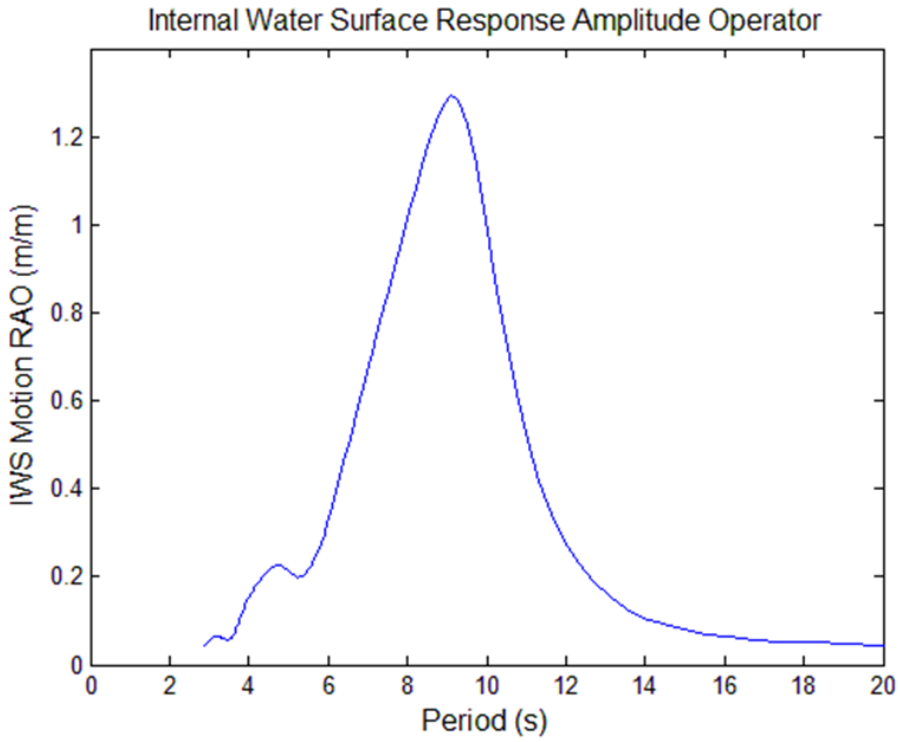

Fig. 4.2: RAO for the IWS of the OWC designed for the M1 site, derived from WAMIT [84].

4.1.2. TURBINE MATCHING

The BBDB design is driven by the expected conditions at the chosen deployment site, and it has a direct effect on the design of the turbine. Matching the turbine to the BBDB and the deployment site is an important part of the OWC design process. Similar to the hull design, the turbine needs to be matched to the wave conditions at the deployment site with the intention of extracting the maximum amount of power over a 12-month period. To help determine the turbine size, the sea conditions that will have the most power available during a 12-month period have to be identified. This was achieved

based on 12 months of summary statistics for the site, and wave power calculations presented in [57].

As discussed in Chapter 3, the Bretschneider spectrum did not well represent the conditions in Galway Bay, but the Bretschneider spectrum is a good representation of the wave conditions in the North Atlantic off the west coast of Ireland [59]. As the model testing will be based a North Atlantic open water deployment site, the calculations used to estimate the energy available at the selected deployment site were performed based on the Bretschneider spectrum. The power calculations are based on power per unit width and written in (4.1):

$$P_w = \rho_w g \int C_g(f) S(f) df, \tag{4.1}$$

where ρ_w is the density of sea water in kg·m^{-3}, g is the acceleration due to gravity in m·s^{-2}, $C_g(f)$ is the group velocity of the waves in m·s^{-1}, $S(f)$ is the spectral density of each frequency component of the wave spectrum in m^2·Hz^{-1}, and df is the frequency in Hz. For the North Atlantic, this equation can be rewritten based on the site summary statistics using (4.2):

$$P_w = 0.59 H_s^2 T_z, \tag{4.2}$$

where P_w is the average power in W·m^{-1}, H_s is the significant wave height in m, and T_z is the zero-crossing period in s [57].

The summary statistics from the M1 buoy for the 12-month period from January-December 2005 were collected and used to find the total power available for the year and the percentage of the total power available in all recorded sea state conditions. Fig. 4.3 is the scatter plot of the percentage energy contribution based on the zero-crossing period, T_z, from the data collected.

In Fig. 4.3, the numbers inside the boxes represent the percentage of total energy available at a given period, T_z, and significant wave height, H_s, for the 12-month period from January-December 2005. The data collected shows that over 20% of the available energy contribution for 2005 was found in sea conditions with zero-crossing periods between 6.5 s and 8.5 s with significant wave heights of between 2.5 m and 5.5 m. The design conditions for the turbine were selected to match the BBDB IWS response as closely as possible within the parameters of the sea states where the majority of the energy is available. The design point sea state was selected using the midpoint period

and significant wave heights, where the period, T_z, is 7.5 s and the significant wave height, H_s, is 4.0 m.

The dimensions of the plenum chamber of the OWC and the RAO presented in Fig. 4.2 were used along with the summary statistics presented to find the expected average flow across the turbine in the sea conditions which provide the most energy annually. For simplicity, the waveform used to calculate the air flow generated by the motion of the IWS was based on a sinusoidal wave with a period and amplitude based on the chosen sea conditions. The formulae used to calculate the flow are shown in (4.3) through (4.5):

$$T_p = 1.4T_z, \tag{4.3}$$

$$h_i = H_s f(T_p), \tag{4.4}$$

$$Q_c = A_C \frac{2h_i}{T_p}, \tag{4.5}$$

where T_p is the peak period found in a Bretschneider wave spectrum, h_i is the significant wave height within the air chamber, $f(T_p)$ is the result of applying the RAO graph from Fig. 4.2 to the peak period, Q_c is the flow at the design point, and A_C is the area of the IWS.

When applying the design point period of 7.5 s and significant wave height of 4.0 m, the amplitude response of the IWS is found to be approximately 0.74 m/m, meaning that at the given period, the motion of the IWS versus the amplitude of the waves acting on the buoy is a ratio of 0.74. Therefore, if the significant wave height is 4.0 m, the motion of the IWS of the OWC is 2.96 m, and with a peak period of 10.5 s, the value of Q_d was found to be approximately 82.9 $m^3 \cdot s^{-1}$.

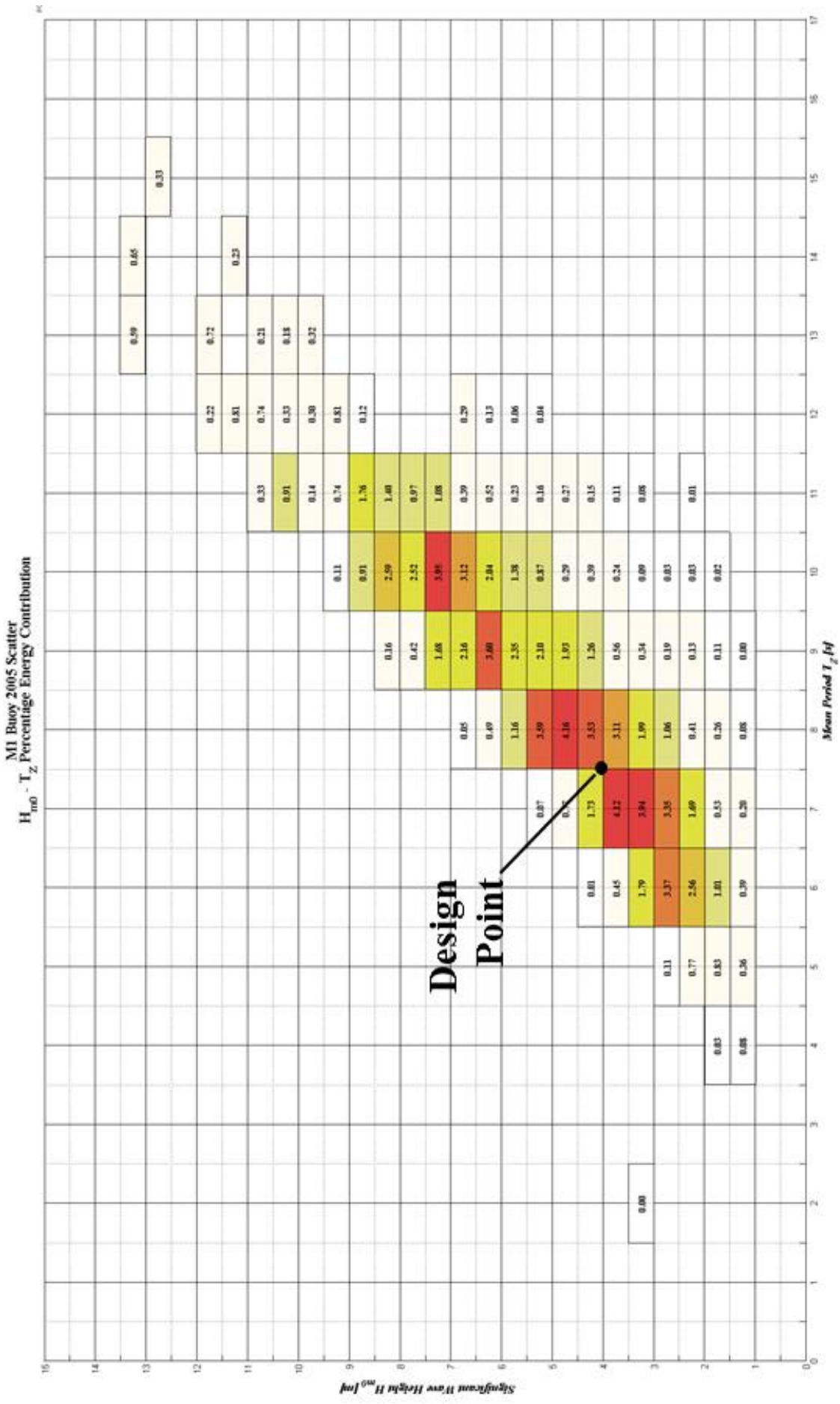

Fig. 4.3: Percentage energy contribution scatter plot from the M1 buoy for 2005.

The goal of the turbine design was to maximise device efficiency at the flow value given above. To achieve this, the flow coefficient, ϕ, of the turbine at Q_d was selected to be a value of approximately 1.25, which represents a flow coefficient with a high conversion efficiency that is far beyond the flow coefficient of 0.75 where below this value the conversion efficiency quickly drops towards zero. During the design phase, the flow coefficient was calculated using (4.6):

$$\phi = \frac{v_a}{U_R} = \frac{Q_d}{\omega D^3}\left\{\frac{16}{\pi(1+\xi)^2(1-\xi)}\right\}, \tag{4.6}$$

where v_a is the air speed velocity in m·s^{-1} at mid blade, U_R is the mid blade linear velocity in m·s^{-1}, ω is the rotational velocity in a rads·s^{-1}, D is the turbine diameter in m, and ξ is the hub-to-tip ratio, which is 0.7 for the impulse turbine being designed. Equation (4.6) is rewritten:

$$D = \sqrt[3]{\frac{Q_d}{\omega\phi}\left\{\frac{16}{\pi(1+\xi)^2(1-\xi)}\right\}}, \tag{4.7}$$

where ϕ is the flow coefficient, v_a is the air speed velocity in m·s^{-1} at mid blade, U_R is the mid blade linear velocity in m·s^{-1}, ω is the rotational velocity in a rads·s^{-1}, D is the turbine diameter in m, and ξ is the hub-to-tip ratio, which is 0.7 for the impulse turbine being designed.

The designed flow coefficient was selected to be a value of 1.25 because it represented an expected conversion efficiency of approximately 38%, which is near the maximum efficiency expected from an impulse turbine with fixed guide vanes based on experimental results [43]. Due to the sharp drop in efficiency of the impulse turbine at low flow coefficients, the maximum efficiency point was not selected. This allows the turbine to have effective power take off at lower flows and should lead to better overall conversion. When (4.9) and (4.10) are applied to the turbine design parameters, the optimum diameter was found to be 2.35 m.

The next step in the design process is to find the expected damping of the turbine under the conditions presented to make sure that it matches the optimal damping of the system, which is the previously presented value of 66 Pa·s·m^{-3}. The expected damping of the turbine is found from equations (4.8) through (4.10).

$$C_a = \Delta p Q_d / \{\rho_a (v_a^2 + U_R^2) b l_r z v_a / 2\} \quad (4.8)$$

$$\Delta p = C_a \{\rho_a (v_a^2 + U_R^2) b l_r z v_a / 2\} / Q_d \quad (4.9)$$

$$\kappa = C_a \{\rho_a (v_a^2 + U_R^2) b l_r z v_a\} / 2 Q_d^2, \quad (4.10)$$

where C_a is the input power coefficient, ρ_a is the air density in $kg^3 \cdot m^{-3}$, b is the blade height in m, l_r is the blade chord length in m, z is the number of blades, r_R is the turbine mean radius in m, and κ is the damping value.

When calculations (4.8) through (4.10) were used for the turbine with a diameter of 2.35 m and a rotational velocity of 30 $rads \cdot s^{-1}$, the damping value of the turbine was found to be 96 $Pa \cdot s \cdot m^{-3}$, which is approximately 50% greater than the optimal system damping. Because of the significant difference in actual and designed damping, the design parameter of 2.35 m diameter was rejected, and a new design with a larger diameter was investigated because a larger turbine would have lower damping at the same flow velocity. The larger turbine will also have a lower operating rotational velocity, which will also lower the turbine damping. The new turbine design point diameter was selected to be 2.5 m, and the new matching rotational velocity for the turbine was 24 $rads \cdot s^{-1}$, which represents a flow coefficient of approximately 1.3. The difference in efficiency between a flow coefficient of 1.25 and 1.3 is less than 0.5% and the lower rotational velocity will lower the damping of the turbine during operation.

The new values for the turbine were inserted into (4.8) through (4.10), where the damping of the 2.5 m turbine was found to be 76 $Pa \cdot s \cdot m^{-3}$. The larger and slower turbine shows a much closer match to the optimal damping of the OWC. The turbine design points for this project then will be a diameter of 2.5 m with an operational design speed of 24 $rad \cdot s^{-1}$. The turbine model was then drawn in SolidWorks, simulated, and characterised with these selected values dictating the full design and characterisation testing.

4.2. BUILDING THE TURBINE IN SOLIDWORKS

With the build ratios known and diameter of the turbine selected, the turbine was drawn in SolidWorks CAD software and tested using Computational Fluid Dynamics (CFD). The turbine was drawn in sections and then assembled to be tested with Flow Simulation, which is the CFD engine available within SolidWorks. The sections of the turbine were built independently and include the turbine hub, the upstream and downstream guide vanes, the nose cones, and the pipe in which the turbine resides. The

turbine was derived from the same design rules used for the 300 mm turbine studied in [39, 41, 43, 52, 94, 101, 102, 103, 105]. This was accomplished using the ratios identified in Section 2.3.

4.2.1. TURBINE HUB

The turbine hub and blades were the first elements of the turbine to be designed. Using the established ratios, Table 4.1 was created to determine the design parameters for the 2.5 m turbine hub and blade dimensions.

Using the information gathered in Table 4.1, the turbine hub was drawn and built in SolidWorks, and the final design is presented in Fig. 4.4. With the chord length of the blade set at 445.1 mm, the width of the base of the turbine hub was set to be 460 mm, so that the hub of the turbine could support the blades comfortably.

Parameter	300 mm Design (mm)	2.5 m Design (mm)	Ratio	
Turbine Radius (r_t)	150	1250.0	N/A	
Hub Radius (r_h)	105	875.0	r_h/r_t	0.7
Blade Height (b)	45.0	375.0	b/r_t	0.3
Blade Pitch (S_r)	26.7	222.5	$2\pi\, r_R/30$	0.21
Blade Chord Length (l_r)	54.0	445.1	l_r/S_r	2.00
Pressure Side Cup Radius (r_r)	30.2	249.2	r_r/l_r	0.56
Suction side semi-minor axis (e)	41.4	341.9	e/r_r	1.37
Suction side semi-major axis (a)	125.8	1039.3	a/e	3.04

Table 4.1: The dimensions of the 2.5 m diameter impulse turbine hub and blades calculated using the design ratios based on the original 300 mm diameter turbine.

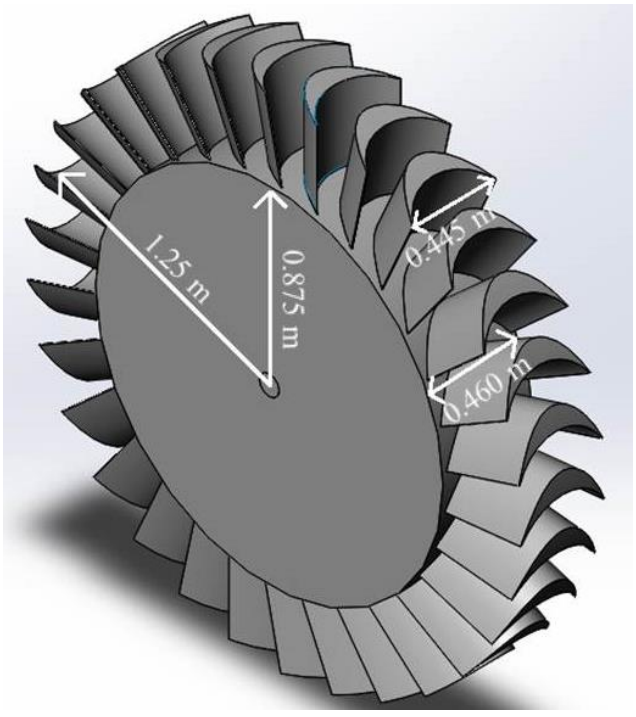

Fig. 4.4: 2.5 m diameter impulse turbine hub and blades drafted using SolidWorks.

4.2.2. GUIDE VANE HUBS

Following the turbine hub and blades, the upstream and downstream guide vanes and guide vane hub were designed. The ratios established in previous sections were used to determine the dimensions of the guide vanes and the guide vane hubs. Table 4.2 shows the design parameters for the 2.5 m guide vanes.

Parameter	300 mm Design (mm)	2.5 m Design (mm)	Ratio	
Guide Vane Pitch (S_g)	69.2	256.7	S_g/S_r	1.15
Chord Length (l_g)	70.0	577.2	l_g/l_r	1.30
Gap (G)	20.0	164.7	G/l_r	0.37
Straight Part of Guide Vane (l_s)	34.8	286.9	l_s/l_g	0.50
Curve Radius (R_a)	37.2	306.5	R_a/l_g	0.53

Table 4.2: The dimensions of the 2.5 m diameter impulse turbine guide vanes calculated using the design ratios based on Setoguchi's 300 mm turbine.

With the information from Table 4.2, both the upstream and downstream guide vane hubs were built in SolidWorks. The final designs are presented in Fig. 4.5 (a) and (b), where both upstream and downstream guide vane hubs can be seen. To maintain the optimum gap between the guide vanes and the turbine blades, *G*, the length of the guide vane hub and the placement of the guide vanes were calculated by considering the width of the turbine hub and the chord length of the turbine blades. The distance between the edge of the turbine blades and the edge of the turbine hub was 7.45 mm, while the calculated gap between the guide vanes and the blades was 164.7 mm. In Fig. 4.5 (b), the distance between the vanes and the turbine side edge of the hub is evident, and the distance was set to 157.25 mm thus maintaining the gap of 164.7 mm between the guide vanes and the turbine blades.

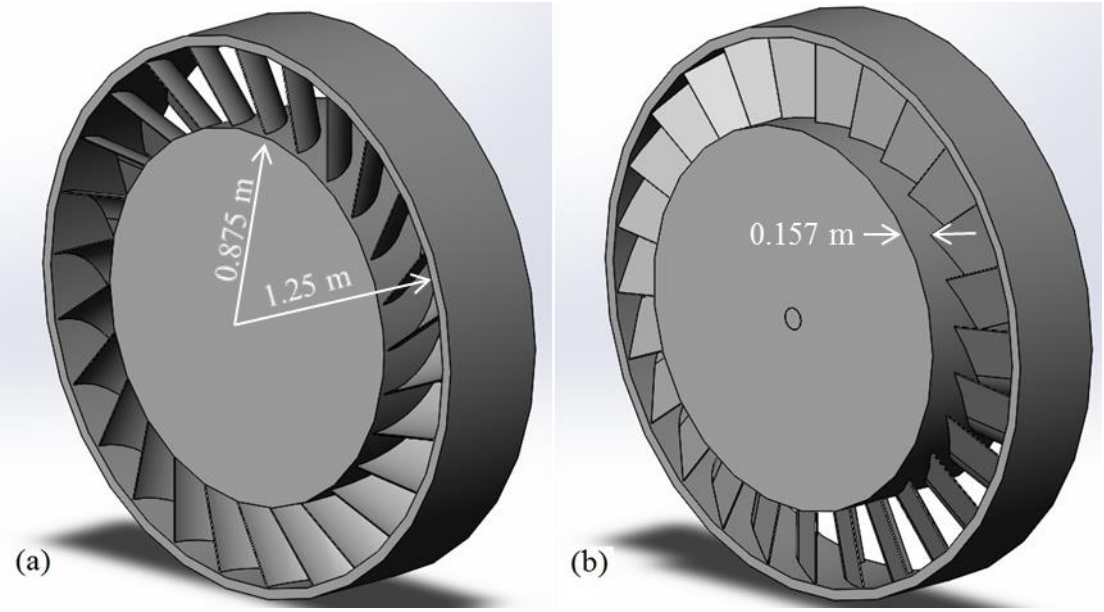

Fig. 4.5: (a) upstream and (b) downstream guide vanes for the 2.5 m diameter impulse turbine drafted using SolidWorks.

4.3. COMPUTATIONAL FLUID DYNAMICS PREPARATION

It was not possible to build a physical 2.5 m turbine and test it experimentally to determine the turbine performance characteristics for use in the mathematical model presented in Chapter 3. Instead, Computational Fluid Dynamics (CFD) simulations were performed on the turbine model to ascertain the performance characteristics, which would allow the turbine to be used in the numerical model presented in Chapter 3.

CFD has been applied in many studies of impulse turbine performance both alongside and in lieu of experimental testing, including in [104, 106, 115]. The main turbine characteristics needed to model the impulse turbines for this project were the pressure drop across the turbine and the mechanical power output at expected flow coefficients for various rotational velocities. The characteristics found from the CFD simulations were compared to the results published in [41, 43, 101, 102, 103, 39, 52, 94, 105] which were from laboratory experiments carried out using a 300 mm diameter turbine, to confirm that the CFD simulations accurately represent the experimentally observed behaviour of the turbine.

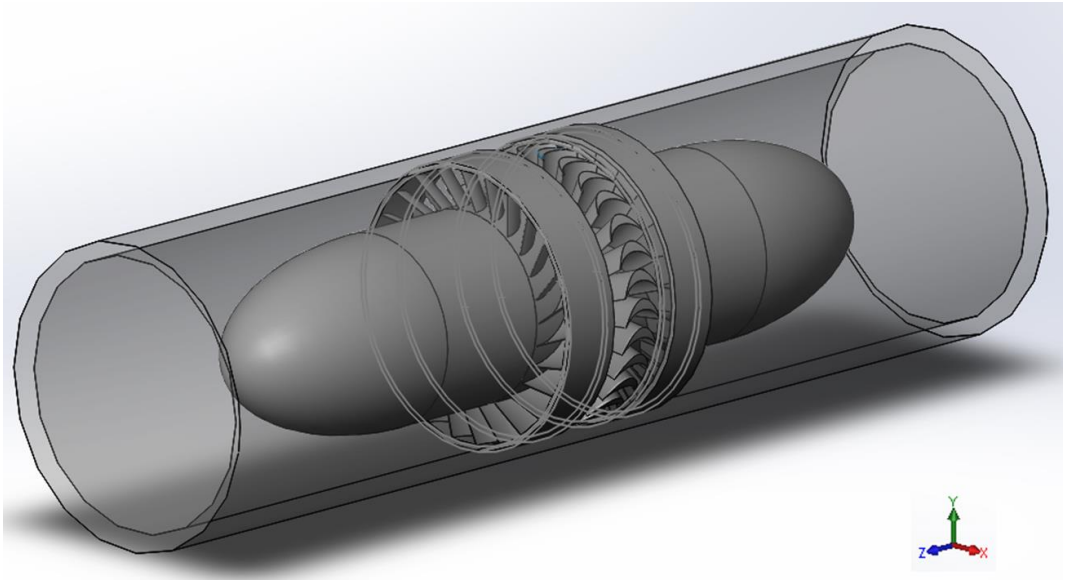

Fig. 4.6: Full turbine within duct as created for CFD simulations.

SolidWorks Edition 2014 SP4.0 and Flow Simulation 2014 SP4.0 were the software versions used for the CFD simulations. SolidWorks and Flow Simulation were chosen for this project based on software availability, as well as an opportunity to investigate the performance of the SolidWorks CFD engine. For the CFD simulations, a circular duct was created for the turbine rotor and guide vane to exist in a manner similar to how the turbine would be installed in an OWC. Fig. 4.6 shows the final assembly of the turbine hub, guide vanes, and duct for in SolidWorks Flow Simulation.

4.3.1. Methodology for Characterisation of the Turbine Model

As the suitability of SolidWorks Flow Simulation was being investigated as part of the work performed for this thesis, the first step of the CFD analysis of the turbine was to establish the dependability of Flow Simulation. This was accomplished by building a 300 mm diameter impulse turbine model in SolidWorks that matched the turbine that was experimentally tested and used to attain the design criteria for the 2.5 m turbine. The 300 mm turbine was tested using Flow Simulation at a rotational speed of 36 rads·s^{-1}, and the turbine characteristics determined through the CFD analysis were compared to the published results of the turbine experimentally tested in [39, 41, 43, 52, 94, 101, 102, 103, 105].

Following CFD testing and analysis of the 300 mm turbine, CFD simulations were then performed on the 2.5 m turbine. As the turbine will be controlled by a variable speed controller, CFD analysis was carried out on the turbine at several rotational velocities. The rotational velocities chosen were 18 rads·s^{-1}, 21 rads·s^{-1}, 24 rads·s^{-1}, 28.5 rads·s^{-1}, and 36 rads·s^{-1}. The rotational velocities used for CFD analysis were

chosen to gather a wide database while remaining within the expected operational speeds of the turbine.

The values sought during the CFD analysis of the turbines were the volumetric flow rate of air across the turbine, Q_p, the pressure differential across the turbine, Δp, the mid-blade air velocity, v_a, and the total mechanical torque applied to the turbine, T_o. These values were collected at approximately 15 different flow coefficients for each of the 5 rotational velocities investigated. A CFD simulation had to be executed for each combination of rotational velocity and flow coefficient, with each simulation taking between 5 and 15 hours to complete. Table 4.3 presents the basic information on the hardware and software used to perform the CFD calculations presented in this chapter.

Tool	Description
Computational Fluid Dynamics Engine	Flow Simulation® 2014, SP 4.0, Build: 2765
Processors	Intel® Xeon® CPU E5620@2.4 GHz (x2)
RAM	12.0 GB
CAD Software	SolidWorks® 2014, SP 4.0
Operating System	Windows 7 Professional 64-bit SP 1.0

Table 4.3: Basic information on the computing hardware and software used to perform the CFD calculations presented in Chapter 4.

4.3.2. INITIAL SETTINGS

The majority of the initial settings for each CFD simulation remained static for every run. The only changes to the simulations were the inlet pressure, the rotational speed of the turbine, and the initial air velocity on the Z-axis, which is the axis of rotation for the turbine. These variables will be further discussed in the following sections, while this section will present the settings that were not changed over the course of the simulations. Table 4.4 presents the initial setting parameters available in Flow Simulation as well as the settings chosen for the CFD calculations performed for this project.

The units that were used throughout the CFD analysis were the standard SI units which were used for CFD and all other aspects of the models created. The analysis type selected was internal because the turbine was built within an open pipe, and the airflow within the pipe was treated as a fully developed flow. While it is acknowledged that during real operation it is unlikely that the flows created by the motion of the IWS will be uniform, there was not a method for accurately modelling the irregular flow, so for turbine characterisation, applying a uniform flow was the best available option for the CFD simulations. With this observance, the fluid velocity parameters were set for each

of the three axes, X, Y, and Z. The X and Y axis velocities were set at 0 m/s for all the simulations, but the Z axis velocity was set depending on the pressure differential across the turbine. Setting an initial velocity along the Z axis based on the expected air velocity of the simulation allowed for the simulation to run quicker. Applying this initial condition also avoided unstable systems during the CFD calculations, which were common when the initial conditions were set using high flow velocities.

Parameter	Setting
Units	SI
Analysis	Internal
Exclude cavities w/out flow	on
Physical Features	
Heat conduction in solids	off
Radiation	off
Time-dependent	off
Gravity	off
Rotation	Local
Reference axis	X-axis
Fluid	Air (gas)
Flow type	Laminar-turbulent
Humidity	off
Gravity	off
Default wall thermal conditions	Adiabatic wall
Roughness	off
Parameter definition	User defined
Thermodynamic	Pressure and temperature
Pressure	101325 Pa
Pressure potential	off
Temperature	283.15 K
Fluid Velocity Initial Conditions	
X-axis	0 m/s
Y-axis	0 m/s
Z-axis	variable
Relative to rotating frame	off
Turbulence	Energy and dissipation
Energy	1 J/kg
Dissipation	1 W/kg

Table 4.4: Flow Simulation initial settings and values selected for the CFD calculations presented in Chapter 4.

4.3.2.1. BOUNDARY CONDITIONS

The boundary conditions are used to define the flow simulations, and they govern the final steady-state flow patterns, which determine the turbine performance. There were

3 boundary conditions set for the CFD simulations presented in this chapter. For all non-rotating walls of the model, the boundary conditions were selected to create an ideal wall condition, which fixes all the selected surfaces as adiabatic, frictionless walls. The ideal wall boundary conditions were set to create a flow symmetry plane that minimises the computational resources needed to complete a simulation. The two other boundary conditions set were static and environmental pressures at either end of the duct. The pressure difference, coupled with the initial flow condition, create the pressure drop and flow across the turbine that would be expected in practical experiments. The pressure at the outlet duct is set to constant environmental pressure of 101,325 Pa, or 1 atm, for every simulation, while the input pressure is adjusted for each simulation to achieve the required flow conditions needed to characterise the turbine.

4.3.2.2. SIMULATION GOALS

The CFD simulations of the turbines were run to determine the performance characteristics of the turbines so that they could be modelled in the full system. To find the necessary characteristics, various goals were specified in the model so that the software knew what values were to be calculated. The types of goals available in SolidWorks Flow Simulation were global, point, surface, volume, and equation goals, but only point and surface goals were used during the CFD simulations in this thesis. Point goals calculate the chosen parameter at a given three dimensional point within the developed mesh. Surface goals calculate the chosen parameter over the entirety of a selected surface of the three dimensional geometric model.

Each goal selected for a simulation had an option to set the goal criteria, which determined when the calculation was considered finished. The criteria, by default, were set to automatic, but for the simulations run on the turbine, the criteria were set manually to maintain continuity with the results of all simulations. When the amplitude excursion over the analysis interval reckoned backward from the most recent iteration becomes less than the criterion, the goal is considered complete. When all selected goals are complete, the simulation is concluded. The simulations run on the turbine had 5 separate goals: 4 surface goals and 1 point goal.

Of the four surface goals, two were based on static pressure, one was volumetric flow, and one was torque in the Z direction. As the most referenced variables in the turbine performance equations are the flow coefficients, ϕ and Φ, which are based on airflow velocity and volumetric flow respectively, the criteria initially were chosen to determine the airflow velocity and volumetric flow rate to the accuracy of one decimal

place. The volumetric flow criterion, which was based on the flow across the inlet cap of the duct, was set to a value of 0.1 $m^3 \cdot s^{-1}$. The flow calculations under this criterion produced data with 3 to 4 significant digits and could be resolved in fewer than 4 travels, where 1 travel is the calculation period required for a flow disturbance to cross the computational domain's fluid region and 4 travels is the standard setting for calculations in Flow Simulation. For consistency, the criteria of the other goals were also selected to produce values with at least 3 to 4 significant digits while being able to be resolved with the 4 travels. The torque goal was a summation of the torque exerted on all 60 faces of the 30 blades of the turbine. This goal was used to calculate the total mechanical torque on the turbine hub, and the criterion for the torque surface goal was 10 Nm. Fig. 4.7 displays how the goal surfaces were selected for the turbine torque calculation, where the selected surfaces are highlighted in blue.

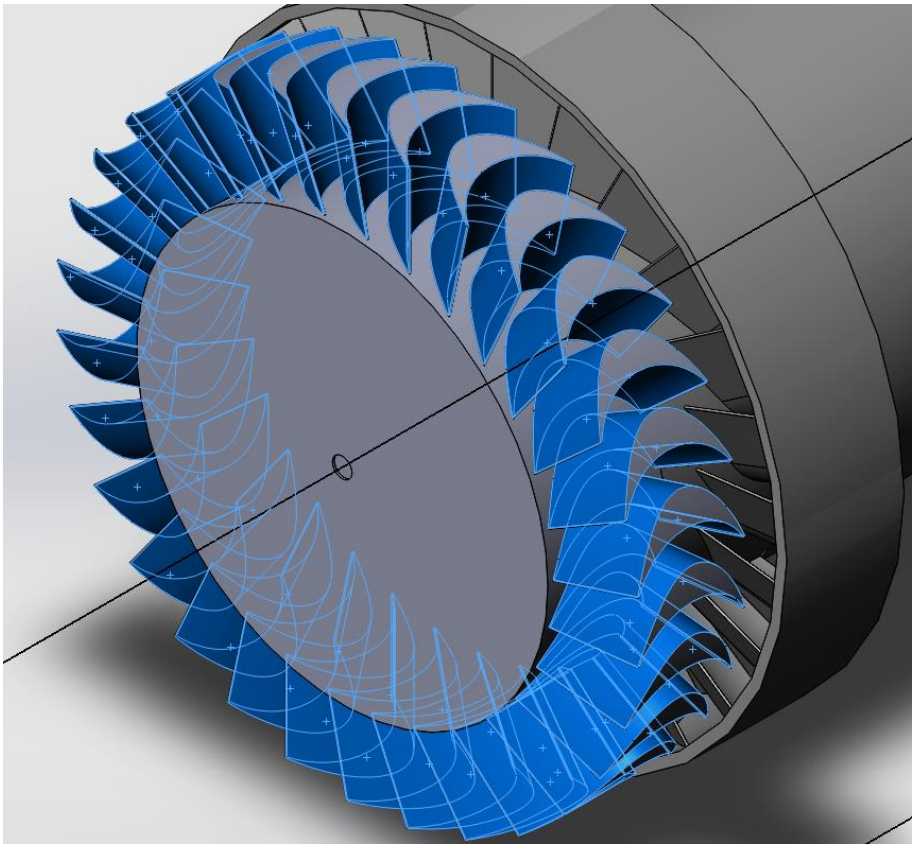

Fig. 4.7: Surface goal selection for turbine torque calculation.

The static pressure goals were on the inlet and outlet caps of the duct that the turbine was encased in and were set boundary conditions, so the criterion for the static pressure was set at 10 Pa without exceeding the 4 travel limit. A point goal is a calculation at a single point on the three dimensional axes. For the CFD simulations of the turbine, a single point goal was used to determine the air flow velocity at the entrance of the inlet

guide vane at mid-blade height; the criterion for the point goal was set to 0.1 $m \cdot s^{-1}$. Fig. 4.8 illustrates where the velocity was measured. location was selected because it is at the upstream entrance of the guide vanes where the flow will be fully developed but will not be greatly affected by vorticity or rotor rotational velocity, and the velocity calculated should represent the turbine system input air speed. The values of the goals reached following each simulation were added to a spreadsheet that was used to mathematically characterise the turbine at the chosen rotational velocities.

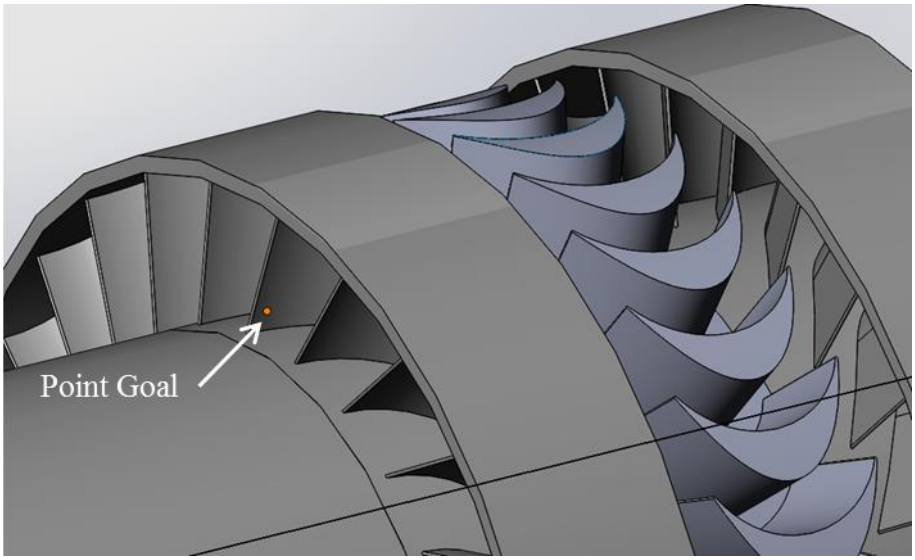

Fig. 4.8: Point goal selection for calculating air flow velocity, the orange point designates the location at which the calculations were performed.

4.3.2.3. ROTATING REGIONS

Accurately modelling the turbine requires that the turbine is rotating in reference to the air flow that is driving it. To achieve this during the simulations run in SolidWorks, a local rotating region was specified that enclosed the entire turbine hub and blades, while the rest of the duct, including the inlet and outlet guide vanes, were outside of the local region so that they remained stationary. The fluid flow within the set rotating region is calculated using local reference frames, and the flow field parameters are transferred from the outside stationary regions to the boundary of the rotating region as boundary conditions.

When the rotating region is created and set, the angular velocity of the rotating region can be set in radians per second. The rotational velocities tested were selected prior to creation of the CFD model and were based on the original design parameters. The simulations were run with the turbine rotating at the angular velocities of 18 $rads \cdot s^{-1}$, 21 $rads \cdot s^{-1}$, 24 $rads \cdot s^{-1}$, 28.5 $rads \cdot s^{-1}$, and 36 $rads \cdot s^{-1}$. The results at each rotational speed are presented in Section 4.4.

4.3.2.4. MESH SETTINGS

In order to analyse fluid flow using CFD, the flow domains are broken up into smaller subdomains that are referred to as a mesh, and the governing equations are discretised and solved inside each of the constructed subdomains. The more subdomains present in the mesh, the higher the resolution of the analysis. However, more subdomains increase the number of calculations performed during the analysis and extend the duration of a single simulation. It is important to find a balance between the duration of the simulations with the resolution of the results. Fig. 4.9 shows the fluid mesh and Fig. 4.10 shows the partial mesh that was generated around the turbine rotor blades.

Work performed in [116] proposed that the difference in results between analyses carried out with 1,013,198 and 1,658,972 subdomains was statistically insignificant enough that the solutions could be considered mesh independent, but before continuing with the work in this chapter, this result needed to be confirmed independently. To do this, CFD simulations were set up using the same input parameters with seven different mesh settings.

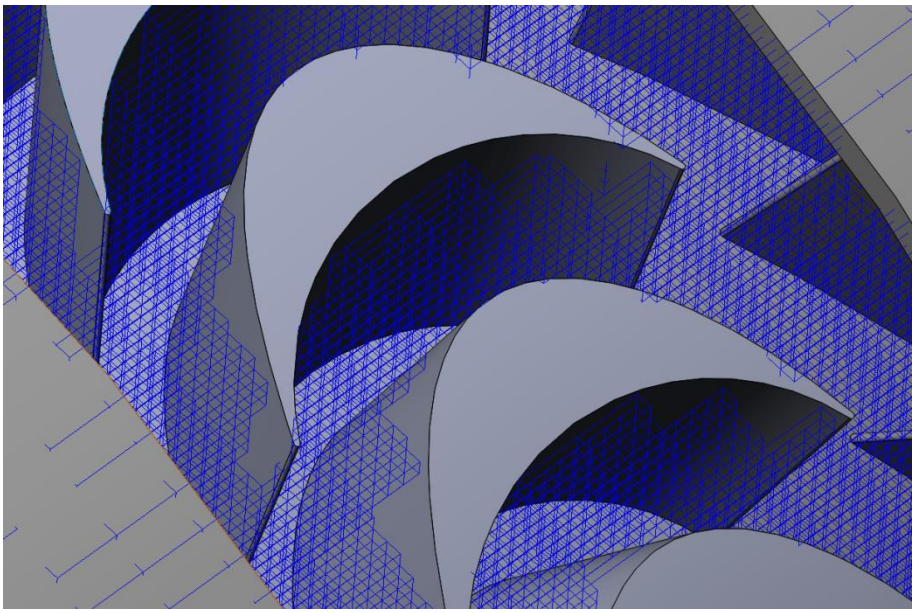

Fig. 4.9: Fluid mesh generated by Flow Simulation to calculate the flow across the turbine.

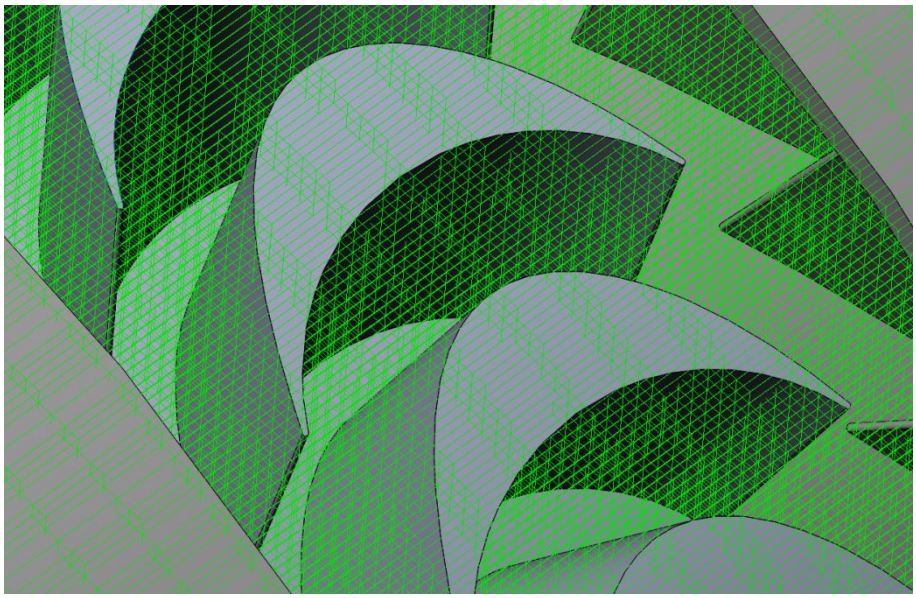

Fig. 4.10: Partial mesh generated by Flow Simulation to calculate the flow across the turbine.

For the initial mesh settings, the options are the number of basic cells in the X, Y, and Z dimensions. Each of the seven simulations was set up with a different number of cells in the X, Y and Z dimension, and the cell allocations for each dimension were adjusted proportionally to each other. The seven simulations initially performed were used to find how the changes in cell numbers affected the results of the CFD simulations, and the cost-benefit analysis of time required to perform a single simulation versus the precision of the results.

Along with the basic mesh settings, the refinement levels for the cells must be chosen. Higher refinement values create more cells, greater precision, and longer simulations. The refinement options include curvature, tolerance, all cell, solid cell, narrow channel, fluid cell, and partial cell refinement. For the seven simulations, the curvature, tolerance, all cell, solid cell, and narrow channel cell refinement remained the same. Only the fluid cell and partial cell refinement was altered during the simulations. This was done deliberately to limit the number of variables investigated. The fluid and partial cells were chosen as the variables because there were more fluid and partial cells present in the CFD model than any of the other cell types and changing their refinement would have the greatest impact on simulation results.

The fixed refinement levels were set first and were based on a scale N=0-9, with 0 being no refinement and 9 being maximum refinement. During refinement, the computational mesh cells are split into cells which size will be 2^N time smaller than the basic mesh's cell size [117]. The curvature, tolerance, all cell, solid cell and narrow channel, refinements were all set to a value of 1. The narrow channel refinement was

also set to a level of 1, and the characteristic number of cells across a narrow channel was set equal to 7, without minimum or maximum height of the narrow channels. There were secondary refinement settings for the curvature refinement, tolerance refinement, and narrow channel resolution referred to as the curvature refinement criterion and tolerance refinement criterion, and characteristic number of cells across a narrow channel respectively.

The curvature refinement criterion establishes the maximum angle normal to the surface inside one cell and should not exceed a certain threshold. If the maximum angle is eclipsed, the cell is split into 8 cells [117]. Smaller criterion dictates to smaller critical angles better resolution. The curvature refinement criterion was set to 0.314159, which represents 10% of the circumference of a circle.

The tolerance refinement criterion limits the approximated set of polygons whose vertices are surface's intersection points with the cells' edges by controlling the precision of the representation of flat faces, through which curved surfaces are approximated. A cell will be split if the distance between the outermost interface's point within the cell and the polygon approximating this interface is larger than the specified criterion value [117]. The tolerance refinement level was also set at 1 with a criterion of 150 mm and optimisation of thin wall resolution.

The characteristic number of cells across a narrow channel specifies the number of initial mesh cells, including partial cells, that are set across the model's flow passages in the normal-to-solid/fluid-interface direction. If possible, the number of cells across narrow channels will be equal to the specified characteristic number, otherwise it will be close to the characteristic number. If this condition is not satisfied, the cells lying in this direction will be split to satisfy the condition [117]. The characteristic number of cells across a narrow channel for these CFD simulations was set to 7.

With the fixed refinement levels set, the mesh used for the simulations using different resolutions could be generated. Table 4.5 below shows the setting variables for the seven simulations and the total number of fluid and partial cells generated for each simulation. Of the seven different meshes, five had fluid and partial cell refinement settings of two and two had a refinement level of three.

Mesh Identifier	Number of Cells X	Y	Z	Fluid Refine	Partial Refine	Total Fluid Cells	Total Partial Cells
ExLow Res Refine 2	27	27	36	2	2	794671	163772
Low Res Refine 2	31	31	40	2	2	1185614	209240
Mid Res Refine 2	36	36	45	2	2	1815094	285159
High Res Refine 2	45	45	54	2	2	3465110	437908
ExHigh Res Refine 2	48	48	58	2	2	4264625	502116
Low Res Refine 3	12	12	24	3	3	843028	169888
Mid Res Refine 3	15	15	30	3	3	1685360	267951

Table 4.5: Flow Simulation settings evaluated during the investigation of CFD resolutions.

The greater the number of cells generated in the mesh, the greater the number of calculations and the higher the resolution of the CFD simulation performed. To investigate the effects the resolution had on the accuracy of the CFD simulation results, the simulations were performed under the same initial conditions for each of the seven settings listed in Table 4.5, and the results are presented in Table 4.6. The initial conditions are based on the inlet pressure, which was set to 108000 Pa and the rotational velocity of the turbine which was set at 24 rads·s^{-1}.

Mesh Identifier	Time (h)	Iterations	Travels	P_{out} (Pa)	v_a (m/s)	T_o (Nm)	Q (m^3/s)	ϕ	C_a	C_t	eff
ExLow Res 2	02:15:51	400	1.973	101323	34.0	8705.0	78.3	1.33	2.72	1.45	39.9%
Low Res 2	05:24:40	638	2.79	101322	32.5	7778.4	75.9	1.27	2.93	1.37	36.9%
Mid Res 2	08:51:25	708	2.702	101322	34.3	8710.4	78.9	1.35	2.68	1.43	39.7%
High Res 2	20:40:21	859	2.676	101321	32.6	7656.6	75.1	1.28	2.86	1.34	36.6%
ExHigh Res 2	32:40:59	1096	3.198	101315	33.6	8486.8	77.5	1.32	2.77	1.44	39.3%
Low Res 3	02:14:32	389	1.889	101323	33.9	8606.1	77.9	1.33	2.72	1.44	39.7%
Mid Res 3	04:46:22	431	1.686	101322	33.6	8445.4	77.2	1.32	2.75	1.43	39.3%

Table 4.6: CFD simulation results for an impulse turbine with a pressure drop of 6675 Pa at a rotational velocity of 24 rads·s^{-1} at seven different resolutions.

Fig. 4.11 is a plot of the values of C_t, C_a, ϕ, and pneumatic to mechanical power conversion efficiency as calculated from the results presented in Table 4.6. There is no obvious pattern in the changes seen as the resolution increases. The decision was made to use the settings labelled as "Mid Res 2" because it represented the higher resolution, above the threshold referred to in [116] while maintaining a calculation time that allowed two simulations to be carried out daily.

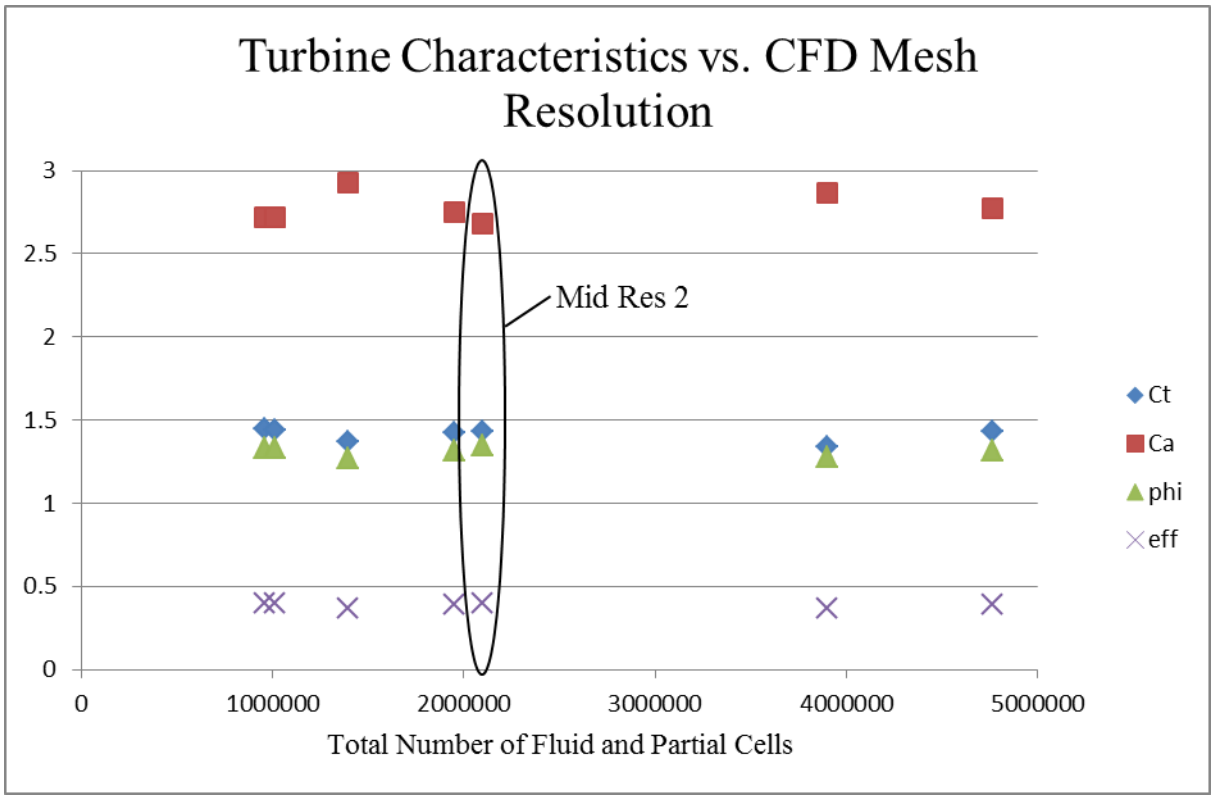

Fig. 4.11: Turbine characteristics determined by CFD simulations against mesh resolution.

4.4. COMPUTATIONAL FLUID DYNAMICS MODELLING

There were two goals for the CFD modelling performed for this thesis: confirm that the SolidWorks Flow Simulation software can accurately model an impulse turbine and numerically characterise the 2.5 m impulse turbine so that it can be applied in thecompletedmodel. To find out if Flow Simulation can accurately model an impulse turbine, a 300 mm diameter turbine was designed using SolidWorks identical to Setoguchi's 300 mm turbine, and the results of the CFD simulations performed on the 300 mm turbine were compared to the experimental results published in [41, 43, 101, 102, 103, 39, 52, 94, 105] to confirm the accuracy the Flow Simulation software.

The original turbine design was based on the impulse turbine with fixed guide vanes published in [41, 43, 101, 102, 103, 39, 52, 94, 105]. The published turbine was a 300 mm diameter turbine, and the four major expressions used to represent the experiment results of the turbine under steady flow conditions, which were originally presented in Chapter 3, are shown again in (4.11) through (4.14).

$$\phi = v_a/U_R, \tag{4.11}$$

$$C_t = T_o/\{\rho_a(v_a^2 + U_R^2)bl_r zr_R/2\}, \tag{4.12}$$

$$C_a = \Delta pQ/\{\rho_a(v_a^2 + U_R^2)bl_r z v_a/2\}, \quad (4.13)$$

$$\eta = \frac{(T\omega)}{(\Delta pQ)} = C_t/(C_A\phi). \quad (4.14)$$

The value of the torque coefficient, C_t, and input power coefficient, C_a, at different flow coefficients, ϕ, were determined experimentally in [103]. To compare the experimental and CFD analysis, the values of the torque and input power coefficients over the changing flow coefficients are graphed against each other.

The experimental results were described in the following paragraph in [41]:

> [A] large piston-cylinder, a settling chamber and 300 mm diameter test section with entry/exit at its two ends which were bell-mouthed. The test-turbine is placed at the centre of the test section. It is coupled through a torque transducer to an electrical generator/motor which is electronically controlled to maintain the rpm constant at any set value. A computer controls a motor which produces a steady flow (for a short period), a sinusoidal flow, or an irregular flow through the turbine. An average flow rate is measured by pitot-tube survey. Settling chamber pressure is measured by a pressure transducer. Turbine performance is evaluated from turbine rpm, turbine output torque, flow rate and total pressure drop between settling chamber and atmosphere. Tests were performed for total pressure drops in the range of 200 to 800 N/m^2, turbine angular velocity up to 370 rad/s and flow rates up to 0.63 m^3/s. The measurement uncertainty in turbine efficiency is about ±2%. For measuring guide vane angle q_p, a potentiometer was used".

The values present in the output graphs were the results of the average values of ϕ, C_t, C_a, and η for flow rates and rotational velocities. The placement of the various sensors, including the pitot-tube and settling chamber pressure transducer, was not made readily available in the various publications produced from the turbine testing, which made replicating these results through CFD analysis more difficult because certain aspects of the setup had to be assumed.

4.4.1. 300 MM TURBINE CFD MODELLING

A 300 mm turbine matching the published dimensions of the experimentally tested turbine was created and tested in SolidWorks Flow Simulation. The purpose of testing a 300 mm turbine using Flow Simulation was to validate the SolidWorks CFD engine against experimental data before testing the full scale turbine model.

The numerical data from the experimental results of the 300 mm turbine tests were not made available in publications. However, the graphs produced from the experiments

were available in several published articles. To compare the published experimental data to the CFD simulation results, the numerical data were manually extracted from the published graphs to find the values of C_a, C_t, and η at 14 values of ϕ. The values of ϕ ranged from 0.375 to 2.0 in steps of 0.125. This method of data extraction was the best available and resulted in a data set that allowed for a direct comparison of experimental and modelled data.

From the CFD results, the values of ϕ, C_a, C_t, and η were calculated using the values of Δp, Q, T_o, and v_a by applying them to equations (4.11) through (4.14). The extracted values of the experimental data and the calculated values from the CFD simulations are presented in Table 4.7.

Extracted Published Results				CFD Results			
ϕ	C_t	C_a	η	ϕ	C_t	C_a	η
0.375	0.083	1.410	0.210	0.365	0.041	1.58	0.071
0.500	0.250	1.800	0.300	0.510	0.245	2.14	0.225
0.625	0.490	2.200	0.347	0.653	0.491	2.51	0.299
0.750	0.708	2.520	0.370	0.785	0.743	2.79	0.340
0.875	0.917	2.750	0.387	0.911	0.978	2.96	0.363
1.000	1.125	2.930	0.395	1.027	1.182	3.07	0.374
1.125	1.333	3.075	0.394	1.136	1.358	3.15	0.379
1.250	1.500	3.150	0.387	1.238	1.509	3.21	0.380
1.375	1.667	3.190	0.379	1.427	1.757	3.27	0.376
1.500	1.792	3.220	0.370	1.597	1.942	3.31	0.367
1.625	1.958	3.235	0.361	1.754	2.088	3.33	0.358
1.750	2.042	3.245	0.353	1.900	2.205	3.33	0.348
1.875	2.167	3.250	0.346	2.039	2.303	3.33	0.339
2.000	2.250	3.250	0.340				

Table 4.7: The values of ϕ, C_a, C_t, and η for the 300 mm impulse turbine as extracted from the experimental results presented in graphs in [41, 102] and as calculated from the CFD simulation results.

Due to the CFD simulation inlet boundary conditions being set as a static pressure, the flow coefficients, ϕ, of the simulations could not be set to match that of the extracted results, so direct numerical comparisons of the two data sets cannot be achieved. To resolve this, polynomial functions of the flow coefficient, ϕ, were developed to represent the values of the torque coefficient, C_t, and the input power coefficient, C_a, for the experimental data.

To determine the order of the polynomial equations, the relationship between C_t and ϕ and between C_a and ϕ had to be established. Rearranging equations (4.11)-(4.13) shows that,

$$v_a = \phi U_R, \tag{4.15}$$

$$C_t = 2T_o/\{\rho_a(\phi^2 - 1)U_R^2 b l_r z r_R\}, \tag{4.16}$$

$$C_a = 2\Delta pQ/\{\rho_a(\phi^3 - \phi)U_R^3 b l_r z\}. \tag{4.17}$$

Thus C_t is a quadratic function of the flow coefficient, ϕ, while C_a is a cubic function of ϕ. Using the curve fitting tool available in MATLAB R2013b, a second-order polynomial function was established for C_t, and a third-order polynomial was established for C_a. The polynomial functions are presented in (4.18) and (4.19):

$$C_t(\phi) = -0.3856\phi^2 + 2.29\phi - 0.7716, \tag{4.18}$$

$$C_a(\phi) = 0.6683\phi^3 - 3.576\phi^2 + 6.372\phi - 0.5388, \tag{4.19}$$

where the R^2-value of $C_t(\phi)$ is 0.9991 and the R^2-value of $C_a(\phi)$ is 0.9994. Due to the high R^2-values, the results from both polynomial equations are considered reliable approximations of the experimental turbine data.

4.4.1.1. TORQUE COEFFICIENT

To assess the accuracy of the data generated from the CFD simulations, the torque and input power coefficients determined from the CFD data were plotted against the published experimental data. Fig. 4.12 is the graph of C_t vs ϕ for the 300 mm turbine experimental results as published in [41, 102] along with results for the 300 mm turbine as found through CFD simulations. The CFD results for the 300 mm turbine closely match the published experimental results. As was done for the data extracted from the published experimental results, a second-order polynomial function was established to represent C_t as found using the data generated through CFD simulations on the 300 mm impulse turbine. The polynomial function is presented in (4.20):

$$C_t(\phi) = -0.4119\phi^2 + 2.392\phi - 0.844, \tag{4.20}$$

where the R^2-value of $C_t(\phi)$ is 0.9983. The trajectories for the two trend lines do not perfectly overlap, and the beginning of a small separation of the results is evident at both extremes of the data plots.

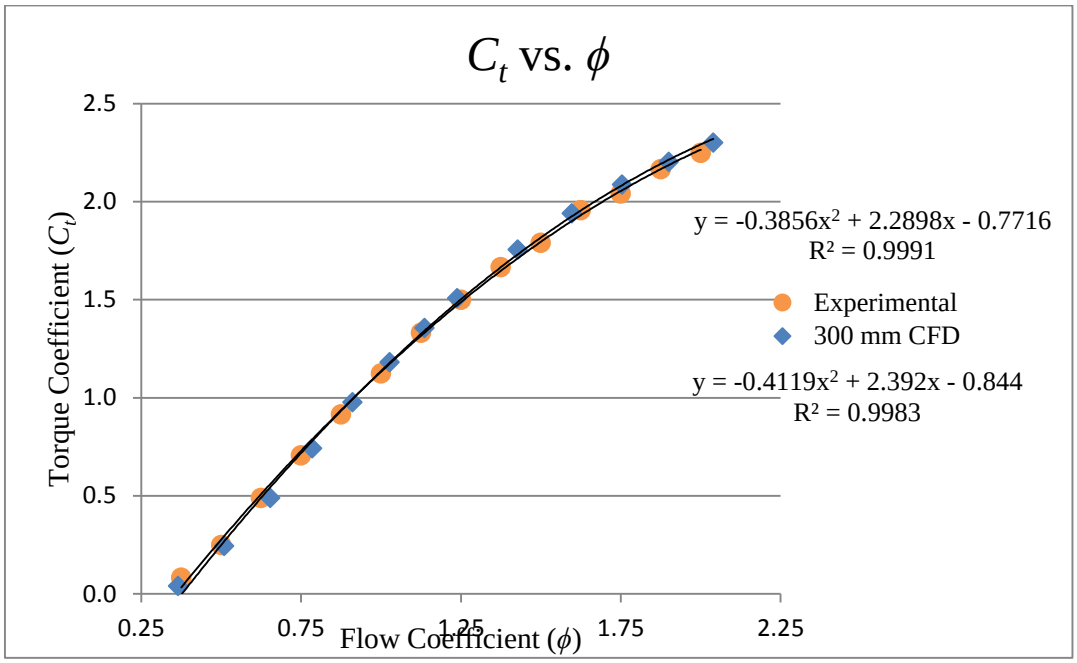

Fig. 4.12: C_t vs ϕ, experimental results for 300mm turbine [41, 102] against CFD results for 300 mm turbine at 36 rads·s-1.

4.4.1.2. INPUT POWER COEFFICIENT

The input power coefficient found from the CFD data was also a close match to the published experimental data, though there was greater variance, especially at low flow coefficients, in the results when compared to the results from the torque coefficient analysis. Fig. 4.13 is the graph of C_a vs ϕ for the 300 mm turbine experimental results as published in [41, 102] along with the results of the CFD simulations performed on the 300 mm turbine. Again, using the data extracted from the published experimental results, a third-order polynomial function was established to represent C_a as found using the data generated through CFD simulations on the 300 mm impulse turbine. The polynomial function is presented in (4.21):

$$C_a(\phi) = 0.7671\phi^3 - 3.8099\phi^2 + 6.3402 - 0.236, \quad (4.21)$$

where the R^2-value of $C_a(\phi)$ is 0.9985. The input power coefficients generated from the CFD simulations are slightly higher than the experimentally determined input power coefficients, which may be a result of how the pressure differential was measured experimentally versus how it was measured in the CFD simulations, may be related to errors in sensors used to collect the experimental, or may be related to unknown errors in the CFD simulation. The trends for both results are clearly very similar, and because

C_a is proportionally affected by the measured values of flow and pressure, the addition of a small offset for either pressure or flow would allow the experimental and CFD generated curves to more closely overlap. As both the location and method of the flow measurements and pressure measurements taken for the published experimental results are only vaguely described, the offset between the two results does not undermine the confidence in the ability of the CFD modelling to accurately replicate laboratory testing.

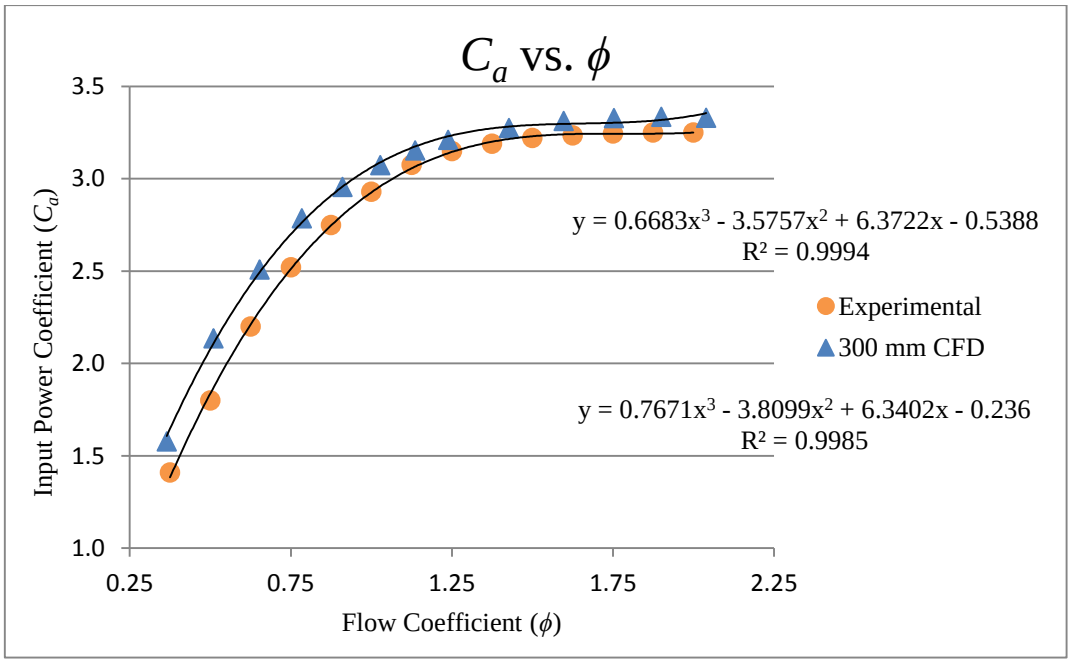

Fig. 4.13: C_a vs ϕ, experimental results for 300mm turbine [41, 102] against CFD results for 300 mm turbine at 36 rads·s^{-1}.

In the plots presented in Fig. 4.13, the value of C_a is represented mathematically by a 3rd-order equation. A third order equation was applied to enhance the comparison of the characteristics of the impulse turbine determined through experimental observations and CFD simulations. It must be noted that in practice, the input coefficient converges to a constant value at high flow coefficients, ϕ, and there for, at high values of ϕ the 3rd order equation used to model the value of C_a is no longer valid. However, the equations to represent C_a are not applied to the models used in this thesis and high values of the flow coefficient, where the equation becomes invalid, were not considered during CFD analysis, so the inconsistency does not affect the results produced in this thesis.

4.4.1.3. MEAN SQUARED ERRORS

Using the flow coefficients established from the CFD results in equation (4.18) and (4.19), the corresponding values of C_t and C_a were established for the experimental data. The statistical tool Mean Squared Error (MSE) is used to measure the difference

between a predicted estimation and measured results. The MSE was used to assess the accuracy of the CFD simulation results and the published experimental results by giving a numerical value to the difference between the experimental and CFD simulated data. The smaller the value of the MSE; the more accurate the model estimations. The MSE between the experimental and simulated data for C_t was found to be 0.0013, while the MSE between the experimental and simulated data for C_a was found to be 0.023. Fig. 4.14 is a plot of the MSE for the 300 mm turbine experiential and the 300 mm turbine CFD generated data for both C_t and C_a vs. the flow coefficient, ϕ.

The majority of the disparities between the experimental and CFD results occur at the low flow coefficients, ϕ, with the largest squared error value being 0.072 where ϕ = 0.51, while the values of the squared error drops below 0.01 where $\phi > 1.03$. The only measured value used in the calculation of the input power coefficient, C_a, that is not also used in the calculation of the torque coefficient, C_t, is the pressure differential, Δp, and therefore the pressure values are most likely the cause of the disparities. The pressure differential is calculated in the experimental data by measuring the pressure in the settling chamber and subtracting the measured environmental pressure [41, 102], while in the CFD data, the pressure differential is calculated from measuring the average input static pressure at the turbine duct inlet and subtracting average environmental pressure at the turbine duct outlet. These differences in measuring the pressure drop, as well as the means in which the experimental data were extracted from published graphical representation each had influences on the errors found between the experimental and modelled data as all other parameters were known and well-defined. The CFD results were also a potential source of error, as the R^2-values of the polynomials generated from the CFD data were lower than those related to the polynomials generated from the experimental data. While the difference were minimal, the MSE errors were also small enough that the greater inconsistencies found in the CFD data most likely also contributed to the MSE values.

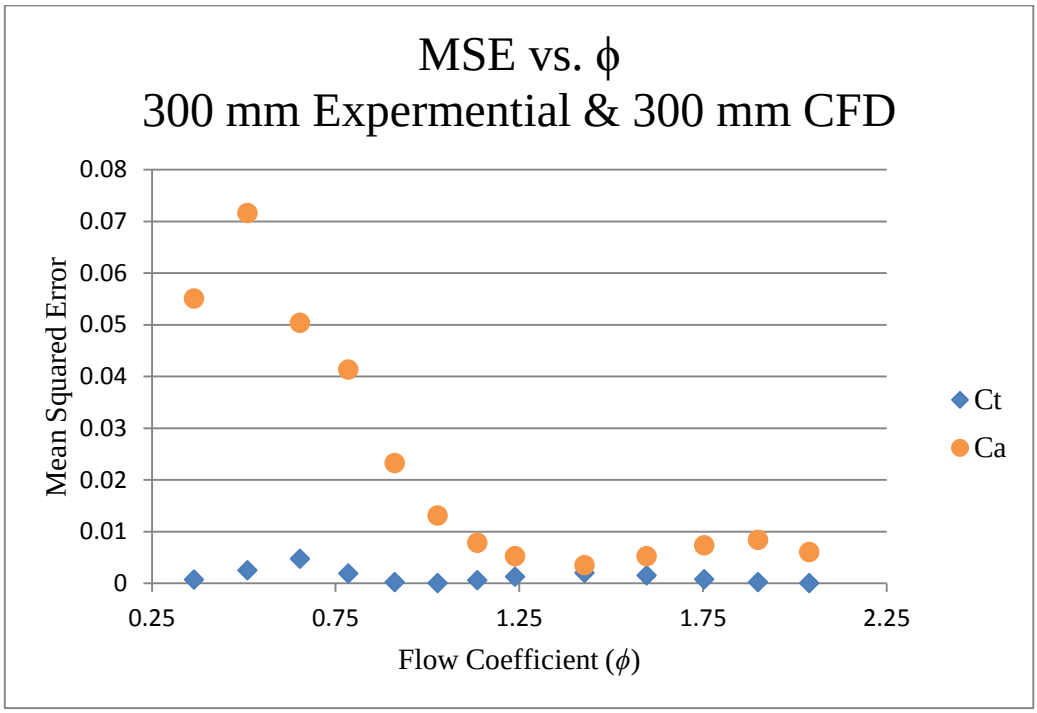

Fig. 4.14: Mean Squared Error vs ϕ for 300 mm experimental results and 300 mm CFD generated results of C_t and C_a.

The data collected for 300 mm turbine modelled using SolidWorks Flow Simulator have shown good agreement with the published experimental data, with the MSE of 0.0013 for the torque coefficient, C_t, and an MSE of 0.023 for the input power coefficient, C_a, and the plots exhibit the same trends. With these results, the SolidWorks Flow Simulator CFD modelling has demonstrated that it can accurately model an impulse turbine, and so the 2.5 m turbine that was designed to fit the OWC modelled for this thesis was then tested using the same software under the same conditions.

4.4.2. 2.5 M TURBINE CFD MODELLING

Following the assessment of the 300 mm turbine results, the 2.5 m turbine was modelled using CFD. The simulations performed on the 2.5 m turbine were carried out to create equations based on air flow, rotational velocity, and the physical turbine characteristics that can be used to model turbine and system behaviour mathematically. As the coefficients used to characterise the turbine were non-dimensional, the results from the 2.5 m turbine could also be compared to the published experimental results, which provided a second check on the accuracy of the CFD accuracy. Table 4.8 presents the CFD data recorded at maximum efficiency for the 2.5 m impulse turbine for all 5 rotational velocities simulated.

Maximum efficiency of turbine at tested rotational velocities					
ω (rads·s^{-1})	18.00	21.00	24.00	28.50	36.00
U_r (m·s^{-1})	19.13	22.31	25.50	30.28	38.25
Q_p (m^3·s^{-1})	68.81	75.77	94.14	103.26	122.82
v_a (m·s^{-1})	28.04	30.88	38.40	42.15	50.22
ϕ	1.47	1.38	1.51	1.39	1.31
Φ	0.24	0.23	0.25	0.23	0.22
P_{in} (Pa)	105750	107000	110000	112750	120000
P_{out} (Pa)	101323	101323	101322	101322	101317
ΔP (Pa)	4427	5677	8678	11428	18683
T_o (Nm)	6735.58	8176.33	13575.00	16578.10	25377.00
C_a	3.08	3.09	3.14	3.18	3.30
C_t	1.80	1.71	1.89	1.77	1.72
P_p (kW)	304.61	430.17	816.98	1180.08	2294.65
P_m (kW)	121.24	171.70	325.80	472.48	913.57
η (%)	0.398	0.399	0.399	0.400	0.398
κ (Pa·m^{-6}·s^2)	0.94	0.99	0.98	1.07	1.24
k (Pa·m^{-3}·s)	64.34	74.92	92.18	110.67	152.12
Ψ	0.163615	0.144215	0.178319	0.150662	0.135809
Y	1.680267	1.564554	1.781142	1.622774	1.562264

Table 4.8: CFD results for the 2.5 m impulse turbine at maximum efficiency for 5 different rotational velocities.

The general settings for the CFD simulations of the 2.5 m turbine were carefully selected to match the settings used during simulations of the 300 mm turbine, as presented in previous sections. The only exceptions to this were directly related to the difference in scale between the two turbines. Those exceptions included the input pressure, and the initial flow velocity in the Z direction. The pressure and velocity were adjusted so that the flow coefficient remained within a range of $0.5 < \phi < 2.0$, and the convergence criteria were selected to match the larger scale of the turbine.

The CFD calculations were performed on the 2.5 m turbine at 5 rotational speeds; for comparison to the experimental data, the results from the CFD testing with the turbine rotational speed set to 24 rads·s^{-1} was used because it was the median rotational speed value. The values of ϕ, C_a, C_t, and η for the 2.5 m turbine were calculated using the values of Δp, Q, T_o, and v_a that were produced from the CFD simulations and applying them to equations (4.11) through (4.14). The calculated values from the CFD simulations are presented in Table 4.9. The calculated coefficients are all normalised, non-dimensional values. This allows for the published experimental results of a 300 mm turbine to be compared directly to the results of CFD simulations performed on the 2.5 m turbine.

2.5 m Turbine			
ϕ	C_t	C_a	η
0.426	0.106	1.79	0.139
0.527	0.260	2.14	0.230
0.621	0.425	2.42	0.283
0.713	0.595	2.62	0.318
0.800	0.759	2.78	0.341
0.883	0.916	2.90	0.358
0.966	1.068	2.97	0.372
1.044	1.206	3.03	0.381
1.122	1.336	3.06	0.389
1.192	1.449	3.09	0.393
1.264	1.559	3.10	0.398
1.329	1.652	3.11	0.400
1.388	1.732	3.13	0.398
1.450	1.815	3.13	0.400
1.506	1.886	3.14	0.399
1.611	2.011	3.15	0.396
1.708	2.119	3.16	0.392
1.797	2.212	3.17	0.388
1.881	2.294	3.18	0.383
1.958	2.368	3.19	0.379
2.030	2.433	3.21	0.374

Table 4.9: The values of ϕ, C_a, C_t, and η for the 2.5 m impulse turbine as calculated from the CFD simulation results with a rotational velocity of 24 rads·s^{-1}.

4.4.2.1. TORQUE COEFFICIENT

Fig. 4.15 presents the graph of C_t vs ϕ for the 300 mm turbine experimental results as published in [41, 102] along with the graph of C_t vs ϕ for the 2.5 m turbine as found through CFD simulations. Similar to the CFD results from the 300 mm turbine, a second-order polynomial function was established to represent C_t as found used the data generated through CFD simulations on the 2.5 m impulse turbine. The polynomial function is presented in (4.22):

$$C_t(\phi) = -0.3828\phi^2 + 2.428\phi - 0.9115, \quad (4.22)$$

where the R^2-value of $C_t(\phi)$ is 0.9994. While the results of the 2.5 m turbine CFD modelling also show good agreement with the experimental data, the separation between modelled and experimental data at high flow coefficients is more apparent for the 2.5 m simulated data than it is for the 300 mm CFD results. The exaggerated separation may be influenced by the increased scale of the turbine. While the coefficients are non-dimensional, the separation, which was apparent in the 300 mm

simulations, could have been magnified by the increased scale of the torque generated by the turbine or a non-scalable aerodynamic property such as fluid viscosity.

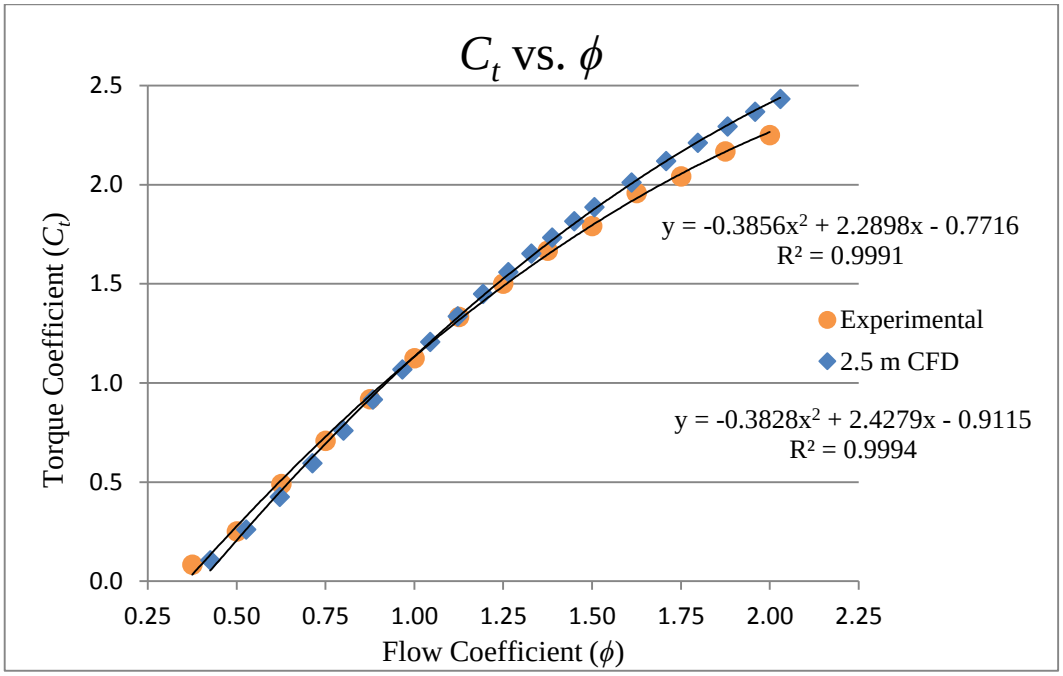

Fig. 4.15: C_t vs ϕ, experimental results for 300 mm turbine [41, 102] against CFD results for 2.5 m turbine at 24 rads·s^{-1}.

4.4.2.2. INPUT POWER COEFFICIENT

Fig. 4.16 shows the graph of C_a vs ϕ for the 300 mm turbine experimental results as published in [41, 102] along with the results of the CFD simulations performed on the 2.5 m turbine. The results from the 2.5 m CFD simulations also closely match the experimental results, though they have a greater variance than the results of the C_t comparison. Again, using the data extracted from the published experimental results, a third-order polynomial function was established to represent C_a as found using the data generated through CFD simulations on the 300 mm impulse turbine. The polynomial function is presented in (4.23):

$$C_a(\phi) = 0.977\phi^3 - 4.517\phi^2 + 6.93 - 0.392, \qquad (4.23)$$

where the R^2-value of $C_a(\phi)$ is 0.9977. As discussed earlier in section 4.4.1.2, the value of C_a flattens out at high values of the flow coefficient, ϕ, so the 3rd order equation used to model the value of C_a is no longer valid. However, the equations to represent C_a are not applied to the models used in this thesis and high values of the flow coefficient,

where the equation becomes invalid, were not considered during CFD analysis, so the inconsistency does not affect the results produced in this thesis. Unlike the results from the 300 mm turbine, the input power coefficient of the 2.5 m turbine generated from the CFD simulations is not consistently higher than the experimentally determined input power coefficient. At lower flow coefficients, the CFD determined input power coefficient is again higher than the experimentally determined value, but at higher flow coefficients, the inverse is true. The resulting trends for both the CFD simulations for the 300 mm turbine and the 2.5 m turbine are clearly very similar, and much of the difference could be corrected by adding an offset to the measured pressure or flow results. Adding an offset will not be as affective in addressing the differences between the 2.5 m turbine model and the 300 mm experimental results because C_a levels off at a lower value of ϕ for the CFD results. This could be related to the change in scale and the effects they have on compressibility and fluid flow and are not so profound as to undermine the quality of the CFD generated results. When taken along with the data for C_t, these CFD results for both the 300 mm and 2.5 m turbine, when compared to the experimentally published data of the 300 mm turbine, suggest that neither of the CFD results is better than the other, but both simulation results adhere closely to the original experimental results published by Setoguchi [102].

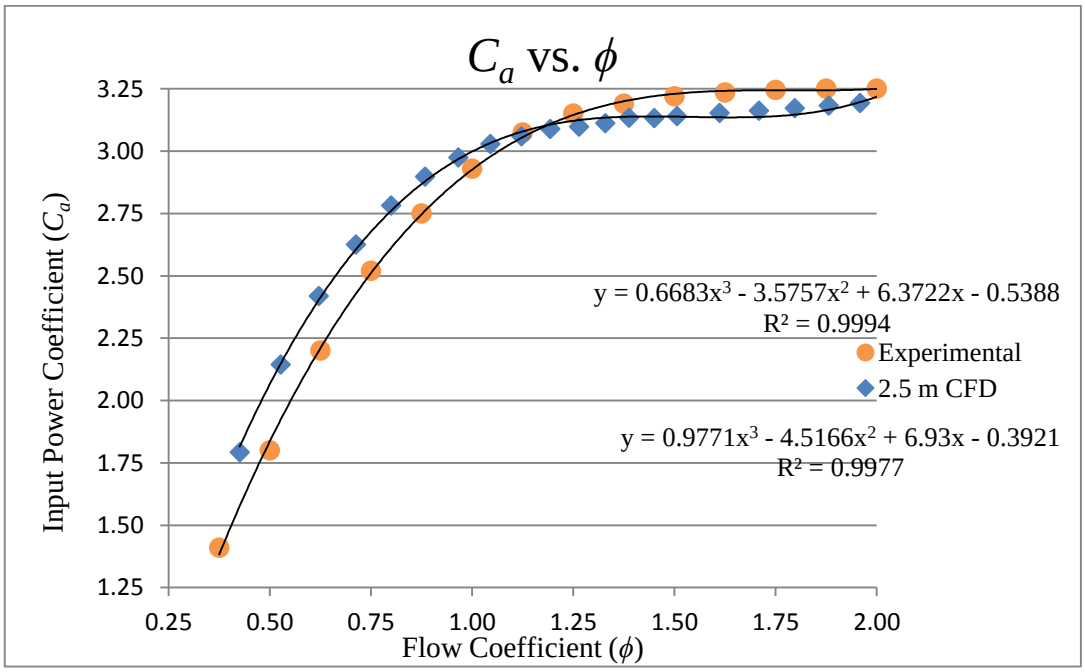

Fig. 4.16: C_a vs ϕ, experimental results for 300mm turbine [41, 102] against CFD results for 2.5 m turbine at 24 rads·s^{-1}.

4.4.2.3. MEAN SQUARED ERRORS

For further analysis, the flow coefficients from the CFD results for the 2.5 m turbine were used in equation (4.21) to calculate the corresponding values of C_t and C_a that were established for the experimental data for the 300 mm turbine. Fig. 4.17 is a plot of the MSE for the 300 mm turbine experiential and 2.5 m turbine CFD generated data for both C_t and C_a vs. the flow coefficient, ϕ.

The torque coefficients, C_t, of the 2.5 m turbine that were established through CFD simulations using SolidWorks Flow Simulation were similar in deviation from the experimental data to the 300 mm CFD results at lower flow coefficients, but as the flow coefficient increases, the deviation of the 2.5 m turbine is higher than that of the 300 mm turbine. The average MSE of the experimental and simulated data for C_t was found to be 0.00082. As stated earlier, this potentially is related to the difference in scale and how it may affect torque generated by the turbine blades. Even with this deviation, the MSE of the results is just slightly above 0.02, which correlates to 1% of the value of the torque coefficient.

The error between the CFD generated and experimental data were found using the flow coefficients from the CFD results in equation (4.18) to calculate the corresponding experimentally determined values of C_a, the calculated value of the MSE was 0.014. The higher errors found between the experimental data and the simulated data were again present at low values of the flow coefficient, ϕ, with the largest squared error value is 0.049 where $\phi = 0.53$, while the values of the squared error drops below 0.01 where $\phi > 0.9$.

The same uncertainties in pressure calculations that existed when comparing the 300 mm turbine simulations to the experimental data are present when comparing the 2.5 m turbine simulations to the experimental data. The CFD results for the torque coefficient, C_t, and the input power coefficient, C_a, from both the 300 mm and 2.5 m turbine simulations have a maximum MSE of 0.023, and the graphs of the results show that the experimental and simulated data follow the same trends. These results, coupled with the prior use of CFD in place of experimental results in evaluating impulse turbine performance, lend confidence to the accuracy of information gathered on the 2.5 m turbine from CFD. Therefore, the performance data collected from the CFD simulations were used to determine the mathematical formulas necessary to incorporate the 2.5 m impulse turbine into the model presented in Chapter 3.

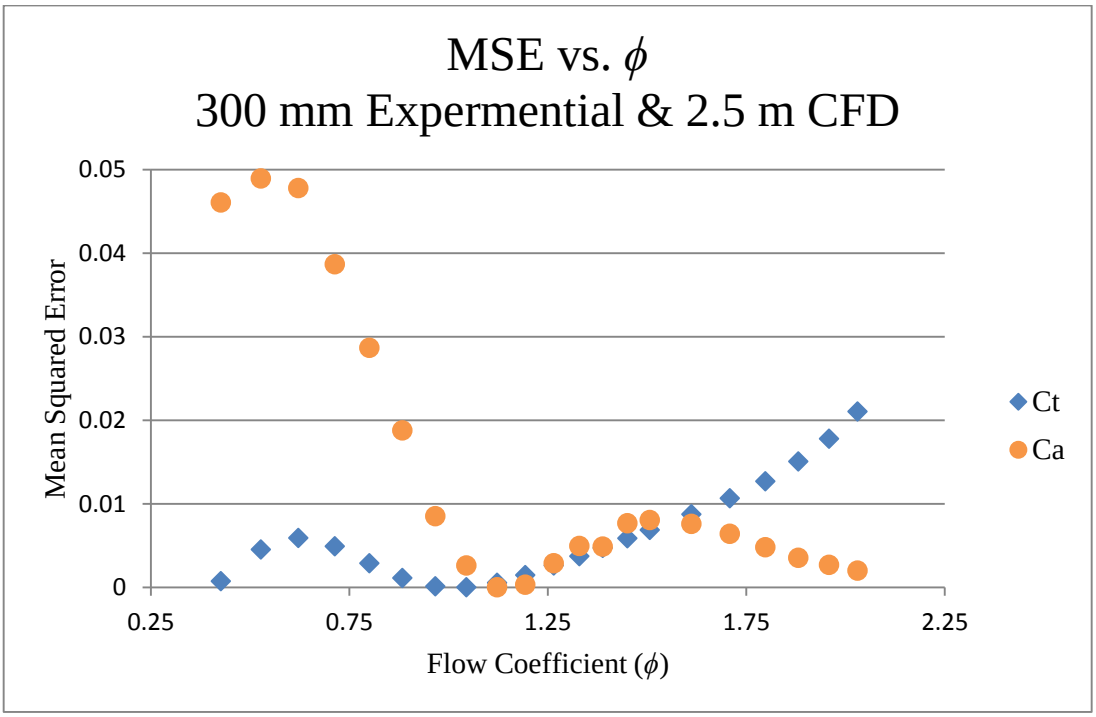

Fig. 4.17: Mean Squared Error vs ϕ for 300 mm experimental results and 300 mm CFD generated results of C_t and C_a.

4.5. MATHEMATICAL PERFORMANCE CHARACTERISTICS FOR MODEL

Upon confirming the accuracy of the CFD results, the data were used to create polynomial equations governing pressure drop across the turbine and mechanical power conversion based on those presented in [52]. The data collected though CFD modelling contained enough information to determine the coefficients of the polynomial functions based on the flow coefficient, Φ, presented in Chapter 2 in (2.22) though (2.24) and (2.30). The performance characteristics used in the numerical model, are related to, but different from, those presented by Setoguchi [102]. These equations were used because they are a less complex means for evaluating device and control algorithm performance. For convenience, the flow coefficient, Φ, its relationship to Setoguchi's flow coefficient, ϕ, and the related functions are reprinted below:

$$\Phi = \frac{Q_p}{(\omega D^3)} = 0.17\phi, \tag{4.24}$$

$$\Psi = \frac{P_m}{(\rho \omega^3 D^5)} = f(\Phi), \tag{4.25}$$

$$\Upsilon = \frac{\Delta p}{(\rho \omega^2 D^2)} = g(\Phi), \tag{4.26}$$

$$H = \frac{P_m}{\Delta p Q_p} = \frac{\Psi}{\Upsilon \Phi} = h(\Phi), \tag{4.27}$$

$$k = \frac{\Delta p}{Q_w^2} = k(\Phi). \tag{4.28}$$

The functions $f(\Phi)$, $g(\Phi)$, and $k(\Phi)$ are polynomials with 3rd-order, 2nd-order, and 2nd-order relationships, respectively, with the flow coefficient as dictated by the formulas presented in (4.25), (4.26), and (4.28). The polynomial equations are developed by using the data created during CFD simulations to find the values of Ψ, Y, and k for each data set.

The CFD simulations provided the values of the flow across the turbine, Q_p, the rotational velocity of the turbine, ω, the pressure drop across the turbine, Δp, and the mechanical torque exerted on the turbine, T_o. These values were used to calculate the values of the flow coefficient¸ Φ, the non-dimensional power coefficient, Ψ, the non-dimensional pressure coefficient, H, and the damping coefficient, k, of the turbine at steady state conditions with set rotational velocities. There were five different rotational velocities chosen for the CFD simulations that were based on the anticipated operating range of the turbine. The five velocities were 18 rads·s^{-1}, 21 rads·s^{-1}, 24 rads·s^{-1}, 28.5 rads·s^{-1}, and 36 rads·s^{-1}. Using five different rotational velocities created five subsets of data, and each set had unique results for the values of the various calculated coefficients.

With the data collected, the MATLAB curve fitting application was used as before to find the coefficients of the polynomials for the non-dimensional power, Ψ, non-dimensional pressure, Y, and damping functions, k, so they could be used in the numerical model to model the behaviour of the turbine based on the rotational velocity of the turbine and the volumetric flow across it. A single curve was fitted to the five resulting curves for each of the three polynomials. A single average curve was chosen because the turbine is applied in the model as a variable speed turbine. The rotational velocity will constantly change during model simulation and will never remain at a single value. Having found through the CFD simulations that the power, pressure, and damping curves of the turbine change as the rotational velocity changes, it was decided to use a single curve rather than apply the five curves depending on rotational speed. This was done because neither solution would be perfect, and applying a single curve for each function simplified the model without significantly compromising the accuracy of the model.

4.5.1. POWER COEFFICIENT

Curve fitting was performed by combining the results of each of five rotational velocities to find the equations characterising the mechanical power output, the pressure drop across the turbine, and the damping coefficient of the turbine. Fig. 4.18 is a plot of the graphs generated from the CFD data for the non-dimensional mechanical power equations.

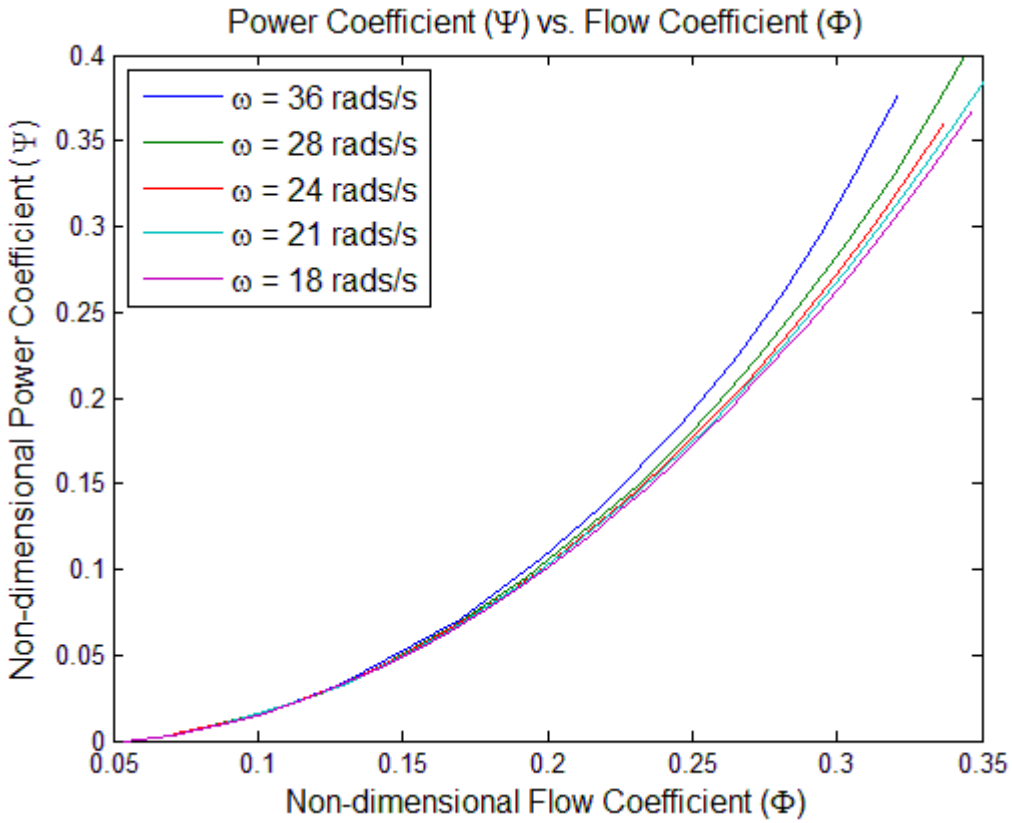

Fig. 4.18: Non-dimensional mechanical power, Ψ, vs. flow coefficient, Φ, for 2.5 m impulse turbine based on the results of CFD simulations.

As the flow coefficient increases, the values of Ψ at the various rotational velocities begin to diverge; at higher flow coefficients, Φ, a higher rotational velocity of the turbine leads to sharper gains in the power coefficient, Ψ. Due to this divergence at high flow coefficients, the equation of the curve fit to the data will not have a perfect R^2-value. As presented in (4.25), the power coefficient is a cubic polynomial of the flow coefficient, Φ, so the curve fit was based on the 3rd-order polynomial:

$$\Psi = 3.766\,\Phi^3 + 2.03\,\Phi^2 + 0.01036\,\Phi - 0.009798, \qquad (4.29)$$

with an R^2-value of 0.9911. Fig. 4.19 shows the results of the MATLAB curve fitting application when it was applied to all five of the data subsets.

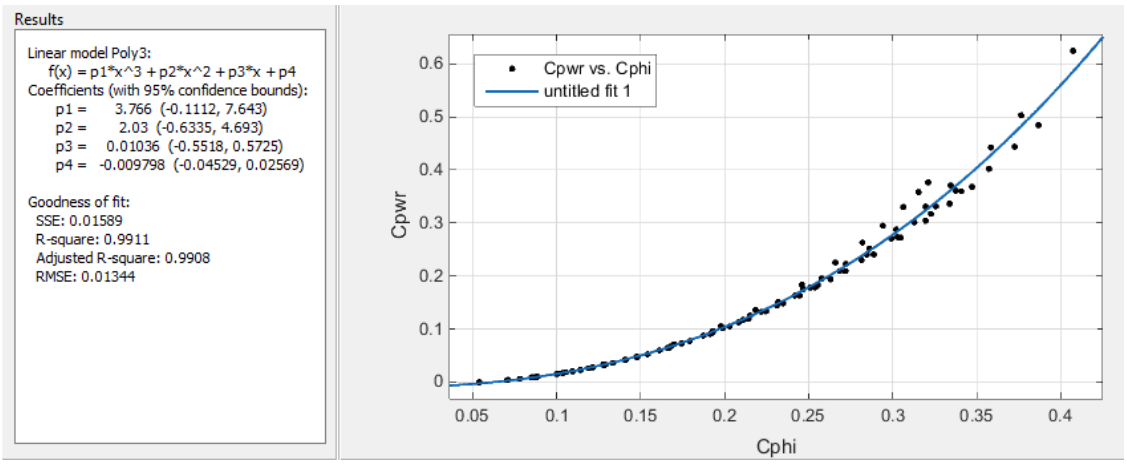

Fig. 4.19: MATLAB curve fitting application for the non-dimensional mechanical power data generated through CFD simulations.

4.5.2. PRESSURE COEFFICIENT

The same method was used to establish the non-dimensional equation that represents the pressure drop across the turbine. Fig. 4.20 is a plot of the graphs generated from the CFD data for the non-dimensional pressure drop equations. Similar to the divergence seen for the power coefficients, the values of Y at the various rotational velocities diverge as the flow coefficient increases. The changes in the pressure coefficients are more pronounced at higher flow coefficients than those of the power coefficients. The divergence will therefore have a greater effect on the R^2-value for the equation for Y created from the CFD generated data.

As presented in (4.26), the pressure coefficient is a quadratic polynomial of the flow coefficient, Φ, so the curve fit was based on the 2nd-order polynomial:

$$Y = 23.69\,\Phi^2 + 0.1413\,\Phi + 0.311, \tag{4.30}$$

with an R^2-value of 0.9481. Fig. 4.21 shows the results of the MATLAB curve fitting application when it was applied to the 5 data subsets.

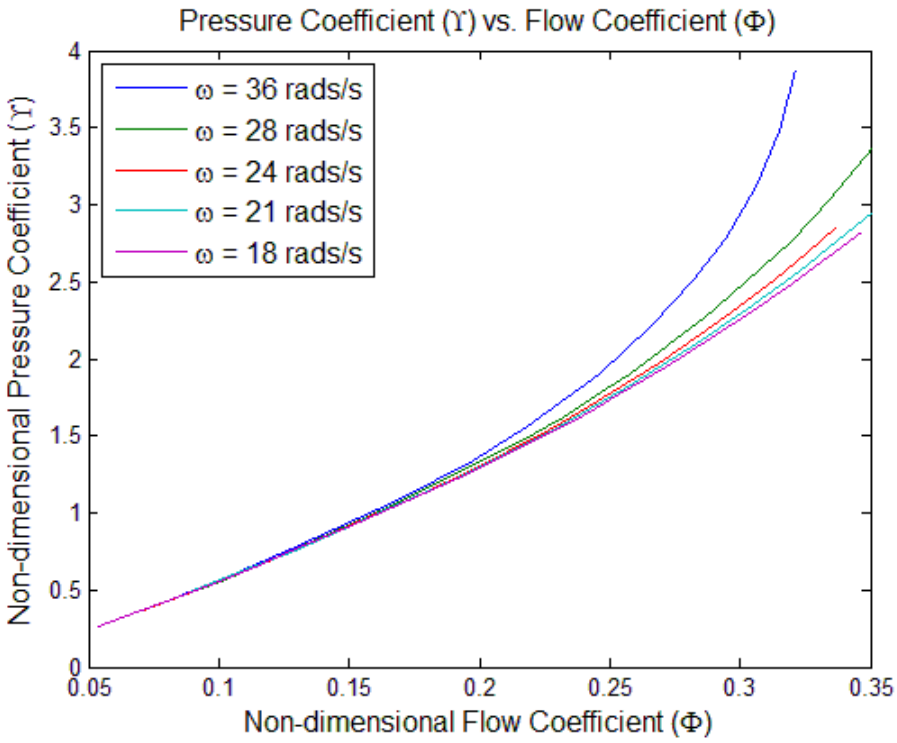

Fig. 4.20: Non-dimensional pressure vs. flow coefficient for 2.5 m impulse turbine based on the results of CFD simulations.

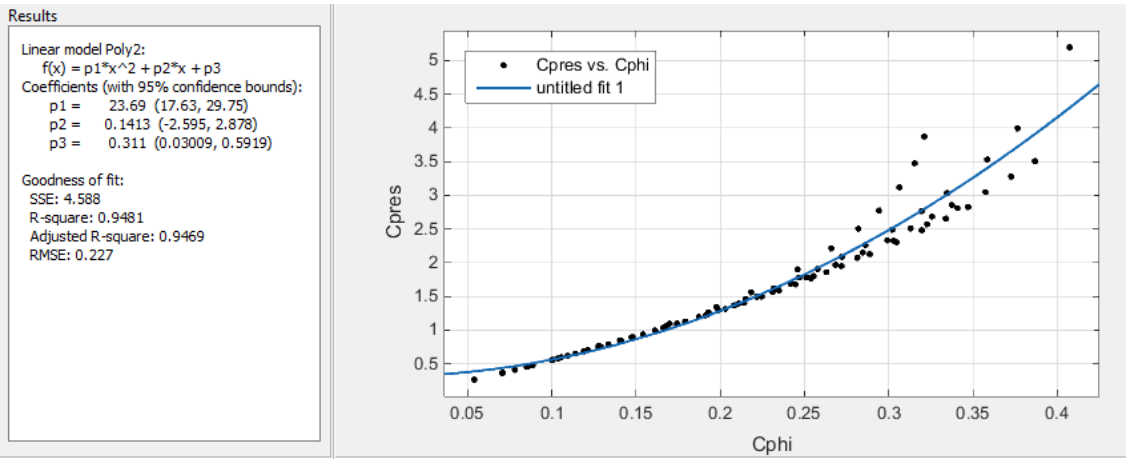

Fig. 4.21: MATLAB curve fitting application for the non-dimensional pressure drop across the turbine at a rotational velocity of 24 rads·s^{-1}.

4.5.3. DAMPING COEFFICIENT

The curve fitting was again used to find the quadratic equation used to represent the changing damping coefficient, *k*, of the turbine at different flow coefficients. The changes in the turbine response for the different rotational velocities at higher flow coefficients were most pronounced when determining the damping coefficient. Fig. 4.22 is a plot of the graphs generated from the CFD data for the non-dimensional

pressure drop equations. The graphs show a similar, more pronounced increase in slope and separation of the data as the value of Φ increases.

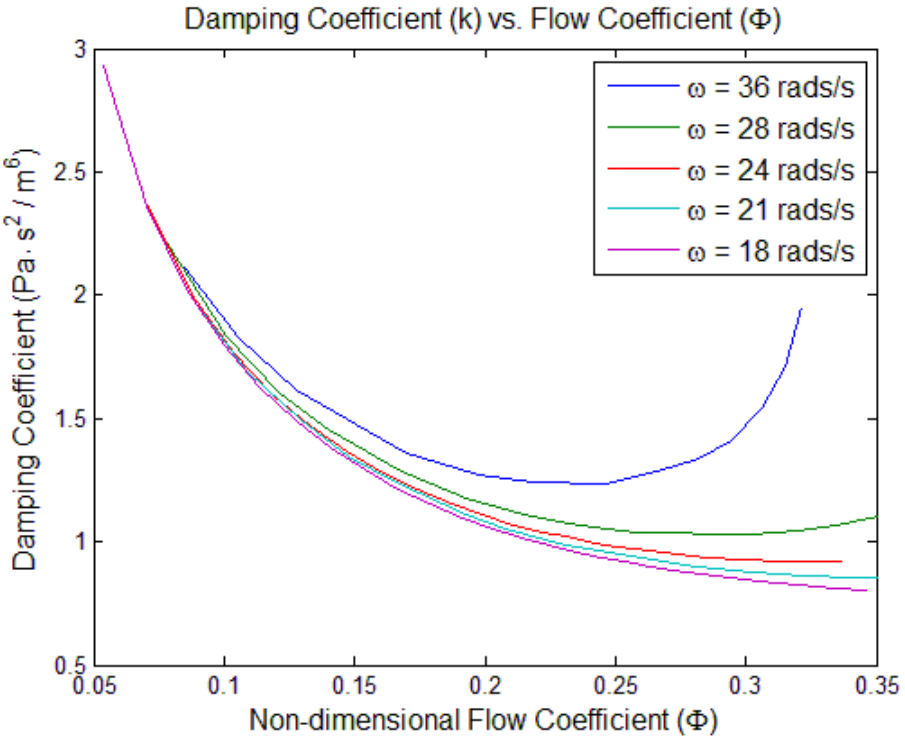

Fig. 4.22: Damping coefficient vs. flow coefficient for 2.5 m impulse turbine based on the results of CFD simulations.

As seen in Fig. 4.22, at flow coefficients above 0.25, the damping coefficient of the turbine at a rotational velocity of 36 rads·s^{-1} diverges sharply from those calculated at lower rotational velocities. This result had an outsized influence on the equation generated with MATLAB to represent the damping of the 2.5 m impulse turbine. As the data for all five rotational velocities was generated through the same procedure and no valid reason can be found to disregard the results of the CFD simulations at 36 rads·s^{-1}, the data was included in the curve fitting procedure and the resulting equation was used in the model. The effects of this change were noted and addressed where necessary in this thesis.

As presented in (4.28), the damping coefficient is a quadratic polynomial of the flow coefficient, Φ, so the curve fit was based on the 2nd-order polynomial:

$$k = 27.47\,\Phi^2 - 15.55\,\Phi + 3.156, \tag{4.31}$$

with an R^2-value of 0.776. Fig. 4.23 shows the results of the MATLAB curve fitting application when it was applied to the five data subsets.

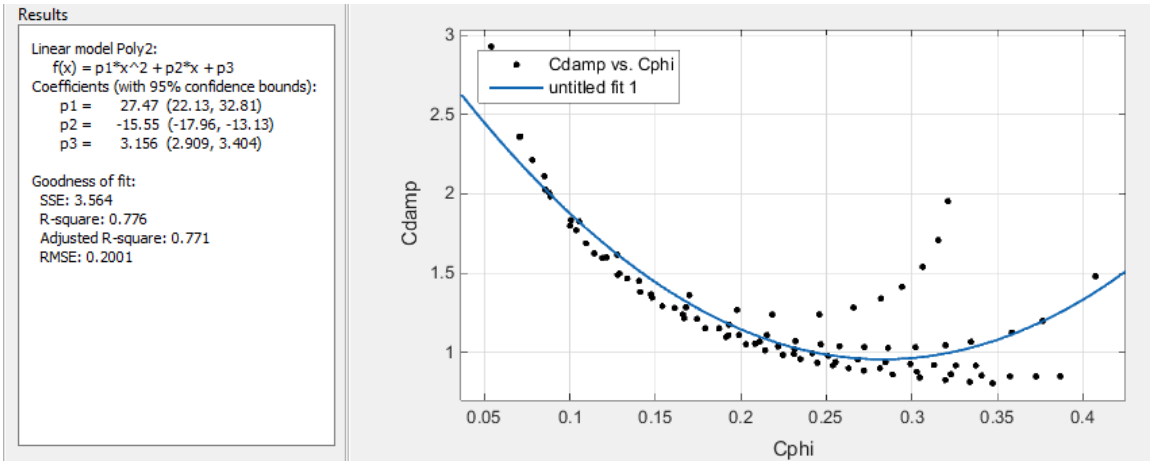

Fig. 4.23: MATLAB curve fitting application for the non-dimensional pressure drop across the turbine at a rotational velocity of 24 rads·s^{-1}.

The R^2-values of equations generated for the power and pressure coefficients were 0.9911 and 0.9481 respectively, showing that results from the CFD testing for the five rotational velocities lend to high rates of confidence in using the presented equations for the wave-to0wire model. At 0.776, the R^2-value for the equation generated to represent the damping coefficient of the turbine was less consistent, with the results of the turbine tests at 36 rads·s^{-1} significantly contributing to a weaker R^2-value and affecting the damping values, particularly at the low and high flow coefficients.

4.6. CONCLUSIONS

In this chapter, a 300 mm diameter impulse turbine was drawn in SolidWorks and CFD simulations were then performed using Flow Simulation. To verify that the CFD engine was able to produce accurate models, the results of the simulations were compared to the published results from experimental laboratory tests of the 300 mm turbine. Following the verification of the CFD engine, a 2.5 m diameter impulse turbine, based on the original 300 mm turbine, was designed to fit a full scale BBDB OWC with the deployment location chosen to be off of the west coast of Ireland. A geometric model of the design was drawn using SolidWorks, and the turbine was then simulated using Flow Simulation. The 300 mm and 2.5 m turbine CFD results were compared to identify any differences that may be caused by the difference in scale between the 2.5 m turbine and the experimentally evaluated 300 mm turbine.

The data generated though the CFD simulations for both the 300 mm and 2.5 m turbine showed good agreement with the experimental data available through publications. The CFD results did not perfectly match the experimental data, but the shapes of the curves developed for both the input power and torque coefficients were similar. There were many possibly origins for the discrepancies between modelled and experimental data, including the locations where both flow and pressure were measured during simulations and experiments. The CFD modelling results were deemed accurate enough to be used to generate the equations needed to add the 2.5 m turbine to the numerical model.

The power, pressure, and damping coefficients were developed by fitting curves to the data points generated by the CFD simulations. The curve fits for the power and pressure coefficients were better approximations of the data points than was the curve for damping coefficient. The principal reason for the uncertainty found in all three was the results of the simulations performed at the highest rotational velocity. The results from the CFD simulations at 36 rads·s^{-1} diverge significantly from the rest of the results at high flow coefficients. A similar behaviour in the simulations at 28 rads·s^{-1} can also be seen, although, it is not as significant. These results act to weaken the accuracy of the model is limited at high rotational velocities and flow coefficients. More testing needs to be carried out on the turbine at higher rotational velocities both experimentally and mathematically, but such in depth studies were beyond the scope of this thesis, and the accuracy of the results at lower speeds and flows allowed for the single model to be applied to the testing performed in Chapter 5. As a results, the equations generated from the curve fitting were introduced to the full model in Chapter 5, where the model was used to test control and energy storage strategies.

5. CONTROL STRATEGY AND SHORT-TERM ENERGY STORAGE TESTING

The final stage of the work performed for this thesis involved using the new turbine model in the full model to investigate the short-term energy storage capacity of an impulse turbine in an OWC and to compare its performance against a more traditional turbine with no short-term energy storage. The models used in this chapter included two variables, turbine inertia and the turbine control algorithm. There were two values for the turbine inertia: one turbine inertia was designed to be as low as realistically possible and the other was as high as realistically possible, while both turbines remained aerodynamically identical. The different inertias cause different behaviour in the turbines and unique control algorithms had to be designed for each turbine to maximise design performance. For the high-inertia design, a second control algorithm was created, and it was designed to be adjusted depending on sea conditions. This second high-inertia turbine control algorithm was tested to investigate potential benefits of incorporated a more proactive controller. The turbine and controller design is detailed in this chapter, along with the process for selecting the sea states that were modelled.

The ultimate goal of an Oscillating Water Column (OWC) is the same as any conventional power station: to produce electricity of grid-acceptable quality at a reasonable cost of production. Two of the greatest challenges faced by OWCs and other Wave Energy Converters (WECs) are related to the quality of the power produced and the overall efficiency of energy conversion. New innovations are consistently being developed and tested in an attempt to improve device efficiency and output power quality. Often these innovations, such as movable guide vanes [118], airflow control valves [69], and supercapacitors [119], add extra mechanical and electrical complexity to the initial system. The added complexity can introduce additional failure points to the device, which can increase down time and maintenance costs. There are methods for improving device performance without increasing device complexity and adding points of failure to the device. The solutions explored in this chapter, controller adjustment and increasing turbine inertia, offer an opportunity to improve device output performance without greatly increasing device complexity.

Due to the quick fluctuations of the pneumatic power available in an OWC, the turbine must be able to swiftly respond to the changing conditions to maximise conversion efficiency. To achieve the maximum efficiency during the trials presented

here, the turbine was designed and built using an aluminium alloy to be as light as possibly to minimise turbine inertia. By minimising the inertia, the turbine was more able to respond quickly to the demands of the controller, and the control algorithm for the aluminium turbine was designed to match the turbine to the oscillating airflows. Together the turbine and controller were able to maintain a pneumatic to mechanical power conversion efficiency throughout the duration of the testing that was near the turbine's maximum expected efficiency.

Simply maximising the conversion efficiency of a WEC ignores another major challenge of wave-to-wire energy conversion, as it maximises the oscillations in the output power generated by WECs. The power oscillations are caused by the nature of waves and how the energy is extracted, and OWCs, both fixed and floating, are no exception to these swings in energy production. To minimise the amplitude of the oscillations in the OWC modelled in this thesis, a second turbine model was designed using two materials of different densities. The turbine model was created to maximise the moment of inertia of the turbine while maintaining a realistic design that could be applied in practice. The added inertia of the turbine was used as a flywheel for mechanical power storage which could be used to mitigate the natural power fluctuations of the OWC. Due to the slower response of the high-inertia turbine to changes in the system, two control algorithms were designed to try to find a balance between maximising the turbine efficiency and minimising the power output fluctuations. One high-inertia control algorithm was designed to operate the turbine in all sea conditions. The second control algorithm was designed so that each sea state had a controller designed to match the expected conditions.

In all, two turbine models and three control algorithms were tested using the models presented in Chapters 3 and 4 in an effort to improve device performance. Both the turbine changes and the controller changes can be implemented without introducing new physical points of failure to the original design. They were tested over a range of ten different sea state conditions, with five 30-minute intervals for each of the ten sea states, resulting in 150 data sets. The results were presented and compared to determine the effects these changes had on the energy conversion of the device.

5.1. POWER QUALITY OF WAVE ENERGY CONVERTERS

The power quality of the electricity generated by renewable energy sources has long been an important issue in electricity distribution and delivery. Traditional sources of electrical generation such as fossil fuel and nuclear plants have full control over the energy used to generate electrical power and therefore have full control over the quality of the electricity produced. With renewable energy generation systems like wind, solar, and ocean energy, the input energy used in generation is not controllable. Inconsistencies in voltage, frequency, and current found in renewable energy generators can produce real power fluctuation, reactive power generation and absorption, and voltage waveform distortion resulting from harmonic currents injected into the grid [120]. These issues can cause problems on local grids, particularly weaker grids, which are common in areas where ocean energy is often available for generation. Power quality standards for grid-connected wind turbines have been well established to regulate issues like voltage flicker, power ramp rates, and voltage transients that can be caused by wind turbines [121]. Though no power quality standards designed specifically for WECs have yet been adopted into existing grid codes, they are certain to face similar scrutiny as wind turbines. To successfully produce usable electrical power, the fluctuations inherent to power generated from ocean waves must be successfully addressed.

Most WECs, including OWCs, are subjected to significantly higher fluctuations in output power when compared to wind turbines due to the cyclical energy available in ocean surface waves. Large power fluctuations can lead to load shedding on local grids and also cause unexpected disconnections in adjacent areas and even local blackouts [122]. The power fluctuations can also lead to the grid phenomenon of flicker. The term flicker was coined to describe the varying light intensity seen in light bulbs due to voltage variations on the grid. While flicker is generally not harmful to the physical grid and its components, it is a visual disturbance to electricity customers. Due to slow nature of the oscillations found in WEC generated electricity, WECs are particularly likely to generate flicker at rates that are widely noticeable to humans. In [122], a study simulating the impact of a wave energy farm producing up to 19 MW was producing using the data collected from the CORES project deployment investigated the potential impact of a small wave farm on the local grid. The study found that an OWC based

wave farm does not pose either an over-voltage or under-voltage threat, but that flicker level is of serious concern. It also concluded that increasing the number of units in a farm can decrease the level of flicker, and that the introduction of means of power storage may dramatically decrease the number of units required to decrease flicker levels.

5.2. ENERGY STORAGE

Energy Storage Systems (ESSs) have long been considered as a tool to help mitigate the uncertainty in quality and availability posed by renewable energy generation [123]. There are several methods of energy storage that have been investigated over recent years. The solutions that have been explored include pumped hydro [124], chemical batteries [125], hydrogen production [126], compressed air [127], supercapacitors [128], and flywheels [129]. Each ESS solution has strengths and weaknesses, and when selecting an ESS solution for a renewable energy system, the solution should best match the requirements of the renewable energy generator. The main requirements of an ESS for an OWC are quick response time and high cycle lifetimes. These requirements are necessary to combat the flicker caused by the oscillating nature of the waves. The two forms of ESS that best match the needs of a single WEC are supercapacitors and flywheels. Each can be added on to a WEC to improve the quality of the output power of an individual device, and the use of supercapacitors and flywheels in an OWC with a Wells turbine were investigated and compared in [130]. The study determined that the use of supercapacitors allowed for maximisation of turbine efficiency but requires over-rated power electronics due to high peak-to-average power ratios. Conversely, the use of the flywheel does not add any complexity to the electrical system, but it does sacrifice turbine efficiency. A study investigating the application of flywheels as ESS in more general WECs found that while flywheels are not as efficient as batteries, they are suitable for offshore WECs because they require little maintenance, have a long life, and a fast response time [131].

Due to the power take-off design of the OWC, the turbine offers the opportunity to add a flywheel ESS into the system without adding any additional mechanical or electrical complexity to the system. While using a high-inertia Wells turbine for ESS in OWCs has been investigated, the use of high-inertia impulse turbines has remained largely unstudied. The operational rotational velocity of a full scale impulse turbine,

approximately 200-400 rpm, is much lower than the operational rotational velocity of the Wells turbine, approximately 1200-1500 rpm, and can therefore not store as much energy. However, the impulse turbine is not susceptible to aerodynamic stall, making it less likely to suffer large efficiency losses at high flow coefficients. One aim of this chapter is to investigate the effectiveness of using a high-inertia impulse turbine as an ESS. Simulations were performed using both a high-inertia and low-inertia impulse turbine to evaluate the benefits and drawbacks of using each type of turbine.

5.3. TURBINE INERTIA SELECTION AND DESIGN

The goal of the turbine design was to have two aerodynamically identical impulse turbines with different moments of inertia, so that the feasibility of using mechanical power storage to improve the output power quality of a BBDB OWC with an impulse turbine could be investigated. The differences in inertia were created by using materials with different densities to fabricate the turbine and thus how the mass was distributed throughout the turbine. The materials were selected based on the ability to be used in genuine OWC design. The SolidWorks Mass Properties Application was used to determine the mass and moment of inertia of the turbines, and the moment of inertia was used in the model to determine turbine behaviour.

The low-inertia turbine was selected to be fabricated out of the aluminium alloy A356.0. Alloy A356.0 has very good corrosion resistance, is excellently suited for all common welding methods, has good machinability, and good tensile strength. It also has one of the lowest densities of all aluminium alloys, and a turbine fabricated using the alloy would have one of the lowest available moments of inertia. The hub of the turbine was hollowed out to minimise the amount of mass and inertia that the turbine possessed.

The data produced by the Mass Properties Application available in SolidWorks showed that the impulse turbine, if fabricated using the aluminium alloy A356.0, had a mass of 1621.82 kg, and that it had a moment of inertia at the rotational point of the turbine of 1381.42 $kg \cdot m^2$. The available energy storage of the low inertia turbine at a rotational velocity of 24 $rads \cdot s^{-1}$ was approximately 397.8 kJ, which would be equal to 99.5 kW if the energy was extracted over a half wave period of 4 seconds.

The high-inertia turbine was designed to be fabricated out of two separate materials in order to maximise the inertial potential of the turbine while striving to keep the mass at a reasonable value. The majority of the hub of the turbine was again designed to be

hollowed out and composed of aluminium alloy A356.0. The outer ring of the hub and the turbine blades were selected to be composed of ferritic stainless steel. Stainless steel has a very high density and is relatively corrosion resistant. Although stainless steel can be more susceptible to corrosion in high-salinity environments and more research would be required before final application in an OWC, it was considered to be a good candidate for use in the high-inertia turbine model design for this thesis. By minimising the mass of the hub of the turbine, while maximising the mass of the outer ring and blades, the design seeks to maximise inertia to mass ratio. Fig. 5.1 shows the aluminium alloy turbine and the stainless steel turbine with aluminium alloy hub side-by-side as they appear in SolidWorks.

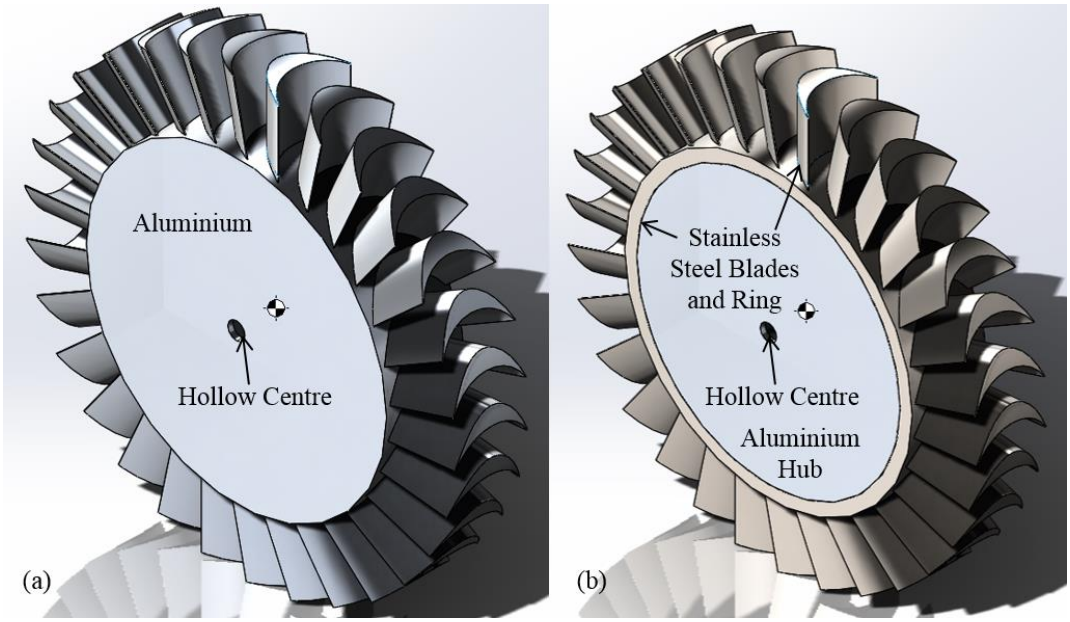

Fig. 5.1: Presents (a) the low-inertia aluminium alloy A356.0 impulse turbine minimises turbine mass and inertia and (b) the high-inertia impulse turbine composed of blades and outer ring of stainless steel with an inner hub hollow made of aluminium alloy A356.0 maximise inertia while minimising turbine mass.

The data produced by the Mass Properties Application available in SolidWorks showed that the impulse turbine, if fabricated in two parts using stainless steel for the outer portion of the turbine and the aluminium alloy A356.0 for the inner hub, had a mass of 6270.29 kg, and that it had a moment of inertia at the rotational point of the turbine of 4546.71 kg·m^2. The available energy storage of the low-inertia turbine at a rotational velocity of 24 rads·s^{-1} was approximately 1309.5 kJ, which would be equal to 327.4 kW if the energy was extracted over a half wave period of 4 seconds. The high-

inertia turbine thus had approximately 3300 times as much energy storage capacity as the low-inertia turbine. With the high and low-inertia turbines designed and categorised, the sea states to be tested were determined and the turbine control algorithms were developed for final model testing.

5.4. SIMULATED SEA STATES AND INTERNAL WATER SURFACE MOTION

The performance of the system was tested in irregular seas created through MATLAB modelling and simulated with low and high inertia impulse turbines and several torque-speed control algorithms. The wave climate simulations were formulated using various Bretschneider spectra based on the common significant wave heights and wave periods seen at the selected site of the M1 buoy in the North Atlantic (53°7.6'N 11°12'W) [111]. Equation (2.1) represents the Bretschneider spectrum and is reproduced below for convenience:

$$S(f) = \frac{5}{16} H_s^2 * {f_m^4}/{f^5} * e^{-1.25\left({f_m}/{f}\right)^4}. \quad (5.1)$$

Irregular sea state surface elevation arrays were produced by combining sinusoidal waveforms as described in Section 2.1.1. To find the motion of the Internal Water Surface of the BBDB chamber in the generated sea, the surface elevation arrays were combined with the RAO produced by the WAMIT model. The RAO was multiplied to the initial amplitude for every sinusoidal waveform before the wave forms were added together. The sum of the waveforms results in the motion of the Internal Water Surface given in equation (2.5) and is reproduced here for convenience:

$$IWS(t) = \sum_{n=0}^{n-1} RAO(n\,df) A_w(n\,df)\ \sin(2\pi n\,dt + \theta_n). \quad (5.2)$$

In Chapters 2 and 3, the RAO that was applied to the wave surface elevation arrays came from the hydrodynamic analysis of the 1:4 scale BBDB OWC deployed in Galway Bay during the CORES project. For the simulations performed in this chapter, a full scale BBDB OWC was tested, and the full scale buoy required its own unique RAO function. The plot in Fig. 4.2 represents the RAO of the IWS of the BBDB OWC vs. wave period in s and is reproduced below in Fig. 5.2.

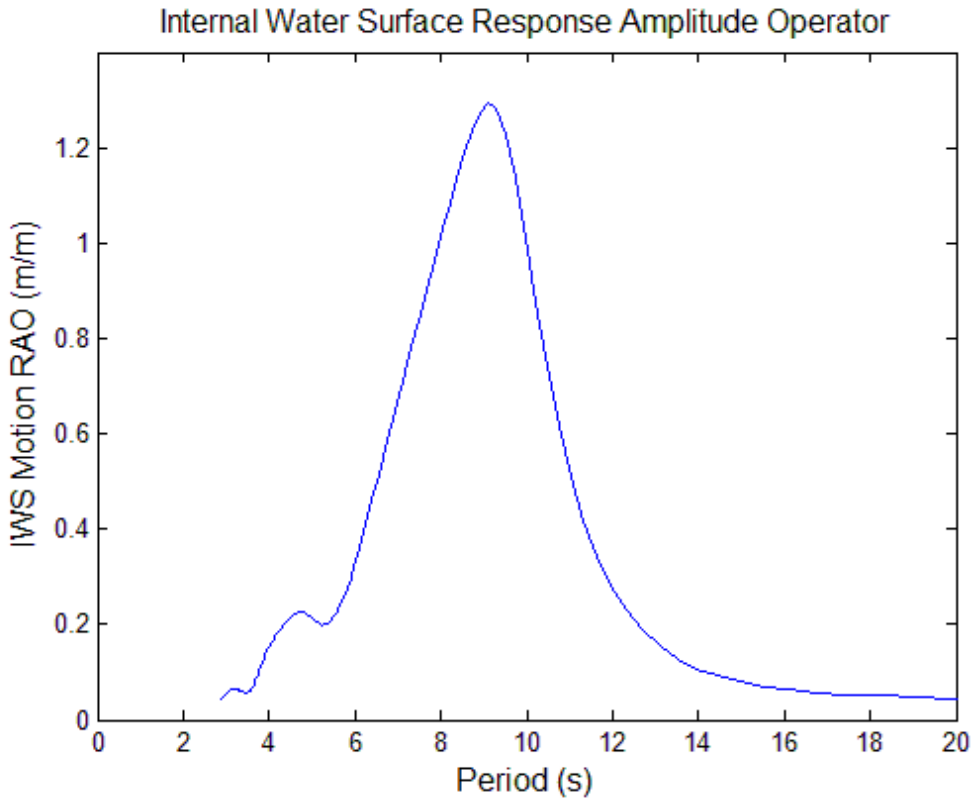

Fig. 5.2: RAO vs. wave frequency for the BBDB tested, as determined by WAMIT simulations.

While this method is a good way to create a realistic motion of the IWS based on an irregular sea state, it is not without limitations. Due to the linearity of the WAMIT simulations, the RAO can only be applied to sea states where the significant wave height, H_s, is below 4 m. The WAMIT RAO model is calculated based on a linear response for all wave heights, however as H_s approaches 4 m, the real device response becomes non-linear. Due to the linearity inconsistency of OWC, the scaling of the IWS calculated by the WAMIT RAO becomes increasingly uncertain, and the model can no longer be relied upon. This limits the amount of sea states that can be modelled for this thesis and required some adjustments in Bretschneider sea states selected for testing.

The typical Bretschneider conditions experienced off the west coast of Ireland are represented by fifteen different sea states, which are shown in Table 5.1, with the dashed line indicating the 4 m H_s cut-off point. These sea states are based on the average conditions seen throughout a 12-month period.

T_p(s)	5.65	7.07	8.49	10.61	12.73	14.14	17.68
H_s(m)							
9							
8					B10	B14	
7.5				B08			
7						B13	
5			B05	B07	B09		B15
3.5							
3		B02	B04	B06		B12	
2	B01						
1			B03			B11	

Table 5.1: Bretschneider sea state conditions found along the west coast of Ireland; the dashed line represents the limitations of the hydrodynamic model.

Due the inability to affectively simulate a number of sea state conditions represented in Table 5.1, an alternative set of sea states was created for testing to widen the number of conditions that could be tested. Additionally, the sea states B01, B03, and B11 did not produce enough pneumatic energy to consistently drive the turbine, so they were also replaced by more energetic sea state conditions.

The sea states selected for the testing carried out in this chapter were required to meet two necessary conditions. The first was that the significant wave height was limited to below 4 m; the second was that there had to be enough energy in the sea state to continuously drive the turbine during operation. The first condition was easily met, but to be assured that the second condition was also met, the sea state had to be tested with both the low and high inertia turbines and all three control laws. The final result of the selection process resulted in ten sea states chosen for testing, and the ten sea state conditions presented in Table 5.2.

T_p(s)	6.35	7.07	7.74	8.49	9.5	10.61	11.64	12.73	14.14	15.9
H_s(m)										
3.5			B03		B05		B07			B10
3		B02		B04		B06		B08	B09	
2.5	B01									

Table 5.2: Bretschneider sea state conditions found along the west coast of Ireland and were tested in the model for the simulations performed in Chapter 5.

Once the ten sea states were selected, five iterations of IWS motion for each sea state were created using (5.1) through (5.5). They resulting arrays were tested within the

SIMULINK model used to represent the thermodynamic and turbine systems of the BBDB OWC as presented in Chapter 3. The five different iterations were created to minimise any bias that could be found in a single sea state test. The results for the different iterations were averaged, and the average values are presented in the results section of this chapter.

5.5. DEVICE CONTROL STRATEGIES

The amount of pneumatic energy produced by an OWC varies significantly from sea state to sea state, wave group to wave group, and wave to wave. As the pneumatic energy changes, so too does the airflow across the turbine, and these fluctuations negatively affect the performance of the turbine. Therefore, the turbine efficiency depends significantly on the implemented control strategy [132]. Two distinct control strategies have been deployed and tested in OWCs; turbine rotational speed control and air flow control [14]. Turbine rotational speed control is achieved using a variable speed drive with the system generator [133]. Airflow control has been attempted both using valves mounted in parallel with the turbine and using valves mounted in series with the turbine duct. Turbine by-pass valves have also been used to control the air flow across the turbine to help avoid stall in Wells turbines [69]. For the simulations carried out in this section, turbine rotational speed control was used to investigate the effectiveness of using a high-inertia impulse turbine as a form of on-board power storage. The results investigated were output power, conversion efficiency, and power quality.

Three different turbine control strategies were implemented in the model simulations. The control strategies were based on optimum speed control through turbine torque estimation. For each controller, the electrical braking torque applied to the generator was calculated using the rotational speed of the turbine. The control of the low-inertia impulse turbine controller was based on Maximum Power Point Tracking (MPPT), which sought to optimise instantaneous turbine efficiency by matching the electrical braking torque to the torque expected to be produced by the turbine at maximum efficiency. Due to the slower response of the high-inertia turbine, the MPPT strategy applied to the low-inertia turbine was unsuitable for the high inertia turbine. Two different strategies were implemented for the high-inertia turbine controller: i) used a fixed control algorithm regardless of the sea conditions, and ii) each sea state had its own unique algorithm. The two strategies were used to test the hypothesis that adjusting the controller to match the sea conditions will increase turbine and device efficiency.

5.5.1. LOW-INERTIA TURBINE CONTROLLER

The low-inertia turbine allowed for the control of the operating point to be almost instantaneous, as the turbine speed could respond more quickly to changes in mechanical torque induced by changes in flow as well as changes in the applied electrical braking torque. Thus, it offered the opportunity to maximise the overall efficiency of the turbine. A trade-off when using a low-inertia turbine is that the output power quality will suffer as the turbine offers little power storage, and the poor power quality will have to be offset elsewhere. However, to maximise the benefit of using a low-inertia turbine, the output power quality was not considered when selecting and optimising the controller.

To date, the only published impulse turbine control laws available were the result of the CORES project [54, 95] and the methods used to determine controller coefficients were not disseminated. Therefore, the control law for the low-inertia turbine was based on controllers designed for a Wells turbine in [130], which was built for MPPT by speed control through turbine torque estimation. The control law was designed to optimise turbine efficiency based solely on using the turbine rotational velocity to estimate the mechanical torque exerted on the turbine. The controller acts to match the electrical braking torque to the estimated mechanical torque, while maintaining a minimum speed below which the electrical braking torque applied goes to zero.

To match the turbine rotational velocity to the air flow, an optimal flow coefficient must be determined. The optimal flow coefficient, Φ_{opt}, was selected to match the point of the highest conversion efficiency of pneumatic-to-mechanical power by the turbine. The turbine characteristic equations determined in Section 4.5 were used to find the maximum efficiency point. The equations are reprinted here for convenience:

$$\Phi = Q_p/(\omega D^3), \tag{5.3}$$

$$\Psi = \frac{P_m}{(\rho\omega^3 D^5)} = 3.766\,\Phi^3 + 2.030\,\Phi^2 + 0.01036\,\Phi - 0.009798, \tag{5.4}$$

$$\Upsilon = \frac{\Delta p}{(\rho\omega^2 D^2)} = 23.69\,\Phi^2 + 0.1413\,\Phi + 0.3110, \tag{5.5}$$

$$H = \frac{P_{mech}}{\Delta p Q_p} = \frac{\Psi}{\Upsilon\Phi}, \tag{5.6}$$

where H is the turbine conversion efficiency. Fig. 5.3 is a plot of the pneumatic-to-mechanical power conversion efficiency of the impulse turbine for different values of the flow coefficient, Φ.

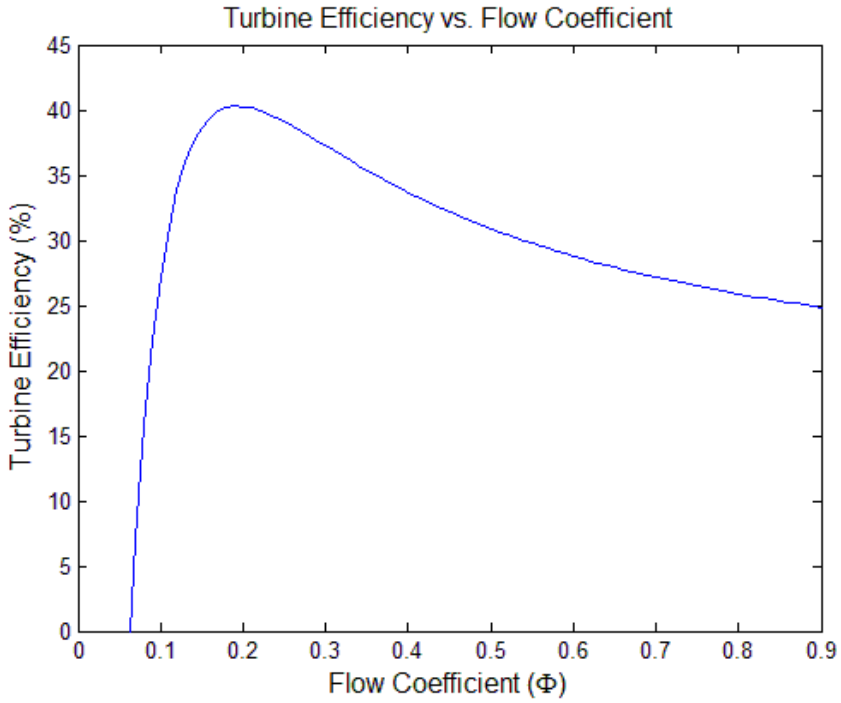

Fig. 5.3: Turbine efficiency vs. flow coefficient for the 2.5 m impulse turbine.

From the plot in Fig. 5.3, turbine efficiency peaks at flow coefficients between approximately 0.15 and 0.20 before trailing off beyond 0.25. To confirm turbine maximum efficiency, numerical model simulations were performed on the turbine at various flows and turbine speeds. By combining (5.3) through (5.5), the pneumatic and mechanical power can be calculated based on the flow coefficient and the rotational velocity of the turbine using:

$$P_m = \rho\omega^3 D^5 \,(3.766\,\Phi^3 + 2.03\,\Phi^2 + 0.01036\,\Phi - 0.009798), \quad (5.7)$$

$$P_p = \Delta p Q_p = \, Q_p \rho\omega^2 D^2 (23.69\,\Phi^2 + 0.1413\,\Phi + 0.311), \quad (5.8)$$

$$\eta = \frac{P_m}{P_p}, \quad (5.9)$$

where P_p is pneumatic power and η is turbine conversion efficiency.

To find the maximum efficiency of the turbine over various rotational velocities and flow coefficients, equations (5.7) through (5.9) were evaluated for a series of flows and rotational velocities. The pneumatic power values, P_p, were selected as fixed values from 50 kW – 1,000 kW in steps of 50 kW, and the values of the flow coefficient, Φ, were selected as fixed values from 0.05 – 0.90 in steps of 0.01. The rotational velocity of the turbine for a given pneumatic power and flow coefficient was calculated by combining (5.3) and (5.8) to produce

$$\omega = \sqrt[3]{\frac{P_p}{\rho \Phi D^5 (23.69\,\Phi^2 + 0.1413\,\Phi + 0.3110)}}. \tag{5.10}$$

After the rotational velocity was calculated, the flow across the turbine was calculated using (5.3). With the rotational speed determined, equations (5.7) and (5.9) were used to find the mechanical power and conversion efficiency of the turbine at each level of pneumatic power and flow coefficient. Fig. 5.4 is a plot displaying the mechanical power output of the turbine at different rotational speeds for each level of pneumatic power, represented by the coloured lines, and the optimal mechanical power based on rotational speed, represented by the black line.

From the results of the calculations, an optimal value for the flow coefficient, Φ_{opt}, was determined based on the maximum mechanical power potential for a given pneumatic power. The value of Φ_{opt} was confirmed at a value of 0.19, and the black optimum trend line in Fig. 5.4 represents the mechanical power output of the turbine when the conditions for Φ_{opt} are met.

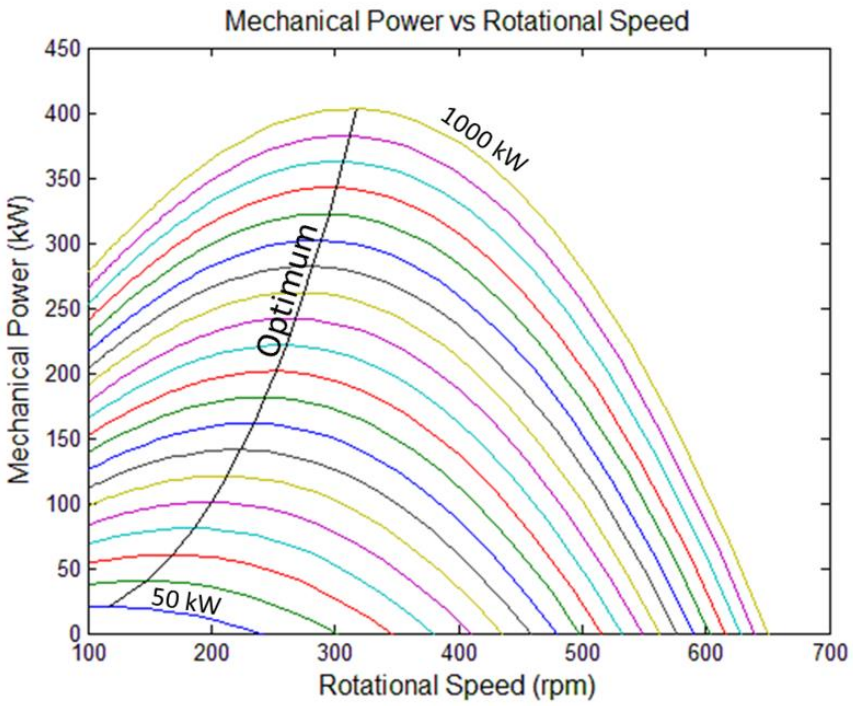

Fig. 5.4: Mechanical power output of the impulse turbine at different rotational speeds for pneumatic power from 50 kW to 1,000 kW in 50 kW steps and is represented by the various coloured curves. The optimal mechanical power based on rotational speed is represented by the black curve.

Using the optimal flow coefficient value, Φ_{opt}, and the optimal mechanical power values found in Fig. 5.4, an equation was developed to determine the electrical torque demand required for maximum power point tracking using turbine speed in rpm as the only variable in the equation:

$$T_{ref} = \rho\omega^2 D^5 \left(3.766\,{\Phi_{opt}}^3 + 2.030\,{\Phi_{opt}}^2 + 0.01036\,\Phi_{opt} - 0.009798\right), \quad (5.11)$$

$$T_{ref} = .1198 N_{rpm}^2, \quad (5.12)$$

where N_{rpm} is the rotational speed of the turbine in rpm. The equation used to estimate the optimal electrical braking torque depends on the turbine speed in rpm rather than rads·s^{-1} as it was the standard control algorithm input used in the publications researched for the work performed in this Chapter [95, 130].

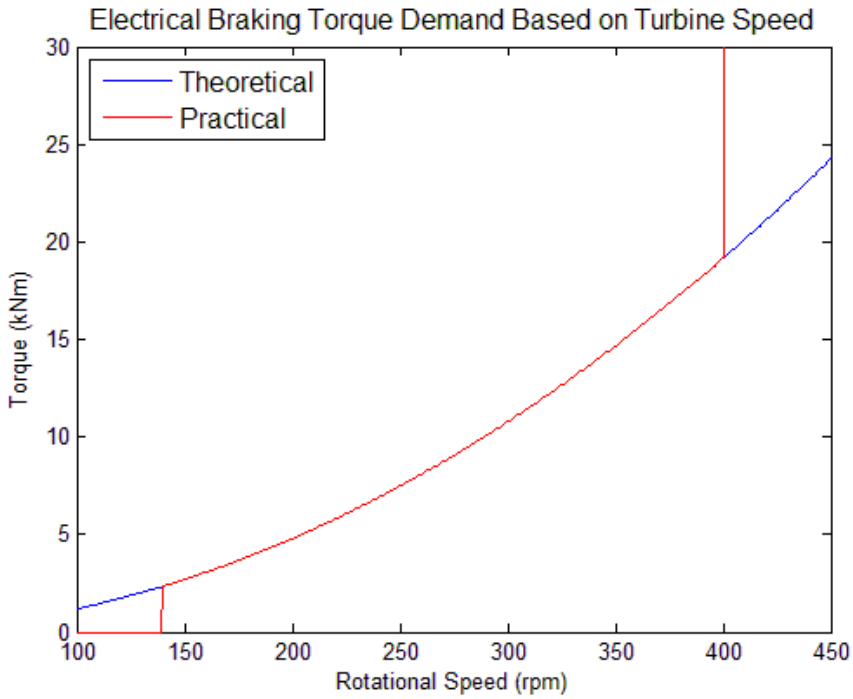

Fig. 5.5: Theoretical and practical values of the estimated electrical braking torque based on turbine speed produced by the low-inertia turbine control algorithm.

During operation of the controller, the braking torque determined in (5.12) is immediately applied to the electrical generator to control the turbine speed. For practical application, it is necessary to maintain a maximum and minimum rotational speed to keep the generator within its operating range of 140 to 400 rpm. Thus, when the rotational speed of the turbine drops below 140 rpm, the braking torque demand drops to zero, and when the speed is above 400 rpm, the maximum torque is applied to the turbine. Fig. 5.5 presents the theoretical and practical torque-speed curves used for maximum power point tracking of the low-inertia impulse turbine.

5.5.2. HIGH-INERTIA TURBINE CONTROLLERS

The nature of the power output of wave energy converters like an OWC can have negative impacts on the power systems and grids that they are feeding into. As previously discussed, the output power quality of an OWC has been shown have strong influences on local distribution systems, producing noticeable harmonic interference and causing events like flicker [23]. In an effort to mitigate the undesirable effects of wave energy conversion on output power quality of the OWC, the high-inertia impulse turbine was also tested using the model present in Chapter 3. A significant amount of

mass was added to the turbine, as detailed in section 5.3, to create a flywheel that could be used as a short-term energy storage system on board the BBDB OWC.

The added mass increases the inertia of the turbine, and the extra inertia acts as the ESS for the OWC power take-off system. Due to the flywheel behaviour of the turbine, the controller presented in the previous section for a low-inertia turbine does not present an ideal control solution for the high-inertia turbine, and a new control algorithm had to be adopted. Two separate approaches were taken when developing a controller for the high-inertia turbine. One approach, Control Law 1 (CL1), was based on a single torque-speed curve that would control the turbine in all sea conditions, while the second approach, Control Law 2 (CL2), involved developing a different torque-speed curve for each of the ten sea state conditions tested for this project.

For CL1, a single torque-speed equation was generated to match all expected sea states. The applied electrical braking torque increases gradually as the rotational velocity of the turbine increases, which minimises the change in output power and allows for a much more uniform injection of power into the grid during generation. It also allows for the turbine speed to self-correct; if the energy in the sea waves increases over time, the average rotational speed of the turbine will increase to match the changing sea conditions. CL1 requires no external input during operation, making it simple to apply.

The application of CL2 by contrast requires that the summary statistics of the current ocean conditions be fed into the controller. For the different sea states, different torque-speed equations were developed in an effort to maximise the pneumatic-to-mechanical power conversion of the turbine while allowing for the power smoothing effects of the flywheel ESS. The torque-speed curves applied in CL2 were designed to keep the turbine near the predetermined optimal speed for each sea state. The optimal speed was initially determined for the MPPT controller applied to the low-inertia turbine. The selection of the torque-speed curve applied to the turbine would be determined from outside data streams like high frequency wave radar, surface buoys, or medium term wave forecasts [134]. The methods applied for determining the torque-speed curves used in CL1 and CL2 are presented below.

5.5.2.1. CONTROL LAW 1: SINGLE TORQUE-SPEED CONTROL

A controller based on a single torque-speed curve was developed from a similar controller designed for a Wells turbine that was presented in [130]. The control

algorithm was built as a variable-speed solution that sought to set the changes in the rotational speed of the turbine on a sea state to sea state basis. The rotational speed of the turbine would change until it reached an optimum value according to the current sea state, and the transitions between optimal speeds would happen automatically without any outside information about the sea conditions.

To develop this control algorithm, Table 5.3 was created based on the optimum speed, mean power, and mean mechanical torque of the turbine for the various sea states to be tested. The table was developed based on the simulations run with the turbine set at different fixed speeds ranging from 15 rads·s^{-1} to 35 rads·s^{-1}. The steady rotational speed with the highest pneumatic to mechanical power conversion was selected as the optimum speed. The average mechanical power found during the 30minute simulation was considered to be the optimum power output, and the average torque selected for each sea state was based on the optimum mechanical power output and rotational velocity.

For each of the ten sea states tested, five different 30-minute randomised wave input arrays were created and applied to the model. The data presented in Table 5.3 represents the average results from the five sea states, and in Fig. 5.6 the experimentally-determined mean torque values were plotted against the optimum rotational velocities in rpm. The control algorithm was generated by fitting a curve based on a quadratic equation to the points plotted in Fig. 5.6. A quadratic was used because the torque generated by the turbine is based on the square of the speed, as shown in (5.14).

Sea State	Speed (rads/s)	Speed (rpm)	Mean Pneumatic Power (kW)	Mean Mechanical Power (kW)	Efficiency	Mean Torque (Nm)
B01	16	153	49.71	17.32	34.85%	1083
B02	24	229	121.62	42.03	34.56%	1751
B03	30	286	220.64	77.08	34.94%	2569
B04	28	267	188.15	66.03	35.10%	2358
B05	33	315	275.97	96.62	35.01%	2928
B06	28	267	181.90	63.39	34.85%	2264
B07	29	277	206.52	71.59	34.67%	2469
B08	24	229	116.42	40.06	34.41%	1669
B09	20	191	77.58	26.87	34.64%	1344
B10	19	181	75.87	26.14	34.46%	1376

Table 5.3: Optimum operating rotational velocity of the turbine at the tested sea states, with mean pneumatic and mechanical power, conversion efficiency of the turbine, and the mean torque value required to maintain the steady speed.

To generate the control algorithm, the mean torque was plotted against the rotational speed in rpm, and a curve was fitted to the data to create a torque-speed quadratic equation based on the rotational speed in rpm.

$$T_{ref} = 0.0299n_{rpm}^2 - 2.1779n_{rpm} + 712.84, \quad (5.13)$$

where T_e is the electrical torque demand to be applied to the generator during device operation. This equation will allow for the estimation of the optimum reference torque based on the rotational speed only, which optimises the turbine efficiency while allowing for smoothing of the output power of the generator. As was necessary for the low-inertia turbine control algorithm, a minimum speed at which torque was applied to the generator was set at 140 rpm. Fig. 5.6 presents the theoretical and practical torque-speed curves created from (5.13).

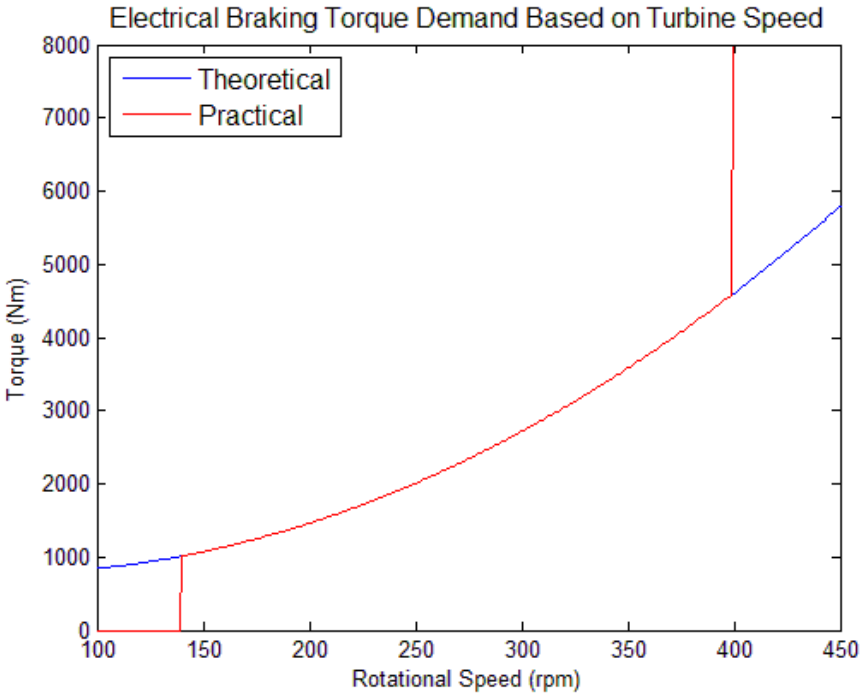

Fig. 5.6: Theoretical and practical values of the estimated electrical braking torque based on turbine speed produced by the high-inertia turbine control algorithm.

The high inertia of the turbine leads to a slower response to changes in energy in the ocean waves or electrical braking torque. Due to the slower turbine response, the range of the applied braking torque for CL1 is much lower than the range found in the low-

inertia MPPT controller. This lower range for the electrical braking torque allows for the excess energy to increase the speed of the flywheel, and the stored energy to be recovered gradually during periods of lower energy. The practical curve, which was the curve applied during simulations, was designed to allow the turbine to free wheel during times of low energy while keeping the turbine from overspeeding during times of high energy. The limits were placed on the turbine speed to maintain high pneumatic-to-mechanical efficiency based on expected average air flow velocities.

5.5.2.2. CONTROL LAW 2: SEA STATE DEPENDANT TORQUE-SPEED CONTROL

The second control law for the high-inertia impulse turbine investigated using the numerical model applied different torque-speed curves to the turbine based on current sea state conditions. Torque-speed curves were generated for the specific sea state conditions tested. The different torque-speed curves were used to attempt to increase the pneumatic to mechanical power conversion efficiency of the turbine while maintaining the power smoothing benefit created with the high-inertia turbine by more closely matching the turbine speed to the sea state conditions.

The sea state dependent controllers applied to the model with the high-inertia turbine were based on Strategy C presented in [132]. The electrical braking torque was determined by a prescribed continuous function of several state variables dependent on the sea state conditions. The controller was designed to allow the speed of the turbine to oscillate about a predetermined value chosen to maximise the efficiency of the turbine. Equation (5.14) presents the function used to determine the electrical braking torque for the sea state dependant controller.

$$T_{ref} = C\left[1 + \left(\frac{a_{CL}N_{max}}{N_{max}-N}\right)^{b_{CL}}\right]\left[1 - \left(\frac{y_{CL}N_{max}}{N-N_{min}}\right)^{z_{CL}}\right]N^2, \quad (5.14)$$

where C, a_{CL}, b_{CL}, y_{CL}, and z_{CL}, are constants that are dependent on the sea state conditions, and N_{max} and N_{min} are the minimum and maximum rotational speeds in rpm for the selected sea state.

The sea state dependent controller was designed to incorporate part of both the MPPT controller for the low-inertia turbine and the torque-speed curve used initially for the high-inertia controller to strike a balance between turbine efficiency and power smoothing. Like the single control algorithm presented in the previous section, the

predetermined rotational speed values were selected based on the values presented in Table 5.3, while the basis of the control law presented in (5.14) is similar to that used for the low-inertia turbine in (5.12) as it was based on a multiplier and the square of the rotational speed of the turbine. The multiplier was adjusted depending on the speed of the turbine and the sea state conditions rather than constant for all conditions. Table 5.4 shows the variables used for each of the ten sea states tested.

Subsets of values for each sea state were simulated for each sea state, and the values which resulted in the highest pneumatic-to-electrical power conversion efficiency are presented in Table 5.4. Initially, the value of T_e for each sea state was set at approximately 120% of the mean torque value at N_{opt}. N_{opt} was the same value used to determine CL1. N_{min} and N_{max} were selected to keep the turbine rotational speed near the optimum value. The determination of N_{min} and N_{max} were based on the value N_{opt} and trial and error, with the objective being to maximise turbine conversion efficiency during testing of the applied sea state.

	rpm			Constants				
Sea State	N_{opt}	N_{min}	N_{max}	C	a	b	y	z
B01	153	120	280	0.15	0.75	0.60	0.03	0.05
B02	229	130	350	0.13	0.60	0.50	0.06	0.05
B03	286	130	380	0.07	0.70	0.65	0.11	0.07
B04	267	130	360	0.06	0.75	0.80	0.11	0.08
B05	315	170	470	0.05	0.80	0.95	0.12	0.11
B06	267	130	370	0.06	0.75	0.80	0.11	0.08
B07	277	140	400	0.05	0.80	0.90	0.10	0.09
B08	229	130	360	0.11	0.60	0.50	0.06	0.05
B09	191	130	300	0.13	0.75	0.60	0.03	0.05
B10	181	130	310	0.12	0.70	0.55	0.03	0.05

Table 5.4: The values of the input variables for the sea state dependant torque-speed control algorithm for each of the ten sea state conditions tested.

The constants were chosen in a similar manner of trial and error, with the curve resulting from the equation to have a rate of increase that reflected the length of the period, T_p, such that the longer the period the slower the rate of increase of braking torque. The variables were first initially set based on the desired shape of the torque-speed curve. The final adjustments were made following simulation. The subset of values for the constants tested were as follows: C [0.05 0.06 … 0.14 0.15]; a [0.5 0.55 … 0.95 1.0]; b [0.5 0.55 … 0.95 1.0]; y [0.01 0.02 … 0.14 0.15]; z [0.01 0.02 … 0.14 0.15]. Fig. 5.7 is a graph of the torque-speed equations used for each sea.

Together, the ten curves plotted in Fig. 5.7 make up CL2. If the simulations were not limited to an H_s of 4 m or the device were being physically deployed, there would be at least 15 curves designed to match the sea states shown in Table 5.1. The range for the reference torque in CL2 is larger than the range in CL1, but it is still much smaller than the range for the MPPT applied for the low-inertia turbine. This is because the objective of CL2 is to allow for power smoothing using the natural ESS available in the high-inertia turbine, while attempting to increase overall turbine efficiency by adjusting the controller to match the energy available in the current sea state.

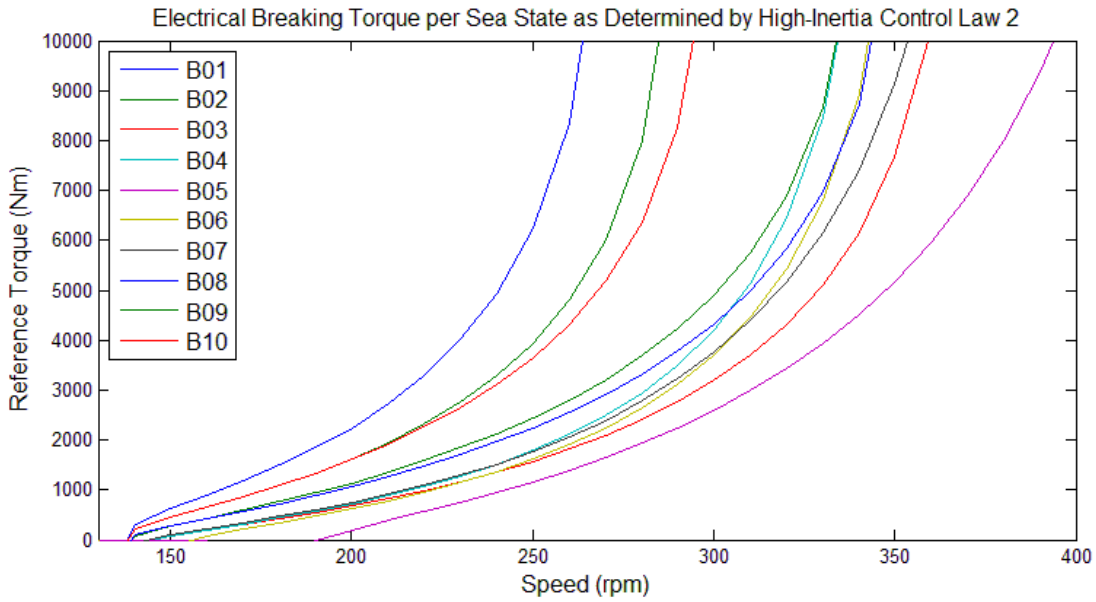

Fig. 5.7: Various torque-speed curves as determined using the high inertia control law equations.

5.6. SIMULATION RESULTS

For the simulations performed, the average electrical power output, average pneumatic-to-electrical power efficiency, and the coefficient of variation for the pneumatic power input and electrical power output were the results of concern for this chapter. The coefficient of variation, c_v, is the indicator used to determine the quality, in terms of grid injection, of the power generated by the BBDB OWC such that

$$c_v = \frac{\sigma}{\mu}, \tag{5.15}$$

where c_v is the power output coefficient of variation of output power, σ is the power output standard deviation, and μ is the power output mean.

For each of the three control strategies describe in Section 5.5, fifty simulations of 30 minutes in duration were performed using the full model presented in Chapter 2 with the impulse turbine developed in Chapter 4. The fifty wave elevation arrays generated were used for testing each of the three control laws, so for each of the three controllers tested, the wave energy input into the system was identical. The fifty simulations were composed of five individual 30-minute wave elevation arrays for each of the ten sea states modelled. The decision to perform five separate simulations per sea state was made in an effort to mitigate any potential anomalies that may arise in a single simulation. The results from the five simulations for each control law simulation were averaged, and the averaged results are presented in the following sections along with a final section which compares and contrasts the results from the three control strategies.

5.6.1. LOW-INERTIA TURBINE

The low-inertia turbine with the MPPT control algorithm was tested first. Over the ten sea states, the averaged pneumatic-to-electrical power conversion efficiencies ranged from 34.0% to 36.4%. The coefficient of variation for the pneumatic input power raged from 1.430 to 1.549, and the coefficient of variation in electrical power output ranged from 1.080 to 1.381. From coefficients of variation, there was little power smoothing achieved by the turbine and controller. Table 5.5 presents the results from the tests performed for each of the ten sea conditions, which include the average pneumatic and electrical power output, the pneumatic-to-electrical power conversion, the coefficient of variation, as detailed in (5.18), and the average turbine speeds. The values are calculated by averaging the results from five separate 30-minute simulations for each of the ten sea states investigated.

The maximum pneumatic-to-mechanical power conversion efficiency of the low-inertia impulse turbine as calculated through the CFD simulations is approximately 39%. The results of the low-inertia turbine tests show that the MPPT algorithm is effective at maximising the turbine efficiency over all sea states. The nature of the changes in flow across the turbine found in an OWC make it very difficult to operate the turbine at constant maximum efficiency, leaving little opportunity for improvement through varying the controller with changes in sea conditions. Fig. 5.8 is a 90-second sample of the pneumatic and electrical power outputs of the model during a simulation

of the OWC in sea state B07, while Fig. 5.9 illustrates the varying rotational velocity of the turbine over the same 90-second period.

Sea State	Average Power Output (kW)		Power Conversion Efficiency	Power Coefficient of Variation		Average Turbine Speed (rpm)
	Pneumatic	Electrical		Pneumatic	Electrical	
B01	48.69	17.40	35.54%	1.445	1.381	142.4
B02	118.15	41.59	35.20%	1.546	1.179	156.9
B03	218.87	74.74	34.15%	1.466	1.081	176.1
B04	184.07	64.58	35.08%	1.430	1.080	170.6
B05	275.73	93.75	34.00%	1.482	1.126	185.5
B06	176.14	62.40	35.42%	1.479	1.137	169.4
B07	200.96	70.43	35.05%	1.524	1.187	173.2
B08	109.74	39.87	36.34%	1.490	1.215	155.9
B09	73.54	26.75	36.38%	1.440	1.262	148.1
B10	72.16	26.17	36.27%	1.549	1.355	147.6

Table 5.5: Low-inertia turbine with MPPT control algorithm simulation results, which represent the averaged values from the five iterations run for each of the ten sea states.

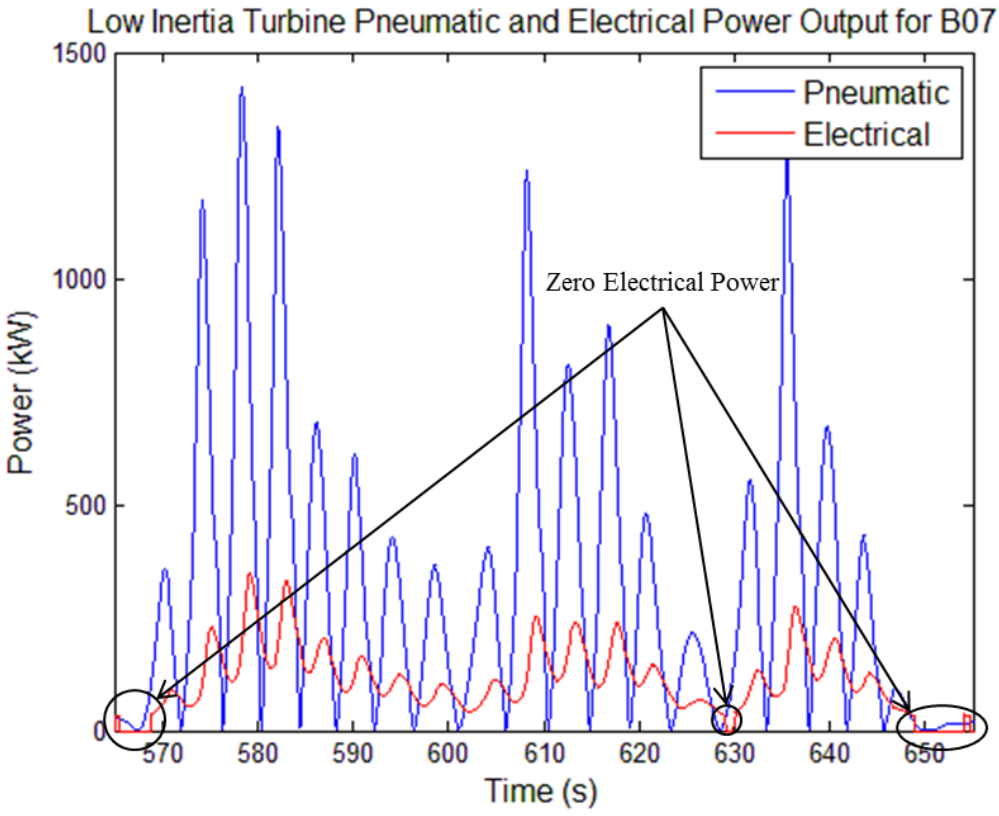

Fig. 5.8: Pneumatic and electrical power output of the OWC model simulated with conditions created to match sea state B07.

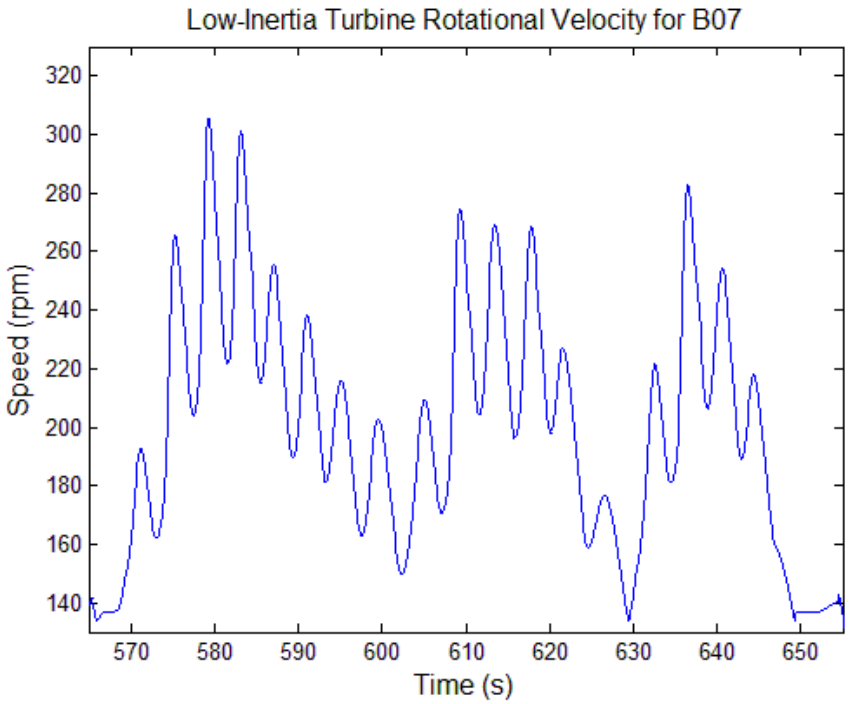

Fig. 5.9: Turbine rotational velocity from of the OWC model simulated with conditions created to match sea state B07.

The swings in pneumatic and electrical power are evident in the both Fig. 5.8 and Fig. 5.9 where the changes in electrical power and rotational velocity can be seen to have 18 different peaks over the 90 second span. The peaks in the electrical power lag behind the peaks in pneumatic power. The lag is the result of delay in the adjustment of the electrical braking torque, which is caused in part by the four sample delay added to the model to reflect the behaviour observed in the sea trials. Also seen in Fig. 5.8 are instances where the electrical power output was zero, which are circled and labelled. This drop to zero in output power occurred in each of the fifty simulations. The power drop was caused when the rotational velocity of the turbine dropped below the minimum operating speed of 140 rpm. The braking torque is set to zero to avoid slowing the turbine to a speed where efficiency would be compromised at high flows, where there is more energy available for conversion.

For comparison, Fig. 5.10 and Fig. 5.11 are 90-second samples of the pneumatic and electrical power outputs and rotational speeds of the model during a simulation of the OWC in sea state B01, which had the lowest amount of pneumatic power available of all the seas tested.

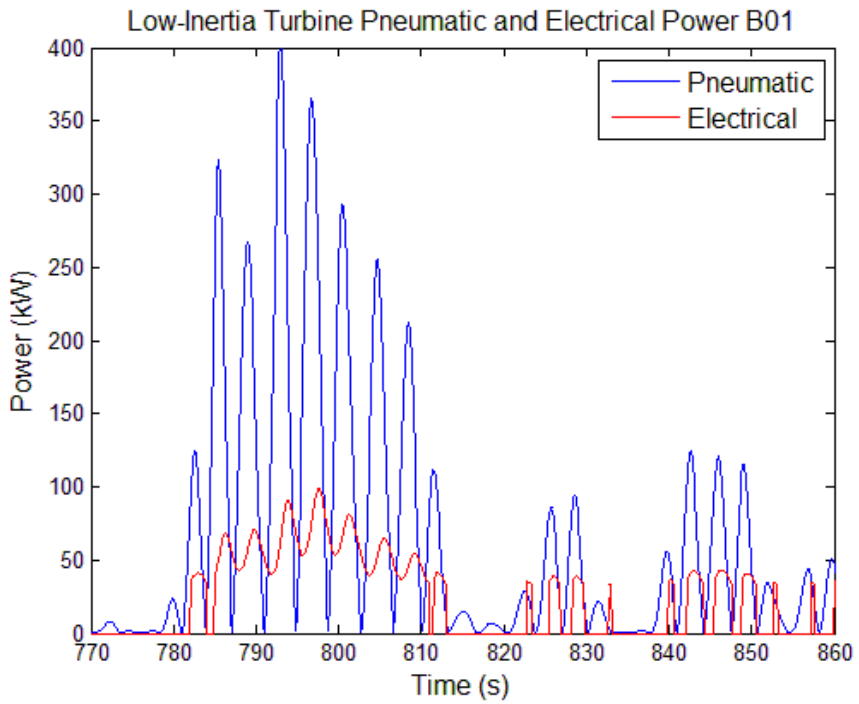

Fig. 5.10: Pneumatic and electrical power output of the OWC model simulated with conditions created to match sea state B01.

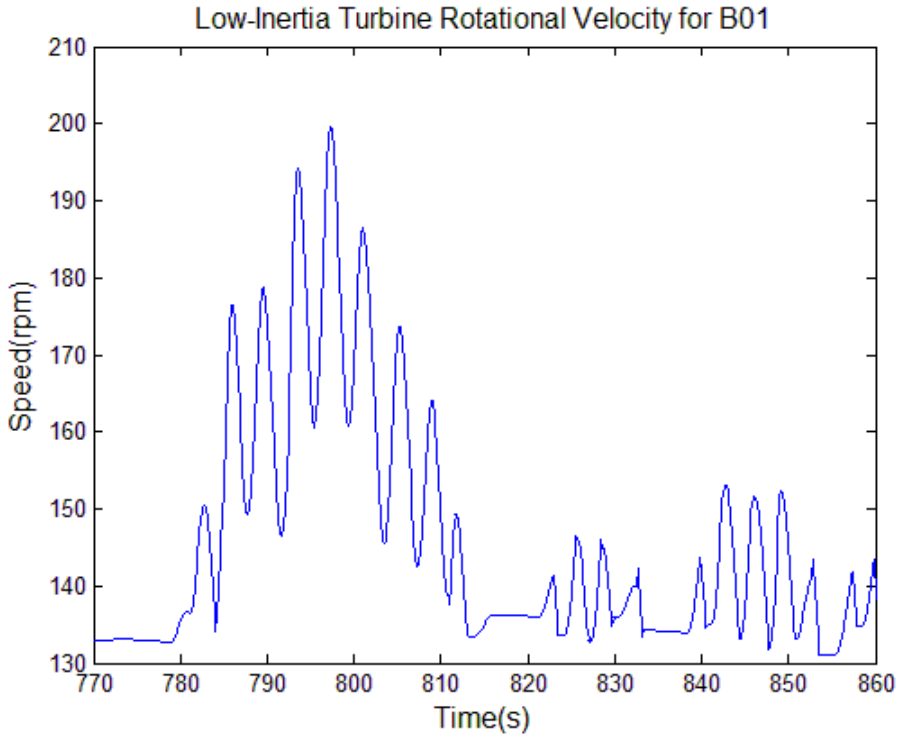

Fig. 5.11: Turbine rotational velocity from of the OWC model simulated with conditions created to match sea state B01.

The data presented in Fig. 5.10 and Fig. 5.11 are from a more energetic period during the B01 sea state simulation. During this time, the differences in energy available in B01 when compared with B07 are obvious, and there are several instances over the 90-second period presented where the electrical output of the OWC is zero because the turbine speed has dropped below the 140 rpm floor. Less energetic sea states than B01 were simulated, but the power available and the electric power output produced were too low to justify device operation and included long periods with no electrical power generation.

Overall, the low-inertia turbine and control algorithm performed well in the simulations carried out for this thesis. The pneumatic-to-electrical power conversion efficiency, which averaged between 34% and 36%, was close enough to the maximum conversion efficiency of 39% to consider the MPPT algorithm a successful method for low-inertia turbine control. The power smoothing of the low inertia turbine and MPPT algorithm was very limited, as the coefficient of variation for the electrical power was not much lower than the coefficient of the variation of the pneumatic input power. The high-inertia turbine and related control algorithms were tested in an effort to increase the power smoothing of the electrical power output and the results of those tests are presented in the ensuing sections.

5.6.2. HIGH-INERTIA TURBINE

For the high-inertia turbine, two different control strategies were implemented. Control Law 1 was based on a single quadratic equation that applied an electrical braking torque based on the turbine rotational speed, and that equation was applied for all sea state conditions. The goal of CL1 was to create a simple single controller that could operate across all seas, require no additional monitoring, and could utilise the natural ESS present in the high inertia turbine.

Control Law 2 was based on creating a separate equation for each major sea state condition. Implementation of CL2 is dependent upon an outside data stream which can update the controller to changes in the sea state conditions in real time. The goal of adjusting the controller equation in CL2 was to increase the efficiency of the turbine when compared to the results in CL1. This was seen as an opportunity to increase device efficiency through implementation of real time data streams through a technique that did not add complexity and physical failure points to the OWC while taking advantage

of advancements in electrical communications methods. The results of the simulations performed with both control laws are presented in the following sections.

5.6.2.1. HIGH-INERTIA TURBINE WITH CONTROL LAW 1 SIMULATION RESULTS

The first of the two controls laws tested with the high inertia turbine, Control Law 1 (CL1), was based on a single algorithm designed to match all possible sea states. CL1 showed the lowest pneumatic-to-electrical power conversion efficiency of the three situations tested, but it also had the lowest electrical power coefficient of variation. The pneumatic-to-electrical power conversion efficiency ranged from 31.6% to 32.3%, so there was less variation in conversion efficiency across the sea states for this set of tests when compared against the efficiency ranges of the low inertia turbine with MPPT control. The coefficient of variation for the pneumatic power ranged from 1.314 to 1.505, and the coefficient of variation for the electrical output power ranged from 0.52 to 0.70, with the higher variations seen in the more energetic sea conditions. In comparison to the results from the low-inertia turbine with the MPPT controller, this indicated a significant power smoothing from pneumatic input power to electrical output power performed by the turbine and controller. Table 5.6 presents the results from the tests performed for each the ten sea conditions. The results presented include the average pneumatic and electrical power output, the pneumatic-to-electrical power conversion, the coefficient of variation, as detailed in equation (5.18), and the average turbine speeds. The values are calculated by averaging the results from five separate 30-minute simulations for each of the ten sea states investigated.

	Average Power Output (kW)		Power Conversion	Power Coefficient of Variation		Average Turbine
Sea State	Pneumatic	Electrical	Efficiency	Pneumatic	Electrical	Speed (rpm)
B01	51.04	16.27	31.88%	1.473	0.519	149.2
B02	122.33	38.65	31.59%	1.462	0.576	210.0
B03	220.05	70.58	32.07%	1.350	0.591	266.3
B04	188.34	60.80	32.28%	1.314	0.630	250.4
B05	275.38	88.76	32.23%	1.351	0.669	286.7
B06	182.42	58.79	32.23%	1.358	0.639	247.3
B07	206.16	66.52	32.27%	1.391	0.700	257.1
B08	117.05	37.51	32.05%	1.407	0.657	205.7
B09	79.10	25.41	32.13%	1.410	0.576	176.6
B10	77.08	24.90	32.30%	1.505	0.560	175.1

Table 5.6: High inertia turbine with Control Law 1 simulation results. The results presented represent the averaged values from the five iterations run for each of the ten sea states.

The high inertia turbine with CL1 showed an average drop in turbine pneumatic-to-electrical power conversion efficiency of 7% from the expected maximum of 39%; however, it also had an improvement in the electrical power output coefficient of variation of over 50% when compared to the pneumatic input power coefficient of variation. The drop in the power coefficient of variation puts the output power in a better position to meet grid quality standards, particularly in a farm which includes multiple devices. To better illustrate the changes in electrical power output between the high and low inertia turbines, Fig. 5.12 presents the same 90-second sample of the pneumatic and electrical power outputs of the model during a simulation of the OWC in sea state B07 with the high-inertia turbine as was presented in Fig. 5.8 for the low inertia turbine, and Fig. 5.13 illustrates the varying rotational velocity of the turbine over the same 90-second period.

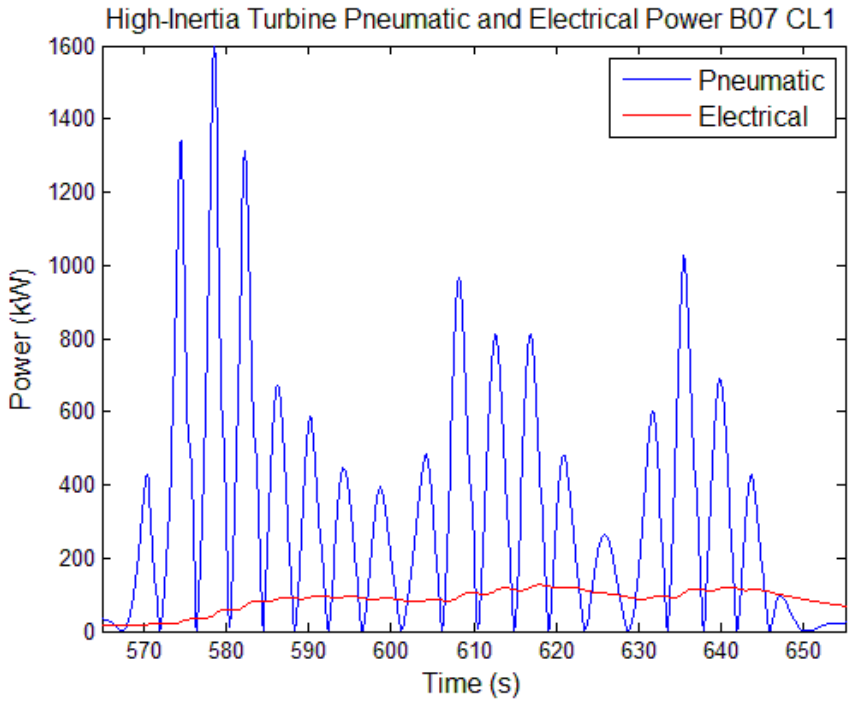

Fig. 5.12: Pneumatic and electrical power output of the OWC model with the high-inertia turbine controlled using Control Law 1 as simulated and conditions created to match sea state B07.

The produced electrical power has much more gradual changes over the 90-second span when compared to the electrical power output produced by the low-inertia turbine and MPPT controller. This is due to both the inertia present in the turbine and the

control law applied to the system. Over the 30-minute simulation presented in Fig. 5.12 and Fig. 5.13, there was only a single instance where the electrical output power fell to zero.

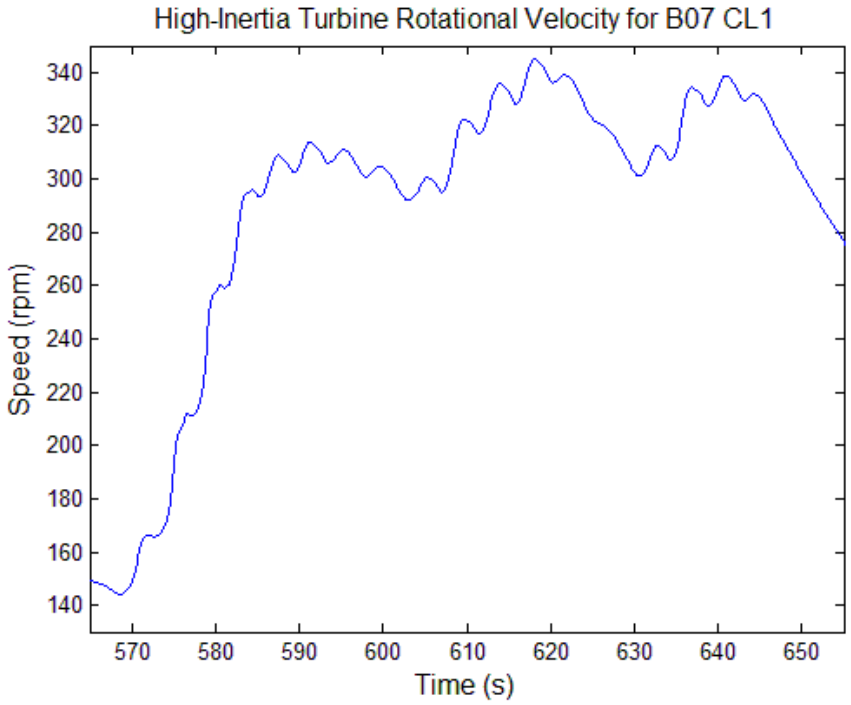

Fig. 5.13: Turbine rotational velocity from of the OWC model simulated with the high-inertia turbine controlled using Control Law 1 and conditions created to match sea state B07.

Fig. 5.14 and Fig. 5.15 below are 90-second samples of the pneumatic and electrical power outputs and rotational speeds of the model during a simulation of the OWC in sea state B01, which had the lowest amount of pneumatic power available of all the seas tested. The samples presented in Fig. 5.14 and Fig. 5.15 were taken over the same time period as the samples presented in Fig. 5.10 and Fig. 5.11 to allow for easier comparison of the results from the various simulations performed for this chapter.

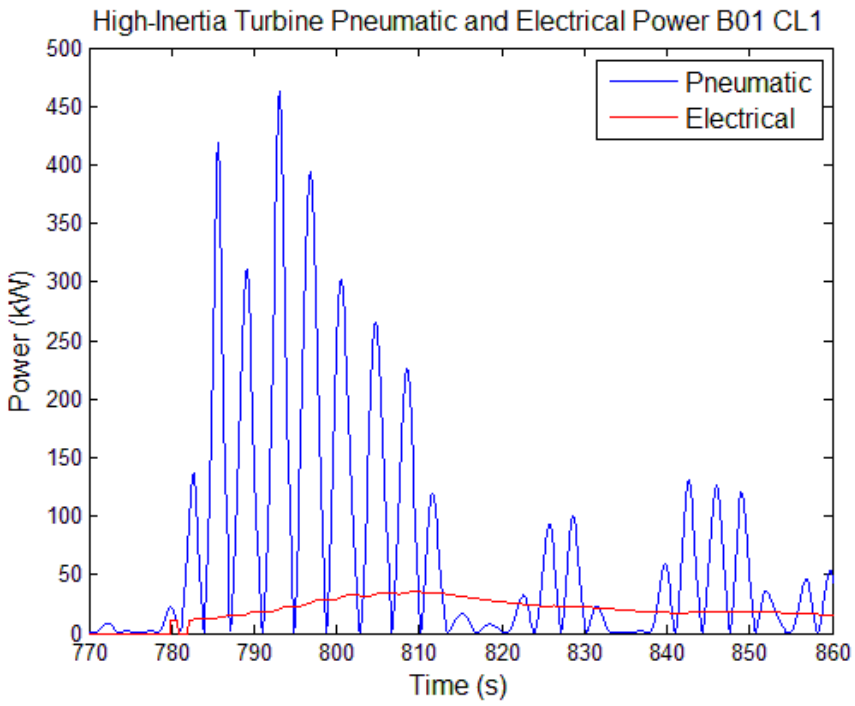

Fig. 5.14: Pneumatic and electrical power output of the OWC model with the high inertia turbine controlled using Control Law 1 as simulated and conditions created to match sea state B01.

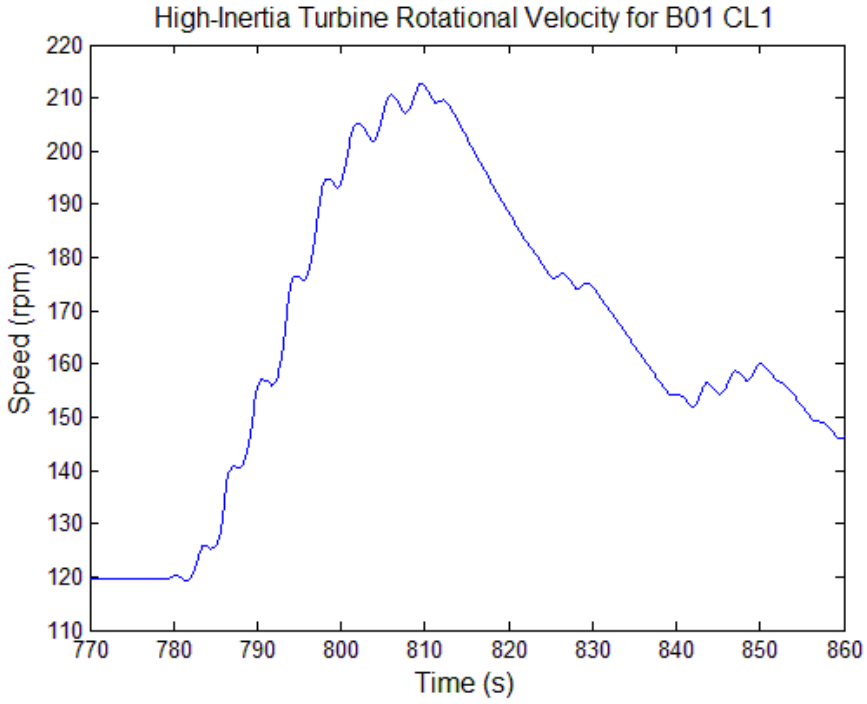

Fig. 5.15: Turbine rotational velocity from of the OWC model simulated with the high inertia turbine controlled using Control Law 1 and conditions created to match sea state B01.

Over the full 30 minutes of the simulation, there were several instances where the power output dropped to zero. All sea states tested saw a reduction in the number of times the electrical power output dropped to zero. This is a result of the power smoothing provided by using a high-inertia turbine as a short-term ESS and was evident at the sea states with the lowest available energy.

The high inertia turbine with CL1 showed that a turbine with a high inertia can be used for short term energy storage to help minimise the coefficient of variance, but at a considerable cost to device efficiency. In an effort to mitigate the efficiency losses while still maintaining the power smoothing benefit of the high inertia turbine, a control strategy was developed that included a different equation for each sea state and was tested and the results are presented in the following sections.

5.6.2.2. HIGH INERTIA TURBINE WITH CONTROL LAW 2 SIMULATION RESULTS

The second of the two controls laws tested with the high inertia turbine, Control Law 2 (CL2), was based on using a unique algorithm designed to match a specific sea state. CL2 was created to increase the pneumatic-to-electrical power conversion of the turbine and generator while still allowing for energy storage in the turbine. CL2 saw an improvement in conversion efficiency when compared to CL1, however the improvement was minor and was not as significant as the change in the coefficient of variation of the output power. The pneumatic-to-electrical power conversion efficiency ranged from 32.1% to 32.9%. The maximum improvement in average electrical power output seen in the ten sea states tested was less than 1.5 kW. The coefficient of variation of the pneumatic input power ranged from 1.324 to 1.518, and the coefficient of variation of the electrical output power ranged from 0.70 to 0.95, again with the higher variations present in the more energetic sea conditions. Table 5.7 presents the results from the tests performed for each the ten sea conditions. The results presented include the average pneumatic and electrical power output, the pneumatic-to-electrical power conversion, the coefficient of variation, as detailed in equation (5.18), and the average turbine speeds. The values are calculated by averaging the results from five separate 30-minute simulations for each of the ten sea states investigated.

Sea State	Average Power Output (kW)		Power Conversion Efficiency	Power Coefficient of Variation		Average Turbine Speed (rpm)
	Pneumatic	Electrical		Pneumatic	Electrical	
B01	50.91	16.35	32.11%	1.460	0.704	151.8
B02	121.96	39.30	32.23%	1.453	0.787	213.5
B03	219.72	71.07	32.35%	1.355	0.806	264.0
B04	188.55	62.07	32.92%	1.324	0.878	250.8
B05	275.27	90.40	32.84%	1.352	0.901	290.9
B06	182.41	58.78	32.22%	1.372	0.835	248.9
B07	206.45	67.49	32.69%	1.401	0.952	258.3
B08	116.92	38.21	32.68%	1.399	0.870	211.3
B09	79.03	25.80	32.64%	1.392	0.801	183.3
B10	76.85	25.24	32.84%	1.518	0.892	172.5

Table 5.7: High inertia turbine with Control Law 2 simulation results, which represent the averaged values from the five iterations run for each of the ten sea states.

The high inertia turbine with CL2 showed an average drop in turbine pneumatic-to-electrical power conversion efficiency of 6.5% from the expected maximum of 39%; and the electrical power output coefficient of variation of over 40% when compared to the pneumatic input power coefficient of variation. The increase in efficiency of the PTO system when compared to the results from CL1 was smaller than originally anticipated, and the increase in the coefficient of variation was higher than anticipated. The increase in the output power variation can be seen in the plots of the pneumatic and electrical power output presented below. Fig. 5.16 presents the 90-second sample of the pneumatic and electrical power outputs of the model during a simulation of the OWC in sea state B07. The oscillation of the electrical output power during the simulations is more pronounced for CL2. Fig. 5.17 illustrates the varying rotational velocity of the turbine over the same 90-second period, which also illustrates the effects of CL2 in the quicker changes in rotation velocity of the turbine.

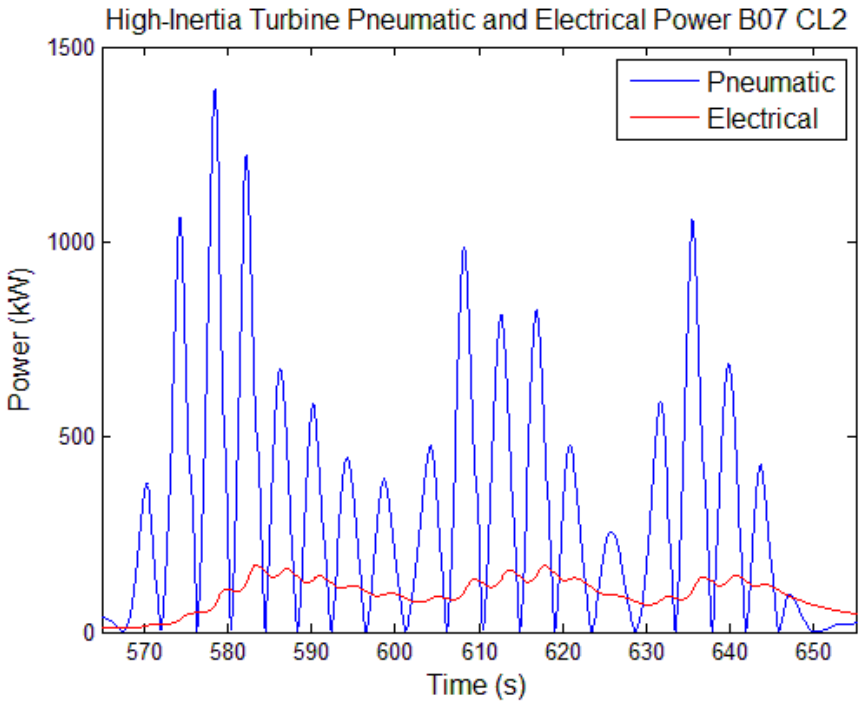

Fig. 5.16: Pneumatic and electrical power output of the OWC model with the high inertia turbine controlled using Control Law 2 as simulated and conditions created to match sea state B07.

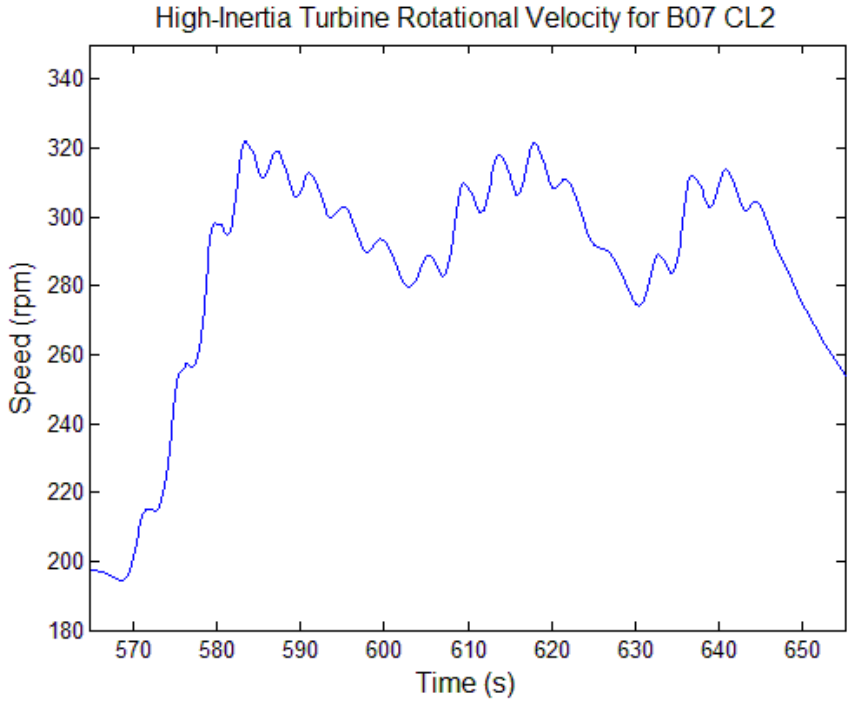

Fig. 5.17: Turbine rotational velocity from of the OWC model simulated with the high inertia turbine controlled using Control Law 2 and conditions created to match sea state B07.

The change in the coefficient of variance from CL1 to CL2 is illustrated in the larger peaks of electrical power output and rotational velocity seen from the simulations using CL2 when compared to the results of CL1. The larger changes in braking torque dictated by the controller are responsible for the change. This was an intended outcome of CL2, however, the benefit in conversion efficiency was smaller than expected. CL2 does manage to avoid any occurrence of zero electrical power output during the simulation, while a single such occurrence was seen using CL1, however the power outputs were similar enough that this difference is considered non-consequential. Fig. 5.18 and Fig. 5.19 below are 90 second samples of the pneumatic and electrical power outputs and rotational speeds of the model during a simulation of the OWC in sea state B01. The samples presented in Fig. 5.14 and Fig. 5.15 were taken over the same time period as the previous plots that represented the results from simulations of sea state B01.

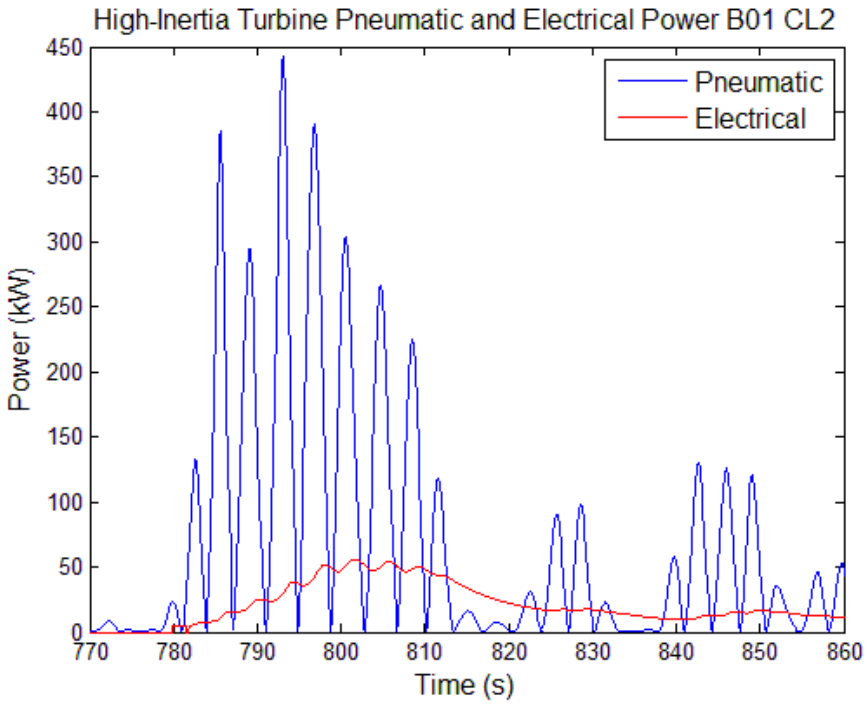

Fig. 5.18: Pneumatic and electrical power output of the OWC model with the high inertia turbine controlled using Control Law 2 as simulated and conditions created to match sea state B01.

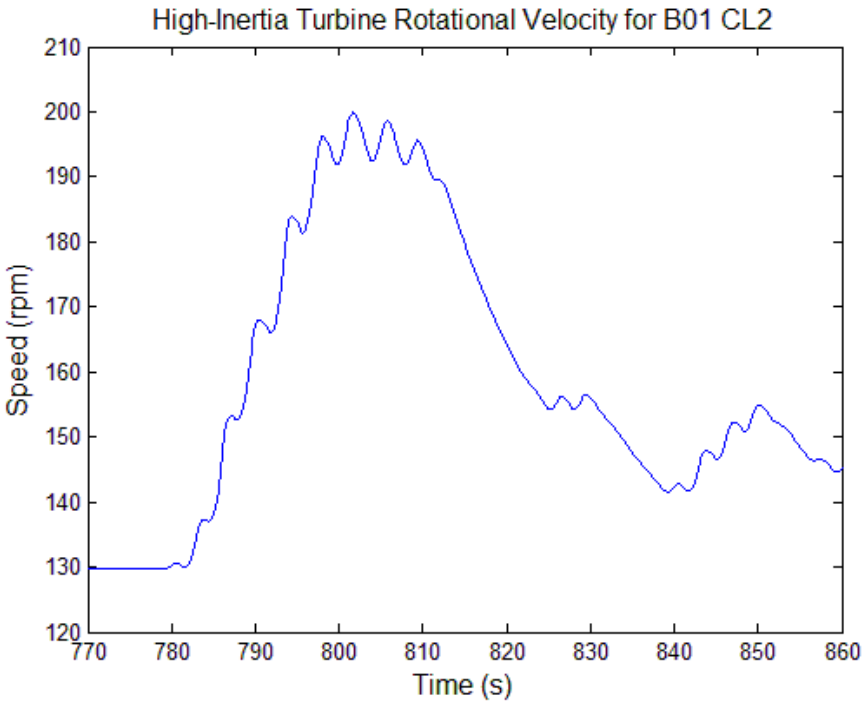

Fig. 5.19: Turbine rotational velocity from of the OWC model simulated with the high inertia turbine controlled using Control Law 2 and conditions created to match sea state B01.

Over the full 30 minutes of the simulation, there were significantly fewer instances where the power output dropped to zero compared to both the low inertia turbine and the high inertia CL1. This appears to be the greatest benefit of CL2 over CL1. Overall, the high inertia turbine with CL2 showed a higher increase in the coefficient of variance, while adding very little improvement to the device efficiency.

5.6.3. Discussion

In general, the simulations presented in Sections 5.6.1 and 5.6.2 realised expected results. The low-inertia turbine with MPPT control had the highest pneumatic-to-electrical conversion efficiency and the highest coefficient of variation for the electrical output power, and the high-inertia turbine simulations produced lower pneumatic-to-electrical power conversion efficiencies and lower coefficients of variation. However, there were behaviours noticed in the simulation outputs that were less anticipated.

The calculations of chamber pressure and flow across the turbine were dependent on the damping coefficient of the turbine, which increases as the turbine rotational velocity increases, and the average rotational velocity of the high-inertia turbine was higher than that of the low-inertia turbine. The differences in pneumatic damping in the simulations resulted in variations in available pneumatic power. These changes seen in the available

pneumatic power reinforce the importance of developing a feedback system between the thermodynamic and the hydrodynamic models.

In the simulations of the high-inertia turbine, it was expected that CL1 would result in lower conversion efficiencies and lower coefficients of variation than CL2. While these results were realised, the change in conversion efficiency between them was smaller than anticipated, while the change in the coefficients of variance was higher than anticipated.

5.6.3.1. OBSERVED AVAILABLE PNEUMATIC POWER

The increase in available pneumatic power when testing the high-inertia turbine control laws was not entirely unanticipated, but the effect it would have on the conversion efficiency was initially underestimated. Due to the lower electrical braking torque by the high-inertia controllers, the turbine had a higher average rotational velocity, which led to higher damping coefficients and slightly higher available pneumatic energy. The higher available pneumatic energy for the high-inertia turbines contributed to higher electrical power outputs than would be predicted simply by applying the difference in conversion efficiency between the low-inertia and high-inertia simulations. Fig. 5.20 shows the average pneumatic power available at the ten different sea states for each of the three control laws tested. The increase in pneumatic power available is only a few kW, but that difference has an effect on the average electrical power output. Fig. 5.21 shows the average electrical power output for all ten different sea states for each of the three control laws tested.

Between Fig. 5.20 and Fig. 5.21, it is evident that the extra pneumatic power available in the high-inertia turbine simulations had an added effect on the calculated efficiencies of the three control strategies. The changes in pneumatic power would probably have an effect on the hydrodynamic response of the BBDB OWC. Due to the lack of hydrodynamic-thermodynamic feedback response system, any changes in the hydrodynamic response of the device are unaccounted for, and it highlights the importance of developing a model that can account for all the systems interactions that are present in an OWC.

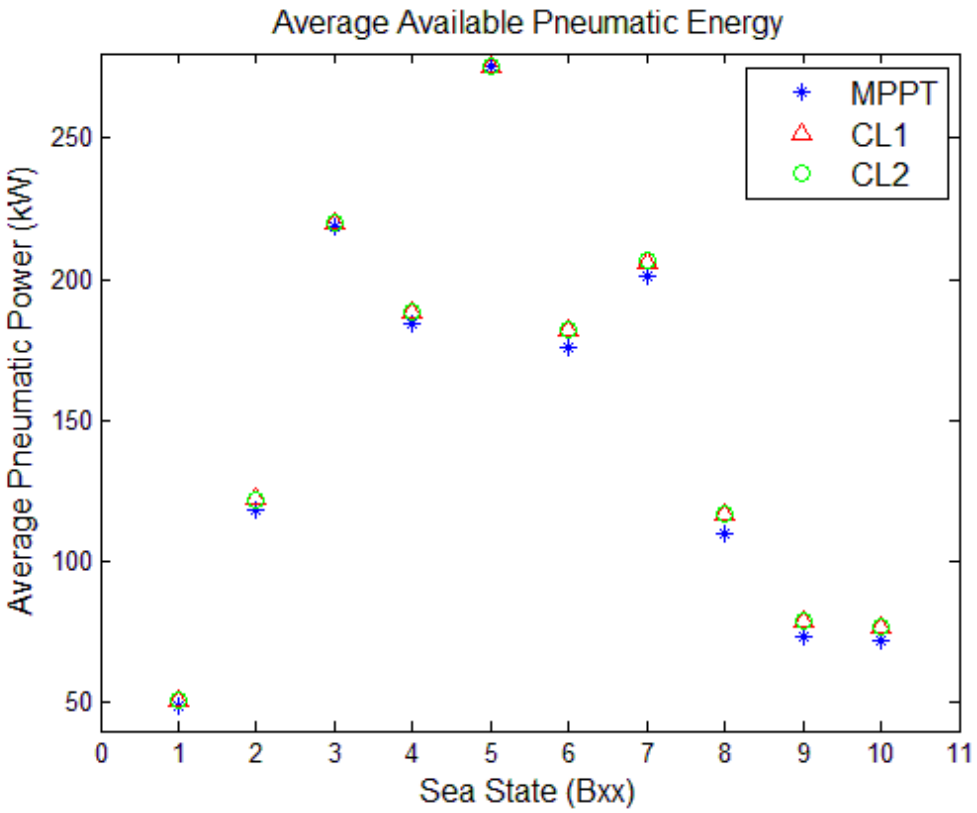

Fig. 5.20: Average available pneumatic energy per sea state for each of the three control laws tested.

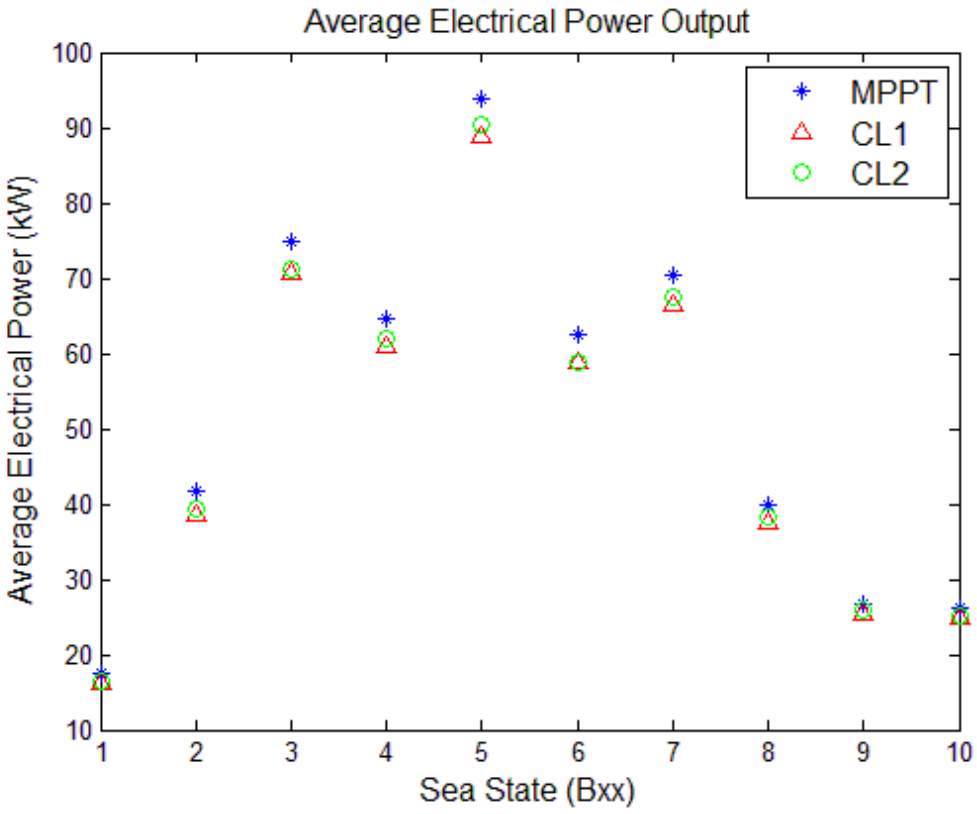

Fig. 5.21: Average electrical power output per sea state for each of the three control laws tested.

5.6.3.2. EVALUATION OF CL1 VERSUS CL2

For the high-inertia turbine, CL1 was designed based on a similar controller used for a high-inertia Wells turbine. While the controller had not been tested on an impulse turbine, the overall strategy had been proven for a short-term ESS-turbine combination and the results published [130]. Conversely, CL2 was designed based on a controller that had not been tested on a high-inertia turbine system, but rather the controller had been developed to allow for the application of controllers that could be adapted to match the changing sea condition [132]. These two different control strategies were investigated to find if overall performance of the OWC could benefit from using a proactive control algorithm in place of a passive control algorithm. It was thought that the proactive controller could improve the average turbine pneumatic-to-electrical energy conversion efficiency without excessively raising the electrical output power coefficient of variation.

Table 5.8 lists the coefficients of variation for the three control strategies for each of the ten sea states simulated as well as the averaged values for each controller. The average increase in the coefficient of variation from CL1 to CL2 was approximately 0.23. Using the coefficient of variation from the low-inertia turbine, the drop in variation from the low-inertia turbine with MPPT control to the high-inertia turbine with CL1 was 49.0%, while the drop in variation when applying CL2 was 29.8%, which is a difference of nearly 20%. To better illustrate the increase in variation between CL1 and CL2, Fig. 5.22 plots the coefficient of variation for each of the three control strategies over all ten sea states modelled for this thesis.

The plot shows that the increase in variation for CL2 was close to half the difference between the variations found using CL1 compared to those found applying MPPT to the low-inertia turbine. This increase, taken along with the much smaller improvement in conversion efficiency from CL1 to CL2, suggest that CL2 offers little improvement in the amount of energy produced while sacrificing a significant amount of output power quality. As CL2 requires additional input to the controller from external sources and could both add to the cost of deployment and controller complexity, the gains made in power produced do not justify the additional systems and costs necessary to implement control strategy CL2 over CL1.

	Coefficient of Variation		
Sea State	MPPT	CL1	CL2
B01	1.381	0.519	0.704
B02	1.179	0.576	0.787
B03	1.081	0.591	0.806
B04	1.080	0.630	0.878
B05	1.126	0.669	0.901
B06	1.137	0.639	0.835
B07	1.187	0.700	0.952
B08	1.215	0.657	0.870
B09	1.262	0.576	0.801
B10	1.355	0.560	0.892
Average	1.200	0.612	0.842

Table 5.8: Coefficients of variation for the three control strategies over each of the 10 sea states simulated.

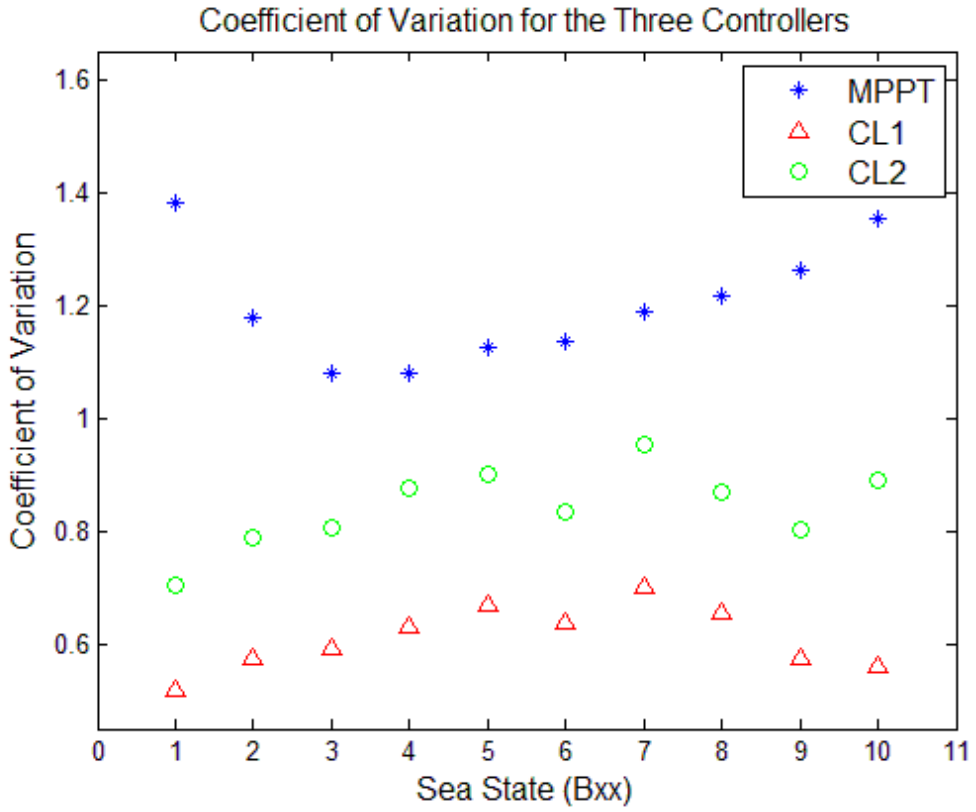

Fig. 5.22: Coefficient of Variation for the three controllers for each of the ten sea states tested during modelling.

5.7. CONCLUSIONS

The MPPT control algorithm performs well as the controller of the low-inertia impulse turbine, allowing the turbine to operate near the maximum efficiency over the duration of the simulations performed. As a single device in a large array of devices, it may be the best turbine and controller combination for a BBDB OWC farm. However, in a smaller array or in the deployment of a single device, the high inertia turbine with CL1 would be a preferred option. The simulations show that the lower average rotational velocity of the impulse turbine, as compared to the Wells turbine, does not preclude the turbine from being used as an on-board ESS for an OWC. The increases in efficiency in CL2 when compared to CL1 do not justify the necessary additional monitoring capability that would be required to properly adjust the controller to match the sea state, making CL1 a better option for control of the high inertia impulse turbine as tested in this thesis.

The differences in the available pneumatic power observed in the various simulations reinforce the importance of creating models that can account for the dynamic system damping created by controllable PTOs. The variation of the rotational velocity of the turbine not only affected the electrical power output, but also the response of the thermodynamic and hydrodynamic systems of the BBDB OWC. The full numerical model was able to account for the changes in the thermodynamic system, but it was unable to do so for the hydrodynamic system. These results lend themselves to work that could be carried out in the future to further improve on the accuracy of the model in representing a real device.

6. CONCLUSIONS AND FUTURE WORK

6.1. CHAPTER TWO

In Chapter 2, the numerical model of the BBDB OWC was presented, along with an introduction to the CORES project that provided the data used to verify the model and the design parameters of the impulse turbine that was investigated later in the thesis. The model was created by combining four different models together using MATLAB and SIMULINK, such that the inputs to the model were the sea state summary statistics and the turbine controller, and the output of the model was the electrical power generated by the device. The four separate models were the irregular sea waves, modelled using the Bretschneider spectrum, the hydrodynamic response of the Internal Water Surface (IWS) based on WAMIT modelling results, the thermodynamic response of the air in the plenum chamber, and the mechanical response of the turbine to the generated air flow. With the exception of the irregular sea wave model, the behaviour of the models was interdependent. The aerodynamic damping of the turbine is affected by its rotational speed, a change in aerodynamic damping changes the thermodynamic damping response of the plenum chamber, and the change in the thermodynamic system alters the hydrodynamic response. The greatest challenge in creating the full model was the integration of these systems.

Each model was presented individually from the sources that were used to build the full model. Section 2.1.1 described the hydrodynamic model and how the sea surface elevation array was generated. The most commonly used wave spectra were presented, and the reason for selecting the Bretschneider spectrum was clarified. The numerical theory behind the Bretschneider spectrum was explained, and the method for generating the array used to represent the changing elevation of the sea surface was disclosed. Following the explanation of the Bretschneider spectrum, the theory behind the hydrodynamic model was described, and the Response Amplitude Operator (RAO) results for the IWS from the WAMIT model were illustrated along with the referenced WAMIT model verification.

The thermodynamic model was disclosed in Section 2.1.2 along with the equations that govern the interaction between the changes in volume and pressure within the plenum chamber. The interdependence between the turbine damping and the thermodynamic response was introduced, and the method by which the equations were applied to the model was outlined.

The approach to modelling the impulse turbine for use in the numerical model was illustrated in Section 2.1.3, and the various methods for characterizing an impulse turbine were specified. The connection between the methods was resolved mathematically to prove that they were interchangeable, and the rationale for selecting the method integrated into the complete model was revealed. Section 2.1.4 described the final stage of the model which was the controller-generator set. The controller was modelled after the system used in the CORES project. Each of the eight data sets included a unique control algorithm, and the model was updated with the appropriate algorithm for each data set. The process for determining the coefficients applied to the controller was explained. The electrical output of the model was derived from the electrical braking torque applied by the controller and the rotational speed of the turbine.

Having presented the various models used to create the numerical model, Section 2.1.5 clarified how the full model was utilized in the work performed for this thesis. The approach for integrating the three interdependent models was explained, and the difficulties faced in building the full model were chronicled. The interdependence of the various models was reiterated, and the method linking the models by applying dynamic turbine damping was explained. The CORES FP-7 project was described, and the reasoning behind applying an impulse turbine to the model was identified. Finally, Section 2.3 divided the turbine into the various physical dimensions required for turbine design. The relationships between the different dimensions of the rotor blades, guide vanes, and hub diameter were found, so that a 1:1 turbine used for the full scale model could be designed for CFD simulations. With the model explained and the origin of the data used to verify the model introduced, the experiments and the data analysis performed to verify the accuracy could be presented in Chapter 3

6.2. CHAPTER THREE

To verify the accuracy of the numerical model, the model was constructed to match the specifications of the OWC deployed during the CORES FP-7 project, and the data collected from the project was used in the verification process. The process was carried out in three stages, first the turbine model was investigated, followed by the combined thermodynamic and turbine models, and the hydrodynamic model was added to test the full model. The process was divided into three stages to allow for a more thorough investigation of each model. There were a total of eight data sets from the CORES

project that were used during the process, totalling just under three hours of OWC electrical generation time.

The turbine model verification process was performed by eliminating the thermodynamic and hydrodynamic processes from the model, leaving only the turbine and controller-generator model. The air flow data collected directly from the CORES project was used as the input to the turbine model in lieu of output from the thermodynamic model. The control algorithm was extrapolated from the experimental data and integrated into the controller model. Simulations were then performed for each of the eight available data sets. The results of the tests showed that the turbine and controller model performed well overall in estimating the electrical power output of the turbine-generate set based on the flow input, which allowed for the verification process to proceed to the next stage.

For the second stage of the verification process, the movement of the IWS calculated from the CORES experimental data was used as the input to the thermodynamic model rather than the output of the hydrodynamic model. The thermodynamic model was then combined with the turbine and controller-generator model. The feedback from the turbine was instituted when calculating the pressures and flows generated by the thermodynamic model, and model simulations were performed using both static and dynamic turbine damping. As with the first stage of the verification process, the turbine speed and electrical power output of the model and experimental data were compared and discussed. In addition to this, the pressures and flows generated by the model were compared to the pressures and flows measured experimentally. The model simulations revealed that applying dynamic turbine damping positively influenced thermodynamic and turbine model performance, as the results from the dynamic damping simulations were a much closer match to the experimental results than those carried out using static turbine damping. The discrepancies between modelled results and experimental results were greater than those seen during turbine-only testing and causal effects of difference in model and experimental flows were evident in the electrical power output values. However, the overall model performance was sufficiently accurate, and the verification process could progress to the final stage.

For the final stage of the verification process, the spectra data for the sea states was not available to be applied in the model presented, so in their place, Bretschneider generated wave spectral array were combined with the hydrodynamic model to create IWS motion. The Bretschneider based IWS motion was used as the input to the

thermodynamic model to create the complete model. The summary statistics used to generate the spectral array were taken from the wave rider buoy deployed in Galway Bay near the deployment site of the CORES OWC. The summary statistics taken from the wave rider buoy were matched chronologically with the eight experimental data sets taken from the CORES project. As the IWS movement was synthetically generated, only the average values from the simulations and experimental data could be compared. During this stage of the verification process, it was discovered that the Bretschneider spectrum does not well represent the conditions in Galway Bay, and it was determined that the hydrodynamic model could not be verified using the data available, leaving the final step in the model verification to be considered for future work.

Chapter 3 also discussed an anomaly discovered during data analysis when comparing the instantaneous modelled and experimental results. Typically, the modelled and experimental outputs match well, but there were times when the experimental data failed to generate electrical power when the model predicted that it would. Following an investigation, it was discovered that there was a problem with the active moving guide vane system. The investigation and results showed that the model could also be used to diagnose system performance problems, and that the model can be valuable during device deployment as well as pre-deployment. Having verified the numerical model accuracy, a full size impulse turbine was designed and characterised using CFD modelling in Chapter 4.

6.3. CHAPTER FOUR

In Chapter 4, the full size, 1:1 scale, impulse turbine used in the final model was designed and modelled in SolidWorks. The SolidWorks model geometry was analysed using the SolidWorks CFD software package Flow Simulation, and the data generated from the CFD simulations were used to numerically characterize the turbine so that it could be used as an alternative to the CORES turbine in the model. To fully assess the validity of the Flow Simulation software package, a 300 mm turbine was also simulated in SolidWorks, and the model results were compared to experimental results published by other authors on physical tests performed on an identical 300 mm turbine.

The design process for the full size turbine was described, and the final dimensions chosen for the full-size turbine were given. The technique for constructing the model turbine and guide vane hubs after selecting the turbine size was explained, and the final turbine system was presented. The completed system included the turbine hub, the

upstream and downstream guide vanes, the air duct in which the turbine resided, and the end caps on either end of the air duct, which were required to perform the CFD simulations.

The settings applied to Flow Simulation were documented in this chapter and identical settings were applied for both turbine sizes. The results of the CFD simulations, which were performed over a range of input pressures and turbine rotational velocities, were presented, and the results of the simulations carried out for both turbine sizes were compared against the published experimental data. It was discovered that Flow Simulator results generally matched the experimental data. The simulation results were not identical to the experimental results, but the values found for the input power and torque coefficients were close matches and the shapes of the characteristic curves were nearly identical. The discrepancies could not be directly traced to how measurements were taken and where sensors were located, but the difference in measurement locations is a potential cause for the inconsistencies. The final conclusion was that the CFD simulations could be used in place of laboratory testing.

With the decision to approve the CFD model results, the CFD data gathered on the full size turbine was used to create the numerical models necessary to implement the turbine in the full model. These included quadratic and 3rd-order polynomial equations that represented the mechanical power, pressure drop, and damping coefficient of the turbine based on the turbine rotational velocity and flow velocities. The characteristic equations produced were applied to the numerical model introduced in Chapter 2, and in Chapter 5, the model, complete with the new turbine, was used to test various control strategies.

6.4. CHAPTER FIVE

In Chapter 5, three separate control strategies were testing using the numerical model presented in Chapter 2 with the turbine designed in Chapter 4. Of the three control strategies, one was applied to a turbine with low-inertia and two were applied to a turbine with high-inertia. The low-inertia turbine controller was based on the Maximum Power Point Tracking (MPPT) algorithm, while the high-inertia controllers included a fixed control algorithm that was applied to all sea state conditions and a control algorithm that was adjusted depending on sea state conditions. The high-inertia turbine was also tested to investigate if an impulse turbine could be applied as a flywheel for

short-term energy storage. The Wells turbine has been found to effectively serve as a flywheel due to the high rotational velocity at which it operates. The impulse turbine operated at much lower rotational velocities and may not be as suitable as an energy storage system, so one aim of Chapter 5 was to investigate this further.

To test the control theories and energy storage capacity of the impulse turbine, the model was simulated in ten different sea states. The summary statistics of each of the ten sea states were disclosed, as was the rational for selecting them. The sea states were generated in MATLAB using the Bretschneider spectrum as described in Chapter 2. The generated sea states were designed to be 30 minutes in duration, and five 30-minute sea wave arrays were generated for each of the ten sea states investigated. The three controller-turbine combinations were simulated using all fifty of the sea wave arrays. From a pneumatic-to-electrical power conversion efficiency perspective, the low-inertia turbine with MPPT control performed best with a conversion efficiency of approximately 36%, which is near the maximum conversion efficiency of the turbine of 39%. For operation in irregular flow conditions, this was a very good result. From the perspective of electrical power quality, the fixed control algorithm performed better than the adjustable control law, which was expected. However, it was discovered that ratio of increased efficiency verses decreased power quality found when applying the adjustable control law was poor, and the determination was made that the adjustable controller tested in this thesis was inferior to the fixed controller tested. The high-inertia impulse turbine did show promise as a short-term energy storage solution for an OWC and further investigation is warranted.

6.5. FUTURE WORK

The work presented in this thesis has shown the importance of accounting for the interdependencies of the subsystems that constitute a BBDB OWC when developing a full numerical model. The majority of the model was verified against experimental data, but due to the difficulties modelling the waves present in Galway Bay and the lack of long term experimental data, the accuracy of the hydrodynamic model could not be satisfactorily proven with the available experimental data. Following a future deployment of a BBDB OWC, a model based on the deployed OWC could be designed, and if the deployment is of a long enough duration in a known ocean environment, the accuracy of the hydrodynamic model could be tested against the experimentally gathered performance data.

As a result of the hydrodynamic model RAO being determined separately through WAMIT by applying a single aerodynamic damping value, the interaction between the hydrodynamic and thermodynamic systems of the OWC could not be fully verified in the model. To improve the model accuracy, a method for creating a better link between the hydrodynamic and thermodynamic models is needed. One solution that could be explored is to perform hydrodynamic modelling of the OWC for a wide array of different static damping values. The results could be used to build a RAO database for the BBDB OWC that could be integrated into the existing numerical model and used to more meticulously represent device behaviour.

The model presented in this thesis was limited to seas with a significant wave height, H_s, below 4 m. This was due to the non-linear response of the device in higher sea conditions. Modelling the non-linear hydrodynamic response of WECs is a difficult problem throughout the wave energy field, and requires an improvement in the understanding of the hydrodynamic interactions of floating bodies and an improvement in computing capabilities in order to create more complete hydrodynamic models. Should a non-linear hydrodynamic model be created to allow the model to account for the more energetic sea conditions, the applications of the model would be significantly increased.

During the verification process of the thermodynamic model with applied dynamic turbine damping, it was discovered that the model more accurately predicted the plenum chamber gauge pressure during the exhalation process; while during the inhalation process, the gauge pressure appeared to be underestimated by the model. Further investigation of this result could be performed to better understand the behaviour of the thermodynamic system, and an improved understanding of the system would help in improving the thermodynamic model, which would lead to a better overall numerical model.

In Chapter 5, the complete model was applied to find out if the performance of the BBDB OWC with a high-inertia turbine could be improved by applying a proactive controller that was adjusted based on the sea state conditions. It was found through simulations that the proactive controller was less effective in overall performance than the passive controller. This was a disappointing result, but the tests were based on only a single active controller. In the future, the model could be used to develop and test better active controllers that could improve device deployment without increasing mechanical or electrical complexity of the BBDB OWC. The reason for continuing to

investigate control theory is that it provides an opportunity to improve device performance without introducing new failure points, which helps to minimise maintenance requirements and increase device lifetime.

APPENDIX A: MATLAB CODE FOR GENERATING RANDOM SEA STATE ARRAYS BASED ON THE BRETSCHNEIDER SPECTRUM

```
load IWS_RAO.mat
load Periods.mat
freqs = 1./Periods;
names = 'PhD B03';
plenum_area = 21*7;              %IWS area

no_sims = 1;
Chamber_Power = zeros(12,15);    %replace 1 with 'i,j' to get each
individual chamber!!

Power_Matrix_V_OWC_M1_Hs_Tz_averaged = zeros(12,15);
Hs = 5;
Tz = 6.06;                       %Average Period (mean)
Tp = Tz * 1.4;                   %Peak Period (mode -most common
period in BretSch-)
add = 0;

for a = 1:no_sims
    dt = 0.1;                    %(simul_time)/(2^12);
    N = 36000;                   % 100 seconds for a sea state
    simul_time = N*dt;
    fm = 1/Tp;                   %modal frequency
    fs = 1/dt;                   %frequency step
    fNyq = 1;
    df = 1/(2*simul_time);
    f = 0:df:fNyq;               % frequency range
    w = 2*pi*f;

    S=(5/16)*((fm^4)./(f.^5)).*(Hs^2).*exp((-5*(fm^4))./(4*(f.^4)));
    % spectral density
    S(1) = 0;
    pers = 1./f;
    pers(1) = 0;
    A = sqrt(2*S*df);            % wave amplitudes

    time_series = zeros(N,length(f)+1);
    time = zeros(N,1);
    p_A_track = zeros(length(f),1);
    IWS_t = zeros(N,length(f)+1);
    phi = 2*pi*rand(length(f),1);   %random phase shift

for k = 1:length(f)
    p_A = IWS_Amplitude(f(1,k), freqs, IWS);

    p_A_track(k,1) = p_A;

for t_step = 1:N
    if t_step == 1
         time(t_step,1) = 0;
    else
         time(t_step,1) = time(t_step-1,1)+dt;
    end
```

```
time_series(t_step,k)=A(1,k)*sin((2*pi*f(1,k)*(time(t_step,1)))+phi(k
,1));
% calculation of sinusoidal components time series
IWS_t(t_step,k)=p_A*(A(1,k))*sin((2*pi*f(1,k)*(time(t_step,1)))+phi(k
,1));

end

end

for t_step = 1:N

      time_series(t_step,length(f)+1)=sum(time_series(t_step,(1:lengt
      h(f))));
      IWS_t(t_step,length(f)+1) = sum(IWS_t(t_step,(1:length(f))));
end

Flow = zeros(N,1);
Flow(1,1) = 0;
WFS = zeros(N,1);       %IWS elevation
Waves = zeros(N,1);     %Ocean surface elevation

for l = 2:N

      Flow(l,1)=((IWS_t(l,length(f)+1)-IWS_t(l-1,length(f)+1))/(time(
      l)-time(l-1)))*plenum_area;
      WFS(l,1) = (IWS_t(l,length(f)+1));
      Waves(l,1) = time_series(l,length(f)+1);

end

end
```

APPENDIX B: MATLAB FUNCTION 'IWS_AMPLITUDE'

```
function [p_A] = IWS_Amplitude(f, freqs, average_RAO)

if f > freqs(1,length(freqs(1,:)))

      p_A = 0;

elseif f < freqs(1,1)

      p_A = 0;

else

for i = 1:length(freqs(1,:))

if f == freqs(1,i)

      p_A = average_RAO(1,i);

break

elseif f > freqs(1,i)

if f < freqs(1,i+1)

p_A = average_RAO(1,i) + (((f-freqs(1,i))/(freqs(1,i+1)-
freqs(1,i)))*(average_RAO(1,i+1)-average_RAO(1,i)));

break

end
end
end
end

return
```

APPENDIX C: BBDB OWC SIMULINK MODEL

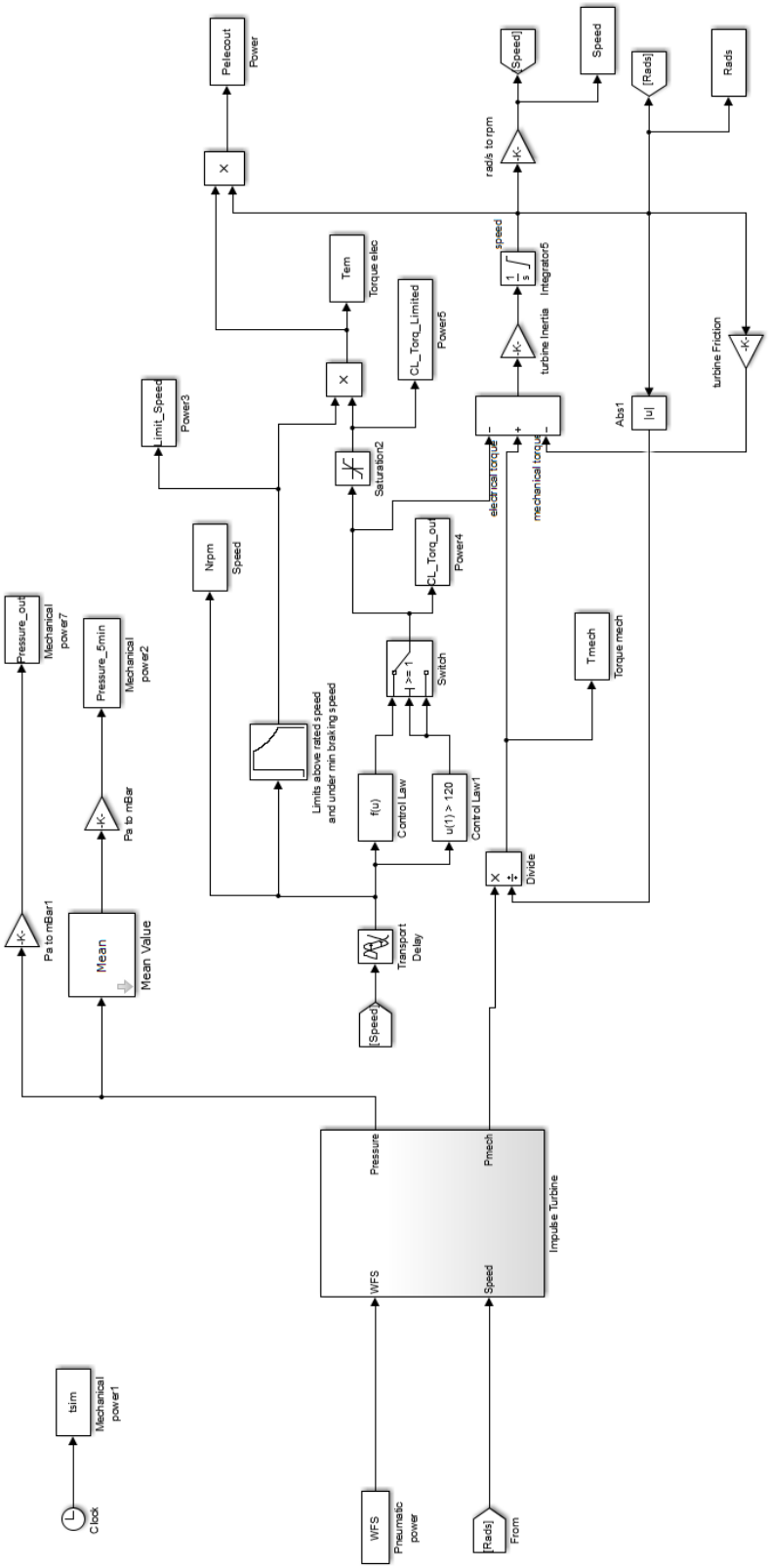

phiavg
Average ND Flow
Output
Input
Average over Simulation1
[phi]
From8
[NDPower]
Goto7
NDPower_out
ND Power output
f(u)
Power Coeff
[phi]
From6
[Ppneu]
Goto6
|u|
Abs
×
Pnumatic Power
[Press]
From5
[Flow]
From4
[Pmech]
Goto8
Saturation1
f(u)
Mech Power Out
[NDPower]
From7
[Rads]
From10
Diam
rho2
rho
rho1
[Rads]
Goto1
[Press]
Goto4
[Flow]
Goto3
[phi]
Goto5
2
Speed
Pressure
Flow
phi
WFS
Speed
Pressure & Flow
[WFS]
Goto2
1
WFS
[WFS]
From3
[Rads]
From2
1
Pressure
[Press]
From9
Scope3
Saturation
Flow
[Flow]
From1
2
Pmech
Pmech_out
Mechanical power3
[Pmech]
From12
Ppneu_out
Mechanical power1
[Ppneu]
From13

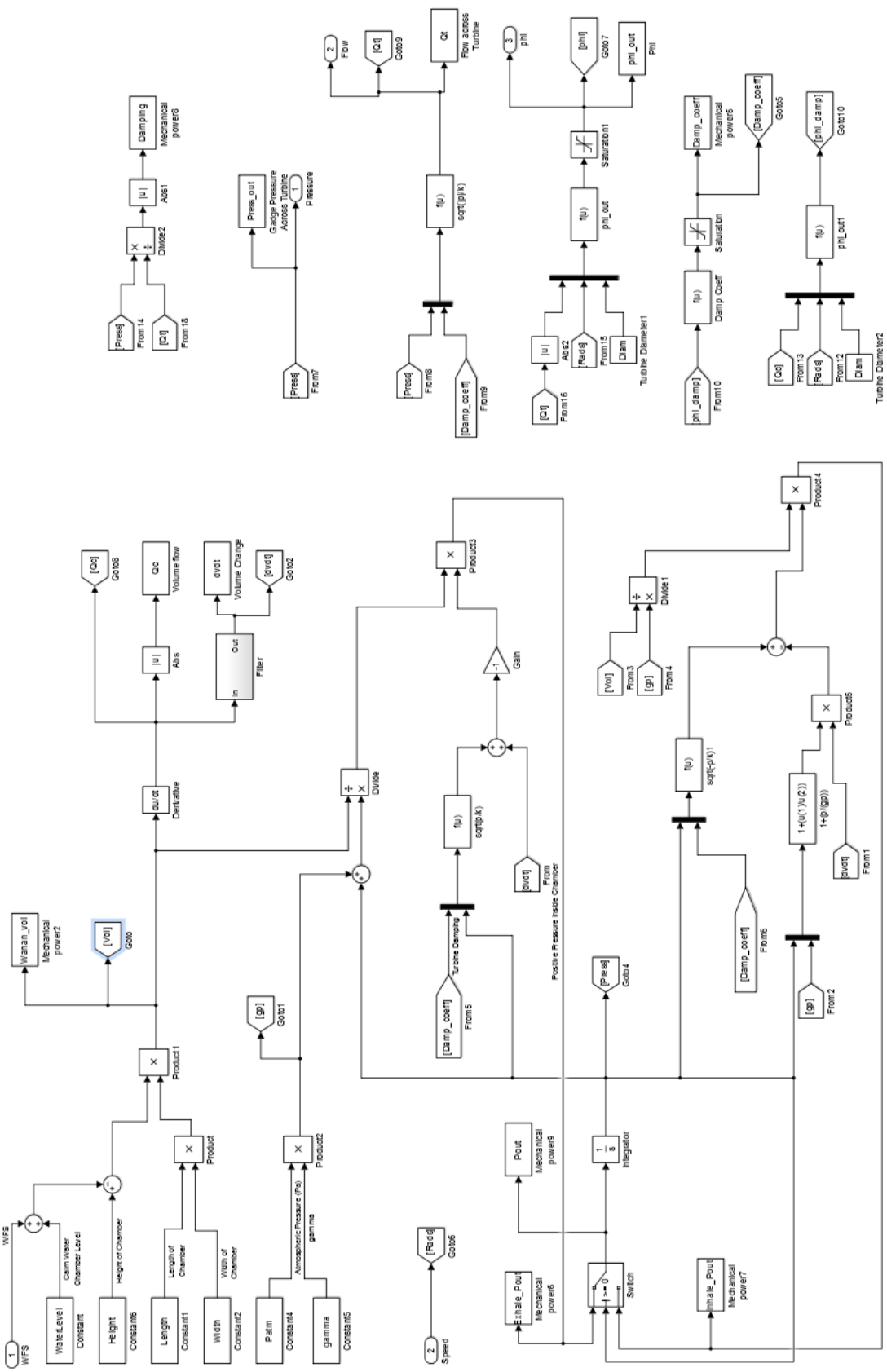
WFS
Water&Level
Calm Water Chamber Level
Height
Height of Chamber
Length
Length of Chamber
Width
Width of Chamber
Patm
Atmospheric Pressure (Pa)
gamma
Product
Product1
Product2
Product3
Product4
Product5
Wanan_vol
Mechanical power2
Goto
Goto1
Goto2
Goto3
Goto4
Goto5
Goto6
Goto9
Goto10
Goto7
Goto8
Derivative
Abs
Volume flow
Volume Change
Filter
Divide
Gain
Turbine Damping
From5
From6
From1
From2
From3
From4
Positive Pressure Inside Chamber
Speed
Pout
Mechanical power9
Exhale_Pout
Mechanical power6
Inhale_Pout
Mechanical power7
Switch
Integrator
Flow
Qt
Flow across Turbine
phi
phi_out
Saturation1
Turbine Diameter1
From16
From15
From8
From9
From7
Pressure
Press_out
Gadge Pressure Across Turbine
Damping
Mechanical power8
Abs1
Divide2
From14
From18
Damp Coeff
Saturation
Mechanical power5
phi_out1
From10
From13
From12
Turbine Diameter2

BIBLIOGRAPHY

[1] F. Umbach, "Global energy security and the implications for the EU," *Energy Policy,* vol. 38, pp. 1229-1240, 2010.

[2] L. Ziska and L. McConnell, "Climate Change, Carbon Dioxide, and Pest Biology: Monitor, Mitigate, Manage," *Journal of Agricultural and Food Chemistry,* 2015.

[3] S. Verma, R. Bhattarai, N. Bosch, R. Cooke, P. Kalita and M. Markus, "Climate Change Impacts on Flow, Sediment and Nutrient Export in a Great Lakes Watershed Using SWAT," *CLEAN–Soil, Air, Water,* vol. 43, no. 11, pp. 1464-1474, 1 November 2015.

[4] J. Paulson, S. Ahdoot, C. Baum, A. Bole, H. Brumberg, C. Campbell, B. Lanphear, J. Lowry, S. Pacheco, A. Spanier and L. Trasande, "Global Climate Change and Children's Health," *Pediatrics,* vol. 136, no. 5, pp. 992-997, 1 November 2015.

[5] S. Seneviratne, M. Donat, A. Pitman, R. Knutti and R. Wilby, "Allowable CO2 emissions based on regional and impact-related climate targets," *Nature,* 20 Janurary 2016.

[6] B. Ang, W. Choong and T. Ng, "Energy security: Definitions, dimensions and indexes," *Renewable and Sustainable Energy Reviews,* vol. 42, pp. 1077-1093, 28 February 2015.

[7] S. Astariz and G. Iglesias, "The economics of wave energy: A review.," *Renewable and Sustainable Energy Reviews,* vol. 45, pp. 397-408, 31 May 2015.

[8] M. Jacobson and M. Delucchi, "Providing all global energy with wind, water, and solar power, Part I: Technologies, energy resources, quantities and areas of infrastructure, and materials," *Energy Policy,* vol. 39, pp. 1154-1169, 2011.

[9] R. Pelc and R. Fujita, "Renewable energy from the ocean," *Marine Policy,* vol. 26, pp. 471-479, 6 July 2002.

[10] M. Esteban and D. Leary, "Current developments and future prospects of offshore wind and ocean energy," *Applied Energy,* vol. 90, no. 1, pp. 128-136, 29 February 2012.

[11] I. López, J. Andreu, S. Ceballos, I. de Alegría and I. Kortabarria, "Review of wave energy technologies and the necessary power-equipment," *Renewable and Sustainable Energy Reviews,* vol. 27, pp. 413-434, 30 November 2013.

[12] J. Cruz, Ocean wave energy: current status and future prespectives., Springer Science & Business Media, 2007.

[13] A. Falcão, "Wave energy utilization: A review of the technologies," *Renewable and Sustainable Energy Reviews,* vol. 14, no. 3, pp. 899-918, 30 April 2010.

[14] Y. Hong, R. Waters, C. Boström, M. Eriksson, J. Engström and M. Leijon, "Review on electrical control strategies for wave energy converting systems," *Renewable and Sustainable Energy Reviews,* vol. 31, pp. 329-342, 31 March 2014.

[15] D. Elwood, A. Schacher, K. Rhinefrank, J. Prudell, S. Yim, E. Amon, T. Brekken and A. von Jouanne, "Numerical modeling and ocean testing of a direct-drive wave energy device utilizing a permanent magnet linear generator for power take-off," in *ASME 28th International Conference on Ocean, Offshore and Arctic Engineering*, 2009.

[16] J. Falnes, "Wave-energy conversion through relative motion between two single-mode oscillating bodies," *Journal of Offshore Mechanics and Arctic Engineering,* vol. 121, no. 1, pp. 32-38, 1 February 1999.

[17] J. Weber, F. Mouwen, A. Parish and D. Robertson, "Wavebob—research & development network and tools in the context of systems engineering," in *8th Europen Wave and Tidal Energy Conference*, Uppsala, Sweden, 2009.

[18] M. Muliawan, Z. Gao and T. Moan, "Application of the Contour Line Method for Estimating Extreme Responses in the Mooring Lines of a Two-Body Floating Wave Energy Converte," *Journal of Offshore Mechanics and Arctic Engineering,* vol. 135, no. 3, p. 031301, 1 August 2013.

[19] R. Hansen, M. Kramer and E. Vidal, “Discrete displacement hydraulic power take-off system for the wavestar wave energy converter,” *Energies,* vol. 6, no. 8, pp. 4001-4044, 7 August 2013.

[20] P. Garcia-Rosa, J. Vilela Soares Cunha, F. Lizarralde, S. Estefen, I. Machado and E. Watanabe, “Wave-to-wire model and energy storage analysis of an ocean wave energy hyperbaric converter,” *Journal of Oceanic Engineering,* vol. 39, no. 2, pp. 386-397, April 2014.

[21] S. Ambühl, F. Ferri, J. Kofoed and J. Sørensen, “Fatigue reliability and calibration of fatigue design factors of wave energy converters,” *International Journal of Marine Energy,* vol. 10, pp. 17-38, 30 June 2015.

[22] F. Gardner, “Learning experiences of AWS pilot plant test offshore Portugal,” in *6th European Wave Energy Conference*, 2005.

[23] H. Polinder and M. Scuotto, “Wave energy converters and their impact on power systems,” in *International Conference on Future Power Systems*, 2005.

[24] R. Henderson, “Design, simulation, and testing of a novel hydraulic power take-off system for the Pelamis wave energy converter,” *Renewable Energy,* vol. 31, no. 2, pp. 271-283, 28 February 2006.

[25] M. Folley, T. Whittaker and J. Van’t Hoff, “The design of small seabed-mounted bottom-hinged wave energy converters,” in *7th European Wave and Tidal Energy Conference*, Porto, Portugal, 2007.

[26] E. Renzi, K. Doherty, A. Henry and F. Dias, “How does Oyster work? The simple interpretation of Oyster mathematics,” *European Journal of Mechanics-B/Fluids,* vol. 47, pp. 124-131, 31 October 2014.

[27] M. Jasinski, M. Malinowski, M. Kazmierkowski, H. Sorensen, E. Friis-Madsen and D. Swierczynski, “Control of AC/DC/AC converter for multi MW wave dragon offshore energy conversion system,” in *International Symposium on Industrial Electronics,* 2007.

[28] T. Thorpe, “An overview of wave energy technologies: status, performance and costs,” *Wave power: moving towards commercial viability,* vol. 26, pp. 50-120, 26 November 1999.

[29] J. Kofoed, P. Frigaard, E. Friis-Madsen and S. H.C., “Prototype testing of the wave energy converter wave dragon,” *Renewable Energy,* vol. 31, no. 2, pp. 181-189, 28 February 2006.

[30] T. Heath, “A review of oscillating water columns,” *Philosophical Transactions of the Royal Society of LondonA: Mathematical, Physical and Engineering Sciences,* vol. 370, no. 1959, pp. 235-245, 2012.

[31] C. Boake, T. Whittaker, M. Folley and H. Ellen, “Overview and initial operational experience of the LIMPET wave energy plant,” in *The Twelfth International Offshore and Polar Engineering Conference*, 2002.

[32] A. Pecher, J. Kofoed, I. Le Crom, F. Neumann and E. Azevedo, “Performance assessment of the Pico OWC power plant following the EquiMar Methodology,” in *The Twenty-first International Offshore and Polar Engineering Conference*, 2011.

[33] Y. Torre-Enciso, I. Ortubia, L. López de Aguileta and J. Marqués, “Mutriku Wave Power Plant: from the thinking out to the reality,” in *8th European Wave and Tidal Energy Conference,* Uppsala, Sweden, 2009.

[34] A. Falcão, “Developments in oscillating water column wave energy converters and air turbines,” in *Renewable Energies Offshore,* 2015, pp. 3-11.

[35] D. O’Sullivan, J. Griffiths, M. Egan and A. Lewis, “Development of an electrical power take off system for a sea-test scaled offshore wave energy device,” *Renewable Energy,* vol. 36, no. 4, pp. 1236-1244, 30 April 2011.

[36] J. Kelly, D. O’Sullivan, W. Wright, Alcorn, R. and A. Lewis, “Challenges and lessons learned in the deployment of an offshore oscillating water column,” *COMPEL: The International Journal for Computation and Mathematics in Electrical and Electronic Engineering,* vol. 33, no. 5, pp. 1678-1704, 26 August 2014.

[37] A. Falcão, J. Henriques and J. Cândido, “Dynamics and optimization of the OWC spar buoy wave energy converter,” *Renewable Energy,* vol. 48, pp. 369-381, 31 December 2012.

[38] Y. Washio, H. Osawa, Y. Nagata, F. Fujii, H. Furuyama and T. Fujita, “The offshore floating type wave power device" Mighty Whale": open sea tests,” in *The Tenth International Offshore and Polar Engineering Conference*, 2000.

[39] M. Takao and T. Setoguchi, “Air turbines for wave energy conversion,” *International Journal of Rotating Machinery,* 7 June 2012.

[40] M. Inoue, K. Kaneko, T. Setoguchi and T. Saruwatari, “Studies on the Wells turbine for wave power generator (turbine characteristics and design parameter for irregular wave),” *JSME international journal. Ser. 2, Fluids engineering, heat transfer, power, combustion, thermophysical properties,* vol. 31, no. 4, pp. 676-682, 15 November 1988.

[41] T. Setoguchi, S. Santhakumar, H. Maeda, M. Takao and K. Kaneko, “A review of impulse turbines for wave energy conversion,” *Renewable Energy,* vol. 23, no. 2, pp. 261-292, 30 June 2001.

[42] A. Falcão, L. Gato and E. Nunes, “A novel radial self-rectifying air turbine for use in wave energy converters,” *Renewable Energy,* vol. 50, pp. 289-298, 28 February 2013.

[43] T. Setoguchi and M. Takao, “Current status of self rectifying air turbines for wave energy conversion,” *Energy Vonversion and Management,* vol. 47, no. 15, pp. 2382-2396, 30 September 2006.

[44] S. Raghunathan, “The Wells air turbine for wave energy conversion,” *Progress in Aerospace Sciences,* vol. 31, no. 4, pp. 335-386, 31 December 1995.

[45] T. Setoguchi, S. Santhakumar, M. Takao, T. Kim and K. Kaneko, “A modified Wells turbine for wave energy conversion,” *Renewable Energy,* vol. 28, no. 1, pp. 79-91, 31 January 2003.

[46] R. Alcorn and W. Beattie, “Observations of time domain data on the wells turbine in the Islay wave-power plant,” in *The Eighth International Offshore and Polar Engineering Conference*, 1998.

[47] A. Brito-Melo, F. Neuman and A. Sarmento, “Full-scale data assessment in OWC Pico plant,” *International Journal of Offshore and Polar Engineering,* vol. 18, no. 01, 2008.

[48] S. Raghunathan and C. Tan, “Performance of Biplane Wells Turbine,” *Journal of energy*, vol. 7, no. 6, pp. 741-742, November 1983.

[49] M. Folley, R. Curran and T. Whittaker, "Comparison of LIMPET contra-rotating wells turbine with theoretical and model test predictions," *Ocean Engineering,* vol. 33, no. 8, pp. 1056-1069, 30 June 2006.

[50] L. Gato and A. Falcão, "Performance of the Wells turbine with a double row of guide vanes," *JSME international journal. Ser. 2, Fluids engineering, heat transfer, power, combustion, thermophysical properties,* vol. 33, no. 2, pp. 268-271, 15 May 1990.

[51] M. Takao, T. Setoguchi, K. Kaneko and M. Inoue, "Air turbine with self-pitch controlled blades for wave energy conversion," *International Journal of Offshore and Polar Engineering,* vol. 7, no. 04, 1 December 1997.

[52] A. Thakker and F. Hourigan, "Modeling and scaling of the impulse turbine for wave power applications," *Renewable Energy,* vol. 29, no. 3, pp. 305-317, 31 March 2004.

[53] C. Xiong and Z. Liu, "Numerical analysis on impulse turbine for OWC wave energy conversion," in *Asia-Pacific Power and Energy Engineering Conference*, 2011.

[54] 2. CORES, "Final Publishable Summary Report," 2011. [Online]. Available: http://www.fp7-cores.eu/CORES%20Final%20publishable%20summary%20report.pdf. [Accessed 21 January 2016].

[55] T. Lewis, "The status of ocean energy development in Europe and some current research questions," in *OCEANS 2011*, 2011.

[56] R. Soulsby, "Calculating bottom orbital velocity beneath waves," *Coastal Engineering,* vol. 11, no. 4, pp. 371-380, 1 November 1987.

[57] B. Cahill and T. Lewis, "Wave period ratios and the calculation of wave power," in *2nd Marine Energy Technology Symposium METS2014*, Seattle, WA, United States, 2014.

[58] B. Cahill and T. Lewis, "Wave energy resource characterization and the evaluation of potential Wave Farm sites," in *OCEANS 2011*, 2011.

[59] V. Venugopal, T. Davey, H. Smith, G. Smith, B. Holmes, S. Barrett, M. Prevosto, C. Maisondieu, L. Cavaleri, L. Bertotti, J. Lawrence and F. Girard, "EquiMar. Deliverable D2. Wave and tidal resource characterization," 2011.

[60] D. V. Evans, “Wave-power absorption by systems of oscillating surface pressure distributions,” *Journal of Fluid Mechanics,* vol. 144, pp. 481-499, 1 January 1982.

[61] M. Folley, A. Babarit, B. Child, D. Forehand, L. O’Boyle, K. Silverthorne, J. Spinneken, V. Stratigaki and P. Troch, “A review of numerical modelling of wave energy converter arrays,” in *31st International Conference on Ocean, Offshore and Arctic Engineering*, 2012.

[62] W. Sheng, R. Alcorn and A. Lewis, “Assessment of primary energy conversions of oscillating water columns. I. Hydrodynamic analysis,” *Journal of Renewable and Sustainable Energy,* vol. 6, no. 5, p. 053113, 1 September 2014.

[63] A. Babarit, J. Hals, M. Muliawan, A. Kurniawan, T. Moan and J. Krokstad, “Numerical benchmarking study of a selection of wave energy converters,” *Renewable Energy,* vol. 41, pp. 44-63, 31 May 2012.

[64] R. Hansen and M. Kramer, “Modelling and control of the Wavestar prototype,” in *9th European Wave and Tidal Energy Conference*, Southampton, UK, 2011.

[65] D. Bull and E. Johnson, “Optimal resistive control strategy for a floating OWC device,” in *10th European Wave and Tidal Energy Conference*, Aaborg, Denmark, July, 2013.

[66] A. G. J. a. R. J. Merigaud, “A nonlinear extension for linear boundary element methods in wave energy device modelling,” in *31st International Conference on Ocean, Offshore and Arctic Engineering*, 2012.

[67] W. Sheng, R. Alcorn and A. Lewis, “On thermodynamics in the primary power conversion of oscillating water column wave energy converters,” *Journal of Renewable and Sustainable Energy,* vol. 5, no. 2, p. 023105, 2013.

[68] C. Josset and A. H. Clement, “A time-domain numerical simulator for oscillating water column wave power plants,” *Renewable Energy,* vol. 32, no. 8, pp. 1379-1402, July 2007.

[69] A. Falcão and P. Justino, “OWC wave energy devices with air flow control,” *Ocean Engineering,* vol. 26, no. 12, pp. 1275-1295, 31 December 1999.

[70] R. Alcorn, “Wave station modelling based on Islay prototype plant,” Queen's Univeristy Belfast, Belfast, United Kingdom, 2000.

[71] M. Folley and T. Whittaker, “The effect of plenum chamber volume and air turbine hysteresis on the optimal performance of oscillating water columns,” in *24th International Conference on Offshore Mechanics and Arctic Engineering*, 2005.

[72] W. Sheng, F. Thiebaut, M. Babuchon, J. Brooks, R. Alcorn and A. Lewis, “Investigation to air compressibility of oscillating water column wave energy converters,” in *32nd International Conference on Ocean, Offshore, and Arctic Engineering*, Nantes, France, 2013.

[73] A. Falcão and R. Rodrigues, “Stochastic modelling of OWC wave power plant performance,” *Applied Ocean Research,* vol. 24, no. 2, pp. 59-71, 30 April 2002.

[74] K. Nielsen, M. Kramer, F. Ferri, A. Zurkinden and M. Alves, “Overview of Wave to Wire Models,” Department of Civil Engineering, Aalborg University, Aalborg, Denmark, 2014.

[75] H. Bailey, J. Ortiz, B. Robertson, B. Buckham and R. Nicoll, “A methodology for wave-to-wire wec simulations,” in *2nd Marine Energy Technology Symposium*, Seattle, WA, United States, 2014.

[76] D. Forehand, A. Kiprakis, A. Nambiar and A. Wallace, “A Fully Coupled Wave-to-Wire Model of an Array of Wave Energy Converters,” *IEEE Transactions on Sustainable Energy,* vol. 7, no. 1, pp. 118-128, 1 Janurary 2016.

[77] Hydraulic and Maritime Research Centre; Marine Institute, “Ocean Energy: Development & evaluation protocol,” University College Cork, Cork, Ireland, 2004.

[78] B. Holmes and K. Nielsen, “Guidelines for the development & testing of wave energy systems,” International Energy Agency Ocean Energy Systems, 2010.

[79] M. Bhinder, C. Mingham, D. Causon, M. Rahmati, G. Aggidis and R. Chaplin, “Numerical modelling of a surging point absorber wave energy

converter," in *8th European Wave and Tidal Energy Conference*, Uppsala, Sweden, 2009.

[80] W. Sheng, R. Alcorn and A. Lewis, "Assessment of primary energy conversions of oscillating water columns. II. Power take-off and validations," *Journal of Renewable and Sustainable Energy,* vol. 6, no. 5, p. 053114, 1 September 2014.

[81] A. Sarmento and A. Falcão, "Wave generation by an oscillating surface-pressure and its application in wave-energy extraction," *Journal of Fluid Mechanics,* vol. 150, pp. 467-485, 1 January 1985.

[82] J. Falnes, Ocean waves and oscillating systems: linear interactions including wave-energy extraction, Cambridge: Cambridge university press, 2002.

[83] WAMIT, "WAMIT v6.4," WAMIT, Chestnut Hill, MA, 2014.

[84] K. O'Sullivan and J. Murphy, "Numerical hydrodynamic and structural analysis of a floating OWC at three Irish Sites," in *33rd International Conference on Ocean, Offshore and Arctic Engineering*, June, 2014.

[85] G. R. A. J. J. M. M. Ramachandran, "Investigation of response amplitude operators for floating offshore wind turbines," in *The Twenty-third International Offshore and Polar Engineering Conference*, Anchorage, Alaska, USA, 2013.

[86] C. Bretschneider, "On the determination of the design ocean wave spectrum," *Look Lab/Hawaii,* vol. 7, no. 1, pp. 1-23, 1977.

[87] W. Pierson and L. Moskowitz, "A proposed spectral form for fully developed wind seas based on the similarity theory of SA Kitaigorodskii," *Journal of Geophysical Research,* vol. 69, no. 24, pp. 5181-5190, 15 December 1964.

[88] K. Hasselmann, T. Barnett, E. Bouws, H. Carlson, D. Cartwright, K. Enke, J. Ewing, H. Gienapp, D. Hasselmann, P. Kruseman and A. Meerburg, "Measurements of wind-wave growth and swell decay during the Joint North Sea Wave Project (JONSWAP)," *Deutches Hydrographisches Institut,* 1 January 1973.

[89] S. Barrett and A. Lewis, "Ireland's ¼ Scale Wave Energy Test Site," in *AGMET Conference*, Dublin, Ireland, 2008.

[90] M. Ochi and E. Hubble, “Six-parameter wave spectra,” *Coastal Engineering Proceedings,* vol. 1, no. 15, 1976.

[91] A. Jerri, “The Shannon sampling theorem—Its various extensions and applications: A tutorial review,” *Proceedings of the IEEE,* vol. 65, no. 11, pp. 1565-1596, November 1977.

[92] A. Sarmento, L. Gato and A. Falcão, “Turbine-controlled wave energy absorption by oscillating water column devices,” *Ocean Engineering,* vol. 17, no. 5, pp. 481-497, December 1990.

[93] S. Anand, V. Jayashankar, S. Nagata, K. Toyota, M. Takao and T. Setoguchi, “Performance estimation of bi-directional turbines in wave energy plants,” *Journal of Thermal Science,* vol. 16, no. 4, pp. 346-352, 1 November 2007.

[94] A. Thakker, J. Jarvis and A. Sahed, “Design charts for impulse turbine wave energy extraction using experimental data,” *Renewable Energy,* vol. 34, no. 10, pp. 2264-70, 31 October 2009.

[95] F. Thiebaut, D. O’Sullivan, P. Kracht, S. Ceballos, J. Lopez, C. Boake, J. Bard, N. Brinquete, J. Varandas, L. Gato and R. Alcorn, “Testing of a floating OWC device with movable guide vane impulse turbine power take-off,” in *9th European Wave and Tidal Eneryg Conference*, Southampton, UK, 2011.

[96] Mathworks, “Simscape Power Systems,” Mathworks, Natick, MA, 2016.

[97] L. Alberti, E. Tedeschi, N. Bianchi, M. Santos and A. Fasolo, “Effect of the generator sizing on a wave energy converter considering different control strategies,” *COMPEL-The international journal for computation and mathematics in electrical and electronic engineering,* vol. 32, no. 1, pp. 233-247, 2012.

[98] MathWorks, “MATLAB R2013b,” MathWorks, Natick, MA, 2013.

[99] R. Alcorn, A. Blavette, M. Healy and A. Lewis, “FP7 EU funded CORES wave energy project: a coordinators' perspective on the Galway Bay sea trials,” *Underwater Technology,* vol. 32, no. 1, pp. 51-59, 1 March 2014.

[100] R. Alcorn, A. Lewis and M. Healy, “Coordinators Overview and Lessons Learned From the Galway Bay Seatrials of the FP7 EU Funded CORES Wave

Energy Project," in *32nd International Conference on Ocean, Offshore and Arctic Engineering*, 2013.

[101] T. K. K. T. H. M. H. Setoguchi and M. Inoue, "Impulse Turbine with Self-Pitch-Controlled Guide Vanes for Wave Power Conversion (Guide Vanes Connected by Link Motion)," in *The Fifth International Offshore and Polar Engineering Conference*, 1995.

[102] T. Setoguchi, M. Takao, Y. Kinoue, K. Kaneko, S. Santhakumar and M. Inoue, "Study on an impulse turbine for wave energy conversion," in *The Ninth International Offshore and Polar Engineering Conference*, 1999.

[103] H. Maeda, S. Santhakumar, T. Setoguchi, M. Takao, Y. Kinoue and K. Kaneko, "Performance of an impulse turbine with fixed guide vanes for wave power conversion," *Renewable Energy,* vol. 17, no. 4, pp. 533-547, 1 August 1999.

[104] Y. Cui, Z. Liu, J. Jin and H. Shi, "Computed Effects of the Number of Guide Vanes on Performance of Impulse Turbine for OWC System," Sciencepaper Online, Beijing, 2013.

[105] H. Maeda, T. Setoguchi, M. Takao, K. Sakurada, T. Kim and K. Kaneko, "Comparative study of turbines for wave energy conversion," *Journal of Thermal Science,* vol. 10, no. 1, pp. 26-31, 1 March 2001.

[106] A. Thakker, P. Frawley, H. Khaleeq, Y. Abugihalia and T. Setoguchi, "Experimental and CFD analysis of 0.6 m impulse turbine with fixed guide vanes," in *The Eleventh International Offshore and Polar Engineering Conference*, 2001.

[107] S. Okuhara, M. Takao, A. Takami and T. Setoguchi, "A Twin Unidirectional Impulse Turbine for Wave Energy Conversion," *Open Journal of Fluid Dynamics,* vol. 2, no. 04, p. 343, 26 December 2012.

[108] M. Webster and L. Gato, "The effect of rotor blade sweep on the performance of the Wells turbine," in *The Eighth International Offshore and Polar Engineering Conference*, 1998.

[109] B. Cahill and A. Lewis, "Wave energy resource characterisation of the atlantic marine energy test site," *International Journal of Marine Energy*, vol. 1, pp. 3-15, 30 April 2013.

[110] F. Fusco and J. Ringwood, "Short-term wave forecasting for real-time control of wave energy converters," *IEEE Transactions on Sustainable Energy,* vol. 1, no. 2, pp. 99-106, July 2010.

[111] "Met Eireann Marine Observations," Met Eireann, 2016. [Online]. Available: http://www.met.ie/marine/marine_map.asp. [Accessed March 2015].

[112] W. Sheng, A. Lewis and R. Alcorn, "Numerical studies on hydrodynamics of a floating oscillating water column," in *30th International Conference on Ocean, Offshore and Arctic Engineering,* 2011.

[113] Y. Masuda, T. Kuboki, A. Thakker, T. Lewis, X. Liang and P. Sun, "Prospect of economical wave power electric generator by the terminator backward bent duct buoy (BBDB)," in *The Twelfth International Offshore and Polar Engineering Conference,* 2002.

[114] A. Kurniawan, J. Hals and T. Moan, "Modelling and simulation of a floating oscillating water column," in *30th International Conference on Ocean, Offshore and Arctic Engineering,* 2011.

[115] B. Hyun, J. Moon, S. Hong and Y. Lee, "Practical numerical analysis of inpulse turbine for OWC-type wave energy conversion using a commercial CFD code," in *The Fourteenth International Offshore and Polar Engineering Conference,* 2004.

[116] P. Sola, "Design and evaluation of a 0.3m impulse turbine with fixed guide vanes," University College Cork, 2012.

[117] SolidWorks, "Flow Simulation 2014 Technical Reference," SolidWorks, 2014.

[118] T. K. K. M. H. Setoguchi, T. Kim and M. Inoue, "Impulse turbine with self-pitch-controlled guide vanes for wave power conversion: performance of mono-vane type," *International Journal of Offshore and Polar Engineering,* vol. 3, no. 01, 1 March 1993.

[119] D. Murray, J. Hayes, D. O'Sullivan and M. Egan, "Supercapacitor testing for power smoothing in a variable speed offshore Wave Energy Converter," *IEEE Journal of Oceanic Engineering,* vol. 37, no. 2, pp. 301-308, April 2012.

[120] Z. Chen and E. Spooner, "Grid power quality with variable speed wind turbines," *IEEE Transactions on Energy Conversion,* vol. 16, no. 2, pp. 148-154, June 2001.

[121] International Electrotechnical Commissioin, "IEC61400-21: Wind turbines – Part 21: Measurement and assessment of power quality characteristics of grid connected wind turbines," International Electrotechnical Commissioin, 2008.

[122] A. Blavette, D. O'Sullivan, A. Lewis and M. Egan, "Impact of a wave farm on its local grid: Voltage limits, flicker level and power fluctuations," in *OCEAN 2012*, Yeosu, South Korea, 2012.

[123] M. Lu, C. Chang, W. Lee and L. Wang, "Combining the wind power generation system with energy storage equipments," in *Industry Applications Society Annual Meeting*, 2008.

[124] H. Ding, Z. Hu and Y. Song, "Stochastic optimization of the daily operation of wind farm and pumped-hydro-storage plant," *Renewable Energy,* vol. 48, pp. 571-578, 31 December 2012.

[125] B. Dunn, H. Kamath and J. Tarascon, "Electrical energy storage for the grid: a battery of choices," *Science,* vol. 334, no. 6058, pp. 928-935, 18 November 2011.

[126] F. Barbir, "PEM electrolysis for production of hydrogen from renewable energy sources," *Solar Energy,* vol. 78, no. 5, pp. 661-669, 31 May 2005.

[127] H. Lund and G. Salgi, "The role of compressed air energy storage (CAES) in future sustainable energy systems," *Energy Conversion and Management*, vol. 50, no. 5, pp. 1172-1179, 31 May 2009.

[128] M. Beaudin, H. Zareipour, A. Schellenberglabe and W. Rosehart, "Energy storage for mitigating the variability of renewable electricity sources: An updated review," *Energy for Sustainable Development,* vol. 14, no. 4, pp. 302-314, 31 December 2010.

[129] B. Bolund, H. Bernhoff and M. Leijon, "Flywheel energy and power storage systems," *Renewable and Sustainable Energy Reviews,* vol. 11, no. 2, pp. 235-258, February 2007.

[130] S. Ceballos, J. Rea, E. Robles, I. Lopez, J. Pou and D. O'Sullivan, "Control strategies for combining local energy storage with wells turbine oscillating water column devices," *Renewable Energy,* vol. 83, pp. 1097-1109, 30 November 2015.

[131] T. Yoshida, M. Sanada, S. Morimoto and Y. Inoue, "Study of flywheel energy storage system for power leveling of wave power generation system," in *15th International Conference on Electrical Machines and Systems,* 2012.

[132] P. Justino and A. Falcão, "Rotational speed control of an OWC wave power plant," *Journal of Offshore Mechanics and Arctic Engineering,* vol. 121, no. 2, pp. 65-70, 1 May 1999.

[133] D. O'Sullivan and A. Lewis, "Generator selection for offshore oscillating water column wave energy converters," *Transactions on Energy Conversion,* vol. 26, no. 2, pp. 603-614, June 2011.

[134] J. Kelly, W. Wright, D. O'Sullivan and A. Lewis, "A Study: Potential supervisory Real Time Integrated Monitoring and Control System (RTIMCS) solutions for wave energy converters," in *European Wave and Tidal Energy Conference*, Aalborg, Denmark, 2013.

[135] M. Govardhan and T. Dhanasekaran, "Effect of guide vanes on the performance of a self-rectifying air turbine with constant and variable chord rotors," *Renewable Energy,* vol. 26, no. 2, pp. 201-219, 30 June 2002.

[136] D. Urban, J. Sheffield and D. Lobell, "The impacts of future climate and carbon dioxide changes on the average and variability of US maize yields under two emission scenarios," *Environmental Research Letters,* vol. 10, no. 4, p. 045003, 30 March 2015.

[137] Y. Cui and Z. Liu, "Effects of solidity ratio on performance of OWC impulse turbine," *Advances in Mechanical Engineering,* vol. 7, no. 1, p. 121373, 2015.

[138] American Petroleum Institute, Standard 2RD, Dynamic Risers for Floating Production Systems, Second ed., American Petroleum Institute, 2013.

[139] R. Alcorn, W. C. Beattie and R. Douglas, "Transient performance modelling of a Wells turbine," in *Third European Wave Energy Conference*, Patras, Greece, 1998.

[140] A. Blavette, D. O'Sullivan, R. Alcorn, A. Lewis and M. Egan, "Impact of a medium-size wave farm on grids of different strength levels," *Transactions on Power Systems,* vol. 29, no. 2, pp. 917-923, March 2014.

[141] D. Cashman, D. O'Sullivan, M. Egan and J. Hayes, "Modelling and analysis of an offshore oscillating water column wave energy converter," in *8th European Wave and Tidal Energy Conference*, Uppsala, Sweden, 2009.

[142] N. Delmonte, D. Barater, F. Giuliani, P. Cova and G. Buticchi, "Oscillating water column power conversion: A technology review," in *Energy Conversion Congress and Exposition (ECCE)*, Pittsburgh, PA, USA, Sept. 2014.

[143] A. Falcão, "First generatino wave power plants: Current status and R&D requirements," in *ASME 2003 22nd International Conference on Offshore Mechanics and Arctic Engineering*, 2003.

[144] M. Marei, M. Mokhtar and A. El-Sattar, "MPPT strategy based on speed control for AWS-based wave energy conversion system," *Renewable Energy*, vol. 83, pp. 305-317, 30 November 2015.

[145] T. Setoguchi, S. Santhakumar, H. Maeda, M. Takao and K. Kaneko, "A review of impulse turbines for wave energy conversion," *Renewable Energy*, vol. 23, no. 2, pp. 261-292, 30 June 2001.

[146] T. Setoguchi and M. Takao, "Current status of self rectifying air turbines for wave energy conversion," *Energy Vonversion and Management,* vol. 47, no. 15, pp. 2382-2396, 30 September 2006.

[147] B. Drew, A. Plummer and M. Sahinkaya, "A review of wave energy converter technology," *Proceedings of the Institution of Mechanical Engineers, Part A: Journal of Power and Energy*, vol. 223, no. 8, pp. 887-902, 1 December 2009.